Characterisation and Friction Reduction Mechanisms of Diamond-Like Carbon Graphene Nanoplatelet Nanocomposites for Lubricated Tribological Applications

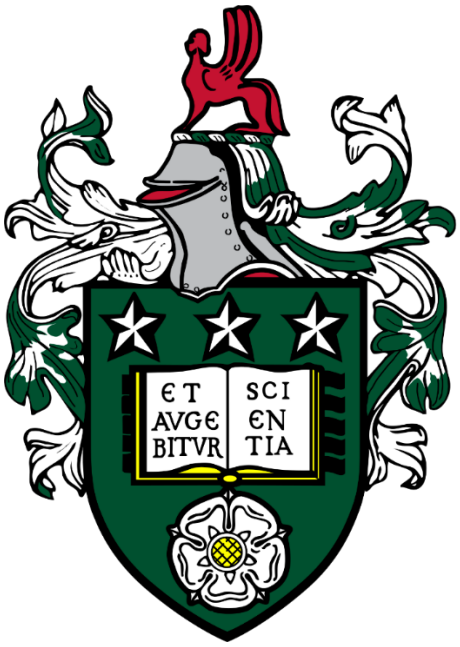

Robbie Nathan Brittain

School of Mechanical Engineering

University of Leeds

June 2023

Submitted in accordance with the requirements

for the degree of

Doctor of Philosophy

The candidate confirms that the work submitted is his own, except where work which has formed part of jointly authored publications has been included. The contribution of the candidate and the other authors to this work has been explicitly indicated below. The candidate confirms that appropriate credit has been given within the thesis where reference has been made to the work of others.

Cross-sectioning of DLC-GNP nanocomposite and scanning electron images of samples was completed under instruction from the author by Stuart Micklewaite using the LEMAS facilities at the University of Leeds. The transmission electron microscope / energy electron loss spectroscopy was conducted under instructions from the author by Dr Zabeada Aslam. Dr Helen Freeman assisted with energy electron loss spectra analysis.

Papers and Conferences Contributing to this Thesis

Papers

"***Graphene Nanoplatelet Nanocomposites for Lubricated Environments",*** *Brittain R, Liskiewicz T, Morina A, Neville A, Yang L. Carbon. 2023 Jan 31. (Published)*

"Diamond-like Carbon – Graphene Nanoplatelets nanocomposites: Effects of sliding distance and thickness on the tribological properties." *Brittain R, Liskiewicz T, Morina A, Yang L. 2023. (Manuscript Prepared)*

Conferences

TriboUK 2019, University of Leeds, "*Effect of GNP Concentration on Friction and Wear in DLC-GNP Nanocomposites*".

China Nano 2019, Beijing, "*Low Friction and Wear DLC-GNP Nanocomposites in base-oil lubricated contacts*".

Patents

International Patent Application No PCT/GB2022/051793 Publication Number WO/2023/285799/A1; WIPO (PCT)Tech Title; Tribological Composite

Ex Nihilo Nihil Fit

Acknowledgements

I would first like to thank my primary supervisor Dr Liuquan Yang, for his help and support throughout my PhD; without your feedback and guidance, I could not have produced any of this work. Secondly, I would like to thank the remainder of my supervision team throughout my PhD; Professor Tomasz Liskiewicz, the late Professor Anne Neville, and Professor Ardian Morina, all your knowledge and guidance has been very welcomed over the past few years.

To my wife Kristine, it has been an absolute pleasure to share the experience of working side by side with you over the previous five years, and something we can treasure forever; your love and support have helped me.

To my best man at my wedding and closest friend Aaron William Thornley, thank you for the time we spent together at the library and my wedding. I will never forget it. My PhD experience would have been a lot less enjoyable without your support.

To my family, thank you for your constant support throughout the last 11 years of my university experience; I can't imagine I have been the most fun person to be around.

To all my friends I have made at the University of Leeds, I appreciate the support and fun that has made my time at university an unforgettable experience, with Simon Barnes, Dongze Wang, Josh Armitage, Samuel McMaster, and Matthew Marshall being of particular note to me.

Abstract

This thesis investigates the combination of Diamond-like carbon (DLC) with graphene nanoplatelets (GNP) to unveil the mechanisms that lead to a low-friction nanocomposite film in boundary lubrication for the first time. The manufacturing of DLC-GNP nanocomposites is provided along with the crucial optimisation parameters (GNP coverage / DLC thickness) that provide increased tribological performance.

The motivation of the composite is to create a low friction and wear composite which does not rely on environmentally damaging additives common to commercial engine oils.

The DLC-GNP coatings in this thesis were evaluated by tribological testing using a reciprocating pin at elevated temperatures in the boundary regime to replicate a demanding cam-follower environment. A base-oil was used to ensure that only the mechanism between the cast iron counter-body and the DLC-GNP coating was observed.

The results show that an optimum GNP coverage (4.5%) reduced the coefficient of friction (~0.03) and wear (< 1.3 x $10^{-19}$$m^2$/Nm), beyond this coverage, the tribological performance decreased, and a breakdown of the coating was observed. The DLC thickness was a crucial factor in friction and wear reduction. A minimum DLC thickness of 1.2µm is required to ensure GNP are not removed during the tribo-tests. Thick DLC >3µm was found to isolate the GNP from the counter-body and not contribute to friction reduction.

The formation of a highly graphitic transfer film on the counter-body was determined to be the primary mechanism for friction and wear reduction. The GNP provided a lubricant reservoir for high-quality graphitic transfer film, which reduced adhesive forces during sliding wear, leading to low friction. The reduced adhesive forces suppressed the graphitisation of the DLC matrix and resulted in lower wear.

Contents

List of Abbreviations

AFM	Atomic Force Microscopy
CNT	Carbon Nanotubes
CPR	Crack Propagation Resistance
COF	Coefficient of Friction
CVD	Chemical Vapour Deposition
DLC	Diamond-like carbon
EDX	Energy Dispersive X-ray Spectroscopy
EELS	Electron Energy Loss Spectroscopy
FFO	Fully Formulated Oil
FIB	Focussed Ion Beam
GLC	Graphitic-like carbon
GNP	Graphene Nanoplatelets
HiPIMS	High Power Impulse Magnetron Sputtering
HSS	High-Speed Steel
HOPG	Highly Orientated Polycrystalline Graphite
MLG	Multi-layer Graphene
MoDTC	Molybdenum Dithiocarbamate
MS	Magnetron Sputtering
NMP	N-Methyl-2-pyrrolidone

PACVD Plasma Assisted Chemical Vapour Deposition

PAO Poly-alpha-olefin

PECVD Plasma Enhanced Chemical Vapour Deposition

POD Pin-on-disk

PVD Physical Vapour Deposition

RF Radio Frequency

rGo Reduced Graphene Oxide

RMS Root Mean Square

SCPR Scratch Crack Propagation Resistance

SLG Single Layer Graphene

SEM Scanning Electron Microscopy

TEM Transmission Electron Microscopy

SAD Selected Area Diffraction

UoL University of Leeds

VAM Velocity Accumulation Model

XPS X-ray Photoelectron Spectroscopy

XRD X-ray Diffraction

ZDDP Zinc Dialkyldithiophosphate

List of Figures

List of Tables

Chapter 1 – Introduction

1.1 Energy Use and Sustainability

The world's demands for fossil fuel use have grown rapidly over the last 30 years [1]. With the rise of nations using more fossil fuels than ever before comes the inevitable consequence of increased greenhouse gas emissions (**Figure 1.1**), which many scientists believe is the leading cause of global warming [2]. Due to emissions and global warming concerns, the UK government has committed to a 'Net Zero' policy [3] so that by 2050, the UK will reduce carbon emissions to net zero.

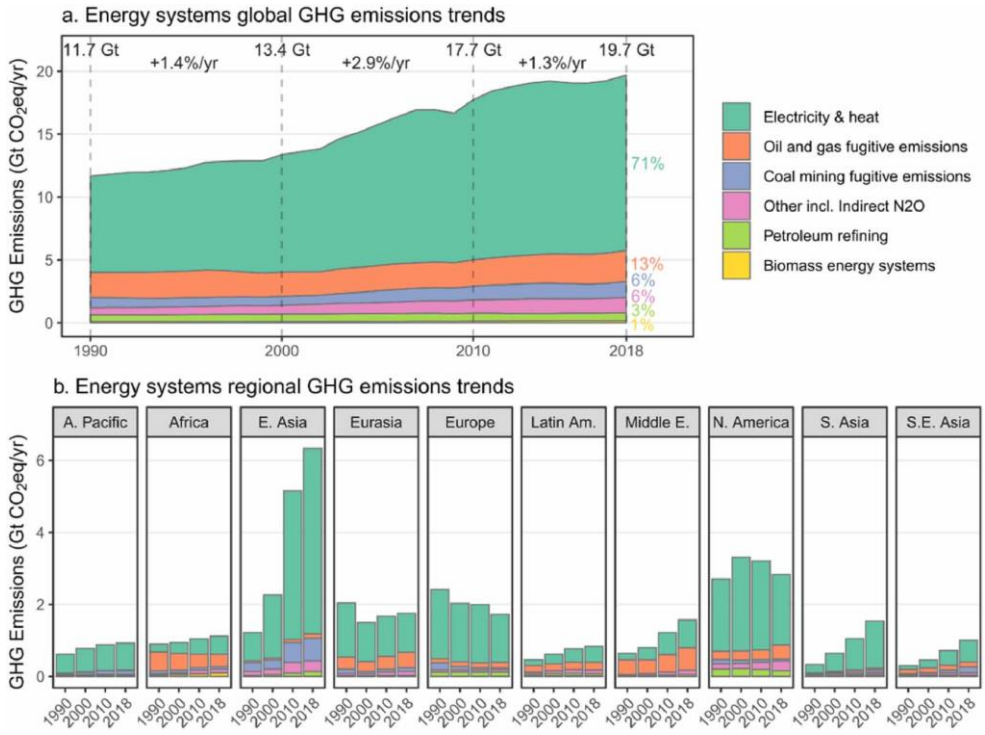

Figure 1.1 *(a) Global Greenhouse gas emission trends and (b) Greenhouse gas emissions for regional areas from the years 1990 - 2018* [2].

Currently, renewable energy supply cannot meet demand, with many applications, such as marine and internal combustion engines (ICE), still relying heavily on fossil fuels. This reliance on fossil fuels contributes to a global energy crisis and rising consumer prices, resulting in many countries signing the Paris Agreement to reduce emissions, including

the UK's Net Zero Strategy [3]. Although this agreement currently contains no financial penalties, it has forced companies to innovate to improve efficiency. One of the areas of focus for emission reduction is automobiles, with many countries setting ambitious targets, but predictions expect growth to continue unless drastic action is taken (**Figure 1.2**).

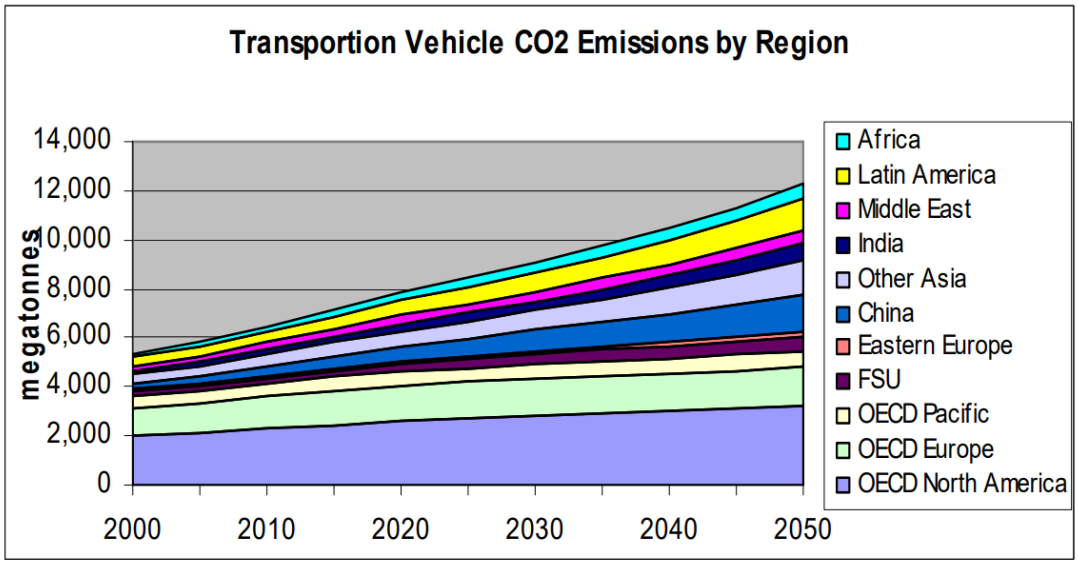

Figure 1.2 *Current and expected transport vehicle CO_2 emissions* [4].

Internal combustion engines (ICE), in particular, experience significant energy losses attributed to friction and wear, reaching reported figures as high as 33% [5,6]. As the energy loss due to friction is substantial, even a minor reduction can yield noteworthy advancements in global greenhouse gas emissions [7]. Through advancements in technology, it is expected that there will be a reduction in frictional energy losses by 61% over the next 15 – 25 years [5]. These significant reductions in energy losses are expected to be achieved by surface coatings, low-viscosity oils, or better-designed engine oil additive packages [8–10].

Engine oils have been tailored over recent years with various additives such as dispersants, detergents, friction modifiers, extreme pressure, and viscosity modifiers [11]. These additive packages reduce friction and increase the component's lifetime. However,

the disposal of engine oils poses environmental hazards and is expensive to recycle due to the additives they contain [12,13]. A recent trend in engine oils is to move towards low-viscosity oils compensated by additional molybdenum additives to reduce friction and wear [10,14]. Developments in greener tribology have focused on combining additive-free or environmentally friendly additives or using hard-wearing coatings such as diamond-like carbon [15,16].

1.2 Coating to Reduce Energy Usage

Protective coatings have been successfully developed to protect the underlying substrate, reduce friction, and control wear. Diamond-like Carbon (DLC) coatings are commonly used solid coatings for ICE engines. An outstanding issue with lubricant additives can be their interactions with protective solid coatings [17]. This is particularly relevant in the case of hydrogenated DLC and the molybdenum dithiocarbamate (MoDTC), as MoDTC can lead to increased wear of the hydrogenated DLC [17].

As stated in **Section 1.1,** significant reductions in friction are expected to be achieved partly by developments in surface engineering, with new and exotic materials such as nanoparticles expected to drive this [18].

The improvements made in DLC technology to incorporate nanomaterials into DLC coatings, leading to drastic reductions in friction and wear have been limited; however, some success with the combination of graphene and DLC has emerged [19].

To effectively address the challenge of emission reduction targets, it is crucial to prioritize the continuous development of coatings through materials engineering. By emphasising ongoing advancements in this field, we can ensure that coatings evolve to meet the demands of emission reduction targets.

Graphene and related graphitic materials (such as graphene nanoplatelets (GNP)) are a relatively new type of material which, in theory could make an excellent lubricant for use in ICE engines. However, it is difficult to ensure that they can get into the contact zone effectively without agglomeration [20]. Developing techniques to combine an already established solid lubricant, such as DLC, with graphene can potentially reduce energy consumption.

1.3. Aims and Objectives

GNP has shown to reduce friction and wear in tribological conditions by themselves or as part of a composite [21–24]. But, so far, the reported work on a diamond-like carbon-graphene nanoplatelet nanocomposite is limited, with no information on the mechanism that leads to the low friction and wear observed [25].

This thesis aims to investigate the mechanism GNP has on the tribological properties when dispersed in a DLC matrix, providing alternative methods to the current reliance on additives contained in commercial oils. The mechanisms for low friction are discussed and evaluated, providing information on strategies to continue to drive better performance.

Objective 1: To study the effect of GNP coverage on the mechanical and tribological properties of DLC-GNP composites.

- Synthesis of coatings using varying GNP concentrations to create DLC-GNP composites with GNP coverages between 0% - 9.15%.
- Measure the mechanical and tribological properties of the coatings as a function of GNP coverage.
- Compare the coatings to a pure DLC sample prepared using the same synthesis method and within a fully formulated oil.

- Evaluate the structure of the composite coatings.

Objective 2: To study the effect of DLC thickness on the tribological properties of DLC-GNP composite.

- Synthesis DLC-GNP coatings with varying DLC thicknesses by controlling the deposition time.
- Measure how the tribological and mechanical properties change as a function of DLC thickness.
- Determine the optimum thickness of the DLC to achieve the lowest friction and wear.

Objective 3: To study the durability of the coating under extended wear testing.

- Compare how a pure DLC and optimum DLC-GNP film respond during extending tribotests.
- Measure the evolution of the transfer film formation as a function of sliding distance.
- Determine the mechanism for the friction and wear reduction as the sliding distance increases.

1.4. Thesis Outline

The thesis is split into 8 chapters, an outline of the chapters 2 - 8 is described:

Chapter 2 provides the literature around DLC and graphene tribology, exploring the tribological response at different scales (nano to macro), and the factors that improve friction. A range of common analysis techniques is described to show the developments in understanding the mechanisms that lead to low friction and wear in a thin carbon film. A current state of the art in DLC and graphitic carbon tribology and research gaps are

presented to identify where the work completed in this thesis will add to scientific knowledge.

Chapter 3 provides the methodology, outlining the synthesis process used to create DLC-GNP films. The tribological testing conditions used are described in this chapter, outlining the loads, speed, lubricants, and counter-materials used.
This section also describes the analysis methods used to characterise the DLC-GNP films before and after wear.

Chapter 4 - 6 provides the following results chapters:

- **Chapter 4:** Effect of GNP Coverage on the Mechanical and Tribological Properties of DLC-GNP Nanocomposite Films
- **Chapter 5**: Effect of DLC Thickness on the Mechanical and Tribological Properties of DLC-GNP Nanocomposite Films
- **Chapter 6**: The Effect of Sliding Distance on the Tribological Properties of DLC-GNP Nanocomposite Films

These chapters provide different aspects which link together to contribute to the friction reduction mechanism shown when GNP is introduced into a DLC matrix where:

- In **Chapter 4** the GNP coverages is shown as the contributing factor to the changes in the mechanical and tribological properties measured.
- In **Chapter 5** the GNP coverage is kept constant, with the measured difference being the DLC thickness and the DLC matrix's role in the friction reduction mechanism.
- **Chapter 6** provides the combination of the two best-performing coatings and studies the durability of the coating.

The samples are all tested using a reciprocating tribometer under demanding conditions (similar to that in a cam-follower environment). In these tribo-tests a Group IV Poly-alpha-olefin (PAO) base-oil is chosen as the lubricating oil, cast iron (CI) as the counter-body, and 100°C as the operating temperature, along with a sliding speed of 20 mm/s. A base-oil is chosen to allow only the interactions of the DLC-GNP film with the sliding counter-body to be analysed. A pure DLC film was used as a baseline, and a fully formulated oil was used as a comparison.

For **Chapters 4 & 5** the tribotesting is limited to 6 hours, and for Chapter 6 the testing duration is limited to 30 hours determined by the limitations of the testing equipment.

Chapter 7 provides a discussion of the results from **Chapters 4 - 6**. In this chapter, the results are analysed, grouping together the different contributing aspects of tribological performance and mechanical properties to provide mechanisms that reduce friction and wear.

Chapter 8 is the final chapter which provides the conclusion of the results of this thesis, with the areas of future work identified.

Chapter 2 - Literature Review

2.1 Introduction

This chapter provides a thorough analysis of the literature on:

- The various forms of carbon and bonding structure.
- DLC application, synthesis techniques, and the current state of the art.
- Graphitic Materials, a comparison of the various types, synthesis, and tribology-related friction mechanisms.
- DLC nanocomposite synthesis and related tribological applications
- Current Research Gaps

Additional comments are made throughout regarding coating characterisation techniques.

2.2 Allotropes of Carbon

To understand DLC or graphitic materials, it is essential first to present their most fundamental building block, “carbon”. The carbon is presented in vastly different configurations and properties, depending on the associated bonding.

Carbon atoms can form three electronic configurations sp^1, sp^2, and sp^3 (**Figure 2.1**). These configurations allow a variety of amorphous and crystalline structures to be formed, with graphene, graphite, diamond, and diamond-like carbon being most relevant for this thesis.

Diamond is the most known structure consisting purely of sp^3 bonds. The bond angle between the carbons is 109.5°, with a bond length of 1.54Å. This combination creates one of the strongest structures known, with the highest density of atoms per unit volume. The sp^3 bonding is hybridised, forming strong σ bonds with neighbouring carbon atoms.

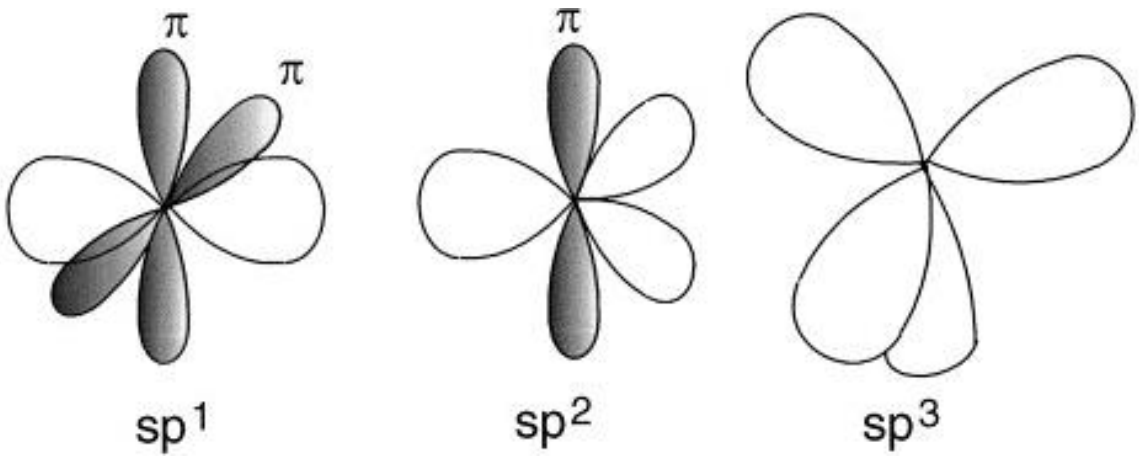

Figure 2.1 *The three electronic configurations of carbon bonding* [26].

The sp^2 bonding is seen in graphene, forming an atomically thin hexagonal (honeycomb) sheet of carbon. Each carbon atom forms three strong in-plane σ bonds with a bond length of 142 Å with a fourth π bond, normal to the σ bonds [27]. The shorter bond length is due to the lopsided nature of the sp^2 orbital, which leads to a greater overlap with other sp^2 orbitals, creating a higher bonding energy [27]. The delocalised π bond will form weak π bonds with neighbouring carbons [26,28]. Graphene layers can stack together to form graphite, either as an ABA or ABC stacking structure. Although the in-plane bonding of graphite is strong, the bonding between each layer (interlayer bonding) is weak, held together by van der Waals forces [29]. The weak forces between the graphene layers can be exfoliated using methods as simple as tape. This incidentally led to the first recorded isolation of a single graphene layer, resulting in a Nobel prize [30].

DLC differentiates itself from graphene and diamond as it contains sp^2 and sp^3 bonding in an amorphous structure, as shown in **Figure 2.2**.

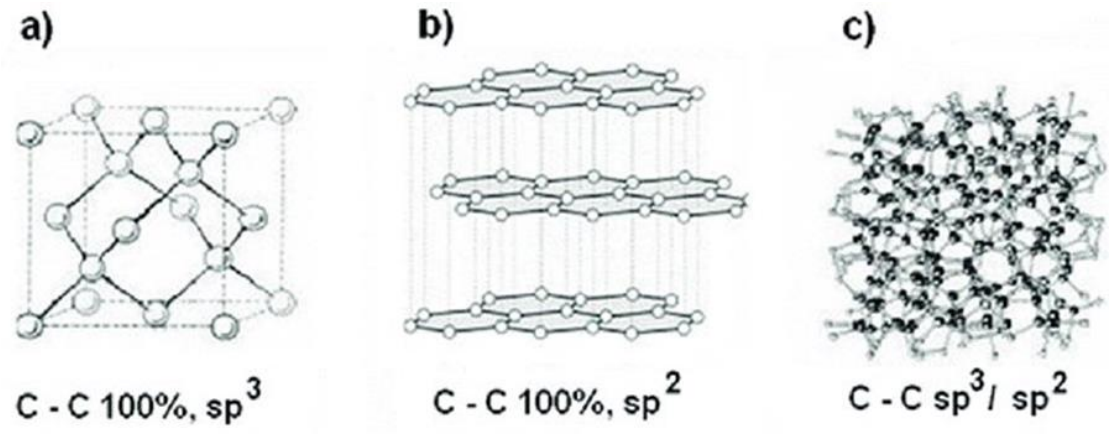

Figure 2.2 *The structure of a) diamond, b) graphite and c) DLC* [31].

2.3 Diamond-like Carbon

DLC coatings can be used to control friction and wear when applied as a protective coating, making them highly desirable in engineering applications (notably the automobile sector). DLC is a broad term encompassing a wide range of amorphous carbon films containing sp^2 and sp^3 carbon bonds, often with some hydrogen. The relative fraction of the sp^2/sp^3 bonds (and hydrogen) can determine the mechanical and tribological properties, typically with higher sp^3 content films being harder [26,32]. The ternary phase diagram in **Figure 2.3** provides the various types of DLC films that can be produced based on the relative concentrations of sp^2, sp^3 and hydrogen.

The phase diagram consists of three distinct regions:

1. The hydrogen-free a-C (amorphous carbon) on the left axis.
2. The bottom right, where the hydrogen content is so large that a film cannot form.
3. The centre region between (1) and (2) where a-C:H (Hydrogenated amorphous carbon) is produced.

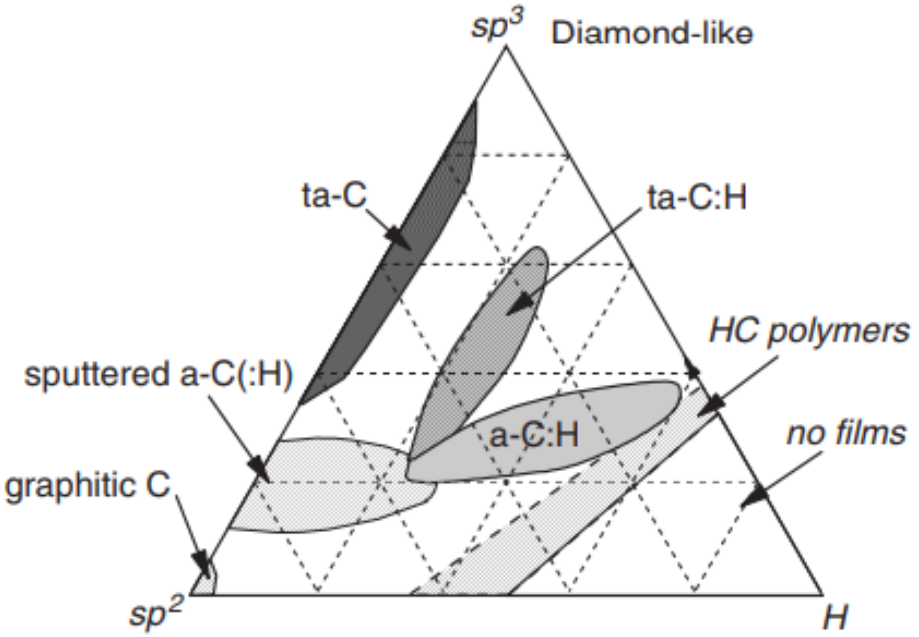

Figure 2.3 *Phase diagram of DLC carbon materials that can be formed* [33].

DLC is often considered to be a random network of sp^2 and sp^3 bonding. The mechanical properties of the network arise from the C-C sp^3 bonding [34]. The sp^2 bonds form clusters, along with the C-H bonds (with the dangling bonds), which do not contribute much to the mechanical properties [33]. The typical mechanical properties of various carbon materials are shown in **Table 2.1**, with Young's modulus and hardness displaying a noticeable increase as the sp^3 fraction increases.

Table 2.1 *The mechanical properties of various carbon material* [35].

Material	Form	Density (g/cm^3)	Covalent bonds	Young's modulus (GPa)	Hardness (GPa)
a-C	Films	~2.2	sp^2-rich	100–200	10–20
a-C:H	Films	~2.2	Intermediate sp^3	100–300	10–30
t-aC	Films	3–3.2	sp^3-rich	300–500	50–80
Diamond	Bulk, films	~3.5	100% sp^3	1000	100

2.3.1. Measurement of DLC Chemical Structure

The bonding structure (sp^2/sp^3 content) of DLC and other carbonaceous materials can be measured quantitively using techniques such as Nuclear Magnetic Resonance spectrometry (NMR), electron energy loss spectroscopy (EELS), and X-ray Photoelectron Spectroscopy (XPS). Often, these methods require specialised sample preparation (NMR/EELS) or small sizes (XPS). Using these techniques can often lead to misinterpretations of the results and require specialist expertise in data analysis. It was observed that as much as 30% of journal papers analysed using XPS contained serious problems, which resulted in erroneous results [36–39]. One of the main concerns is the accuracy of sp^2/sp^3 content in DLC films, which have been shown to provide errors as high as 10% using XPS [40,41].

Qualitative methods to measure the relative sp^3 content are commonly achieved using Raman spectroscopy, which is non-destructive and relatively easy to analyse. The basis of this technique relies on the evaluation of two peaks; $A1_g$ (D peak) and $E2_g$ (G peak) breathing modes, which provide comparative results of sp^2/sp^3 content [42,43]. The methodology section of this thesis discusses a detailed experimental methodology and theory behind Raman spectroscopy and other characterisation techniques.

2.3.2. DLC Deposition

The method for DLC production is achieved by various techniques, allowing the creation of films with greater control of the desired sp^2/sp^3 and hydrogen content, along with dopants that can be incorporated to improve the properties further [44]. The two main techniques for deposition are: Chemical Vapour Deposition (CVD) and Physical Vapour Deposition (PVD). These two techniques are subdivided further, with Plasma Enhanced

Chemical Vapour Deposition (PECVD) covered in the subsequent section related to the work covered in this thesis.

Generally, in CVD deposition, a substrate is exposed to precursor gases that react or decompose on the surface, forming the required final film. Typical precursors include methane (CH_4), ethane (C_2H_6), propane (C_3H_8), and butanes (C_4H_{10}) [45]. The discomposure of the precursor gas is initiated by plasma or high temperatures for reactive radical generation of C and H ions [44]. This reaction is carried out under a vacuum where by-products are removed through the chamber.

In PECVD a plasma is used to reduce the activation energy for the decomposition of reactive gases, allowing the formation of DLC at lower temperatures and a greater variety of substrates that can be used. The mismatch between thermal expansion coefficients, which have traditionally limited film thickness [46,47] can be reduced by lowering internal stresses. The plasma in this thesis is achieved using ionised Argon gas, where a high bias voltage supplies the energy.

2.3.2.1.PECVD Coating Growth

Growth of the DLC film using the PECVD process utilises a high bias and electrically conductive substrate to drive the positive ions from within the plasma to the substrate. The properties of the deposited film are altered by varying the impinging ions' kinetic energy / ion energy (**Figure 2.4)**. This leads to hard carbon films or diamond-like carbon films at high ion energies (≥100 eV) and to polymer-like films at lower ion energies [48]. Films produced by PECVD typically contain more hydrogen (up to 60%) [49].

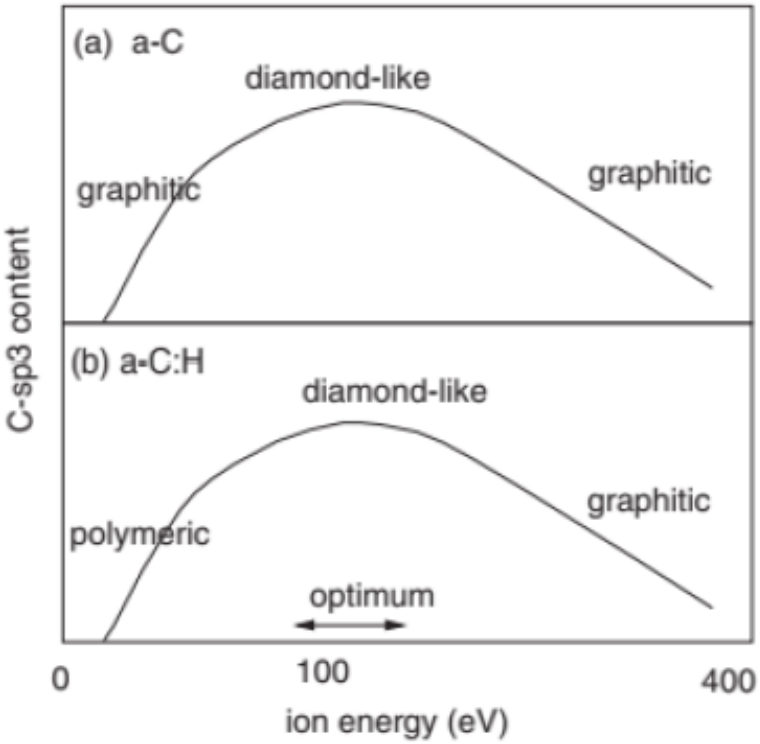

Figure 2.4 *Changes to structure of films as the ion energy changes* [50].

DLC film growth (**Figure 2.5**) using the PECVD process is initiated due to the interaction of the reactive species with the plasma and the surface of the substrate to be deposited. The plasma closest to the substrate (or growing film) consists of ions and neutral species. The film growth is dependent on the type of individual species and their sticking coefficient [26,44,51]:

- Neutrals - The neutrals are closed shells and have the lowest sticking coefficient.
- Mono-radicals - The reaction of atomic hydrogen with surface H bonds, as well as the removal of hydrogen atoms from the coating structure through ion bombardment and the action of unstable radicals like CH_3. The presence of atomic hydrogen increases the sticking coefficient of unstable radicals like CH_3, enhancing their interaction with the growing film's surface.
- Di-radicals – These are chemically unstable species with two unpaired electrons. They invade C-C or C-H bonds in the film, reacting and bonding to the surface due to their high sticking coefficient and reactivity.

- Carbon and Hydrogen - These species integrate into the film, affecting its composition and properties. Hydrogen atoms can be dislodged by ion bombardment, combine to form H_2, and decrease the film's hydrogen content. Increasing ion energy enhances this effect, altering mechanical strength, reactivity, and other properties. Controlling ion energy allows for tuning the hydrogen content and film characteristics.

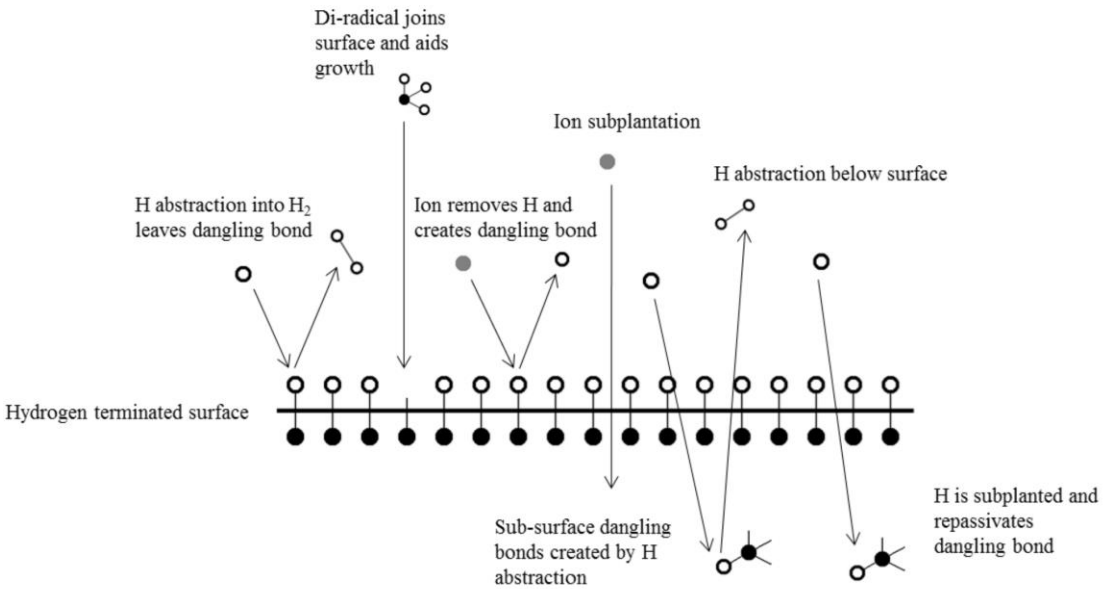

Figure 2.5 *PECVD film deposition process [44].*

The deposition process can take two forms: homogenous or heterogeneous. Heterogenous reactions often result in low-density, poorly adhered films because nucleation happens in the gas phase, leading to particle formation [52]. Homogenous reactions occur on the substrate surface, producing higher quality, better-adhered films. The typical process for the growth of a film by ion supplantation. The resultant film will contain less hydrogen than the precursor gas due to some of the hydrogen being removed either as a by-product or by ion bombardment. The ions will initially subplant as sp^3 sites. However, diffusion and bombardment by other ions will relax the bonds to a lower sp^2 energy.

The PECVD process is a thermodynamic driven process, where at low energy, the growth of a film is surface reaction controlled, and at high energy, it is limited by mass transfer. The resultant deposition rate is dependent on the slowest step. When the deposition process is limited by surface reaction kinetics, the rate depends on the available reactant gases. Where mass transport is the limiting process, the diffusion rate of the reactant and diffusion of by-products through the boundary layer are the controlling factors. The conditions during the deposition process can affect the resultant DLC film produced, as explored by Kim *et al.* [53], where radio frequency (RF) power and pressure were found to be important factors. It was found that increasing the pressure from 106.6 Pa to 900 Pa but keeping the RF power the same reduced the deposition rate, which was credited to the generation of atomic hydrogen, which etched the film, limiting growth. Increasing RF power (and thus ionisation energy) while maintaining low and constant pressure during film growth resulted in increased graphitic clusters observed by higher I_D/I_G ratio in Raman spectra. However, this effect was counteracted at higher pressures due to preferential atomic hydrogen attacking the clusters during film growth. The work by Khun *et al.* [54] using microwave excited PECVD deposition found that as the negative bias increased, the resultant film had a greater sp^3 content. This was due to "greater kinetic energy of film-forming ions during film deposition". A link between improved tribological properties of films synthesised with higher bias was made and is repeatable [54,55].

2.3.2.2.DLC Adhesion

The adhesion of DLC films on ferrous substrates is improved by depositing interlayers (often termed adhesion layers) before the DLC is deposited [56,57]. These interlayers reduce the internal stresses of the resultant deposited films, allowing the deposition of

thicker DLC layers. Cr and W/WC interlayers are relatively common and have been shown to improve the adhesion of DLC to steel substrates and are used in this thesis [58].

Molecular dynamics simulations have studied DLC growth on multi-layer graphene [59]. In this study, the higher the incident energy of the deposited carbon atoms, the greater the adhesion quality of the DLC to the graphene. The resulting structure for the higher incident carbon atoms also showed that the growth process consumed some of the layers of the graphene. When analysing the bonding structure of the carbon atoms close to the graphene, it was found that there was a higher fraction of disordered ring structures (sp^2). This was due to the high-energy incident atoms creating a pressure induced transformation from sp^3 to sp^2. The radial distribution function analysis indicates that sp3 hybridised atoms tend to grow near existing sp^3 atoms [59].

2.3.3. Tribology of DLC

This section will review the fundamentals of DLC coating tribology, with what is known about DLC tribology and areas where improvements in knowledge are required. Over many years DLC coatings have shown to reduce friction and wear in various environmental conditions (vacuum, lubricated and dry) [60]. Due to the wide range of conditions researched over the years, this subsection focuses mainly on the lubricated contacts and the mechanisms credited to friction and wear reduction unless a link can be made to other conditions relevant to the objectives of this thesis.

2.3.3.1. Transfer Layer Formation

DLC coatings reduce friction by either the saturation of dangling bonds or the formation of an easy shear graphitic transfer film between the two articulating surfaces [61]. This transfer layer formation can occur in both dry and lubricated conditions. When a DLC

coating comes into contact with an articulating counter surface, graphitic wear particles transfer to the counter surface, forming a graphitic "transfer layer" [62,63] (**Figure 2.6**).

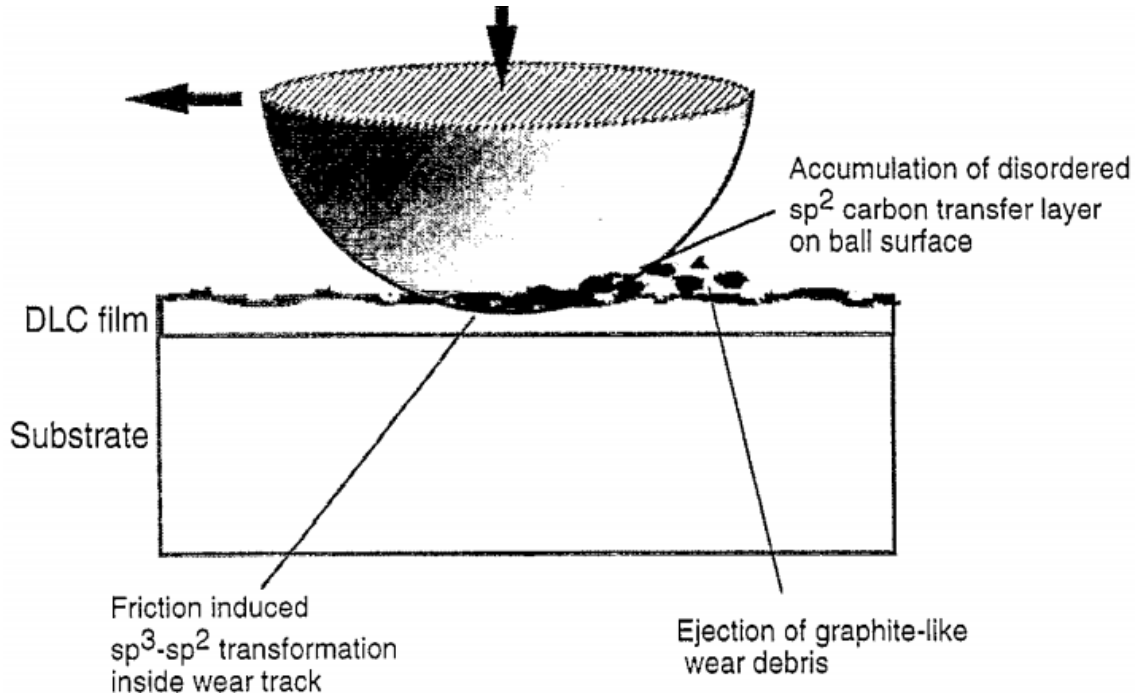

Figure 2.6 *The formation of a disordered graphitic transfer layer on a ball surface* [63].

The transfer layer builds up to form a thin film that protects the softer counter-body surface, where both surfaces wear at a low rate [62]. In an a-C:H coating, graphitisation is speculated to be initiated by temperatures from 200-400°C [64], which results in hydrogen diffusion, collapsing the metastable amorphous covalent structure into a lower energy sp^2 configuration [65]. Huu *et al* [64] claim the transformation of the sp^3 to sp^2 can be obtained at lower temperatures due to the combination of asperity flash temperatures and high contact pressure. This combination facilitates hydrogen desorption, where the carbon atoms rearrange to a more stable sp^2 bonding. Liu *et al.* [66] verified these findings using higher speeds and loads to enhance the shear deformation, leading to a graphitic transformation. Although these arguments for the low graphitisation temperatures due to high pressures are viable, other ideas have been proposed for stress-induced transformations [63,67]. The formation of wear particles and rough edges of

scratches creates localised high-pressure differences, significantly lowering the transformation temperatures [63,67].

To analyse the graphitisation, Raman spectroscopy is commonly used, on the wear track, worn counter-body or debris [68]. Raman analysis can typically provide comparative I_D/I_G values, with higher values indicating that a greater degree of active sp^2 sites from the hexagonal rings become active due to transformation from an sp^3 bond during the frictional wear [69]. Other methods also consider the change in the frequency of the G peak, which can be linked to the formation of graphitic chains [42]. XPS is often used to determine the sp^2 content of worn films quantitively, but it requires cleaning the surface with heptane to avoid contamination of the XPS vacuum chamber [70]. XPS has also shown to provide erroneous results unless very careful interpretations are completed [36–39].

The build-up and growth of a transfer film are generally defined by a velocity accommodation mode (VAM) of third bodies (**Figure 2.7**), with two mechanisms used to explain this growth [71]:

- Shearing and exclusion of wear particles from the DLC between the two articulating surfaces. The particles can cause smoothing from entering valleys and shearing or are removed completely.
- Interfacial sliding, where adhesion leads to wear particles adhering to the counter surface, creating a protective layer between the two articulating surfaces.

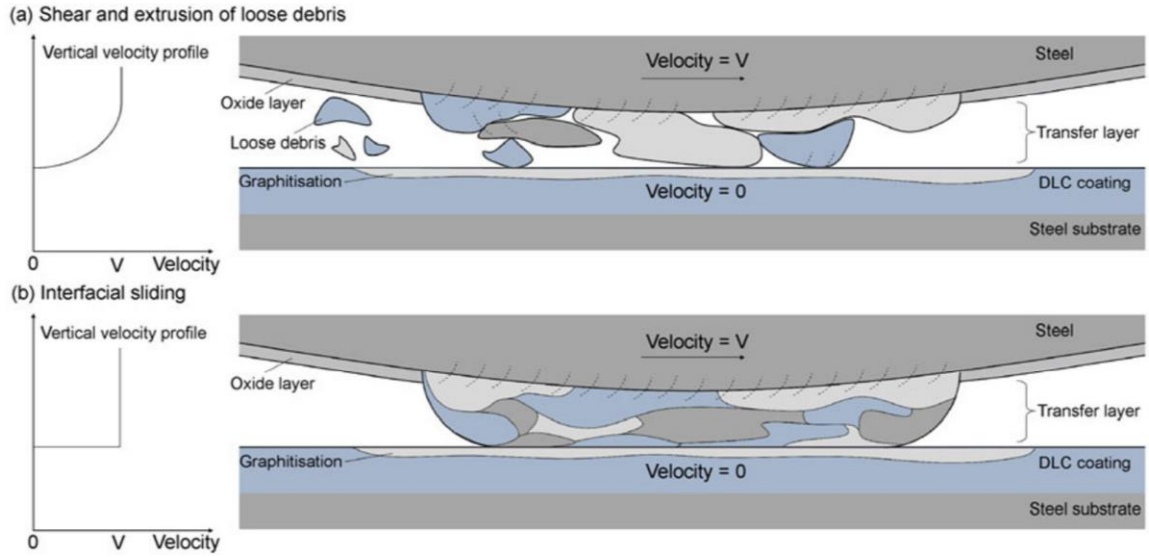

Figure 2.7 *VAM of transfer film formation, (a) shearing and exclusion of wear particles, and (b) interfacial sliding* [71].

Ronkainen *et al.* [72] showed that the transfer layer formation depends on a minimum force, sliding velocity, and the counter material used. A sapphire ball and Alumina ball did not produce a transfer film on the ball. Theoretically, they both put enough into the system to drive the formation of a structural change from sp^3 to sp^2, but a transfer layer was observed on the film surface itself [73].

When DLC films are tested in oil lubricated contacts, a transfer film can still form on the surface of the film itself [17,74], and the counter-body [17]. The graphitized layer on the DLC surface is easily removed during the wear process into the lubricant, or by excess cleaning to remove the oil residue and may not be detected easily [17,74].

2.3.3.2. Environmental Effects on the Tribology of DLC Films

Although this study focuses on the tribology of DLC under oil-lubricated conditions, this section will briefly consider the mechanisms under humid and vacuum conditions for lowering friction by saturation of dangling bonds and their relationship to oil-lubricated conditions.

Ultra-high vacuum (UHV) (10^{-7} Pa) in dry conditions can display COF of <0.01 for a-C:H films against a steel counterpart at contact pressures up to 1.8 GPa, while in ambient conditions for the same films, a COF of 0.1 is experimentally observed [75,76]. The hydrogen in the films is believed to passivate the dangling bonds. In a system where two a-C:H surfaces come into contact, a weak Van der Waals interaction leads to low friction[77,78] **(Figure 2.8)**.

In Hydrogen free DLC, dangling bonds are present at the interface, resulting in direct interaction of $\pi - \pi^*$ bonds which have high binding energy, leading to increased friction [78]. The introduction of water vapour at the interface in a-C:H films increases the COF. It is considered that the water molecules are adsorbed at interfaces, which will then displace the C-H bonds, leading to an increased attractive force [79].

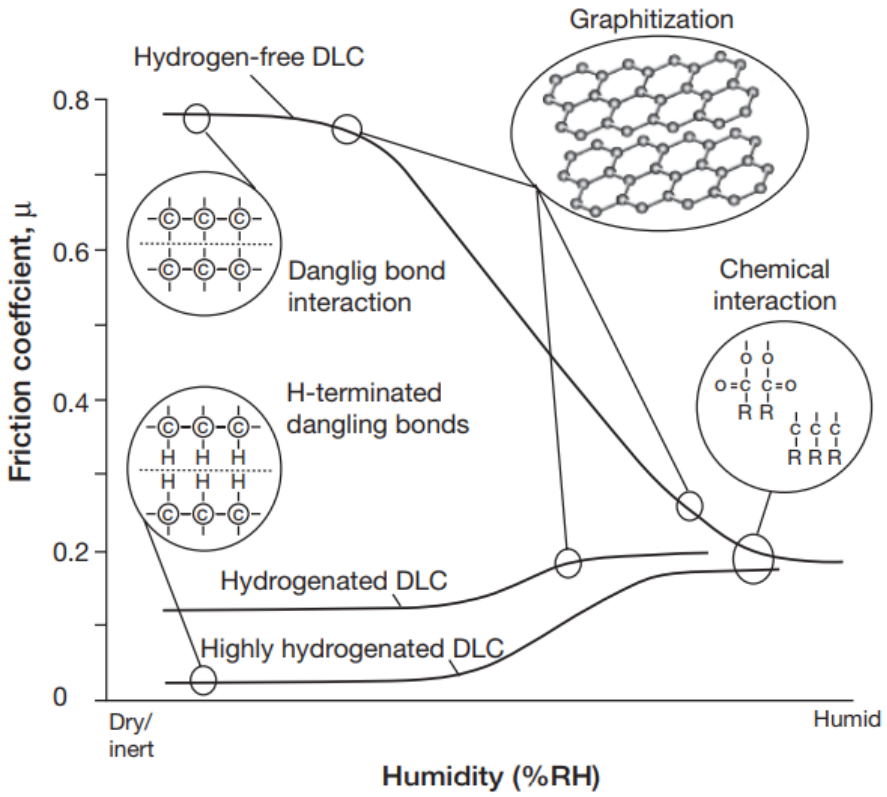

Figure 2.8 *The COF for Hydrogen free, hydrogenated and highly hydrogenated DLC films as a function of humidity* [44].

Although the films synthesised in the current study are tested under oil-lubricated conditions, they are in the boundary lubrication regime where the articulating surfaces will be in close contact, and surface chemistry must be considered. If the interactions at the interfaces are $\pi - \pi^*$ bonds, the friction will likely be high, so efforts to saturate high energy bonds overlapping should be considered.

2.4. Graphene Nanoplatelets

Graphene is a single sheet of purely sp^2 bonded carbons that is the building block of various structures such as buckyballs, graphite and nanotubes, as shown in **Figure 2.9**. Graphene has been known for many years, but only since the first reported isolation has an interest in this material taken off due to its excellent electronic and mechanical properties [80]. The interest in tribological applications is due to its atomically flat surface, high specific surface area and in-plane solid bonding. When graphene layers are stacked on top of each other, they have a low energy interlayer interaction, which allows them to slide over each other easily, which many researchers have speculated to be the origin of the low friction seen in graphite [20,81,82].

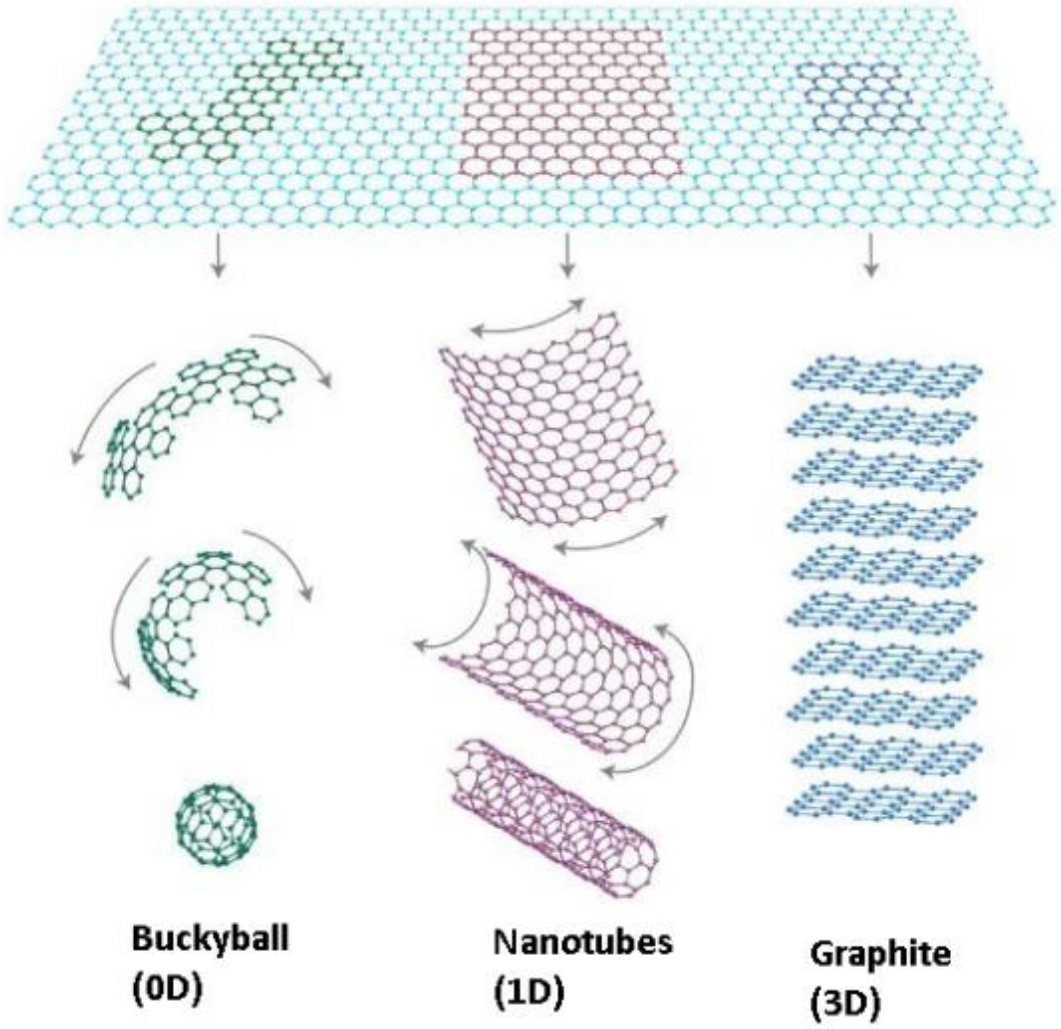

Figure 2.9 *Graphene is a building block of various carbon materials. It can be folded to form buckyballs, it can be rolled to form nanotubes and stacked to create graphite* [30].

Before the first reported isolation of graphene, it was believed that a single free-standing layer would not be thermodynamically stable as the melting point of thin films decreases rapidly as the thickness decreases [83]. Many materials become unstable and decompose when only a few layers are present. The existence of monolayer graphene can be explained due to the strong in-plane bonding, which ensures that the thermal fluctuation does not lead to dislocations or defects even at high temperatures [30]. The term graphene is often misused and should strictly apply only a single 2D layer of carbon atoms arranged in a hexagonal honeycomb lattice. The term few layer / ultra-thin graphene is more appropriate when a few layers are present, with the term graphene nano-platelets (GNP)

given for less than 100 layers. The term graphene is also often misused where large amounts of oxygen are present within the 2D carbon sheet, with graphene oxide or reduced graphene oxide (rGO) being a more appropriate description.

2.4.1. The Graphitisation Process of Carbons

Graphite is naturally found as lump or flake graphite, or can be synthetically produced using high temperature and pressure as highly orientated pyrolytic graphite [84–86]. High-quality synthetic graphite requires significant heat to allow the carbon atoms to reorganise themselves into a more thermodynamically stable graphitic arrangement. Different starting materials and heat treatment processes (higher heat and pressure) can lead to changes in staking or orientation. The graphitisation process for graphite differs from that of DLC, requiring much higher temperatures (**Figure 2.10**). This higher energy requirement is due to graphite needing greater energy to rearrange the carbon atoms into a more organised structure. In contrast, DLC graphitisation is from the collapse of sp^3 bonds to a metastable sp^2 state, which has a highly disorganised and open hexagonal structure [87].

The graphitisation process increases crystallite size in both the c-axis and lateral size. The process becomes progressively difficult, requiring greater energy as the stages of development (organisation) increase, which would not be provided by friction and pressure during reciprocating wear. This energy required to drive the graphitisation process is met by increasing the temperature to higher and higher levels. A small proportion of graphitic carbons can be formed to relax high internal stresses from thermal expansion [88].

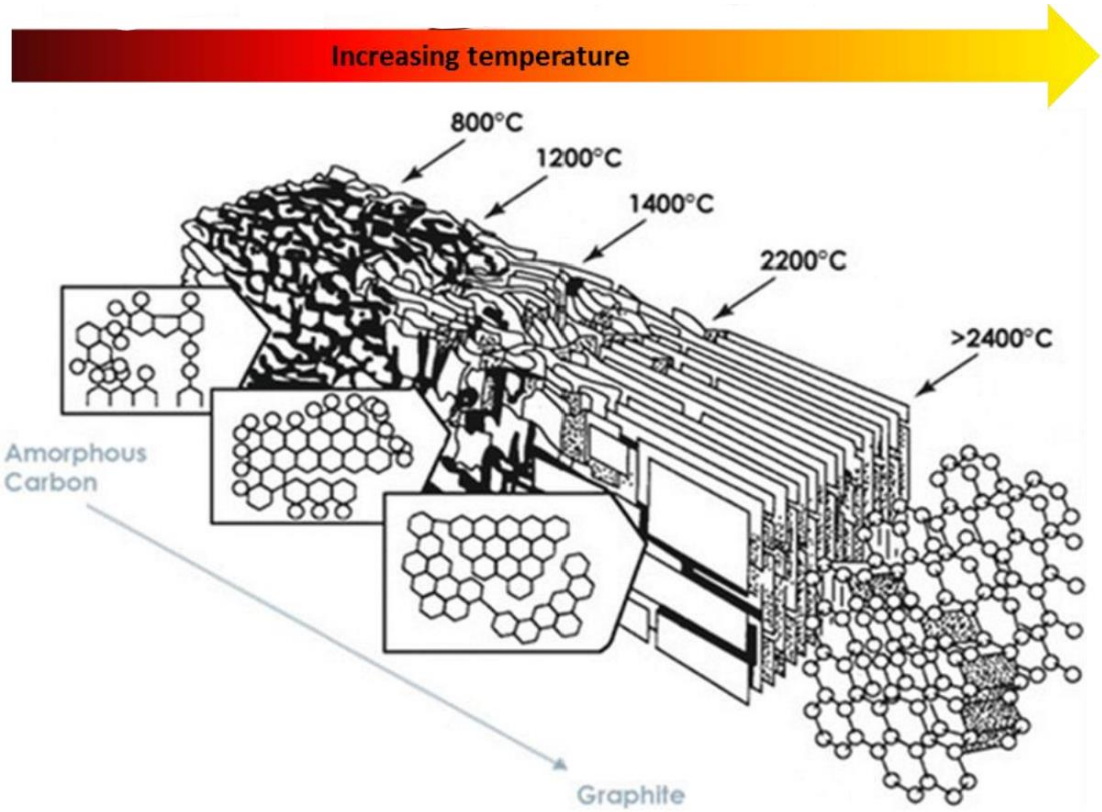

Figure 2.10 *The graphitisation to an organised graphite structure as heat treatment temperature increases* [89].

2.4.2. Mechanical Properties of Graphene Nanoplatelets

The interest in graphene tribology is due to the extraordinary mechanical properties that it can exhibit, namely its in-plane mechanical strength. However, as the number of layers increases, the properties can change, making them less desirable [80]. The extraordinary in-plane mechanical strength of graphene is due to the sp^2 bonding between the carbon atoms, where theoretical calculations show the strength of the bonds to be greater than any other material [90]. The experimental measurements carried out on 'defect-free' graphene flakes have shown graphene to be the strongest material ever measured, displaying a Young's Modulus of 1 TPa with intrinsic strength of 130 GPa, with the Elastic stiffness calculated to be 35 N/m^2 [91]. GNP maintain many of the attractive properties of single layer graphene (SLG) but can be produced cheaply and handled more efficiently, making it an alternative material to be utilised in tribological systems [92].

2.4.3. Tribological Mechanisms of Graphitic Materials

Graphite is not an intrinsic lubricant and will display high friction when tested in dry conditions [93]. Graphite's low friction behaviour becomes apparent when combined with an adsorbed surface film such as oil or water.

This lamellar structure of a graphite crystal structure with each layer containing weakly bonded basal planes that have very low resistance to mechanical shear [94]. However, the fundamentals of these binding energies and how they change with a function of distance must be better understood [95]. There have been efforts using various theoretical methods to calculate these forces using density functional theory (DFT), quantum Monte Carlo (QMC) calculations and meta-generalized gradient approximation approaches. But, difficulties still exist with "the long-range van der Waals nature of interlayer interactions" [96]. Experimental methods have calculated the cleavage energy to separate these layers (0.37 ± 0.01 J/m^2). **Table 2.2** outlines the friction reduction mechanism believed to reduce friction and wear when an adsorbed water or oil surface film is present.

The saturation of dangling bonds is the most convincing mechanism for friction reduction. The relative amount of dangling bonds can explain the difference in friction between the two surfaces on each (**Figure 2.11**). The perpendicular side has a far greater number of dangling bonds, so the effects of water passivation on the adhesion are more significant, with a more considerable reduction in friction. The parallel surface will not have as many dangling bonds, with the edge sites being the leading causes of adhesion during sliding.

Table 2.2 *Graphite friction reduction mechanisms.*

Mechanism	Comments
Water intercalation between the graphene sheets	Water molecules intercalate within the graphite, weakening the bonding between the layers [97]. X-ray diffraction experiments present no increase in d-spacing in water which provides no evidence for this mechanism [98].
Saturation of dangling bonds	Water molecules saturate the dangling bonds at edge sites leading, reducing dangling σ-bonds and reducing the adhesive forces contributing to friction [94]. Results [99] using highly orientated pyrolytic graphite measuring parallel and perpendicular friction indicate that oxygen increases friction, which is especially pronounced on the perpendicular surface, which reduces in a water environment.

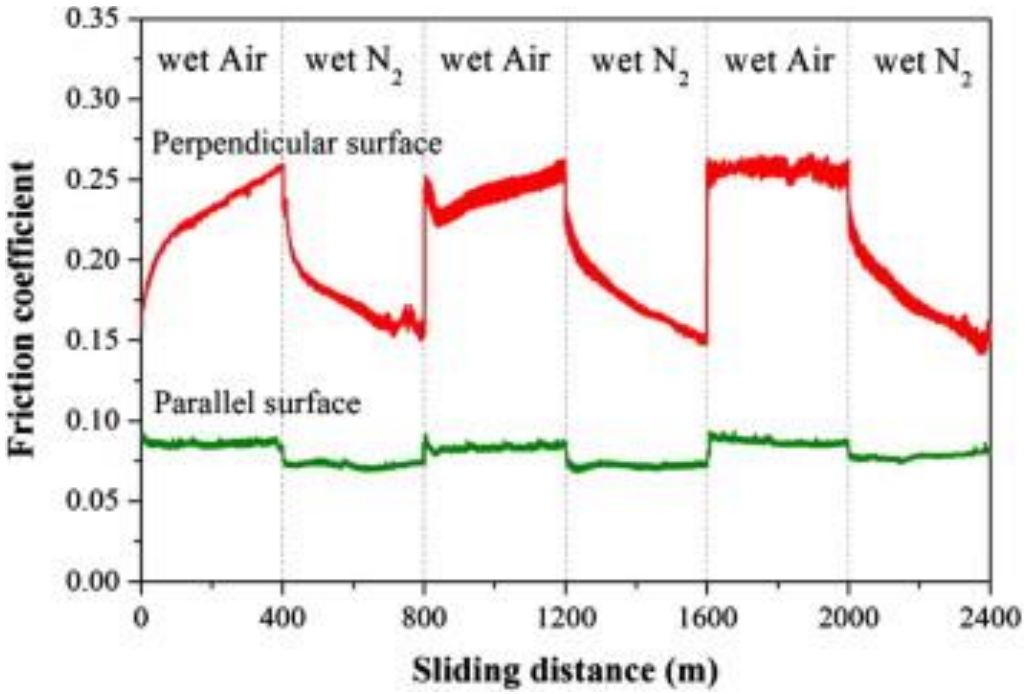

Figure 2.11 *The friction of HOPG in wet air and wet nitrogen on the perpendicular surface and the parallel surface* [99].

Graphite tribology often overlooks the creation and evolution of a transfer layer on the counter-body. Jones *et al.* [100] examined the relationship between a tribologically induced transfer film formation between a graphite surface and a counter-body in dry conditions. The formation of the transfer film was credited to the deformation and agglomeration of wear debris, forming a graphitic stable film. This transfer film in the contact zone was determined to be essential for maintaining low wear in sliding contacts, but no mechanism for how this transfer layer reduced friction was discussed. Xue *et al.* [101] showed that a graphitic transfer layer can also be seen when graphite is used as an additive in an oil lubricant, reducing both friction and wear. The formation of the transfer film was determined to be the result of tribomechanical shearing and heating, which under low contact pressures, did not form a sufficient film to reduce the friction or wear. The low friction seen under the formation of a transfer film could result from easy shear graphitic planes [102], with an oil saturating the dangling bonds lowering the adhesion friction, although the author did not address this.

Although the commercial-scale application of graphene in tribology-related applications is still in its infancy, significant progress has been made through numerous studies exploring its use as an additive, boundary layer, or as part of a composite system. These studies have showcased the potential of graphene to enhance tribological performance and offer unique advantages in terms of friction reduction, wear resistance, and lubrication [20]. The scale at which these studies have been completed ranges from the nanoscale to the macro-scale, using various techniques to measure the frictional responses and the wear produced, with different mechanisms proposed at the various length scales [103]. The experiments completed at the nanoscale generally observe the interactions of only a few asperities, while the macroscale considers the full features of the articulating surfaces. The differences between the scales result from interfacial phenomena that can

dominate at the smaller scales and are difficult to observe at the macroscale [103]. By thoroughly understanding a material's response at both single and multi-asperity contacts, we can make significant strides in enhancing sliding behaviours and mechanisms, thereby opening new avenues for exploitation.

The thickness of graphene for this section ranges from SLG to multi-layer (GNP) thickness, with the number of layers impacting the frictional properties.

2.5. Current state of art of DLC / Graphene Related Tribology

The techniques employed to reduce friction and control wear in the automotive industry primarily use additives, protective films or low-viscosity oils [10]. Unfortunately, commonly used additives such as MoDTC can often accelerate the wear in Hydrogenated DLC films [17], and reducing the viscosity decreases the film thickness therefore increasing wear [10,14]. This section collates the current techniques used in DLC and graphene-related materials tribology and provides details on the mechanisms for reducing friction. A gap analysis (**Section 2.6**) will review the research gaps in the current state of the art.

2.5.1. Graphene / Graphite Based Lubricants

This section examines the current state of graphitic-based lubricants, including dry formulations and suspensions, to examine their mechanisms for reducing friction and wear. By exploring the mechanisms employed by these lubricants, we can establish a foundation for understanding how graphene nanoplatelets (GNP) may also contribute to friction and wear reduction. Additionally, this analysis will help identify gaps in the existing research, highlighting areas that require further investigation. **Table 2.3** presents a comprehensive compilation of significant studies investigating the use of graphitic lubricants as additives and on surface coating, along with their respective mechanisms for

reducing friction and wear. This table is a valuable reference for understanding the diverse research conducted in this field and the various approaches employed to reduce friction and wear. It is shown that graphene as a surface coating [104] provided important information on the effects of adhesion and the relationship for friction for graphene. This work also provides the benefits of graphitic materials combined with amorphous carbon, which reflects some of the work completed in this thesis. Previous studies have primarily focused on investigating the behaviour of graphitic materials at the nanoscale. However, the applicability and synergistic effects of a combined graphitic and amorphous structure under lubricated conditions at the macro scale, particularly in the presence of an iron counter-body, remain largely unexplored.

Graphitic flakes deposited on a surface have shown huge potential in dry conditions [105–107]. The graphitic flakes have provided evidence that thicker flakes reduce friction better than single layers and that the properties of these flakes can protect the surface from mechanical damage. A transfer layer is formed on the counter-body and substrate surface, providing a low friction and wear mechanism. The application of these flakes is limited in a real engineering environment, where they need constant replenishment to maintain low friction [105–107]. The development of graphitic flakes suspended in oil provides some improvements on experiments completed in dry conditions [108,109], where friction is reduced by 400% and wear >50%. These works successfully created a suspension of graphene flakes oil; however, the flocculation of graphitic flakes is observed and limits the long-term use of these as potential additives in oil [20]. A potential solution proposed is adding surfactants to the surface of the flakes [110], which provided low friction results. However, the interaction of these and other additives has not adequately been explored.

The combination of DLC and oil-containing graphitic materials provides a friction and wear reduction mechanism of >40%, creating a highly graphitic transfer layer and a protective film that shears at low energy [24]. This coating is highly effective in the boundary lubrication regime, with a trend of friction reduction as the graphitic content increases to a minimum COF of 0.05. The limitation of using graphene in this work is that it relies on the growth of the tribofilm on the surface of the DLC and that this tribofilm adheres strongly to it for it to be truly effective. This adhesion could be limited if additional additives are provided into the lubricant and could decrease the effectiveness.

Table 2.3 *Lubricant s containing graphitic materials.*

Brief Description of Materials	**Tribological Response**	**Ref.**
CVD Deposited Graphene on SiO_2.	• Transferred graphene performed worse than as-deposited. • Higher adhesion to substrate related in low friction. • Films with an amorphous nature performed better	[104]
Graphene-Containing Oil on (a-C:H) Surfaces	• 50% reduction in friction for DLC/DLC contact • Lowest COF 0.05 in boundary • Graphitic transfer layer formed on both surfaces as the friction reduction mechanism	[24]
Graphene Flakes on SiO_2/Si Substrate.	• Single layers produced higher friction. • Thicker layer produced lower friction. •	[105]
Graphene Flakes on a Textured Steel	• Graphene greatly reduced friction and wear • Steel on steel COF ~0.2	[106]
Graphene nano flakes on a stainless-steel surface.	• Reduced COF from 0.8 to 0.2 • Wear rate for GNF coated steel reduced by around ~80 %	[107]

Table 2.3 Continued from previous page		
Brief Description of Materials	**Tribological Response**	**Ref.**
Graphene Nanosheets (GNS) as Lubricating Oil Additives on a Textured Surface.	• GNS reduced COF from 0.8 to >0.2. • Wear dept reduced by > 50 %	[109]
Graphene Oxide Nanosheets in an Oil Lubricant.	• GO reduced friction and wear by ~20% in boundary lubrication. • Flocculation of the GO at high concentrations reduced effectiveness	[108]

2.5.2. Texturing, and Doping of DLC Films

Texturing and doping of DLC films are two different techniques used commonly in surface engineering to provide more favourable tribological properties. The addition of elements during the DLC deposition process achieves the doping of films. The work completed by Guo *et al.* [111] has shown that doping can inhibit friction reduction mechanisms, the most important being suppressing the formation of the graphitic transfer film. It was put forward that wear, and friction increased if the transfer film was not present, thus providing evidence of the importance of forming a transfer film.

The texturing of films [60,112] has shown to decrease friction and wear by:

- Reduction in the real area of contact.
- Creating a channel for removing debris, reducing third body abrasive particles.

Texturing provides some benefits. However, the loads used, and contact pressures are generally low (1N, < 600 MPa) and completed at the microscale, severely limiting their industrial relevance and leaving gaps in the understanding of behaviour under more realistic macroscale engineering conditions (oil-lubricated).

2.5.3. DLC Nanocomposites

The combination of DLC with nanomaterials is still relativity new, with many avenues to explore. **Table 2.4** provides a range of the most pertinent research related to this thesis. It has been shown [113] that superlubricity can be achieved by combining graphene and nanodiamonds on a DLC structure. The super-low friction was achieved by reducing the real area of contact, creating a rolling effect through the nanodiamonds wrapped up in graphene. Because superlubricity was achieved in a dry environment, little is known about the validity of the experiments under sustained testing durations or if the mechanism can be exploited in lubricated environments. This does leave research gaps in how these materials would behave in an oil environment or if they could be combined with an FFO. There was no discussion about the formation of a transfer film, which may have reduced the adhesive contact during wear tests.

Carbon nanotubes (CNT) [114,115] have previously been doped in DLC films, creating a true nanocomposite that reduces friction and wear. These films were tested in dry environments and showed that the mechanical properties (Elastic Modulus) increased as CNT wt% increased, and the friction decreased linearly. The mechanism provided for friction reduction was due to the increased sp^2 content and higher mechanical properties. The authors did not consider the formation of a transfer film, and the cross-sections of the CNT could be explored further to determine how the bonding between the CNT and DLC was structured. Testing in environments other than dry was not explored and left many research gaps in the behaviour and mechanisms.

Graphitic particles have also been doped in DLC, with two notable examples by Li *et al.* [116] and Nik Binti [25]. These examples provided two different techniques for deposition, the first being completed via magnetron sputtering [116], and the latter via spin coating [25].

The work completed by Nik Binti [25] did not provide a mechanism for friction reduction. In that work [25] DLC-GNP nanocomposites were created using varying GNP concentrations, these delaminated during sliding wear. The work completed does however, provide a background for this thesis, allowing GNP to be dispersed by spin coating and providing:

- The most effective solvent and conditions to disperse the GNP.
- The amount of solvent to be used, spin speed and time for the spin coating procedure.
- A protocol for heat treatment to ensure the GNP would adhere to the interlayer after spin coating.

The deposition of graphitic-like carbon (GLC) particles via magnetron sputtering (MS) provides a technique which allows the film coating to be synthesised using a “one pot” method. The authors [116] did not explore the bonding between the GLC and the DLC matrix, and testing was completed only in dry conditions. The mechanism provided by the authors considered only the reduction in the real area of contact and has not explored the formation of a transfer film on the counter, which is shown in other DLC-related research [63] to be a primary driving factor in friction reduction. However, using a ceramic ball may have reduced the formation of a transfer film [73]. The authors did explore the sliding of the GLC on the film surface and provided evidence to show that the GLC did shear and cover a slighter greater area, which may also have contributed to the friction reduction. The testing conditions again in a more demanding condition, such as heated oil, could change the mechanism proposed by the authors and leaves gaps in the understanding and testing of a material such as a metal counter-body. The mechanical properties of the GLC clusters with the combination of the DLC is an area that should

have been explored more thoroughly by the authors in this paper, as it could change the localised contact pressure between the coating and the counter-body when in contact.

These results allowed the synthesis of the first generation of DLC-GNP nanocomposites, which improved friction and wear. However, many outstanding research questions were then left to be resolved:

1. During the characterisation of these coatings, it was observed that there were discrete areas of GNP and DLC. However, the difference in mechanical properties between the GNP and DLC was not analysed.
2. The GNP were heat treated after deposition with a temperture of 180°C providing the most benifical results, but no reasons were provided for this.
3. The optimum coverage of GNP using the heat treatment protocol.
4. The mechanism for low friction and wear for a composite DLC-GNP nanostructure
5. The bonding mechanism between the GNP and the DLC.

If explored adequately, these research gaps will provide important information to the tribological and engineering community. These can be transferred to other systems and lead to the development of greener coatings and lubricant combinations.

Table 2.4 *Current state of the art of DLC Nanocomposite films.*

Brief Description of Materials	**Tribological Properties**	**Ref.**
Graphite-Like Carbon Films with Varied Thickness.	• Higher contact pressure reduced friction quicker (COF~0.1) • Higher contact pressure resulted in lower wear rate (~2 x 10^{-16} $m^3N^{-1}m^{-1}$. • Sp^3 Fraction decreased with deposition time. • G peak shift to higher wavenumber as test time increased, forming graphitic transfer later on counter.	[117]

Table 2.4 Continued from previous page		
Brief Description of Materials	**Tribological Properties**	**Ref.**
Graphene Nanoscoll Formation on DLC.	• Superlubricity was observed < 0.01 in dry, ~0.3 in humid. • Very low wear for dry environment but high for humid • Formation of nanoscrolls (nanodiamonds wrapped in graphene) was observed, reducing the area of contact.	[113]
DLC-CNT Composite.	• Friction decreased linearly as CNT wt% increased. • Elastic modulus increased as CNT wt% increased. • Lower friction was attributed to the higher sp^2 content of the films	[114,115]
Diamond-Like/Graphite-Like Carbon Composite.	• Raman used as method to determine sp^2 content. • Friction decreased initially as graphitic microparticle content increased then increased over a certain content. • Wear decreased as graphitic microparticle increased. • Graphitisation of the microparticles was credited as the mechanises for friction reduction. • Graphitic microparticles act as a reservoir of lubricant for the counter • Soft GLC microparticles could reduce the real contact area	[116]
DLC-GNP nanocomposites.	• Heat treatment for 3 hours at 200°C provided the best friction results. • Friction reduced to ~0.04. • Dispersion of GNP is stable in NMP for longer storage. • No mechanisms provided for the low friction and wear observed	[25]

2.6. Gap Analysis

Table 2.4 provides the current state of the art of DLC and graphitic-related system research. Lubricated systems (particularly ICE) rely heavily on additives such as MoDTC, which can accelerate wear in DLC coatings [17]. Current research to improve

efficiency was shown by Thornley *et al.* [10] to reduce friction in the hydrodynamic regime using low-viscosity oils. The lower friction in the hydrodynamic regime comes at the expense of increased friction and wear in the boundary regime due to increased asperity contact. This is also combined with the greater addition of greater Mo, which is environmentally toxic [118]. Some researchers [119] have reduced friction to <0.01 using esters. However, the Author neglected to mention that Glycol contamination can block filters and is temperature sensitive, limiting the use in ICE [120,121]. The current methods for reducing friction and wear cannot be achieved by engine oil additives alone if environmental concerns are addressed and need to be improved.

Previous work completed at the University of Leeds [25] provided some promising initial results by doping a DLC film with graphene. However, the research gaps below are outstanding and are investigated within this thesis.

Research Gap 1: Provide a low friction mechanism for boundary lubricated conditions for DLC-GNP nanocomposites.

Recent research for Graphene (and graphitic materials) has shown promise in controlled conditions when either used as a solid coating or as an additive in oil [24,104–109]. The analysis of Graphene containing lubricants [24,108,109] highlights the limitations in the applications of these materials in a lubricating environment, namely, the agglomerations of the graphitic materials and the ability to provide the Graphene into contact areas to provide this low friction and wear. However, these works highlight that forming a graphitic transfer film is essential to reduce friction and wear. In the case of a DLC-GNP nanocomposite, what specific role does GNP play in reducing friction?

Furthermore, is there a limit to the amount of GNP that can be added before it becomes ineffective in reducing friction. Is there a limit to the amount of GNP before it becomes ineffective.

Research Gap 2: Determine how DLC-GNP nanocomposites maintain durability after extended wear tests.

The combination of the two carbonous materials and their interaction at the sliding interface is unknown during extended wear tests. What structural changes the GNP undergoes during extended testing needs to be discovered.

Research Gap 3: Determine how the DLC thickness affects the tribological and mechanical properties of a DLC-GNP nanocomposite.

The thickness of a DLC layer plays a crucial role in ensuring the adequate protection of the substrate. If the DLC layer is excessively thick, it can lead to the build-up of internal stresses, which may hinder its overall performance [122]. Conversely, if the DLC layer is too thin, it is prone to rapid wear and deterioration. The introduction of GNP doping presents an additional challenge, as the thickness of the DLC matrix holding the GNP together becomes a critical factor in determining their behaviour during contact.

If the DLC matrix is too thin, it raises concerns about how the GNP will respond under contact conditions. On the other hand, if the DLC matrix is excessively thick, it may hinder the ability of the GNP to establish contact with the counter-body. Achieving an optimal balance in the DLC-GNP composite structure is essential to ensure adequate contact and enhance overall performance.

Research Gap 4: Provide a comparison on DLC-GNP nanocomposites tribological response in lubricated environments in a base-oil and fully formulated oil.

The combination of diamond-like carbon nanocomposites and their behaviour in an FFO is unknown. Typically, wear increases when a MoDTC-containing oil is introduced into a hydrogenated amorphous carbon film under articulating wear [123].

Another study completed by Wei *et al.* [114,115] doped DLC with CNT to improve friction and wear, providing a lower residual stress and sp^2 rich layer. However, testing this coating under oil-lubricated conditions still needs to be completed. Li *et al.* [116] provided DLC doped with graphitic crystallites, but the test was limited to only dry conditions, leaving the performance of these materials in oil-lubricated conditions unknown.

A few studies have considered dry or base-oil lubricated conditions but still need to determine if the coatings would provide adequate lubrication in an FFO [24,113,117,123].

One of the most relevant studies were provided by Liu *et al.* [123] for GLC coatings under FFO and high contact pressures. Experimental results confirmed that the wear increased for the GLC more than for a-C:H coatings; however, no mechanisms for this were provided.

Investigations are required to consider how GNP, which are larger than graphitic clusters in GLC, respond when tested in a DLC matrix in an FFO.

Research Gap 5: Determine the different mechanical properties of the GNP islands and DLC matrix.

The initial testing on DLC-GNP nanocomposites provided some bulk data on the mechanical properties. However, these were limited and provided no insights into the reasons for the differences observed.

Research Gap 6: Determine the tribological response of DLC-GNP composites under various testing conditions, and environments.

DLC coatings have shown to display different tribological properties under increased load, speed and temperatures [124]. The current understanding of DLC-GNP tribological behaviour is under cam-follower conditions, and it is unknown if the mechanism for friction reduction is limited to this application.

Chapter 3 - Experimental Setup and Procedure

3.1 Introduction

The synthesis, characterisation, and determination of the tribological properties of DLC-GNP coatings form a crucial aspect of this thesis. A thorough understanding of the synthesis methodology, processes, and equipment used for characterisation is vital for accurately interpreting the subsequent chapters' results. **Figure 3.2** provides a visual overview of the experimental and characterisation techniques employed in this research.

All samples were prepared using a consistent method outlined in the flow diagram (**Figure 3.1**). Instead of allowing the samples to dry at room temperature (as per Reference [25]), a slight modification was introduced. The samples were placed on a hot plate at 100°C for 1 minute. This modification significantly reduced GNP agglomeration during the drying process, resulting in a more uniform distribution of GNP.

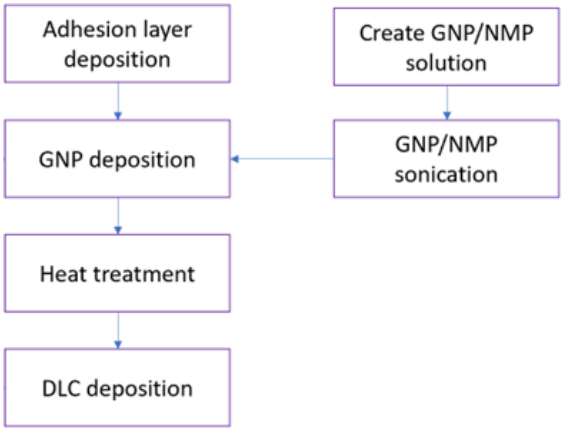

Figure 3.1 *Flow diagram of the process used to create single-layer and multi-layer DLC-GNP Nanocomposites.*

The adhesion and DLC layers were deposited at the University of Leeds using the Hauzer Flexicoat 850 system, which offers the capability to deposit thin films utilizing either PVD or PECVD deposition processes within a vacuum environment.

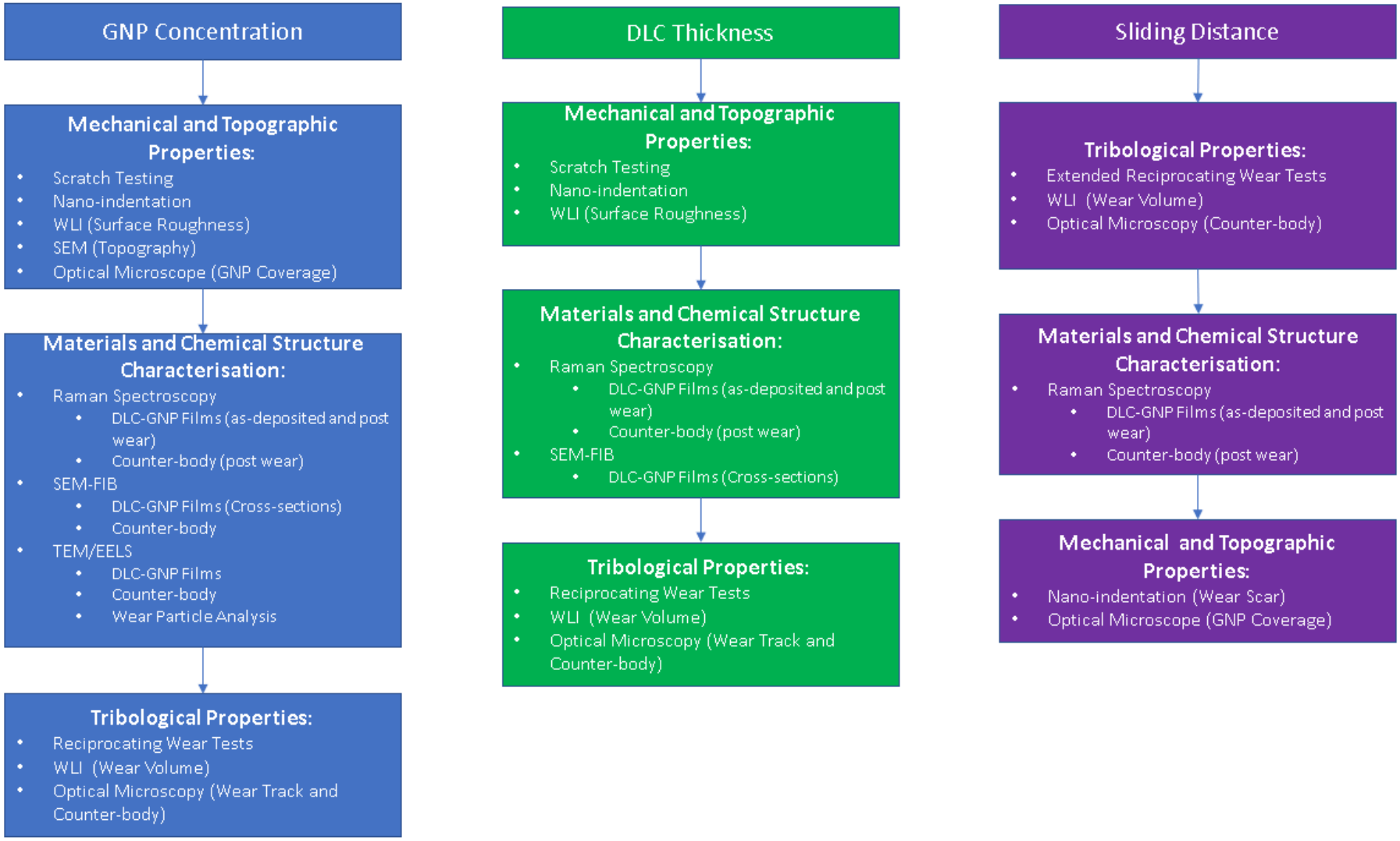

Figure 3.2 *Flow diagram of the 3 results chapters and the experimental and characterisation techniques used.*

3.2 Sample Synthesis

3.2.1 Sample Substrate

The substrate utilised for this thesis was M2 HSS steel, commercially sourced from Yorkshire Steel [125] and not subjected to heat treatment. This material was previously selected for DLC-GNP composites [25] for its excellent strength and toughness, and in keeping this material, it allows a direct comparison to that work. The elemental composition of M2 HSS steel was provided by a Mill certificate outlined in **Table 3.1**.

HSS steel has a high tempering temperature, which ensures the properties remain unchanged throughout the synthesis process experienced in the PECVD chamber (<220°C) [126]. Due to the surface interactions of the active DLC-GNP coating and the CI counter body, it is imperative to ensure that the mechanical properties remain consistent for the substrate. The surface interactions between the coatings and the counter-body are important, and ensuring a cast iron counter-body was used allowed comparisons with other relevant research [17].

Table 3.1 *Chemical composition of M2 HSS steel* [125].

Chemical Analysis	
Element	**Composition wt-%**
C	0.89
Mn	0.36
Si	0.36
S	0.009
P	0.028
Cr	4.06
V	1.84
Mo	4.82
W	6.13

The coupons were cut from a 1 m length, 30 mm diameter commercially purchased rod to a thickness of 6mm. Due to the roughness sustained from the cutting process, the coupons were polished to a surface finish (R_a) of between 0.02-0.06 µm. The Struers LaboPol-60 automatic polisher was utilised for this purpose, combining grinding and polishing functions. Grinding was performed using Si-C carbide grinding paper, progressing from 200 grit to 1200 grit in increments of 200 grit. Subsequently, polishing was conducted using fibre cloths and diamond suspension paste, starting with 9 µm, followed by decreasing sizes of 6 µm, 3 µm, 1 µm, and 0.25 µm. After polishing, the surface roughness was checked for quality and consistency using a white light interferometer (WLI) for each batch.

3.2.2 Adhesion Layer

An adhesion layer is used to improve the bonding at the interfaces of a ferrous substrate and a DLC film [127]. In this thesis, the adhesion layer is deposited using a combination of MS (Magnetron Sputtering) and PECVD (Plasma-Enhanced Chemical Vapor Deposition) processes, which have previously demonstrated effectiveness in improving DLC adhesion to ferrous substrates [128–130].

The adhesion layer utilised in this study is deposited via PVD (Physical Vapor Deposition) and consists of gradients of Cr and WC, with a top layer comprising WC:aC:H. The specific deposition conditions are outlined in **Table 3.2.** The carbon gas source was acetylene, which undergoes cracking through the Ar plasma.

Table 3.2 *Deposition conditions used for adhesion layer.*

Deposition step / conditions	Time (mins)	Temp (°C)	Pressure ($x10^{-5}$ mbar)	Bias Voltage (V)	Cr target power (kW)	WC target power (kW)	Ar flow rate (sccm)	C_2H_2 flow rate (sccm)
Heating	60	200	4					
Target cleaning	20	-	-	500 (DC)	6	3	130	
Plasma surface etching	45	150		200 (PLS low)			50	
Cr	25				3		130	
Cr/WC	30				3-0.5	0.5-3	110	
a-C:H:W	75					3	90	8-30 (30 mins ramp time)

3.2.3 GNP Suspension

The GNP was purchased commercially from Sigma Aldrich, with a typical surface area of 120 to 150 m^2/g, an average thickness of 6-8nm and a particle size of 5μm [131]. To create the GNP suspension, specific concentrations of GNP (mg) were mixed with N-Methyl-2-pyrrolidone (NMP) solution (ml), followed by 6 hours of ultrasonication. The concentrations used in this thesis were: 0 mg/ml, 0.25 mg/ml, 0.5 mg/ml, 0.75 mg/ml, 1 mg/ml, 1.5 mg/ml and 2 mg/ml. The NMP was used over other solvents due to the stability and dispersion presented in previous works [25].

3.2.4 GNP Dispersion

Drop cast spin coating (**Figure 3.3**) was employed to achieve the dispersion of GNP on top of the adhesion layer. The dispersion of GNP was accomplished by flooding the sample with 1 ml of GNP/NMP suspension for 1 minute at 1000 rpm, followed by drying

on a hot plate for 1 minute at 100°C. Drying at 100°C was to prevent agglomeration and ensure consistent GNP dispersion. Initial trials revealed agglomeration issues when samples were left to dry at room temperature.

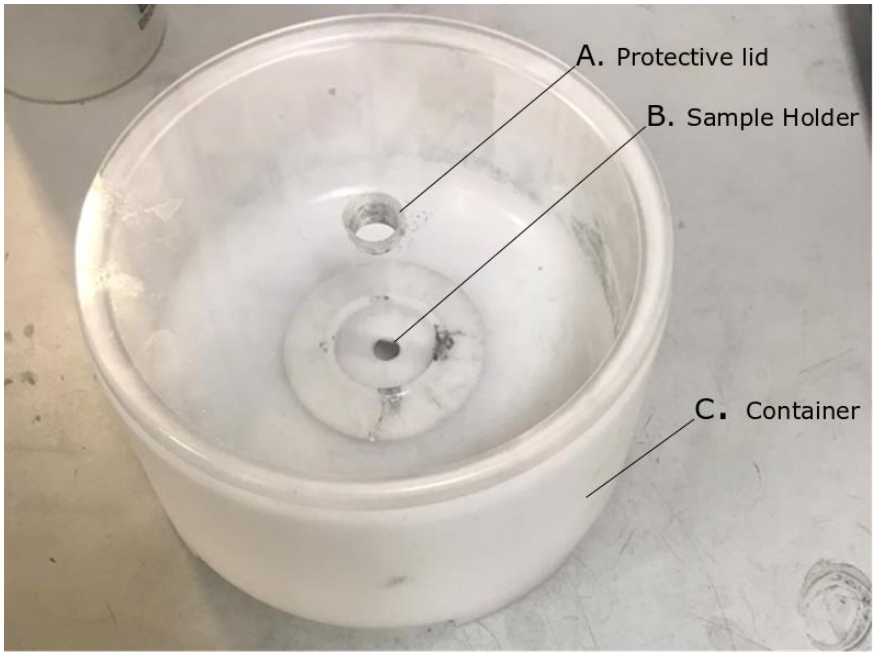

Figure 3.3 *The inhouse spin coater used to deposit GNP.*

To investigate 'The Effect of GNP Coverage on the Tribological and Mechanical Properties,' the experiment involved varying the GNP/NMP suspension concentration during the spin coating process. The specific concentrations used, and their corresponding nomenclature are presented in **Table 3.3**. The measurements of the GNP coverage are as per **Appendix D.**

Table 3.3 *Concentrations used for DLC-GNP nanocomposites.*

GNP/NMP Concentration (mg/ml)	Nomenclature
0	Pure DLC
0.25	DLC-GNP0.25
0.50	DLC-GNP0.5
0.75	DLC-GNP0.75

1	DLC-GNP1
1.5	DLC-GNP1.5
2	DLC-GNP2

3.2.5 Heat Treatment

Previous results [25] have demonstrated that a heat treatment process enhances the adhesion of GNP to the adhesion layer. The optimal heat treatment conditions identified were 200°C for 3 hours. There has been no explanation for the adhesion or tribological improvements after the heat treatment.

It was observed that in the absence of a heat treatment process, the GNP could be removed by cleaning the samples in an ultrasonic bath filled with ethanol for 5 minutes (**Figure 3.4**).

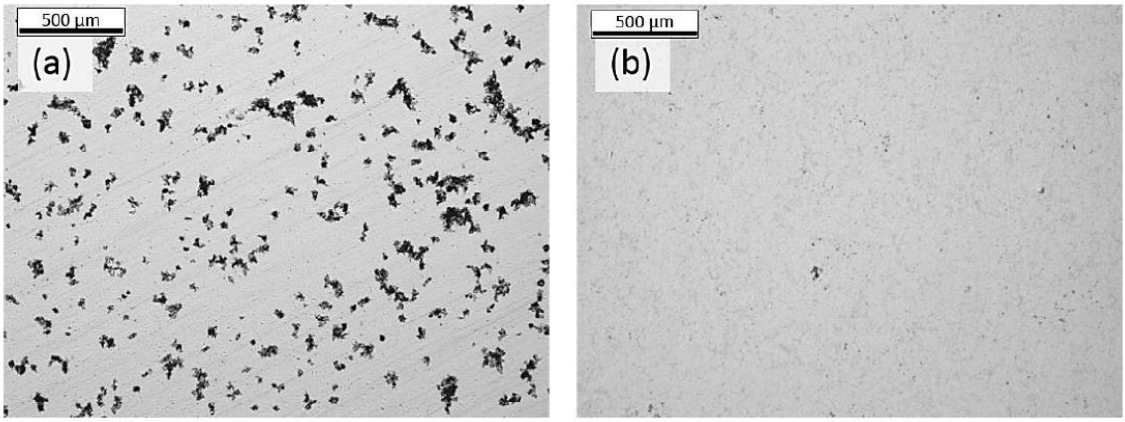

Figure 3.4 *Micrographs of sample surfaces after cleaning in ultrasonic bath post GNP deposition. (a) Completed using heat treatment, and (b) no heat treatment* [25].

The heat treatment process involved the following steps:

- Cover and press with tape: Teflon tape is pressed onto the surface of the substrate after the GNP have been dispersed and dried, ensuring to remove any air bubbles.
- Heat Treatment: The taped samples were then placed into an oven for 3 hours at 200°C.

- Tape Removal and Cleaning: After 3 hours, the samples are removed from the oven with the tape immediately removed and allowed to cool to room temperature. Once cooled, the samples were cleaned by sonication, firstly heptane for 5 mins, then ethanol for 5 mins, to remove any residual solvent (NMP).

It has been shown that heating of graphene at temperatures as low as 300°C can induce doping of O_2 molecules which will be detectable using Raman spectroscopy [132]. During the heat treatment, an experiment was conducted (**Section 4.2.2**) to investigate the potential impact of not covering a sample with Teflon tape. The objective was to compare the Raman spectrographic results obtained from taped and untapped samples.

3.2.6 DLC Deposition

The DLC deposition is performed as the final step in the synthesis process, following the completion of the GNP heat treatment process (and cleaning). The deposition conditions, including the gas used for the process, are detailed in **Table 3.4**. Acetylene gas is the precursor gas employed for the deposition, utilising the PECVD technique.

Table 3.4 *PECVD deposition conditions.*

Deposition step / conditions	**Time (mins)**	**Temperature (°C)**	**Pressure ($x10^{-5}$mbarr)**	**Bias Voltage (V)**	**Ar flow rate (sccm)**	**C_2H_2 flow rate (sccm)**
Heating	60	200	4			
Plasma surface etching	20	150		200 (PLS low)	50	
a-C:H deposition	22.5-180 mins			740 (PLS High)	90	380-270 (8 min ramp)

For Chapter 4, the deposition time was maintained at a constant duration of 90 minutes, while the GNP/NMP concentration served as the distinguishing factor.

In Chapter 5, the deposition times ranged from 22.5 minutes to 180 minutes, with the corresponding nomenclature assigned to the different samples, as outlined in **Table 3.5**.

This variation in deposition time was employed to investigate the impact of DLC thickness on the mechanical and tribological properties.

Table 3.5 *DLC deposition times for single-layer DLC-GNP nanocomposites*

DLC Deposition Time (Minutes)	Name
22.5	DLC-GNP22.5
45	DLC-GNP45
90	DLC-GNP90
180	DLC-GNP180

3.3 Characterisation of Coating

3.3.1. Coating Thickness

The thickness of the coating is measured using a CSM Calotest using a 25mm ball with 6µm diamond paste, which is suitable according to ISO 1071-2 for coating thicknesses between 0.1µm to 50µm. The procedure for the calotest is provided in **Appendix E**.

3.3.2. Optical Microscope

The counter-body and sample surface (before and after wear), as well as calotest scars (**Section 3.3.2**) and GNP coverage (**Appendix D**), were captured and analysed using a Lecia DM6000 optical microscope. This microscope utilises the in-built LAS V3.8 software to record 2D images.

The wear scar of the pins was used to measure the wear rate using the Archard wear equation [133]. In this equation the lost segment of the sphere is calculated using **Equation. 3.1 and Equation. 3.2** below.

$$h = R - \sqrt{R^2 - r^2} \qquad \textit{Equation 3.1}$$

$$V_L = \frac{1}{6}\pi h(3r^2 + h^2) \qquad \textit{Equation 3.2}$$

Where R is the radius of curvature of the pin (m), r is the radius of the wear scar (m), V_L is the volume loss of the counter-body (m^3), and h is the height of the missing sphere after wear (m).

The Archard wear equation is shown in **Equation 3.3**.

$$k = \frac{V}{LW} \qquad \textit{Equation 3.3}$$

Where k is the dimensionless wear coefficient (commonly expressed as $m^3N^{-1}m^{-1}$), *V* is the volume of the wear scar (m^3), W is the applied load (N), and L is the sliding distance (m).

3.3.3 White Light Interferometry

Surface roughness and wear volume measurements were completed using the Bruker NPFlex system and analysed utilising the built-in Vision64 software. The Bruker NPFlex is a non-contact surface roughness measurement system that employs WLI (White Light Interferometry) to measure the surface of the samples accurately. It provides a maximum vertical resolution of <0.15 nm and exhibits an RMS repeatability of 0.0 3 nm, ensuring precise and reliable measurements [134]. The highest resolution lens (50x objective) was employed for surface roughness and wear measurements. The 50x objective yielded highly detailed results, particularly for low-wear testing. However, it should be noted that this higher resolution also resulted in larger file sizes, which imposed limitations on the maximum area size that could be measured. Before usage, the machine is calibrated using a standard block with a known roughness and step height. This calibration procedure ensures accurate and reliable measurements.

3.3.3.1 Surface Roughness

Surface roughness measurements were obtained from five different regions of the sample, each utilising a 1 mm x 1 mm area. The NPFlex system calculates the average surface

roughness (R_a) using the in-built software, with average and standard deviation values calculated from these values. While the ISO 25178 standard specifies a sampling length of 2 mm for 3D metrology, initial testing comparing the 1 mm x 1 mm and 2 mm x 2 mm areas revealed negligible differences in the average and standard deviation, given that five measurements were taken. The reduction in sampling area allowed the measurements to be taken quickly and did not result in the system crashing. WLI was chosen over other surface roughness measurement techniques due to the sensitivity of the results, along with the non-contact methodology reducing the risk of damage to the surface during measurements.

3.3.3.2 Wear Volume Measurements

The wear volume for each sample is measured using a scan of 1mm width and 2.4mm length, with the negative volume calculated using the in-built Vision64 software. Each wear scar had measurements taken in three sections, as shown in **Figure 3.5**. The entire length of the wear scar was not taken due to the limitations of using the 50x lens, making the file size too large.

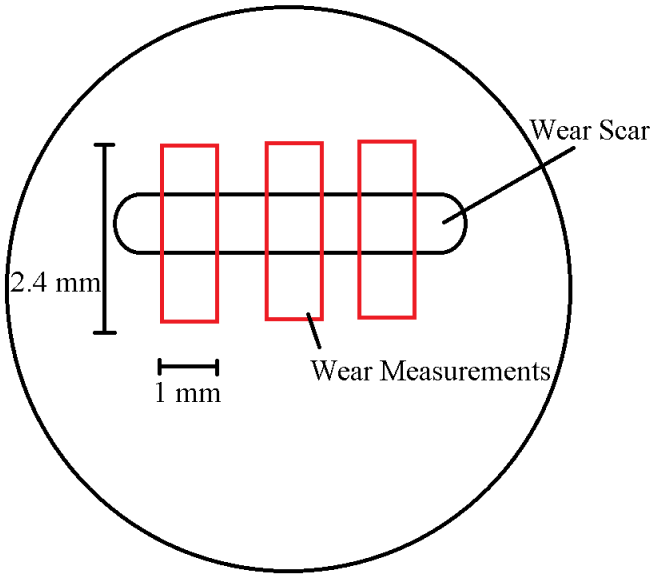

Figure 3.5 *Location of wear volume measurements for each wear scar.*

The wear rate is calculated using the same wear equation presented in **Equation 3.2,** using the average of the measured wear volume. A surface line profile is taken perpendicular to the wear scar (using the inbuilt vision64 software), allowing a visual representation.

3.3.4 FIB-SEM

SEM is a non-contact method used to image DLC samples using highly energetic electrons [135]. In this thesis, the Carl Zeiss EVO MA15 SEM was employed to capture images of the sample surfaces before and after wear, identifying wear mechanisms and analysing surface topography. As-deposited cross-sections and worn counter-bodies were analysed using the FEI Helios G4 CX DualBeam SEM.

The DLC-GNP film surfaces were imaged using secondary electrons (SE) before and after wear. Due to the conductive nature of DLC and the steel substrate, no conductive surface coating is required when preparing the sample for imaging.

Selected samples were cross-sectioned to determine thickness and structure, along with selected worn CI counter-bodies to determine the presence of a transfer film. The focused ion beam (FIB) technique employed in this study involved using gallium ions to mill specific sample areas for imaging the structure, as depicted in **Figure 3.6.** Additionally, thin cross-sections were created using FIB for subsequent analysis in a transmission electron microscope (TEM). A platinum protective layer was used to protect the sample from damage during the milling process, along with a layer of Iridium for the counter-body. EDX was used on selected cross-sectioned samples to determine the elemental composition of the layers.

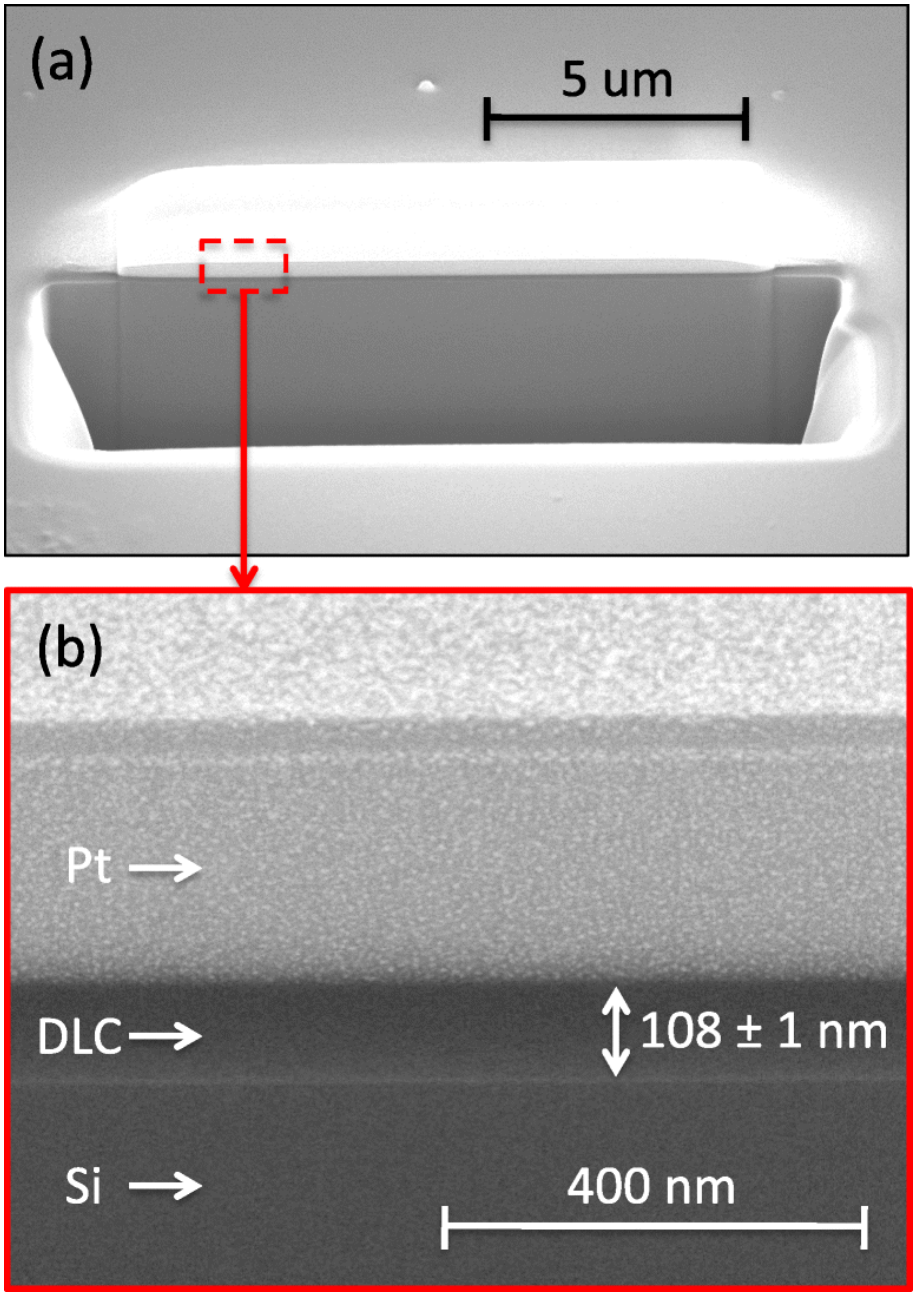

Figure 3.6 *(a) FIB-SEM cross-section with (b) the protective platinum layer on top of the cross-sectioned sample* [136].

The cross-sections allow the structure of the DLC-GNP nanocomposite to be visible and must be under 100 nm to be electron transparent. **Figure 3.7** provides a topside view of a DLC-GNP cross-section which measured 90 nm at the point highlighted.

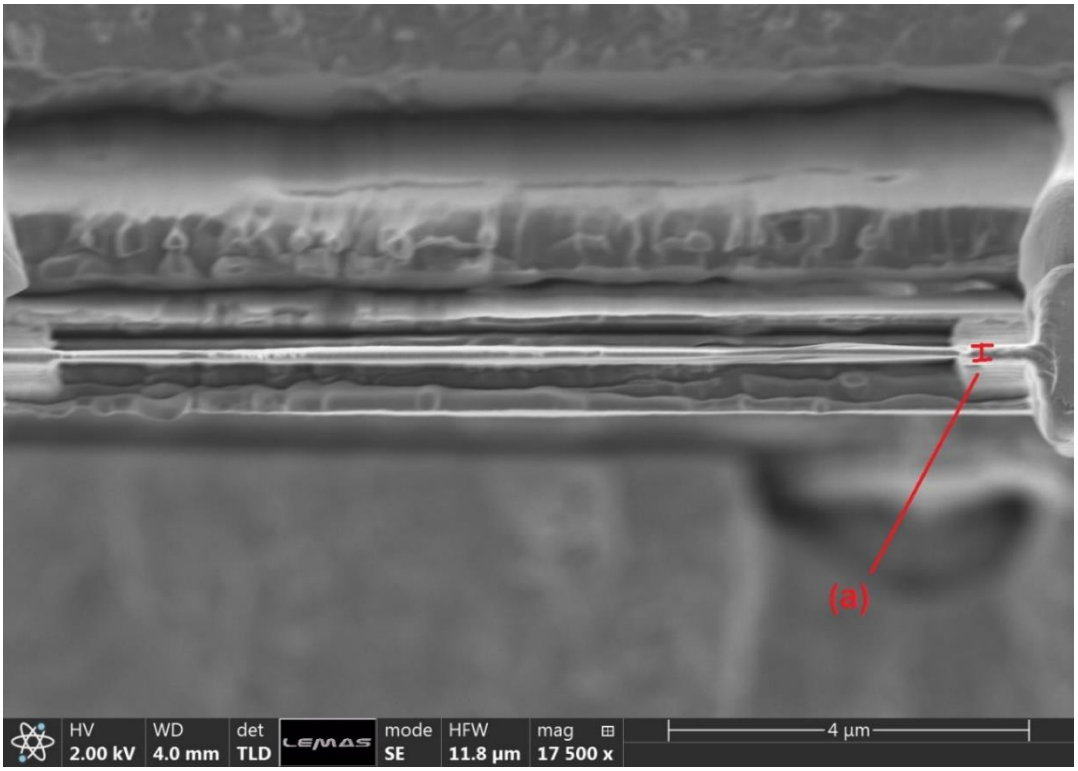

Figure 3.7 *Top-down cross-section of DLC-GNP sample, with (a) indicating the thickness of 90 nm.*

3.3.5 TEM / EELS

The FEI Titan3 Themis 300: X-FEG 300 kV S/TEM with S-TWIN objective lens, monochromator (energy spread approx. 0.25 eV), Gatan Quantum ER energy filter for EELS and EFTEM and Gatan OneView 4K CMOS digital camera was used to image selected pure DLC and DLC-GNP nanocomposite coatings.

EELS was used as the quantitative measurement technique to determine the sp^2/sp^3 content of the DLC-GNP film due to the fine structure measurements that can be analysed from a cross-section.

The configuration of the carbon C-K edge heavily relies on the crystallographic environment surrounding it. Hence, electron energy loss spectroscopy (EELS) emerges as a viable approach for assessing the proportion of sp^2 bonding in carbon-based materials. To quantify this fraction accurately, one can compare the intensity of the π^*

peak within the C-K edge to that of graphite, a substance known for its 100% sp^2 bonding [137].

Traditional non-destructive techniques such as Raman cannot quantify sp^2/sp^3 content at different depths and have limited penetration depth [138]. The accelerating voltage was 300 kV and taken under magic angle conditions to eliminate any orientation-dependent contributions. The EELS data were collected in TEM mode with a parallel beam, so the convergence angle is 0, and the collection semi-angle was 0.7 mrad. The FWHM of the zero-loss peak is 1 eV, and the dispersion was 0.1 eV/pixel. The C K-edge were collected for 30 s and the low loss was collected for 0.002 s. The EELS spectra were analysed using Gatan's Digital Micrograph software.

The EELS spectra were taken close to the adhesion layer and then at 4 depths moving towards the surface. The location and direction of the scans are shown in **Figure 3.8**. The samples were measured at differing depths to determine inhomogeneity within the sample.

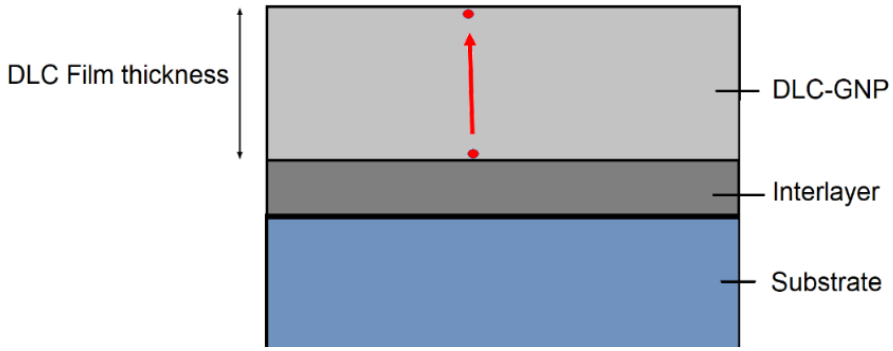

Figure 3.8 *Schematic diagram of cross-section with the red dot and arrows indicating where the EELS spectra will be taken from.*

The quantification of the sp^2 bonded carbon percentage, compared to the total carbon, was achieved by the method proposed by Zhang *et al.* [139] and Mironov [140]. A commercially purchased HOPG was used as the reference material. The core loss area of

the spectra was analysed with the π* peak maximum of all spectra calibrated to 285 eV. Three Gaussian peaks were fit and centred at:

- G1 (282.5 – 285 eV ± 2 eV) centred at 285 eV - (π* component C=C)
- G2 (289.5 – 295 eV ± 2 eV) centred at 292 eV - (σ* component C-C)
- G3 (295.5 – 299.5 eV ± 2 eV) centred at 300 eV – (σ* component C=C)

The intensity of the π* peak (G1) was integrated over an energy window Iπ*, then normalised by the integral of the large energy window $I_{\pi^* + \sigma^*}$ (282.5 – 302.5 eV). This larger energy region encompasses both the π* and σ* components.

The procedure provides suitable fits with very low residuals (observed around 289eV) to ensure each spectrum can be comparable, the origin of any remaining residuals could be due to excitations into the σ* states [141]. The determination of the of sp^2 bonding percentage in each spectrum (against the HOPG reference) is completed using the following equation [142] for graphitic carbon materials:

$$sp^2\% = \frac{\left(\frac{I_{\pi*}}{I_{\pi*+\sigma*}}\right)_{unknown}}{\left(\frac{I_{\pi*}}{I_{\pi*+\sigma*}}\right)_{reference}} \qquad \textit{Equation 3.4}$$

A residual peak around 298 eV was often present during the first fitting and were reduced as far as practicable by moving the fitting bands within the limits provided by the fitting bands ± 2 eV [142].

3.3.5.1. Wear Particle Analysis

Wear particles from selected tribotests were analysed using TEM microscopy. After tribological testing, the wear particles were extracted from the oil by isolating them using a solvent (heptane) and centrifugation. To accomplish this, the collected particles suspended in the oil were transferred into a 50 ml centrifuge vial, and heptane was added until the vial reached its maximum 50 ml capacity. The centrifuge was then set to 10,000 r.p.m and run for 30 minutes. After the first centrifugation cycle, the top 45 ml of the

mixture was carefully removed using a pipette, and an equal volume of fresh heptane was added to the vial. This process was repeated a total of 5 times. To transfer the wear particles onto a copper grid, a pipette carefully extracted the uppermost 49 ml of the mixture from the vial. The remaining 1 ml solution was then deposited onto a copper grid using individual drops.

3.3.6 Raman Spectroscopy

Raman spectroscopy is used in this thesis as it is a widely used surface-sensitive, non-destructive method for characterising carbonous-based films [63,143–145]. Raman spectroscopy is particularly sensitive to carbon-carbon bonds due to their highly symmetric covalent bonds with little or no natural dipole moment. Through careful analysis of their spectra, information such as defects, number of graphene layers, relative graphitisation and morphology of the sample can be obtained [146]. In the typical 1000-2000cm^{-1} range, the dual peak phenomenon is observed, consisting of a D peak around 1350cm^{-1} and a G peak around 1580cm^{-1} (**Figure 3.9)**.

The Raman spectra were obtained for this thesis using a Renishaw inVia Qontor microscope using a 488nm coherent incident laser with a maximum laser power of 10 mW and a scan range of 900 – 2000 cm^{-1} under ambient conditions. The Raman spectra were obtained using a 50x objective lens with a numerical aperture of 0.75. The power of the laser was kept constant at 10% so as not to heat the sample and cause the graphitisation of sp^3 clusters within the DLC, which could affect the results [147]. The analysis of the collected Raman spectra was completed as per **Section 3.3.6.3**.

3.3.6.1. DLC-GNP Film

Due to the discrete structure of the DLC-GNP films (**Figure D.*2***), point Raman spectra scans were taken from:

- GNP islands: The spectra for the GNP islands were collected from the centre of the GNP to avoid signals from the edges, which are often unsatisfied sp^2 clusters.
- DLC areas**:** These were taken away from the GNP islands so as not to interfere with the scans.

In total, 5 scans were undertaken from each feature before and after wear testing. These scans were used to determine if there were any localised differences in the bonding structures of as-deposited films and structural changes to the sp^2/sp^3 bonding structure for films post-wear. DLC and GNP have distinct Raman spectra which must be considered during each scan.

In a DLC sample, the I_D/I_G peak provides a means to evaluate the disorder of the carbon bond network. With the D peak due to the breathing modes of the sp^2 bonded carbon and G peak due to the stretching bond mode of all pairs of sp^2 bonded carbons (both aromatic and olefinic)[87]. The D peak is highly sensitive and will increase rapidly in intensity as the size and amount of sp^2 clusters form [148]. The G peak intensity remains relatively constant as it does not require the presence of the 6-fold graphitic ring [149]. Using this information, the relative intensity of the d and g peaks provides qualitive comparison for the relative increase in formation of sp^2 cluster.

For Graphene (or graphene related materials), the D peak is absent in a perfect crystal, when the D peak becomes active it is because either the edge sites of a spectra have been taken, or that the 6-fold graphitic ring has become Raman active through breaking of a C=C bond [149]. Similar to the DLC the G peak intensity remains relatively constant, and the I_D/I_G ratio provides a means to assess the crystal's defects from mechanical damage during sliding wear.

When these materials are combined into one composite structure (i.e., DLC deposited over GNP), it is essential to consider the contribution of both the collected Raman spectra, and the penetration depth of the laser (< 300- 400 nm). Thus, when the Raman spectra are analysed, cognisance of the contribution of both constituents is considered.

3.3.6.2. Counter-body

The scans for the counter-body were taken inside the centre of the wear scar, with 5 scans taken from each pin. The spectra were collected from the same points of each pin, using the same power to ensure the results could be compared. The G peak intensity was measured for the CI pins to determine if there was a link between the intensity of the G peak and thickness measured by TEM cross-sections. Al-Azizi *et al.* [112] measured the intensity of the G band and related it to the thickness of the transfer film on a counter-body. It was then shown [112] that the increased thickness of the transfer film on the counter-body resulted in higher wear of the film.

3.3.6.3. Raman Analysis

All Raman scans were analysed using the OriginPro 7 software package. The D and G peaks (**Figure 3.9**) were identified, and the corresponding integral intensity ratios (I_D/I_G) were calculated. To ensure accurate readings, Gaussian fitting and baseline subtraction methods were employed [150,151]. For each sample and worn counter-body, the average I_D/I_G values, D and G peak position, and G peak intensity were calculated along with the standard deviation. This provided a comprehensive analysis of the Raman spectra before and after wear.

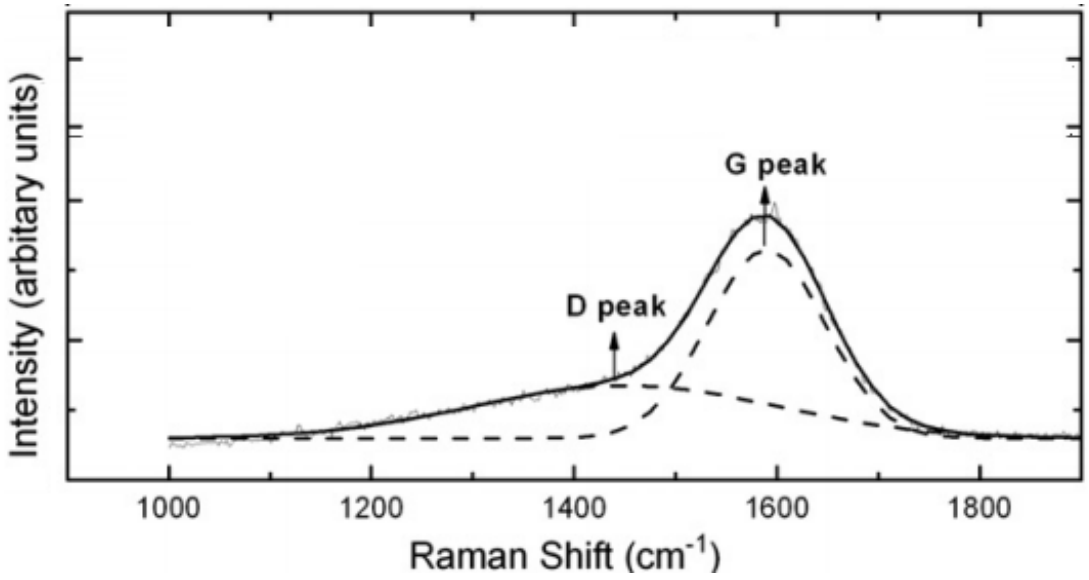

Figure 3.9 *The D and G peaks often observed in Raman scans of amorphous carbons* [152].

The depth of the resolution (penetration) for DLC films is often disputed, with ranges of 100 nm – 1 µm quoted [153,154]. These differences can depend on the wavelength of the incident beam to the sample and the bonding structure of the carbon film itself. Xu *et al.* [138] quantified the relationship between the Raman intensity of a Si substrate under an amorphous DLC film (prepared using PECVD) using the Beer-Lambert law and provided results indicating above ~300 nm, the Si active peak could not be identified. This penetration limitation could mean that GNP deposited below the DLC layer may not be detected or the signal is too weak compared to the signal from the DLC layer.; therefore, it will dominate the resultant spectra.

Understanding the origin of the D and G peaks is helpful in the process of evaluating carbon films. The two peaks are the A_{1g} (D peak) and the E_{2g} (G peak) breathing modes (**Figure 3.10**).

The G peak of graphite is situated around 1581 cm^{-1}, but amorphous carbons can range from 1500 – 1630 cm^{-1}, with the D peak around 1350 cm^{-1} [42]. The G peak is present in

all sp^2 bonded carbons (not just those in an aromatic ring). The D peak is around 1350 cm^{-1} and will not be active in a perfect aromatic ring.

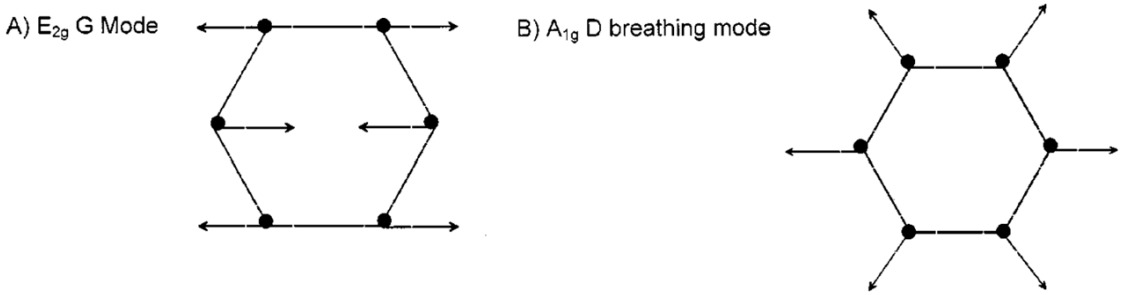

Figure 3.10 *Raman spectra modes of the (a) G peak, and (b) D peak* [42].

The absence of a D peak in pristine graphite/graphene allows researchers to assess the quality of the flakes or film quickly and is often classified by taking the integrals of the relative intensities (I_D/I_G), with the larger number indicating a higher defect density [155]. In DLC films, due to the inherent nature of the bonding, a high I_D/I_G indicates the presence of a greater degree of sp^2 bonding. The difference is due to the amorphous structure of the DLC, where not all sp^2 rings are satisfied, with open aromatic rings being active in the spectra [156].

The Raman spectra of worn DLC films are often used to characterise the degree of graphitisation. The shift in G peak position and D peak intensity relative to the G peak can provide information regarding the structure and changes post-wear for amorphous and disordered carbons (**Figure 3.11**). A shift increase in the G wavenumber will ordinarily correlate to that of a more graphitic film, where clusters of sp^2 bonded carbons are active [156].

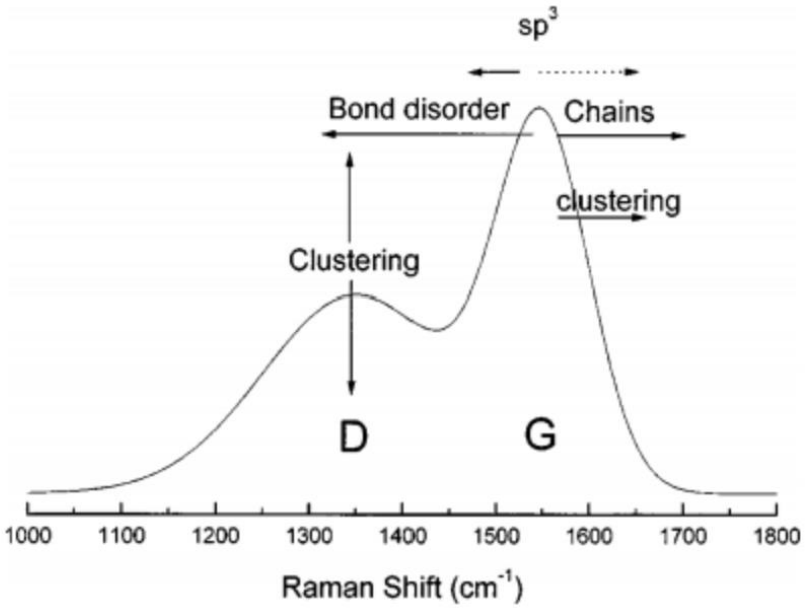

Figure 3.11 *The change in Raman G peak position, and D peak intensity* [42].

3.3.7 Nano-indentation

Nano-indentation was employed in this thesis to ascertain the elastic modulus (E) and hardness (H) of the DLC-GNP films based on experimental measurements. The equipment was calibrated according to the ISO 14577 standard, which sets a maximum indentation depth at 10% of the coating thickness [157]. This standard calibration ensures an accurate and reliable determination of the mechanical properties of the films. The indentations were performed using the Micromaterial Nano-indenter Platform 3 at the University of Leeds. Two types of tests were undertaken;

I. Bulk mechanical properties. A 10 x 10 (250 µm x 250 µm) grid.

II. Targeted single indents at the GNP islands and DLC.

Using a Berkovich-type indenter, the indentations were made in a controlled atmosphere at a temperature of 25°C. The measurement led to the creation of the force-displacement curve typically used for nano-indentation. **Figure 3.12** depicts a typical loading/unloading curve produced using nano-indentation.

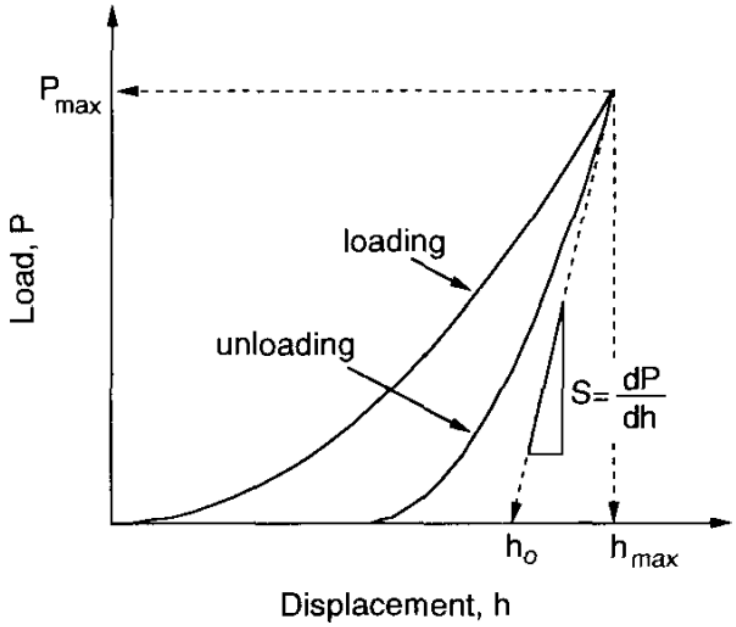

Figure 3.12 *Traditional load vs displacement curve observed in nano-indentation* [158].

In this thesis, nano-indentation analysis was done to determine how the mechanical properties of the DLC coating change based on the GNP coverage and DLC thickness, and any relationship to the tribological properties.

3.3.7.1 Bulk Mechanical Properties

Bulk properties for all samples are calculated using a 250 µm x 250 µm area, with 25 µm between each indent, allowing a total of 100 indents per sample. The depth was controlled to a maximum of 10% of coating thickness for each indent, with a maximum load of 500 mN allowed. The initial contact load was 0.01 mN, with a 0.2 mNs^{-1} loading and unloading rate. The dwell period of 60 seconds was set for thermal drift correction post-indentation. The results produced a loading-unloading curve typical of that seen in a DLC film, and the 'NanoTest' software calculates the reduced modulus by applying the Oliver-Pharr analysis [158]. A larger test area of 500 µm with 50 µm between each indent was originally trialled; however, the space between the indents failed to contact the GNP islands properly and, did not give a relevant representation of the bulk properties.

3.3.7.2 Targeted Indents

Targeted indentations (GNP islands and DLC matrix) were used on the DLC-GNP samples (**Chapter 4**). The conditions for the measurements were the same as for the bulk sample. There were 10 indents for both features, with the mean and standard deviation calculated for each. The elastic modulus and hardness are calculated automatically from the software using the same Oliver-Pharr analysis as used by the bulk mechanical method [158].

3.3.8 Adhesion Testing

The coating adhesion test was completed using Tribotechnic Millennium 200 scratch tester with a 200 μm radius diamond Rockwell C indenter. A progressive load from 0-50 N was used along with a scratch speed of 10 mm / min, a loading speed of 100 N / min and a total distance of 5 mm. When using a progressive load, the coating reaches a sufficient stress and failure events are observed. These failures are termed "critical loads", with 3 critical loads (LC_n) classified:

a) **L_{C1}**, *Cohesive failure*, with forward chevron cracks at the borders of the scratch track.
b) **L_{C2}**, *Adhesive failure*, with wedging spallation at the borders of the scratch track.
c) **L_{C3},** *Adhesive failure*, with gross spallation / wedge spallation in the scratch track

A typical scratch achieved is shown in **Figure 3.13**, using L_{c1}, $L_{c2,}$ and L_{C3}, for the first, second, and third identified adhesive failure modes proposed by Bull [159].

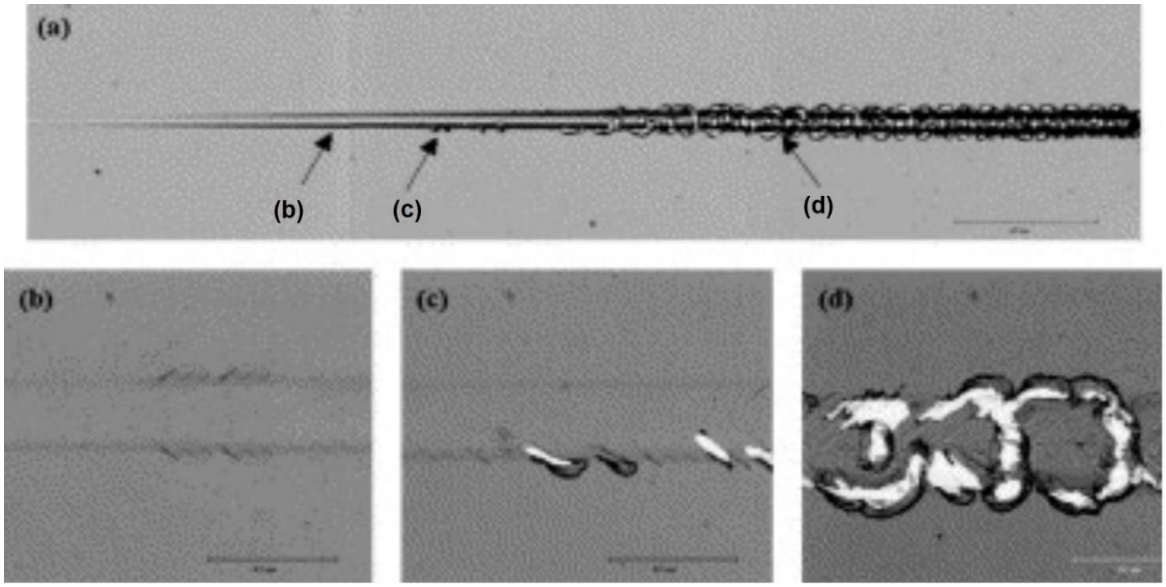

Figure 3.13 *(a) Adhesion scratch test of a DLC film with (b) chevron cracking, (c) chipping, and (d) compressive spallation observed at various points*.[160]

The CPR (Crack Propagation Resistance) measures the ability of the film to withstand crack initiation and propagation during the scratch test, providing a quantitative measure of the film's toughness [161]. This is given by the equation:

$$CPR = L_{C1} (L_{C2} - L_{C1}) \qquad \textit{Equation 3.5}$$

The CRP values have previously been linked to friction and wear properties, supported by multiple reports High CRP and elastic recovery capability are proposed to result in excellent tribological performance. This is due to the elastic deformation that can occur before plastic deformation, resulting in the formation of cracks.

3.4 Tribological Testing of DLC-GNP Coatings

Tribological testing was completed on all DLC-GNP nanocomposite coatings to measure frictional response and create a wear track using WLI to determine the specific wear rate. The test conditions were chosen to closely mimic those in a demanding environment such as a cam/follower, where contact pressures are typically between 500 - 850MPa [164–

166] and in a hot oil-lubricated environment (100°C). The calculated contact pressures are presented in each section (**Chapters 4** – **Chapters 7**).

Tribological testing is essential to evaluate the friction and wear reduction mechanism by combining GNP with DLC into a composite [25], without using an additives package. The following section will outline the conditions used, material properties, and how the results were analysed.

3.4.1 Biceri Pin-on-Flat

The tribological testing was completed at the University of Leeds using a Biceri Tribometer in a reciprocating pin-on-plate configuration. This configuration is shown in **Figure 3.14**. The heating of the sample was achieved under the sample holder with an attached thermocouple used to measure the temperature. The Biceri was calibrated prior to each test using an applied load of 2.732 kg to generate a voltage output which corresponds to a known voltage / force curve.

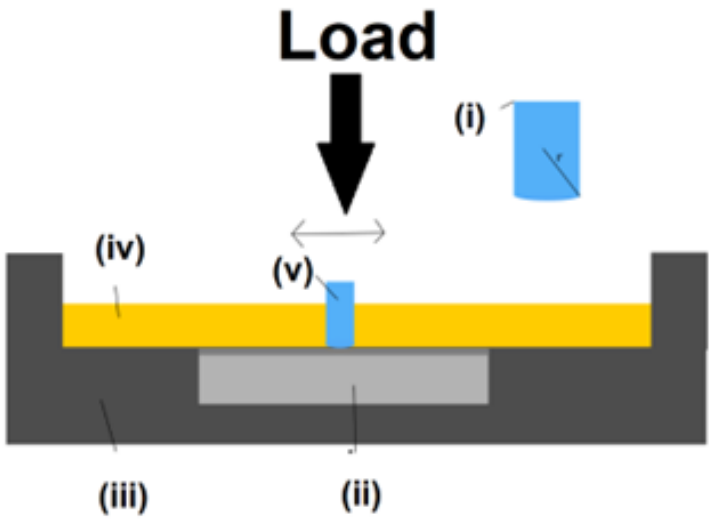

Figure 3.14 *Schematic setup showing (i) the cast iron pin with the equivalent radius head, (ii) sample, (iii) sample holder, (iv) base-oil and (v) pin with the reciprocating movement and load indicated.*

The boundary regime is the most demanding lubrication regime encountered in cam/follower [167]. To determine if the tribological testing is in the boundary lubrication

regime, the load, material and lubricant properties were used in **Equation 3.6** and **3.7** [168]. To calculate a numerical value for the minimum film thickness (h_{min}):

$$\frac{h_{min}}{R'} = 3.63 \left(\frac{U\eta_0}{E'R'}\right)^{0.68} (\alpha E')^{0.49} \left(\frac{W}{E'R'^2}\right)^{-0.073} (1 - e^{-0.68k}) \qquad \textit{Equation 3.6}$$

Where R' is the reduced radius (m) of the two surfaces in contact, α is the viscosity–pressure coefficient (1.1×10^{-8} Pa^{-1}), η_0 is the dynamic viscosity (Pa s), U is the entraining surface velocity (m/s) of the pin, W is the load (N) and E' is the reduced elastic modulus (Pa). The lambda ratio (λ) indicates the lubrication regime, and values of < 1 indicate boundary lubrication. The lambda ratio (λ) is calculated using the following:

$$\lambda = \frac{h_{min}}{\sqrt{R_{a1}^2 + R_{a2}^2}} \qquad \textit{Equation 3.7}$$

Where R_{a1} and R_{a2} are the mean surface roughness of the film (m), and CI pin respectively. The calculated λ is less than 1 for all DLC-GNP nanocomposites tested.

3.4.2 Test Conditions

The pin used in all wear tests was cast iron with a 40mm equivalent radius. Due to leverage, the hanging mass used was 11.5 kg, equating to a load of 280 N. A table of the conditions is shown in **Table 3.6**.

Table 3.6 *Test conditions used for DLC-GNP wear tests.*

Test Conditions	
Speed	20mm/s
Load	280N
Temperature	100°C
Lubricant	Poly-α-olefin (PAO) Group IV
Lubricant Viscosity	3.1 mPa S at 100°C
Counter Material	Cast Iron 40mm equivalent radius
Test Duration	0.5-30 hours

A group IV commercially purchased base-oil was used for all wear tests to ensure no other interactions that are common with oils additive packages would be present. The temperature of 100°C is used to simulate a cam follower environment and is comparable with other literature [169,170]. The material properties are shown in **Table 3.7**. The initial contact pressure was calculated for each test using Hertzian contact pressure equations [171].

The FFO used in this study was commercially purchased Mobil Super™ 3000 0W-16 low viscosity fully synthetic engine oil [172]. This was selected due to having a close Kinematic Viscosity (7.1 cST) to the PAO4 base-oil. This oil was tested as a comparison to a base-oil to understand if the contributions to the friction reduction dominant mechanism were compared to additives contained within an FFO.

Table 3.7 *Material properties used in in Biceri tribometer.*

	SUBSTRATE	**COATING**	**COUNTER MATERIAL**
MATERIAL	M2 HSS Steel	Pure DLC	Cast Iron
ROUGHNESS (R_A)	4-20nm	29-40nm	0.57µm
YOUNG'S MODULUS	210 GPa	204 GPa	170 GPa
POISSON'S RATIO	0.27	0.33	0.27
DIMENSIONS	15mm Diameter 6mm thickness	300-3000nm	Length = 20mm Diameter = 6mm Radius of Curvature = 40mm

3.5 Statistical Analysis

A statistical indicator of the strength and direction of the linear relationship between two variables is the Pearson correlation coefficient, or "r" [173]. The Pearson coefficient's value falls between -1 and +1, with -1 denoting a perfect negative correlation (i.e., when one variable rises, the other decreases), +1 denoting a perfect positive correlation (i.e., when one variable rises, the other also rises), and 0 denoting no correlation (i.e., no relationship between the variables). The formula for calculating Pearson's r is as follows:

$$r = \frac{n(\sum xy) - (\sum x)(\sum y)}{\sqrt{[n\sum x^2 - (\sum x)^2][n\sum y^2 - (\sum y)^2]}} \qquad \textit{Equation 3.8}$$

Where x and y are the individual data points for the two variables, and Σ represents the sum of the values.

The Pearson coefficient is widely used in engineering, medicine and science to study the relationship between variables and to make predictions based on that relationship. Values above +0.7 or below -0.7 are considered strong relationships, with +0.6/-0.6 considered moderate [173].

Chapter 4 - The Effect of GNP Coverage on the Tribological and Mechanical Properties of DLC-GNP nanocomposite

4.1. Introduction

In this chapter, 6 DLC-GNP nanocomposites were synthesised using different concentrations of GNP/NMP suspensions to produce films with different GNP coverages. The synthesis of these DLC-GNP nanocomposites is detailed in **Section 3.2**. An outline of the characterisation techniques used to determine the mechanical, topographic, tribological and material properties, along with the material and chemical structure, is provided in **Figure 3.2**.

The tribological testing was completed in a PAO base-oil, with an FFO used in combination with a pure DLC as a reference to observe how the DLC-GNP structures performed compared to a typical pure DLC.

These tests are relevant to determine the response in a realistic demanding environment (i.e., cam follower) where they must operate in high pressures and temperatures while maintaining a low coefficient of friction and a low wear rate relative to these coatings found in the literature.

4.2. Results

4.2.1. Dispersion of GNP/NMP Suspension

GNP were suspended in NMP at 6 difference concentrations (0, 0.25 mg/ml, 0.5 mg/ml, 0.75 mg/ml, 1 mg/ml, 1.5 mg/ml, and 2 mg/ml). The pure (0%) DLC was used as a comparative reference. The Samples were created as stated in the methodology section of this thesis.

Figure 4.1 gives the GNP coverage as the GNP/NMP concentration used increased (measured as per **Section 3.2.5)**. The results show that GNP coverage increased as the GNP/NMP concentration increased. The standard deviation for the dispersion remains relatively low until the concentration used reaches 1.5 mg/ml. These large deviations indicate that uniformity is lower for these higher concentrations. This inhomogeneity can be observed in **Figure 4.2** where the agglomeration of GNP islands is present (samples 1.5 mg/ml and 2 mg/ml). These largest two concentration result in similar coverage values of 8.97% and 9.15%, each with large standard deviation.

It was identified that GNP began to form small islands at concentrations above 0.75 mg/ml, with larger islands visible at concentrations above 1.5 mg ml. These large islands result from weak van der Waals forces and/or π – π stacking [174]. It should be stated that agglomeration was not apparent in the suspension prior to deposition. It was deposited soon after the sonication to ensure the GNP was dispersed in the solvent [175].

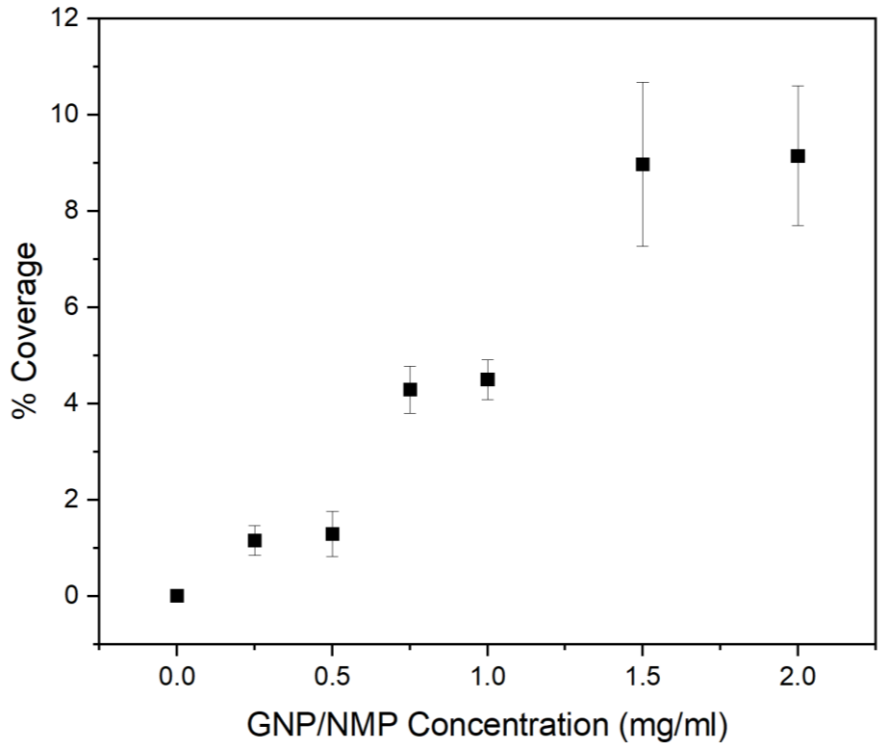

Figure 4.1 *GNP coverage as a function of GNP/NMP concentration used.*

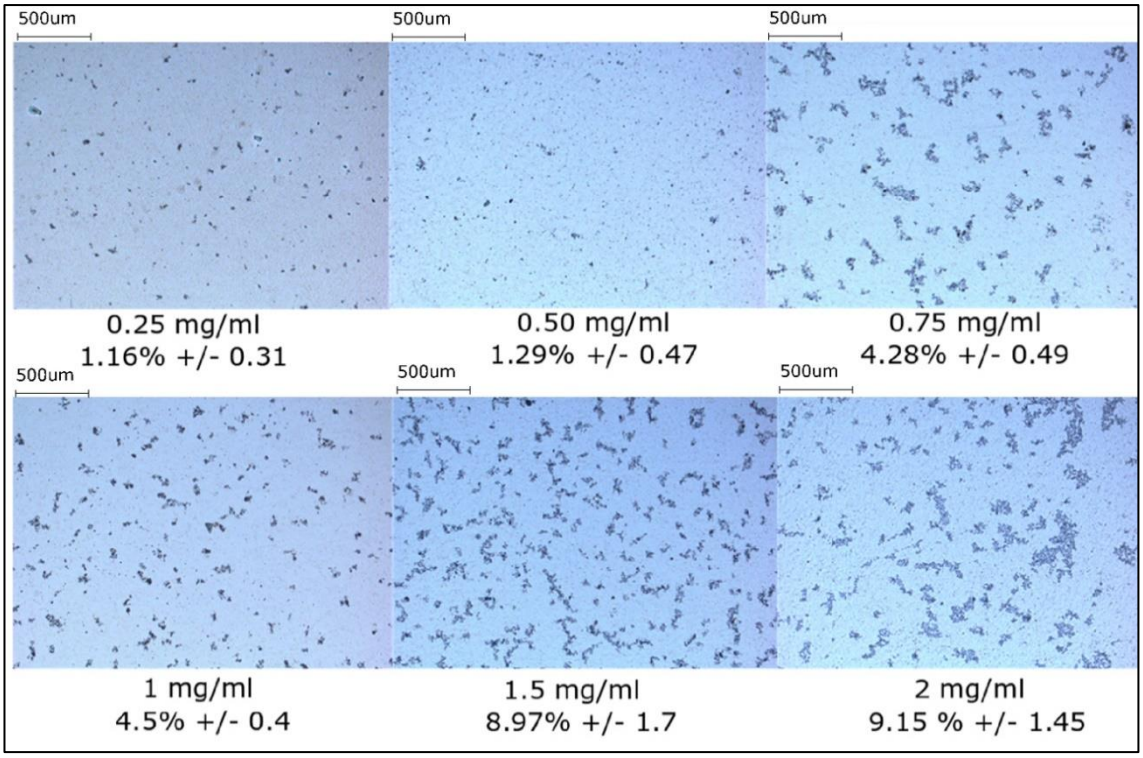

Figure 4.2 *Optical images of GNP coverage and the corresponding GNP/NMP concentration used.*

Figure 4.3 gives the particle size distribution obtained using the ImageJ software in the methodology. The lateral size provided by the GNP supplier is ~5 µm [131]. Measurements taken from the lowest concentration (0.25 mg/ml) provide lateral sizes > 5 µm, which leads to the conclusion that GNP are not fully dispersed and will have some stacking during the deposition process. This stacking supports the observations from the particle size distribution (**Figure 4.3),** where the island sizes increase as the GNP/NMP concentration increases. The particle size distribution observed for the 1.5mg/ml and 2mg/ml display more GNP islands with sizes greater than 2000 μm^2, compared to those made using lower concentrations. The agglomeration of the particles will result in the GNP's stacking, increasing the islands' height. A surface profile of the DLC-GNP is presented in **Figure 4.4.** The size of these graphitic particles are much greater than those created by MS sputtering [116].

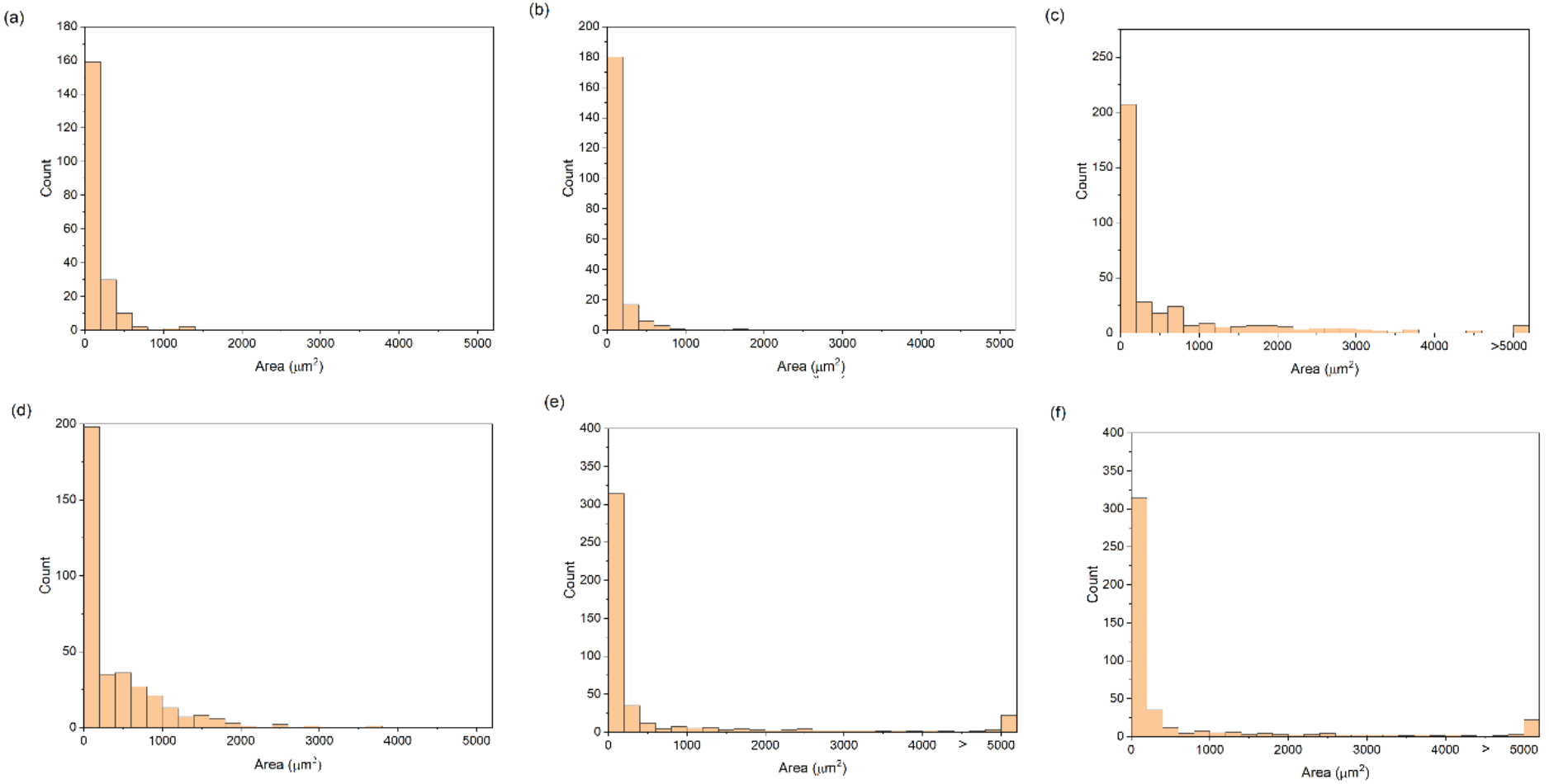

Figure 4.3 *Histogram of the GNP island size for (a) 0.25mg/ml, (b) 0.5mg/ml, (c) 0.75mg/ml, (d) 1mg/ml, (e) 1.5mg/ml and (f) 2mg/ml GNP/NMP concentrations used.*

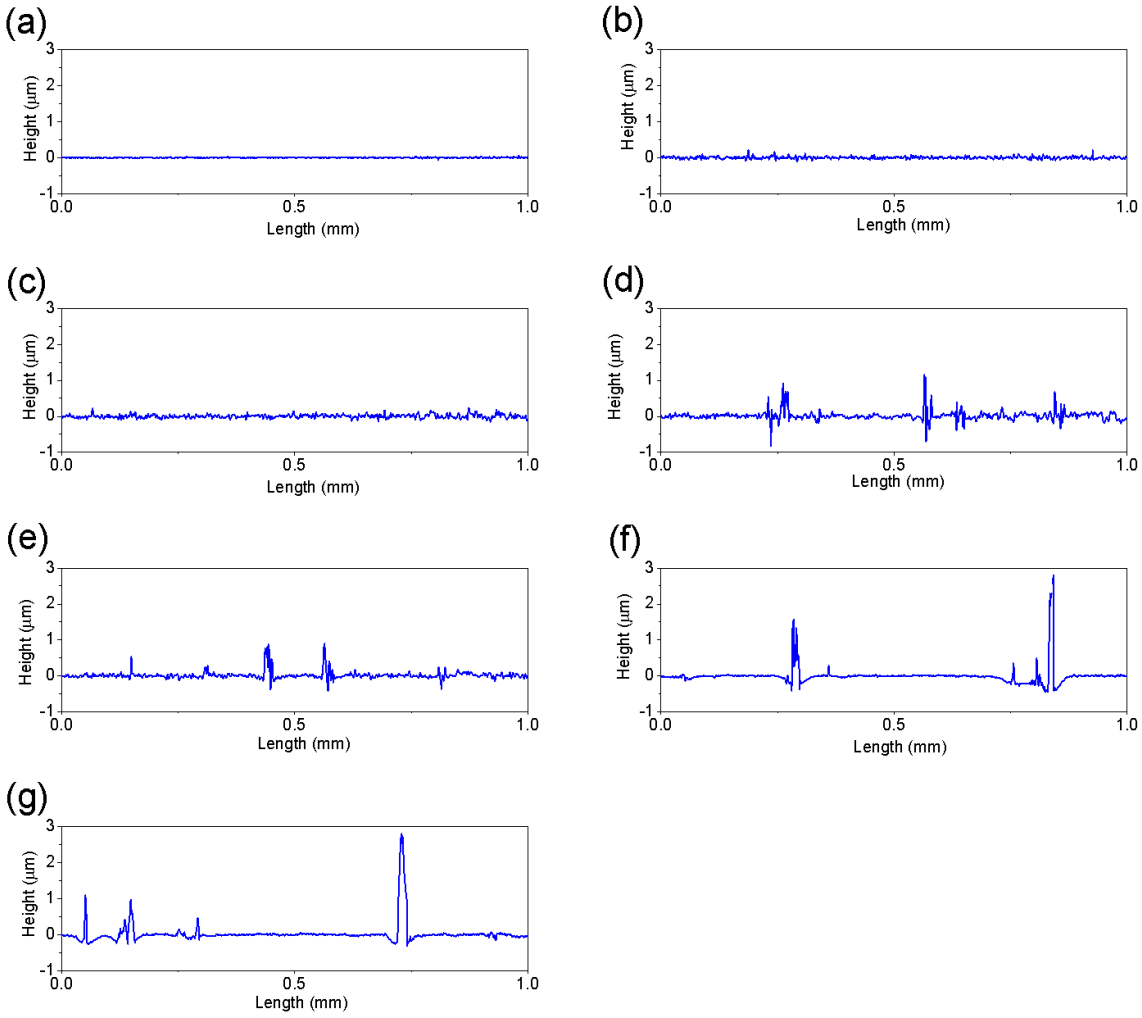

Figure 4.4 *Line profiles showing peak height of DLC-GNP composites at concentrations (a)pure DLC, (b) 0.25 mg /ml (c) 0.5 mg/ml, (d) 0.75 mg/ml (e) 1 mg/ml (f) 1.5 mg/ml, (g) 2 mg/ml.*

The highest peaks were observed for the two highest concentrations (1.5 mg/ml and 2 mg/ml), where peaks of up to ~3 µm are observed.

4.2.2. Effect of Heat Treatment on GNP

The dispersed GNP underwent a heat treatment process described in the methodology **Section 3.2**, which involved being pressed with Teflon tape and heating at 200°C for 3 hours. A small-scale investigation was conducted to review if the application of Teflon tape alters the GNP during the heat treatment process.

The Raman spectra (**Figure 4.5**) of the GNP were measured before and after heat treatment to investigate if any changes in the defect densities or if the edge sites or holes during the heat treatment process could infer the presence of O_2 molecules [132]. The drive behind this is to determine if:

- The Teflon tape suppressed the oxygen attacking the edge sites.
- The Teflon tape suppressed the formation of defects.

One sample was not covered during the heat treatment process and compared to a sample that was pressed, with changes in I_D/I_G ratio compared (**Table 4.1**).

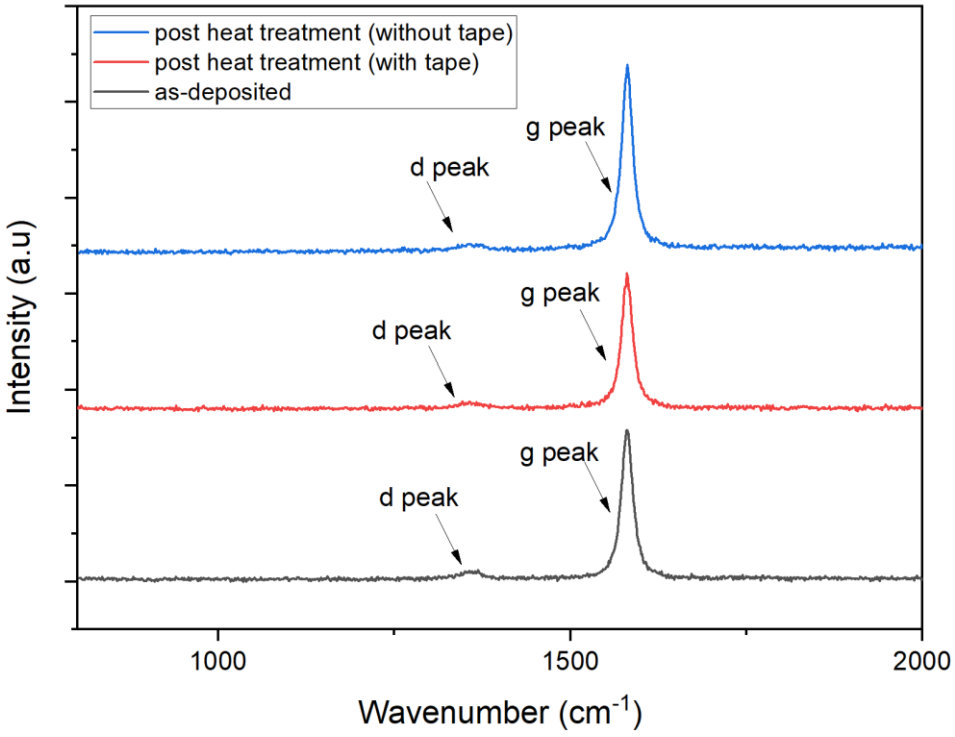

Figure 4.5 *Raman spectra of GNP before and after heat treatment.*

Table 4.1 *I_D/I_G ratio for GNP.*

Sample	I_D/I_G
as-deposited GNP	0.08 ± 0.02
Post heat treated GNP (Tape)	0.08 ± 0.02
Post heat treated GNP (No Tape)	0.04 ± 0.02

The application of Teflon tape showed no differences in the I_D/I_G ratio after heat treatment compared to the as-deposited GNP (I_D/I_G ratio of 0.08). However, without the Teflon tape, an I_D/I_G ratio of 0.04 was measured but overlapped for the standard deviation. These results indicate that the application of tape for the 180 minutes of heat treatment has little / negligible effect on the structure of the GNP for the presence of O_2 molecules or defects, which can be measured using Raman spectroscopy.

4.2.3. Surface Morphology

The surface morphology was measured after DLC deposition. The thickness of all samples was measured to be ~1.27µm using a Calo tester and confirmed by FIB cross-sections. The mean surface roughness (R_a) was taken to assess how the roughness changes with the GNP/NMP concentration used (**Figure 4.6).**

The R_a of the pure DLC sample was 21 ± 1 nm, indicating a very consistent smooth surface. The addition of a small amount of GNP into the DLC matrix increases the R_a, as seen in the DLC-GNP0.25 having a 33 ± 13 nm, which is an increase of 47%. The DLC-GNP0.5 and DLC-GNP0.75 have Ra values of 49 ± 2 nm and 46 ± 7 nm, respectively. The DLC-GNP1 has a relative increase with a Ra of 77 ± 6 nm. The most significant standard deviation is observed in DLC-GNP1.5 and DLC-GNP2 with respective values of 85 ± 23 nm and 112 ± 49 nm; these higher deviations indicate the surfaces have significantly rougher areas, which can be concluded to be due to the addition of GNP.

The increase in the uncertainty for the highest two concentrations (1.5 mg/ml and 2 mg/ml) is the result of the agglomeration of the GNP observed from the particle size distribution (**Figure 4.3**) and line scans for peak height (**Figure 4.4.4**). Comparable work using CNT has shown an increase in roughness as the concentration increases [114].

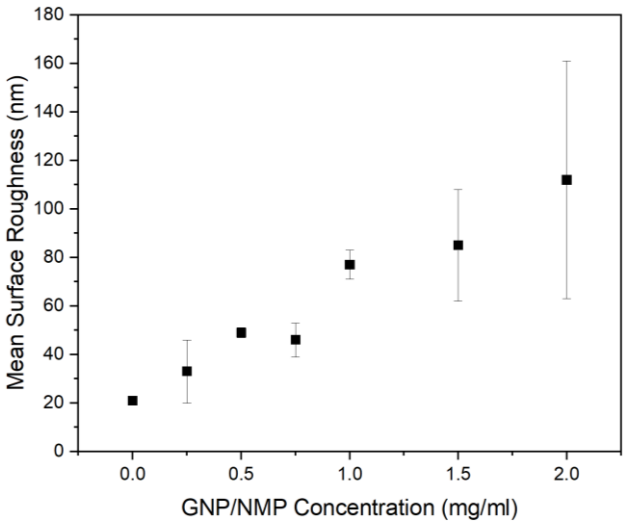

Figure 4.6 *Mean surface roughness for DLC-GNP composites as a function of GNP/NMP concentration used.*

4.2.4. Mechanical Properties

4.2.4.1. Nano-indentation

The hardness and elastic modulus of the pure DLC and DLC-GNP coatings were measured by nano-indentation. **Table 4.2** gives the bulk hardness and elastic modulus, calculated from the average of 100 indentations. The indentations were completed in a 10 (250 µm) x 10 (250 µm) grid, with a 25 µm spacing between each indentation.

The GNP islands vary in size depending on the concentration used, by using a smaller spacing between each indent it ensures that a more accurate reflection of the elastic modulus for the bulk is achieved. In **Figure 4.*1***, the observed spaces between the particles can be ~200 µm, with the width of the particles ~50 µm by using smaller spaces between each indent it reduces the risk of GNP missed by the indenter.

Figure 4.8 presents a colour contour map of the elastic modulus of the indents for DLC-GNP1 with inhomogeneity between each indent. Comparatively, the pure DLC (**Figure 4.7**) displays much less variation between each indent. The differences between the two samples can be related to the presence of the GNP within the DLC matrix; this is observed by comparing the positions on the DLC-GNP1 map and the related optical image. The GNP will form small islands containing GNP stacked together and will be impacted by

the indenter tip during nano-indentation. A review of Reference [114] using CNT within a DLC matrix, did not provide any context on the distribution of the CNT and the impact of the indenter in relation to the measured results.

The wear rate of a coating is theorised to be indicated by the H/E ratio, which is described as the relative deformation to yielding [176]. The tensile elastic stress of a coating is said to increase with increasing H/E ratio, ratio, corresponding to a higher wear resistance [177].

H/E and H^3/E are the two main metrics frequently used in the prediction of the wear performance of coatings [178–180], it has also been used to predict the frictional response of coatings [181]. The lowest H/E and $H^{3/}E^2$ is DLC-GNP1, with the highest being Pure DLC. The GNP islands are observed to have a lower elastic modulus compared to the surrounding DLC matrix, leading to a lower elastic modulus over the average 100 indents compared to the pure DLC. The results show the coatings have discrete areas where the elastic modulus and hardness is lower at the GNP islands than the surrounding DLC matrix.

Table 4.2 *Bulk Elastic Modulus and Hardness for DLC-GNP nanocomposites*

	Elastic Modulus (GPa)	**Hardness (GPa)**	**H/E**	**H^3/E^2 (GPa)**
Pure	204 ± 8	23.7 ± 4	0.116	0.32
DLC-GNP0.25	201 ± 23	23.0 ± 5.6	0.114	0.30
DLC-GNP0.5	195 ± 28	22.7 ± 8.9	0.116	0.31
DLC-GNP0.75	192 ± 29	22.1 ± 7.2	0.115	0.29
DLC-GNP 1	195 ± 13	22.0 ± 6	0.113	0.28
DLC-GNP 1.5	181 ± 37	21.7 ± 8.2	0.120	0.311
DLC-GNP 2	176 ± 36	21.2 ± 9	0.120	0.31

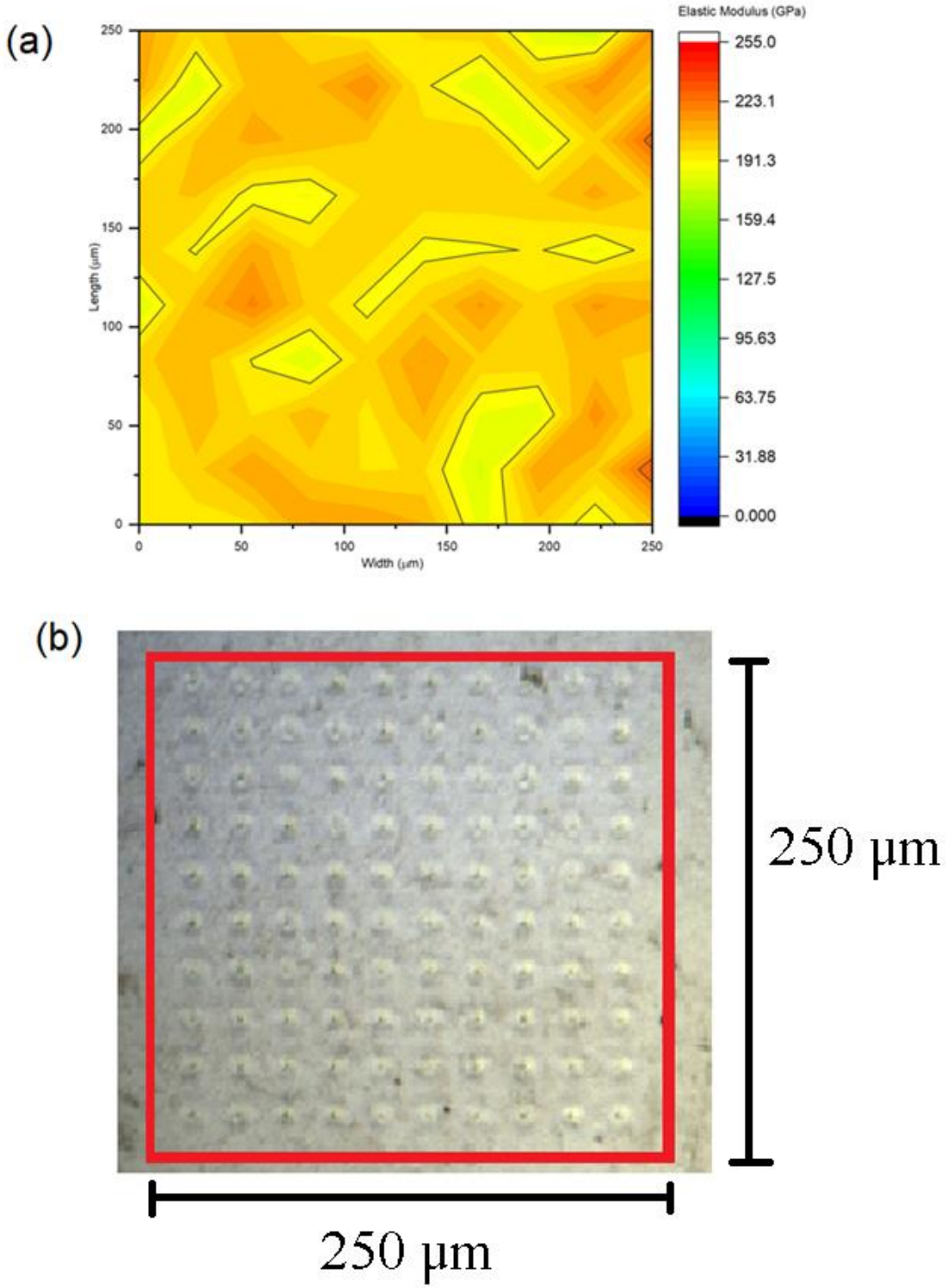

Figure 4.7 *(a) Pure DLC Elastic Modulus map of a 10* x *10 grid, and (b)* optical image of the 10 x 10 map

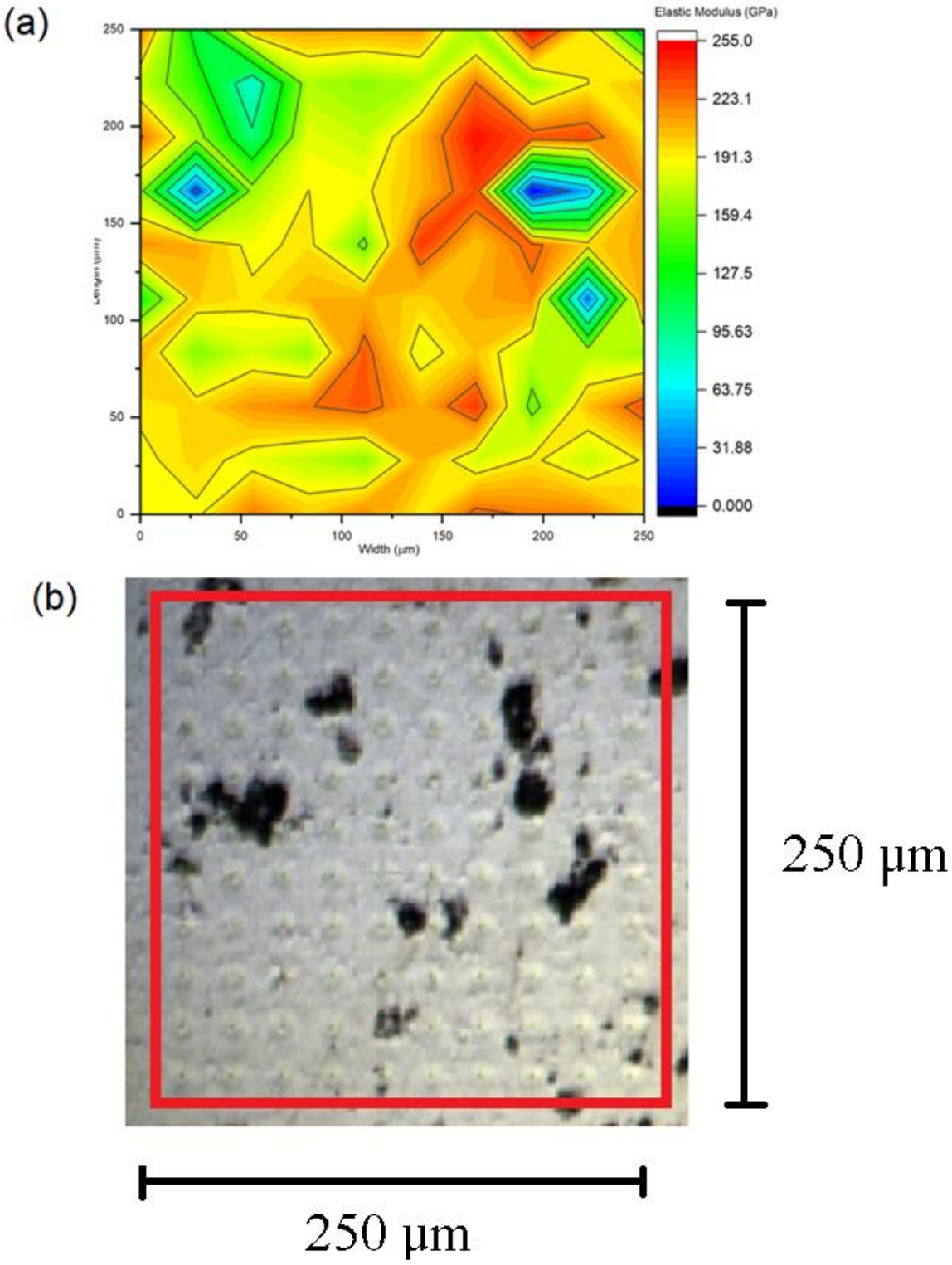

Figure 4.8 *(a) DLC-GNP1 Elastic Modulus map of a 10* x *10 grid and (b) optical image of the 10 x 10 grid area within the red box.*

Targeted single indentations were performed at the GNP islands and DLC areas to investigate how the elastic modulus varies with different GNP/NMP concentrations.

These measurements were conducted with depth control, ensuring a maximum indentation depth of 100 nm, using the same experimental conditions as the bulk indentations.

The results shown in **Table 4.3** indicate that the GNP elastic modulus is much lower than the corresponding DLC matrix, which remains relatively close to the results for the bulk elastic modulus for pure DLC. The pure DLC aligns with other reported results [182]. The low elastic modulus could result from the nano-indentation hitting a GNP with voids underneath, yielding a lower load. Interestingly, the larger GNP islands that form at the higher GNP/NMP concentrations have little effect on the resultant elastic modulus.

The uncertainty results from the stacking of the GNP along with the DLC deposited above. However, the results align with literature values for HOPG of 18 – 21 GPa [183].

Table 4.3 *Elastic Modulus for DLC-GNP samples separated by discrete areas.*

	Elastic Modulus (GPa)	
	DLC Areas	**GNP Islands**
Pure DLC	204 ± 27	N/A
DLC-GNP0.25	203 ± 31	18 ± 26
DLC-GNP 0.5	208 ± 11	42 ± 6
DLC-GNP 0.75	201 ± 13	19 ± 21
DLC-GNP 1	195 ± 13	21 ± 23
DLC-GNP 1.5	219 ± 24	12 ± 17
DLC-GNP 2	202 ± 9	20 ± 11

4.2.4.2 Adhesion Testing

Scratch testing of the samples was completed to determine the adhesion of the DLC-GNP film to the HSS substrate, as shown in **Figure 4.9**. Before testing, the machine is

calibrated to standard EN 1071-3 [184] using a 200 μm radius diamond Rockwell C indenter. **Table 4.4** details the L_{C1}, L_{C2}, L_{C3} values determined by optical microscope. The L_{C1} value for all coatings was from the formation of Chevron cracking (cohesive failure), with the L_{C2} value being for wedging spallation (adhesive failure) and L_{C3} value for gross / conformal spallation (adhesive failure).

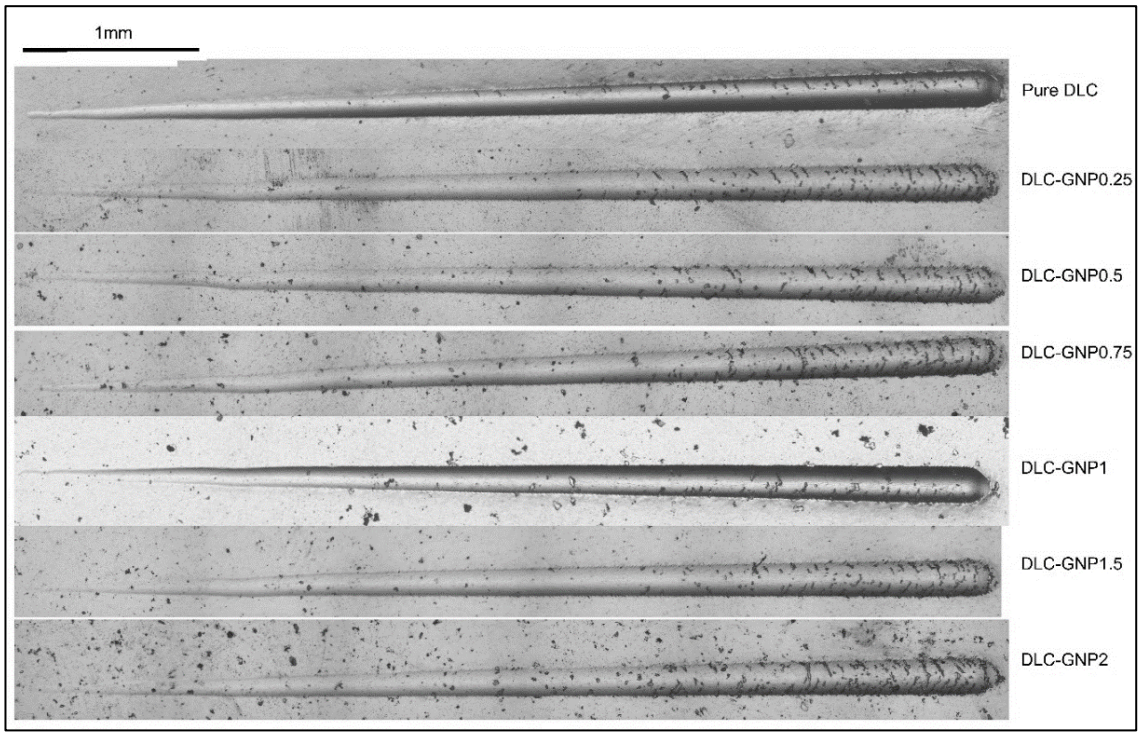

Figure 4.9 *Scratch test for DLC-GNP nanocomposites.*

No gross spallation was observed within the tested load range. However, the first cohesive failures observed in all samples were Chevron cracks, but their occurrence was relatively lower in DLC-GNP compared to the pure DLC sample. This suggests that the inclusion of GNP in the DLC matrix reduces the cohesive strength of the film. The reduced cohesive strength in DLC-GNP films can be attributed to the weaker bonding between the GNP and DLC, in contrast to the strong covalent bonding within the DLC matrix itself. The occurrence of Chevron-cracks as the first failure mode is consistent with previously reported findings on DLC films [185].

Table 4.4 *Critical failure loads of DLC-GNP nanocomposites*

	Load (N)		
	L_{C1}	**L_{C2}**	**L_{C3}**
Pure DLC	14.7	32.1	-
DLC-GNP0.25	10.3	32.0	42.3
DLC-GNP0.5	9.1	34.2	39.7
DLC-GNP0.75	9.7	37.8	42.4
DLC-GNP1	9.5	37.8	-
DLC-GNP1.5	9.0	33.9	42.1
DLC-GNP2	10.1	35.9	42.8

The L_{C2} failure observed in all samples was wedging spallation, where the DLC-GNP0.75 and DLC-GNP1 films provided the highest values (10% more than pure DLC film). In DLC films, L_{C2} adhesive failures are often associated with high internal stresses, which are shown to be reduced by the incorporation of metal doping [135]. The effect of doping using CNT has also been shown to be effective at reducing internal stresses [115], although other comparative work [114] provided a sharp decrease in critical load as the CNT% increases due to increases in Von Mises stresses.

The L_{C3} failure is due to high residual stress where the cracks nucleate through the coating, leading to interfacial failures between substrate/adhesion layer/DLC coating [186]. In graphene epoxy composites, crack propagation is inhibited by small weight volumes of graphene; however, this deteriorates as the graphene content increases [187]. However, the DLC-GNP nanocomposites, the lowest concentration DLC-GNP films 0.25 mg/ml and 0.5 mg/ml had a lower L_{C3} value with the 1mg/ml sample maintaining adhesion at 50 N.

4.2.5. Structure of DLC-GNP Nanocomposites

4.2.5.1. SEM Cross-sections

Cross-sections of a selected DLC-GNP (DLC-GNP1) nanocomposite and pure DLC reference samples were taken.

In **Figure 4.10** cross-section of pure DLC presents an EDX scan displaying the platinum protective layer, DLC layer, adhesion layers, and the HSS substrate. The thickness of the DLC is measured to be 1.27 µm, supporting the Calo test results. The structure of the pure DLC film differs from the two DLC-GNP samples due to the introduction of GNP at the interface between the DLC and the adhesion layer. The adhesion layer consisting of a Cr/WC/W-DLC layered structure is visible, with no visible void between the two interfaces (adhesion layer / substrate). Scratch testing was used to quantify the adhesion strength of the coating (**Section 4.2.4**).

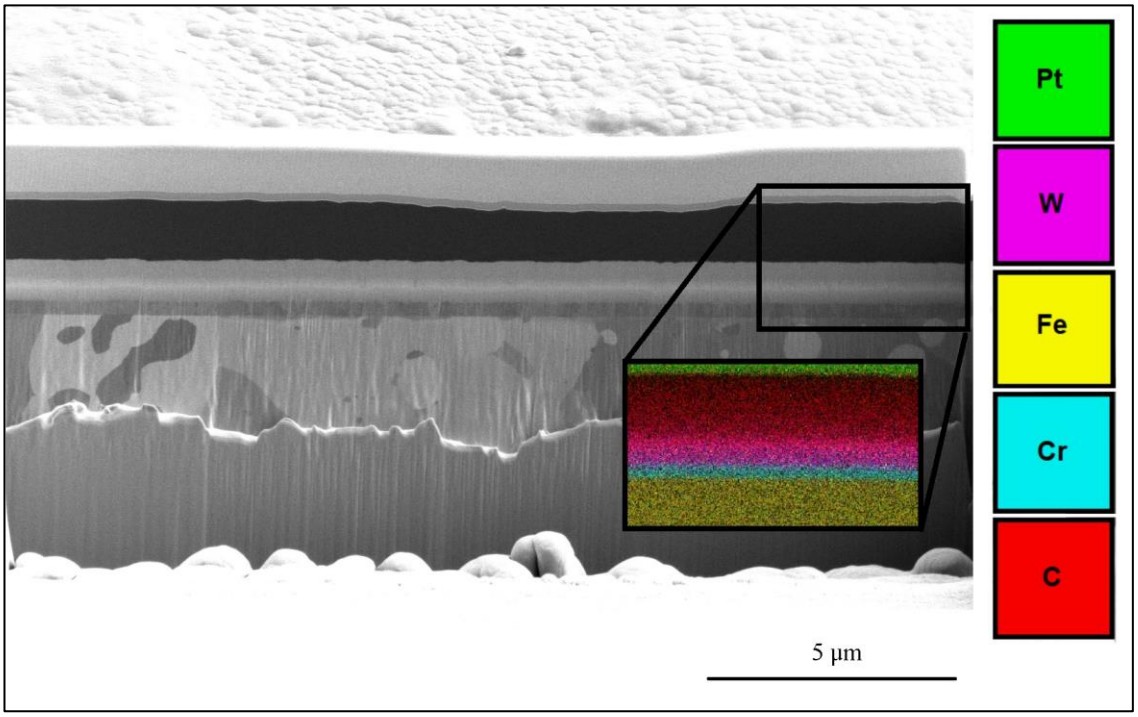

Figure 4.10 *Cross-section of pure DLC film, Pt protection layer, DLC, Adhesion layer (Cr / WC) and HSS (Fe) substrate identified.*

The cross-section for the DLC-GNP1 is presented in **Figure 4.11** & **Figure 4.12**. The addition of GNP into the matrix is easily visible in all samples. The GNP is observed lateral size to be around 5 µm in either micrograph.

The peak height above the GNP is observed in **Figure 4.11**, where the height is ~2.85 µm, compared to the DLC either side (1.27 µm). These results support the line profiles observed in **Section 4.2.1**.

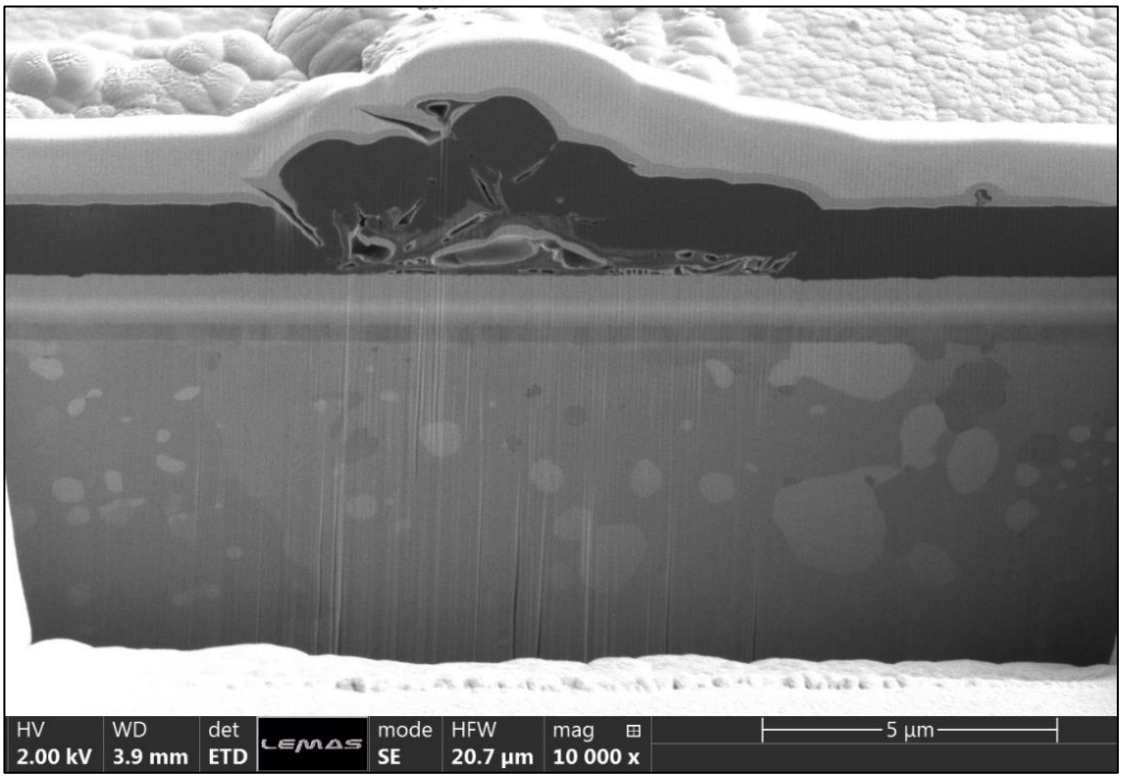

Figure 4.11 *Cross-section of DLC-GNP1, with the GNP located throughout the DLC layer.*

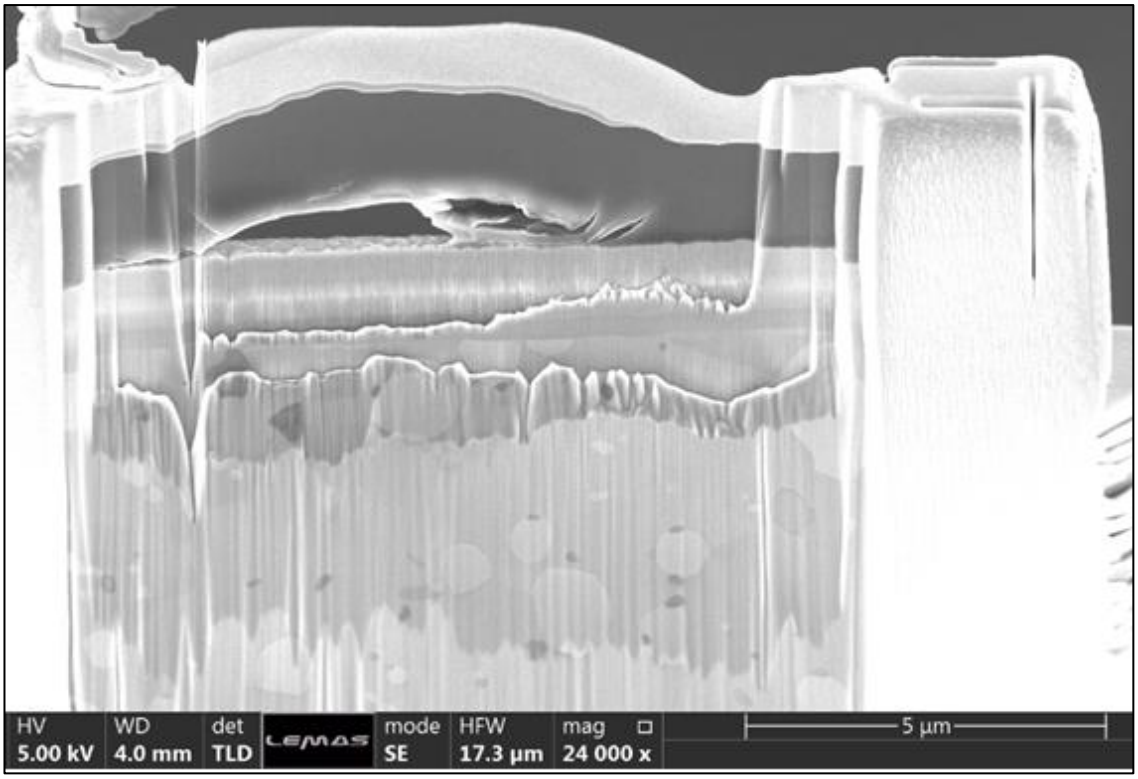

Figure 4.12 *Cross-section of DLC-GNP1 structure, this cross-section displays GNP structure parallel to the substrate.*

The GNP within the DLC matrix displays two different structures, designated either type 1 or type 2, where;

- Type 1 - The GNP at the interface between the adhesion layer and the DLC layer displays penetration through the DLC close to the surface.
- Type 2 - GNP at the interface between the adhesion layer DLC are isolated from the surface with no GNP penetration.

In both types of structures, small voids are observed. In the type 2 structure, the GNP is detached from the adhesion layer, indicating a lower adhesion strength than the pure DLC sample. On the other hand, the type 1 structure exhibits voids within the GNP islands themselves. These voids may result from the stacking of GNP during the spin coating process.

4.2.5.2. TEM/EELS Spectroscopy

To investigate their bonding structure, the pure DLC and DLC-GNP1 cross-sections prepared using FIB were analysed using TEM/EELS spectroscopy. To ensure electron transparency for EELS analysis, both samples were thinned to a thickness of less than 100 nm. The TEM images of the pure DLC and DLC-GNP samples are presented in **Figure 4.13 & Figure 4.14**.

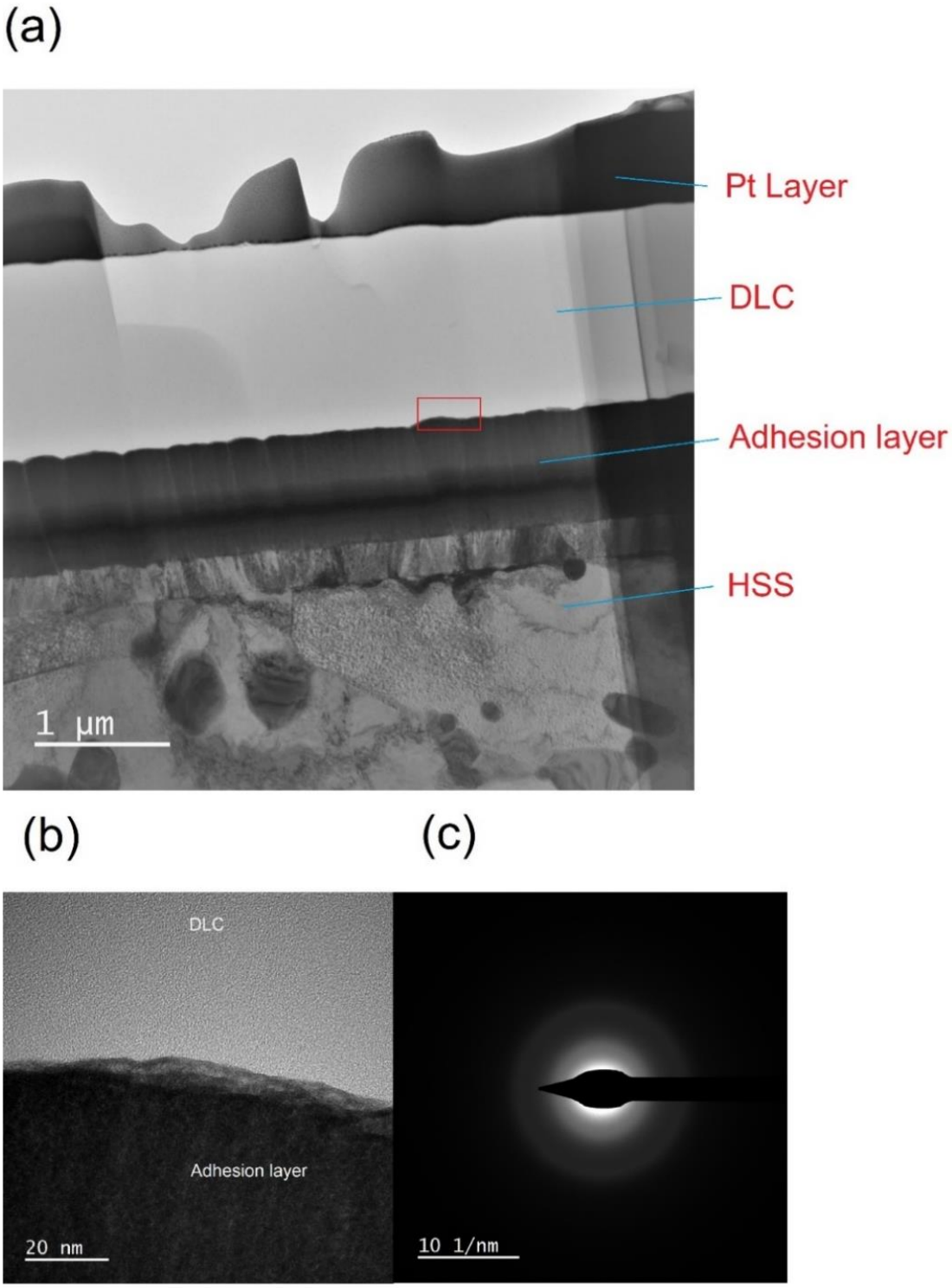

Figure 4.13 *(a) TEM image of pure DLC, (b) HRTEM of red box at DLC/adhesion layer interface, and (c) SAED diffraction pattern for DLC area.*

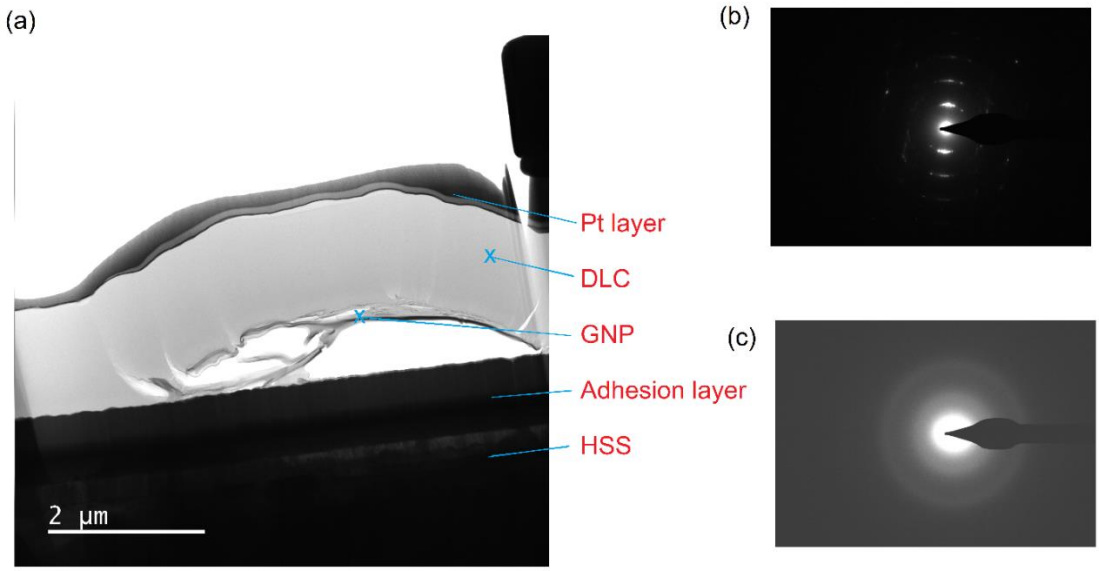

Figure 4.14 *(a)TEM image of DLC-GNP1, with "x" designating areas taken for SAED (b) GNP and (c) DLC areas.*

The DLC-GNP1 sample clearly shows the presence of GNP within the structure, with a visible void between the GNP and adhesion layer. In contrast, the pure DLC sample exhibits a uniform adherence to the substrate without any voids, suggesting that the interfacial bond strength between GNP and the adhesion layer is weaker compared to DLC. High-resolution TEM (HRTEM) images of the pure DLC reveal an amorphous structure, which is further supported by the observation of concentric halos in the selected area electron diffraction (SAED) pattern [188]. The DLC-GNP1 sample exhibits an amorphous concentric halo pattern and bright spots, indicating the presence of crystalline and amorphous regions depending on the measured area. In order to confirm the presence of a graphitic structure, HRTEM images were captured at the marked area "x" as shown in **Figure 4.15**. A repeating lamella structure consistent with the d-spacing of graphite (0.323 nm)[189] is observed from the line scan of the GNP (0.336 nm).

The line scans taken from the DLC display a line scan with no ordered structure with intensity profiles of between ~0.25 nm to ~0.50 nm is observed. The amorphous nature

of the DLC is consistent with results obtained from literature [190] and previous SAED diffraction patterns. Notably, no voids were observed at the DLC/GNP interface.

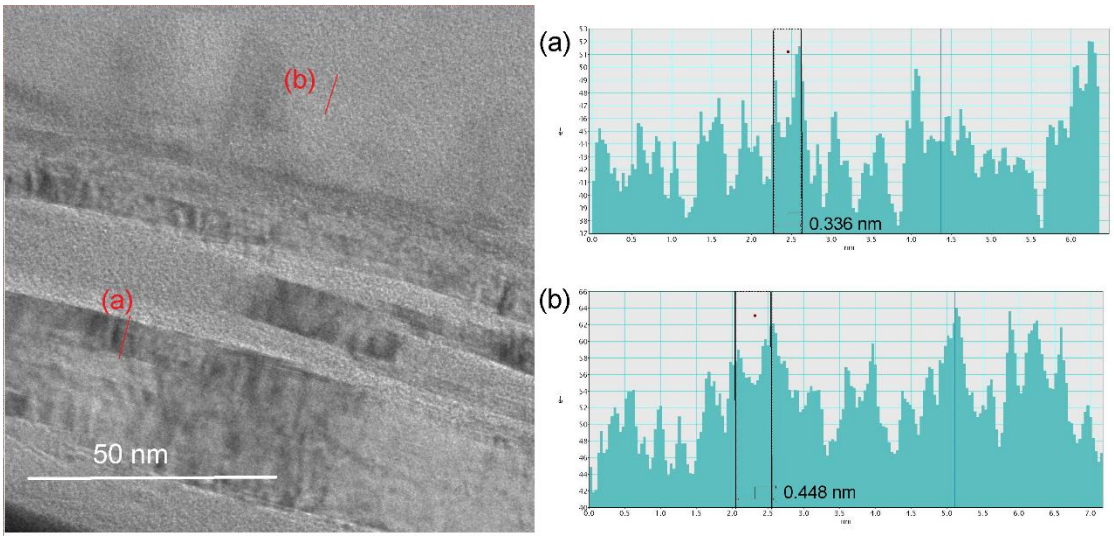

Figure 4.15 *(a) HRTEM image of DLC/GNP area, in DLC-GNP composite. The red line profiles (a) GNP, and (b) DLC profile corresponding to the intensity profile where a d-spacing of 0.336 nm is measured for the GNP.*

As no voids observed at the GNP/DLC interface (compared to the GNP/Adhesion layer), it indicates a strong chemical bond between the two carbonous materials. During the process of depositing DLC (on top of the GNP), the strong bond is formed. The high energy ions in this process breaks the C-C π-bonds, converting them into σ-bonds. As a result, four covalent σ-bonds are formed. Molecular simulations [59] have shown that this breaking and formation of bonds leave dangling bonds on the GNP surface, which serve as growth sites for DLC.

EELS spectra were fitted using the method described by Zhang *et al.* [139] and Mironov [140] to determine the sp^2/sp^3 bonding ratios at the areas indicated in **Figure 4.16**. The C-K edge spectra are collected at the magic angle to remove any orientation effects often presented in 2D materials [191]. The π* peak (sp^2 component at 285eV is visible, followed by the σ* peak (sp^3 component) around ~ in all spectra collected. The positioning of the spectra was strategically chosen to investigate potential variations in

carbon bonding as a function of depth and distance from the GNP. By analysing the spectra at different positions, we aimed to understand any changes in the carbon bonding characteristics and their relationship to the proximity of the GNP. The results are displayed in **Table 4.5**, with **Figure 4.17** displaying EELS spectra for the key areas.

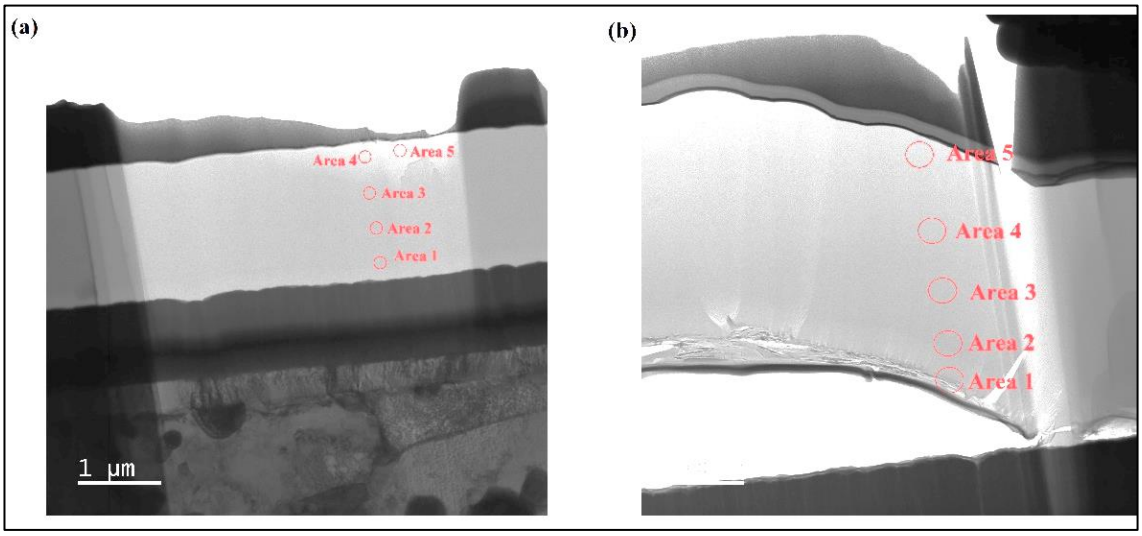

Figure 4.16 *TEM cross-sections of (a) pure DLC, and (b) DLC-GNP1 with the areas where EELS spectra were obtained.*

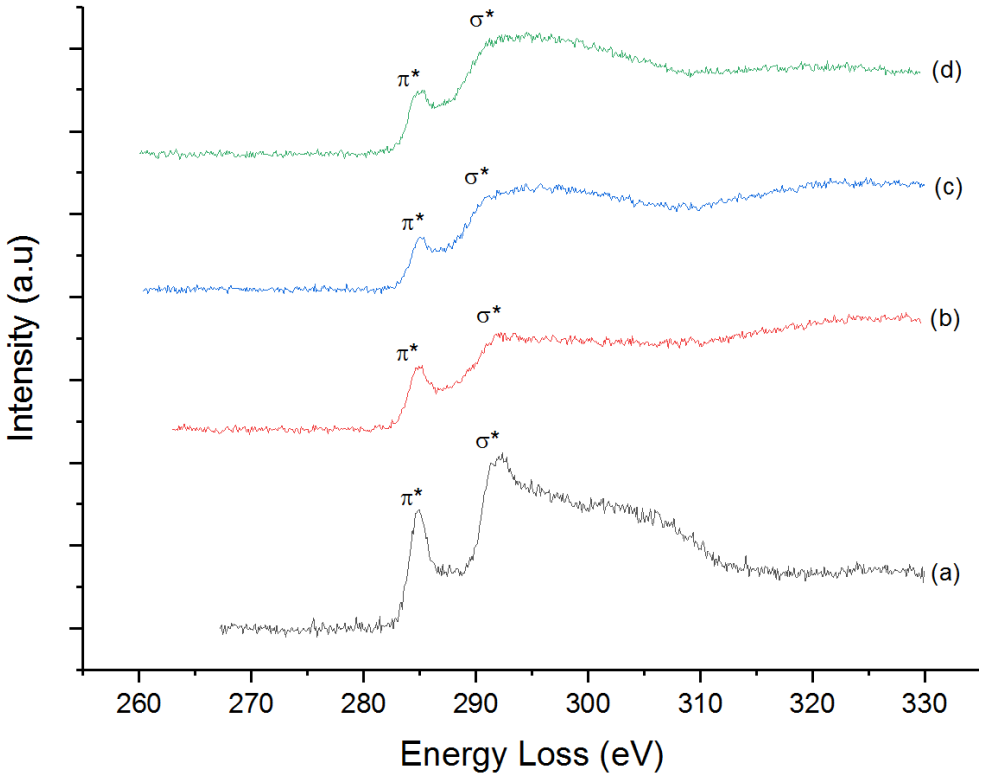

Figure 4.17 *EELS spectra obtained from (a) HOPG reference, (b) DLC-GNP1 area 1, (c) DLC-GNP1 area 4 and (d) pure DLC area 2. The π* peak and σ* component is shown.*

Table 4.5 *sp^2/sp^3% of pure DLC and DLC-GNP1 samples.*

	sp^2/sp^3%	
Area	**DLC**	**DLC-GNP1**
1	62.7	74.7
2	54.2	72.2
3	56.2	65.4
4	56.8	56.4
5	55.2	56.4

HOPG was used as a pure sp^2 bonded reference sample and supplied by Leeds electron microscopy and spectroscopy centre (LEMAS). The DLC-GNP1 area 1 and HOPG show some expected similarities as GNP are highly graphitic, but the shoulder of the σ* peak after 295eV presents a steeper decline for the HOPG due to the lack of sp^3 bonding. This indicates that the spectra from the GNP area have some sp^3 bonding and are not 100% sp^2. The spectra obtained from DLC-GNP area 1 and area 4 exhibit noticeable differences, particularly in the characteristics of the σ* peak. The broader and more dominant σ* peak in area 1 suggests a lower degree of graphitic structure than area 4, indicating that the film becomes less graphitic as it moves away from the GNP. On the other hand, the spectra of DLC-GNP area 4 and pure DLC are quite similar, suggesting a similar level of graphitic content in both samples.

The results obtained from the analysis, as presented in **Table 4.5**, validate that the sp^2/sp^3 % content in DLC-GNP1 varies as the collected spectra move away from the GNP. In contrast, the pure DLC sample exhibits minimal differences, except for a slightly higher

graphitic content in the region closer to the substrate. These results tie into the molecular simulation work of Liu *et al.* [59], where a DLC film is grown on multi-layer graphene. In that work, the edge sites and surface of the GNP will have more energetically favourable sp^2 bonding sites, with some graphene layers broken down during the deposition process. The high sp^2 bonding diminishes further away from the GNP, leading to the theory that it becomes less energetically favourable for sp^2 sites to form, with a more amorphous structure dominating as the deposition process continues [59].

The pure DLC sample displays some inhomogeneity in the sp^2 ratio due to small sp^2 clusters [192]. However, this difference is not significant compared to the DLC-GNP sample.

4.2.5.3. Raman Spectroscopy

Raman spectroscopy was employed to investigate the structural modifications of DLC-GNP coatings as the GNP/NMP concentration increased. The spectra were carefully analysed following the methodology outlined in **Section 3.3.6**.

Table 4.6 presents the positions of the D and G peaks for each coating, while **Figure 4.19** shows the I_D/I_G ratio**.** The D and G peak positions and their relative intensities are closely linked to the size and density of sp^2 clusters [193]. Obtaining a quantitative measurement of the sp^2 content using these parameters can be challenging due to the non-linear relationship. Nevertheless, they are valuable for qualitative comparisons [152,156,194]. The pure DLC sample serves as a baseline for comparing how the introduction of GNP into the DLC matrix affects the peak positions and I_D/I_G ratio in the DLC-GNP composite samples. Raman results using CNT in a DLC matrix observed an increase in I_D/I_G ratio which related to a higher graphitic content, however no link to the distance from the surface was present in these results [114].

It is essential to consider that the analysis of DLC-GNP composites should account for the significant amount of DLC above the GNP islands, and contributions of both to the collected spectra. Additionally, it is worth noting that Raman spectroscopy in carbon coatings has a limited penetration depth and is highly surface-sensitive [145]. This is demonstrated in **Figure 4.18** where Raman spectra are taken on a GNP island before and after DLC is deposited on top, where the 2D peak is impossible to detect through a 1.2µm DLC layer.

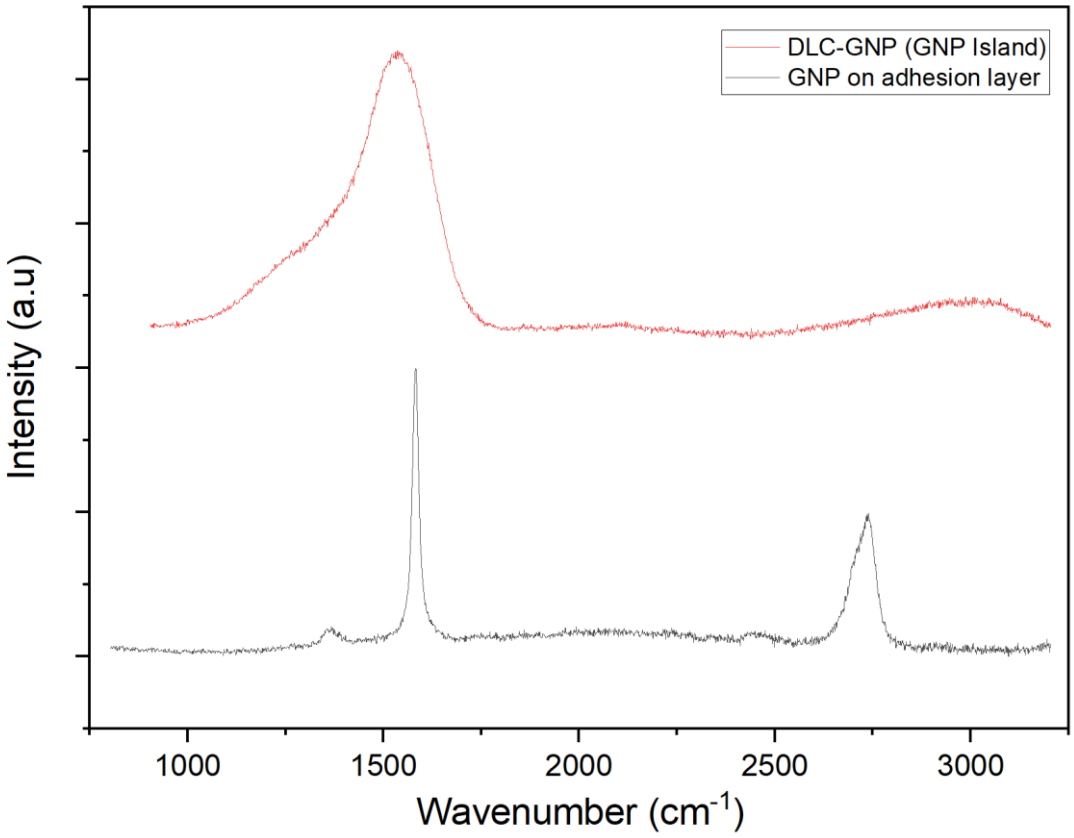

Figure 4.18 *Raman Spectra of GNP on adhesion layer and GNP islands after DLC deposition.*

Table 4.6 provides the D and G peak positions for the DLC and GNP islands in all nanocomposite coatings and for pure DLC and GNP before DLC deposition as reference. The G peak position for all DLC areas shows consistent values, while the DLC-GNP1 increases to 1557 cm^{-1}, indicating a shift towards a more graphitic structure [42]. Furthermore, the G peaks of all DLC areas appear at higher wavenumbers than the

corresponding GNP islands, suggesting a higher degree of graphitic structure in the DLC regions.

The I_D/I_G ratio for all samples was calculated in **Figure 4.19**. The trend observed in the DLC areas shows an increase in the results up to 1 mg/ml GNP concentration, after which a decline is observed.

Similarly, the GNP islands exhibit a similar trend. It is important to note that the GNP islands are covered with DLC deposited above them. However, as seen in the SEM cross-sections, some edges of the GNP may still be present. These edge sites could contribute to the D peak intensity, increasing the I_D/I_G Ratio, while the G peak would remain constant.

Table 4.6 *D and G peak positions for as deposited DLC-GNP Nanocomposites.*

	DLC Area		**GNP Island**	
	Peak Position (cm^{-1})		Peak Position (cm^{-1})	
	D Peak	**G Peak**	**D Peak**	**G Peak**
GNP on Adhesion layer	-	-	1364 ± 2	1582 ± 0
Pure DLC	1377 ± 6.5	1553 ± 1	-	-
DLC-GNP0.25	1383 ± 3.5	1554 ± 0.5	1385 ± 18	1551 ± 1
DLC-GNP0.5	1383 ± 2.5	1555 ± 1	1380 ± 7	1551 ± 1
DLC-GNP0.75	1378 ± 2.5	1553 ± 0	1371 ± 3	1549 ± 1
DLC-GNP1	1402 ± 11	1557 ± 1	1388 ± 16	1552 ± 3
DLC-GNP1.5	1376 ± 2	1553 ± 0.5	1388 ± 8	1551 ± 3
DLC-GNP2	1378 ± 3.5	1553 ± 0.5	1380 ± 6	1550 ± 3

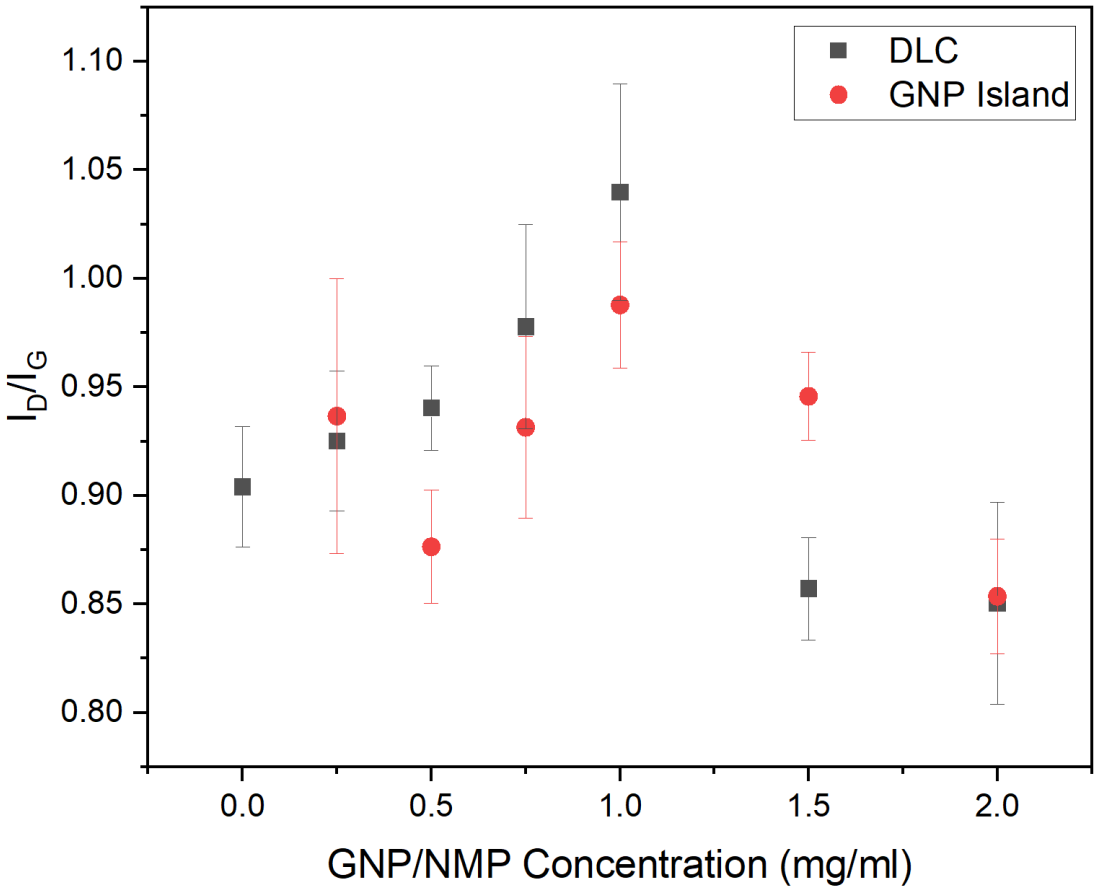

Figure 4.19 *I_D/I_G for as-deposited DLC-GNP Nanocomposites created using various GNP/NMP concentrations.*

4.2.6. Tribological Testing

4.2.6.1. Friction Results

Figure 4.20 presents the representative frictional traces of the DLC-GNP/CI system with different GNP/NMP concentrations. The tests were conducted per the methodology, with a constant load of 280 N applied for 6 hours in a hot (100°C) base-oil (poly-α-olefin Group IV) lubricated environment. The frictional traces provide insight into the tribological behaviour of the coatings. **Table 4.7** presents the calculated initial contact pressures using the bulk elastic modulus.

The pure DLC coating served as a baseline comparison in FFO testing, maintaining a relatively constant coefficient of friction (COF) of approximately 0.11 throughout the test. When tested in a base-oil, pure DLC exhibited higher friction than all DLC-GNP

coatings. However, at 17,500 seconds, the friction of the pure DLC coating decreased to a similar level as the DLC-GNP1.5 coating. Among the DLC-GNP coatings, the DLC-GNP0.25 coating took the longest to reduce friction, followed by the DLC-GNP0.75 coating. The two coatings with higher GNP concentrations, DLC-GNP1.5 and DLC-GNP2, demonstrated reduced friction; however, the COF of DLC-GNP2 increased rapidly towards the end of the wear tests.

DLC-GNP1 exhibited the best repeatability during the wear tests among all the DLC-GNP composites. It showed a rapid drop in friction at approximately 2,500 seconds, followed by a consistently low friction coefficient of around 0.03 at approximately 5,000 seconds.

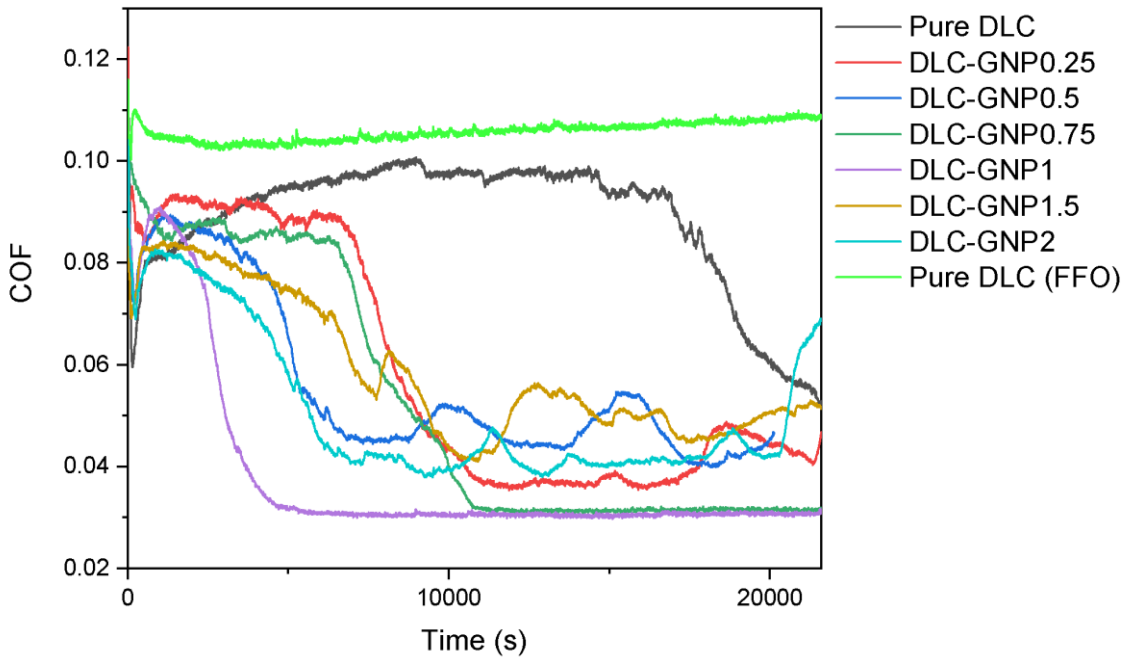

Figure 4.20 *Representative friction coefficient as a function of time for DLC-GNP nanocomposites.*

Table 4.7 *Initial contact pressure for DLC-GNP Nanocomposites*

Sample	Initial contact pressure (GPa)
Pure DLC	715
DLC-GNP0.25	700
DLC-GNP0.5	694
DLC-GNP0.75	690
DLC-GNP1	685
DLC-GNP1.5	671
DLC-GNP2	666

The first and last 3 hours (**Figure 4.21** and **Figure 4.22**) of friction were averaged to compare steady-state friction and the "wear-in" (n =3). The pure DLC sample exhibits the highest COF (~0.09) with a minor deviation in the first 3 hours. The DLC-GNP1 presented the lowest COF (~0.04) but with the highest deviation due to the sudden reduction in friction.

For the final 3, the differences between pure DLC and DLC-GNP composites become more pronounced, with the pure DLC maintaining the highest COF with a high standard deviation. The DLC-GNP1 has the lowest steady, measured friction, represented in the raw friction results by a steady line with a COF ~0.03. Research [114] using a DLC-CNT nanocomposite provides a decrease in COF as the CNT concentration increases to similar values obtained for 0.75 mg/ml and 1 mg/ml (~0.03) in **Figure 4.22**.

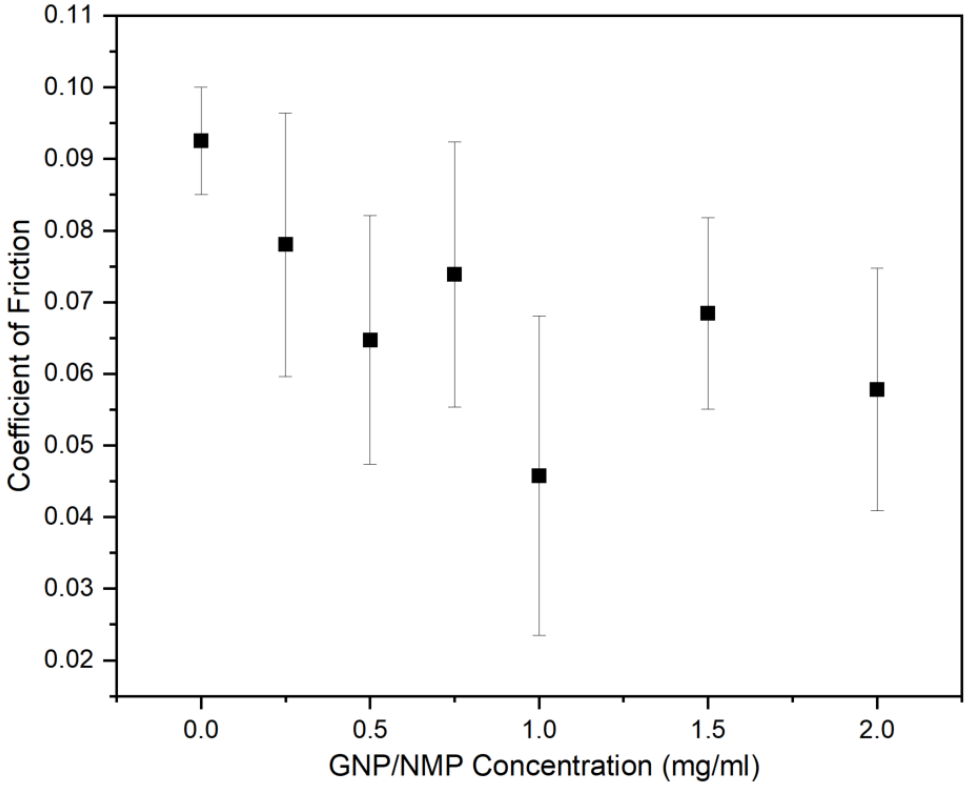

Figure 4.21 *Average coefficient of friction for the DLC-GNP composites for the first 3 hours.*

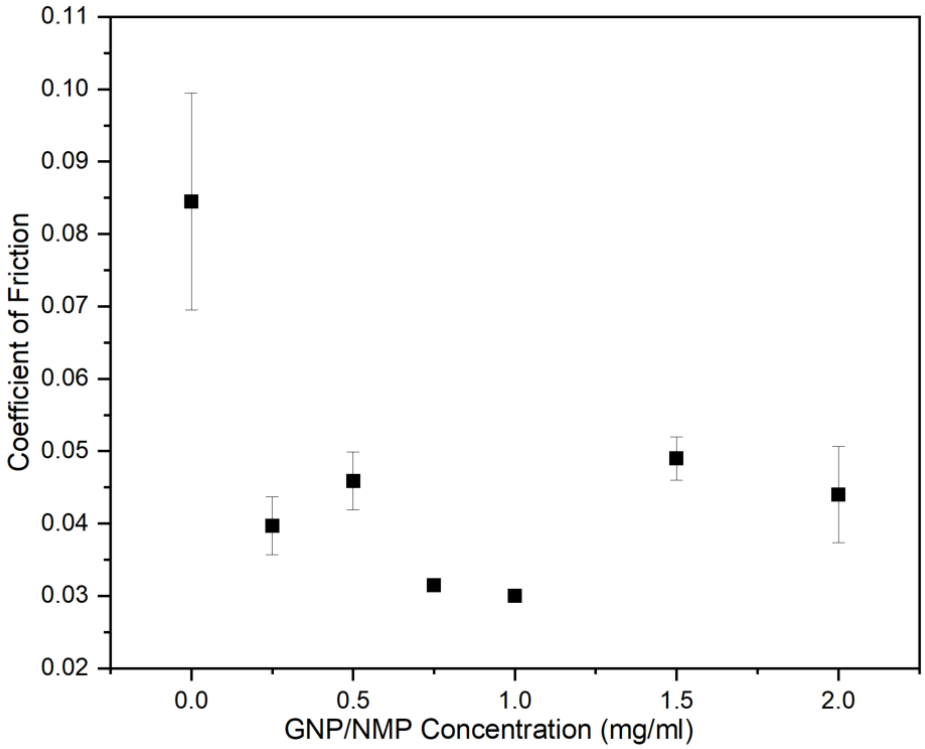

Figure 4.22 *Average coefficient of friction for the DLC-GNP composites for the last 3 hours.*

The coverage of the GNP was measured after the tribotests and compared to the as-deposited samples, which are shown in **Figure 4.23**. The coverage increased for all the samples except DLC-GNP2. The peak heights observed previously in **Figure 4.4** would facilitate high asperity contact and removal, this has been shown in Reference [195], where micro-cracking and micro-delamination on asperity tips. As the peak heights result from the GNP islands, the removal of the GNP is concluded as the reason for the decrease in coverage.

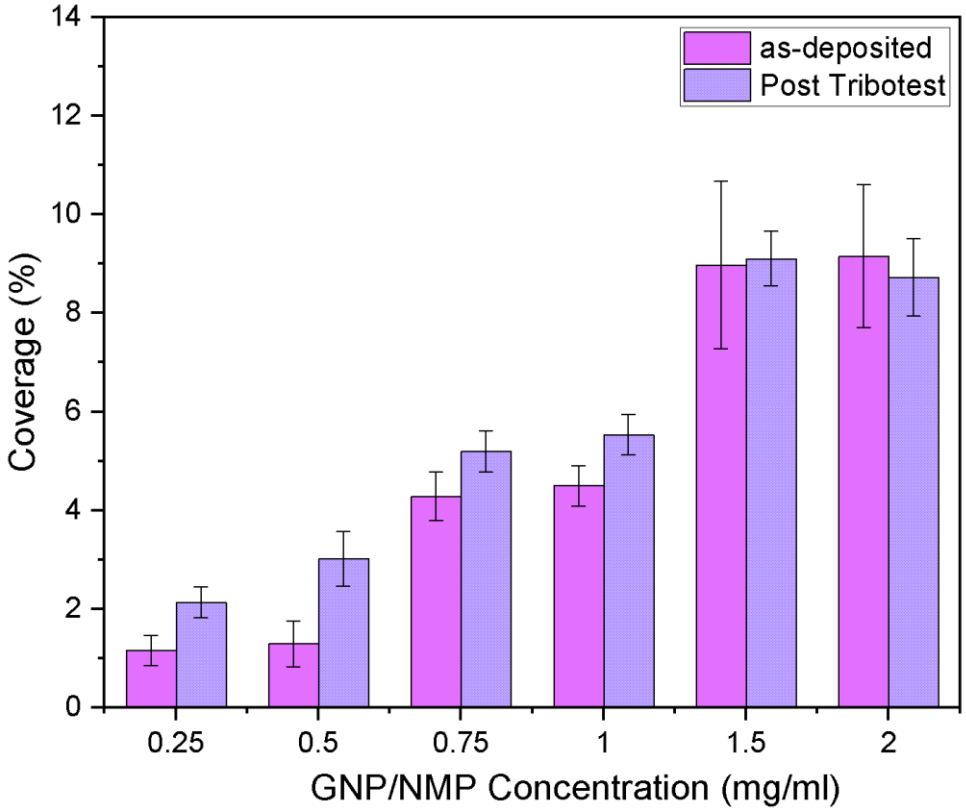

Figure 4.23 *GNP coverage before and after tribotests.*

4.2.6.2. Wear Measurements

4.2.6.2.1. Film Measurements

The wear measurements shown in **Figure 4.24** were obtained after 6 hours of tribological tests, as per **Section 3.3.3** (n=3), with the average taken. The DLC-GNP composites display lower wear than pure DLC, implying that even the smallest addition of GNP into the matrix improves the wear properties. The wear rate initially decreases as the

GNP/NMP concentration increases to 1 mg/ml. Above 1 mg/ml, the wear rate increases. The DLC-GNP1.5 and DLC-GNP2 show a considerable increase (~2 times) compared to the lowest wear rate. Other studies using DLC coatings using FFO oils provide specific wear rates in the same ranges (10^{-18} – 10^{-19} m^3/Nm) [17,170].

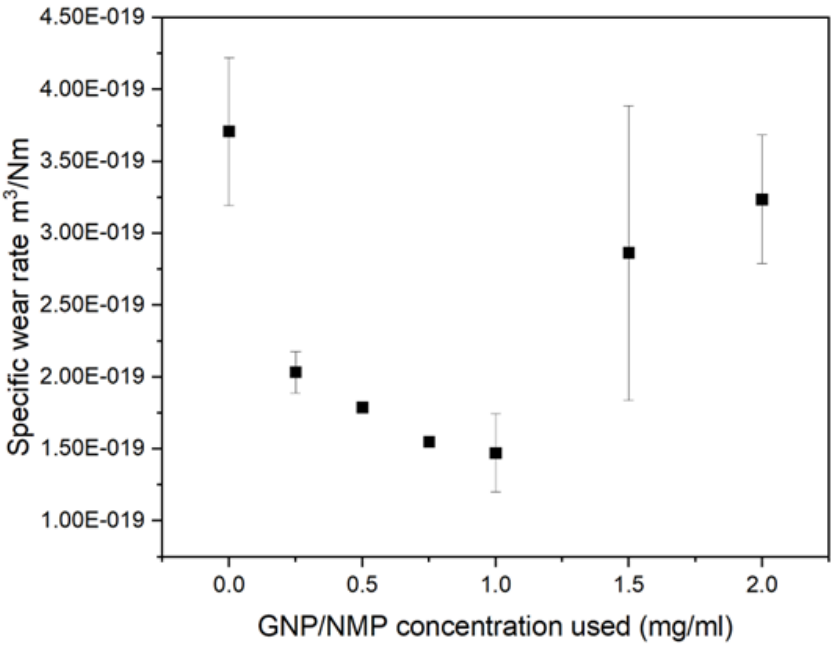

Figure 4.24 *Specific wear rate DLC-GNP composites after 6 hours of wear.*

Wear particles were collected and separated from the oil for DLC-GNP1(**Figure 4.26**) and pure DLC (**Figure 4.25**) samples after 6 hours of wear using the method shown in **Section 3.3.5**.

The SAED for pure DLC wear particles contained areas (denoted A & D), which provided some spots indicating combined with rings indicative of a polycrystalline material (**Figure 4.28**) [196]. The SAED taken from (B & C) regions (**Figure 4.25**) provided more spots and less of a halo, and assumed to be a higher ordered crystallinity than areas A and D). When reviewing the size of the particles from the DLC-GNP1 and pure DLC, the pure DLC is more prominent in size. The DLC-GNP1 produced wear particles with more size diversity. The particles contained small oval shapes (denoted B & D) and the presence of graphene (denoted A).

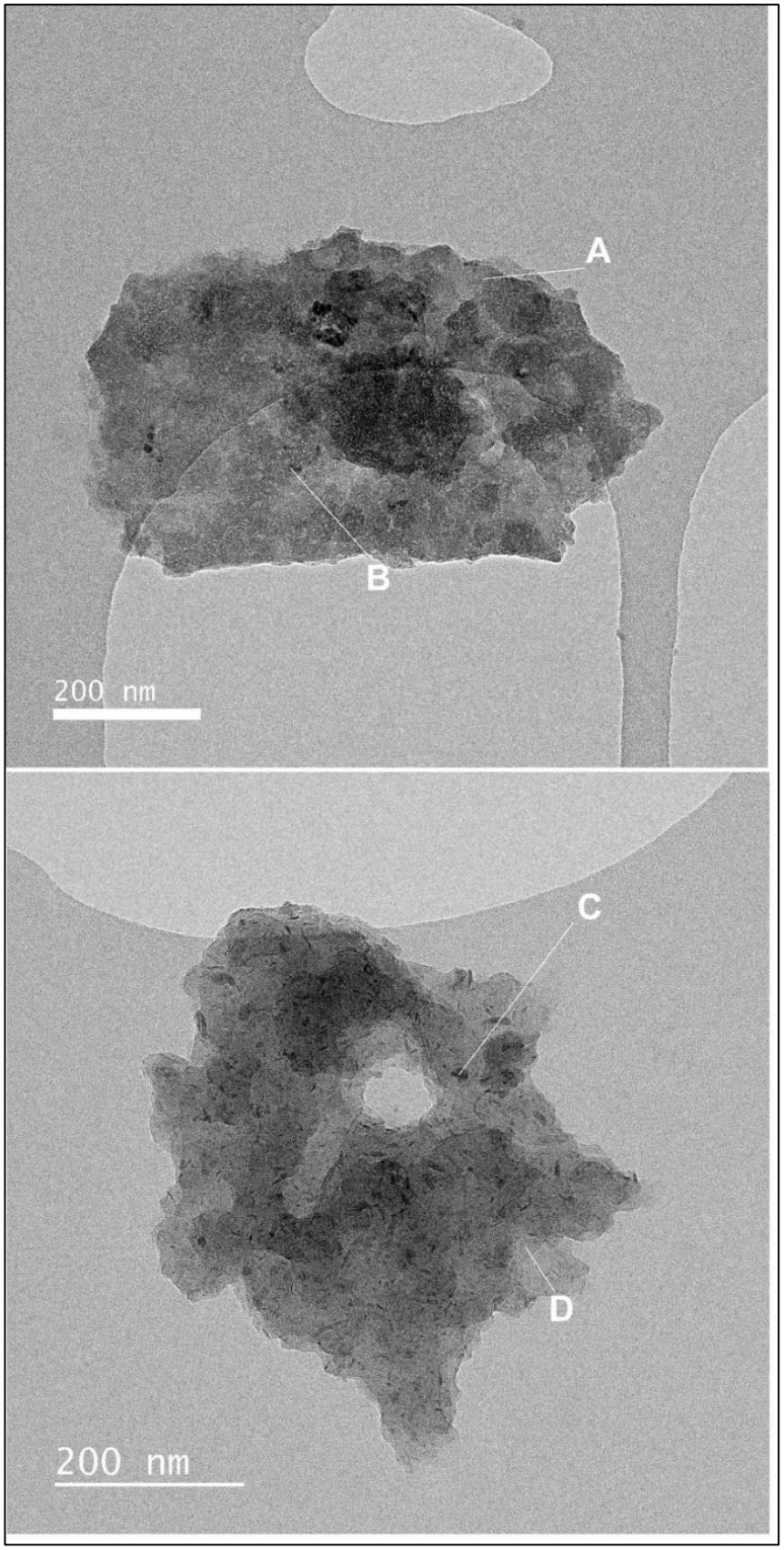

Figure 4.25 *TEM micrographs of pure DLC wear particles.*

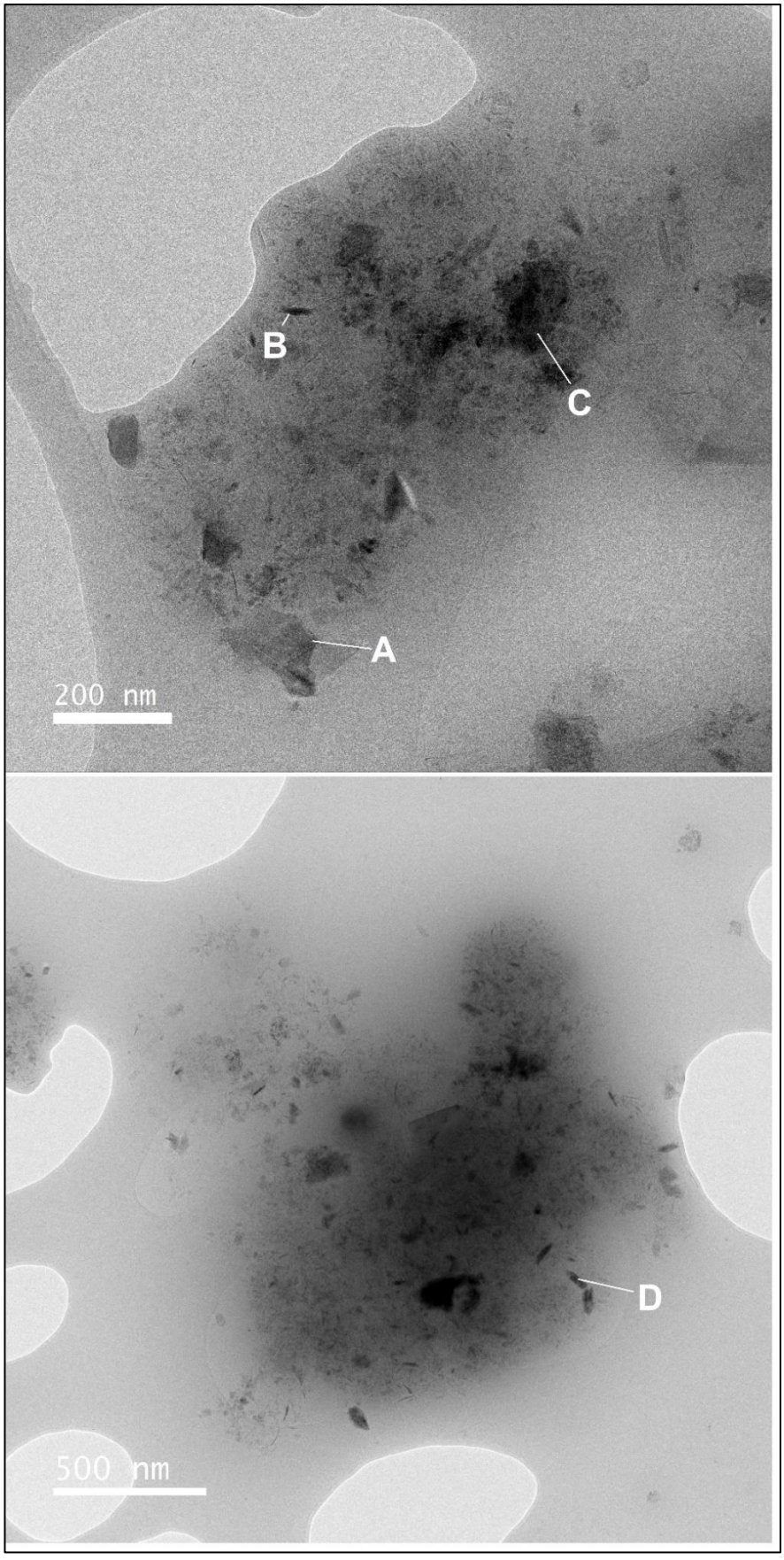

Figure 4.26 *TEM micrographs of DLC-GNP wear particles.*

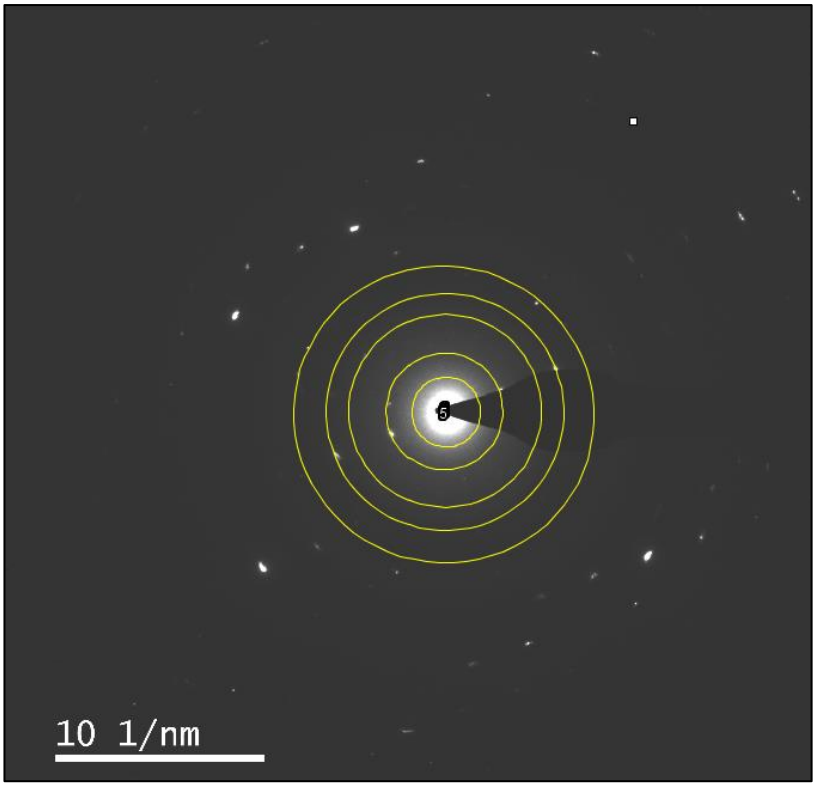

Figure 4.27 *SAED pattern for pure DLC wear particle taken from* ***Figure 4.25*** *Area C*

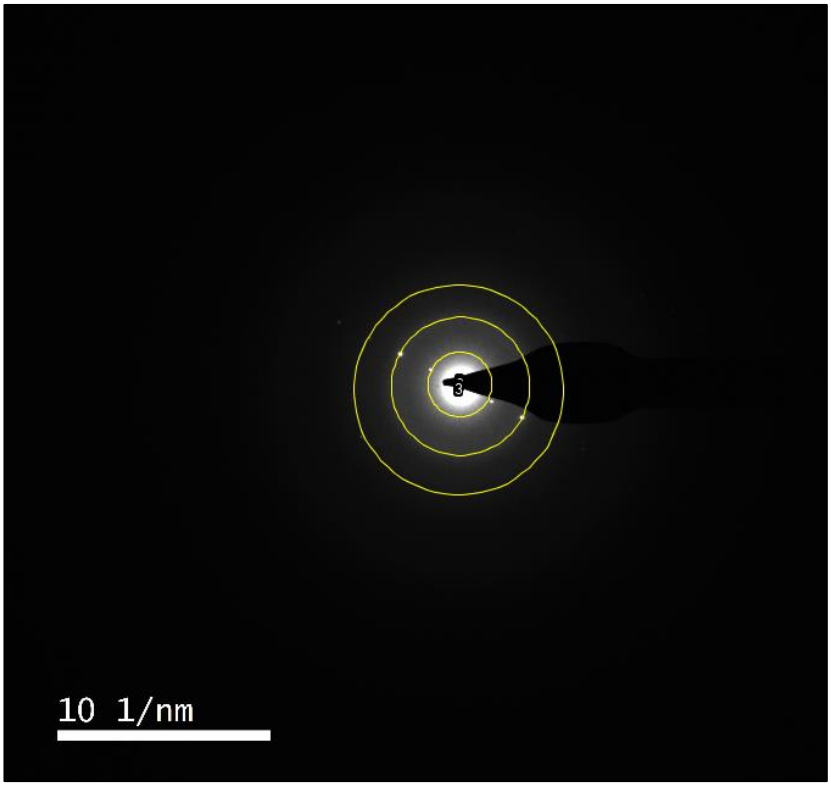

Figure 4.28 *SAED pattern for pure DLC wear particle taken from* ***Figure 4.25*** *Area A.*

The d-spacing for the pure DLC wear particles were calculated and are shown in **Table 4.8**.

Table 4.8 Wear particle d-spacing for pure DLC.

SAED Area	**d- spacing (Å)**
Pure DLC (Area C)	6.07
	3.6
	2.17
	1.76
Pure DLC (Area A)	6.67
	3.11
	2.04

The 3.6 Å 2.17 Å and 1.76 Å d-spacing correspond to the (0 1 2) (1 1 3) and (1 1 6) h k l values of iron oxides [197]. Iron oxides have been observed previously from DLC wear particles and support the results obtained [17]. The Area A contained heliocentric rings and some faint spots, but this could not be matched. The diffraction patterns from the DLC-GNP sample produced no crystalline readings due to repeated charging and, thus, could not be analysed. The TEM technician attempted these results to analyse the DLC-GNP wear particles twice during COVID with the same charging effects both times.

Figure 4.29 provides the SEM images of the wear scars after 6 hours of tribo-tests. In pure DLC, the prominent feature inside the wear track was micro-grooving. Adding GNP into the DLC matrix reduces the wear scar depth for concentrations up to 1mg/ml. There were also changes to the wear mechanism, moving from adhesive wear to more abrasive. It is evidenced by a smoother polished surface. We can postulate that the polishing wear is from the formation of fine 3rd body particles between the CI/DLC-GNP tribo-pair that

become trapped in the contact and are shown in the wear particle micrographs (**Figure 4.26**).

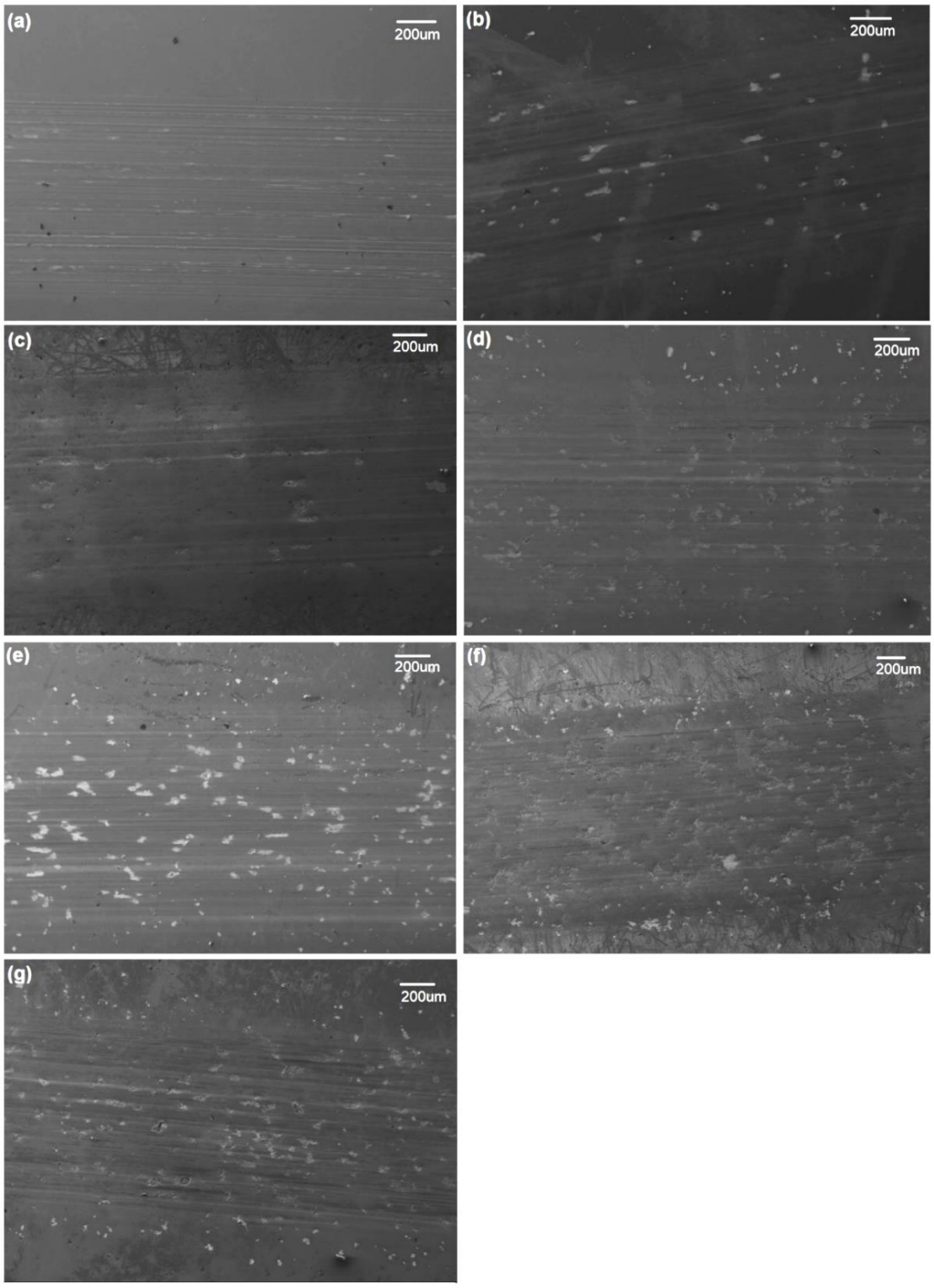

Figure 4.29 *SEM wear images of (a) pure DLC, (b) DLC-GNP0.25, (c) DLC-GNP0.5, (d) DLC-GNP0.75, (e) DLC-GNP1, (f) DLC-GNP1.5 and (g) DLC-GNP2 after 6 hours of wear.*

Guimarey *et al.* [198] reported on a GNP polishing mechanism / tribo-film formation when used as a lubricant additive. However, in DLC-GNP nanocomposites (1 mg/ml or below), the GNP is held within the DLC matrix with no signs of being removed. For the DLC-GNP1.5 and DLC-GNP2 concentrations, deep valleys appear due to GNP being removed from the film.

Figure 4.30 provides accompanying line scans to the SEM micrographs. In pure DLC, a deep conical wear scar is present; there are also areas where the DLC was not removed. This was due to ploughing wear from the CI into the film not wearing the counter-body uniformly, as shown in **Figure 4.30(b).** The DLC-GNP1.5 and DLC-GNP2 also presented these deep wear scars, with large sudden deviations due to the removal of GNP.

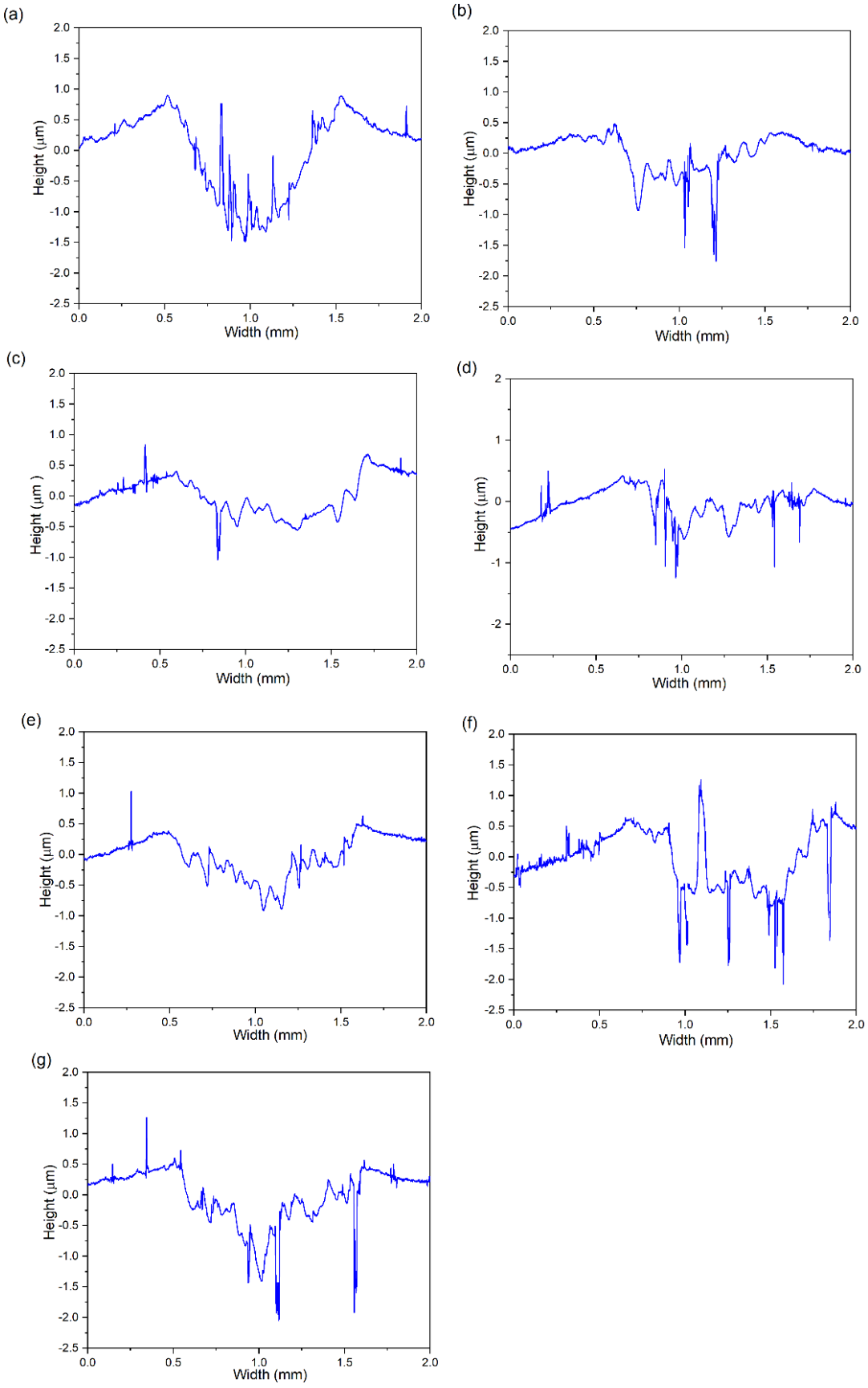

Figure 4.30 *Line scans for (a) pure DLC, (b) DLC-GNP0.25, (c) DLC-GNP0.5, (d) DLC-GNP0.75, (e) DLC-GNP1, (f) DLC-GNP1.5 and (g) DLC-GNP2 after 6 hours of wear.*

4.2.6.2.2. Pin Wear

The CI pin wear rate is shown in **Figure 4.31**, with optical images of worn CI pins shown in **Figure 4.32**. The wear of the CI is just as crucial in a tribological system to prevent catastrophic failure in applications. The wear rate decreases significantly, achieving the lowest value for the DLC-GNP1 composite. However, when the GNP/NMP concentration exceeds this threshold, the wear rate increases dramatically. The pure DLC and DLC-GNP1.5 coatings exhibit the highest wear rates. These findings align with the observed wear rate of the DLC-GNP films illustrated earlier in **Figure 4.24**.

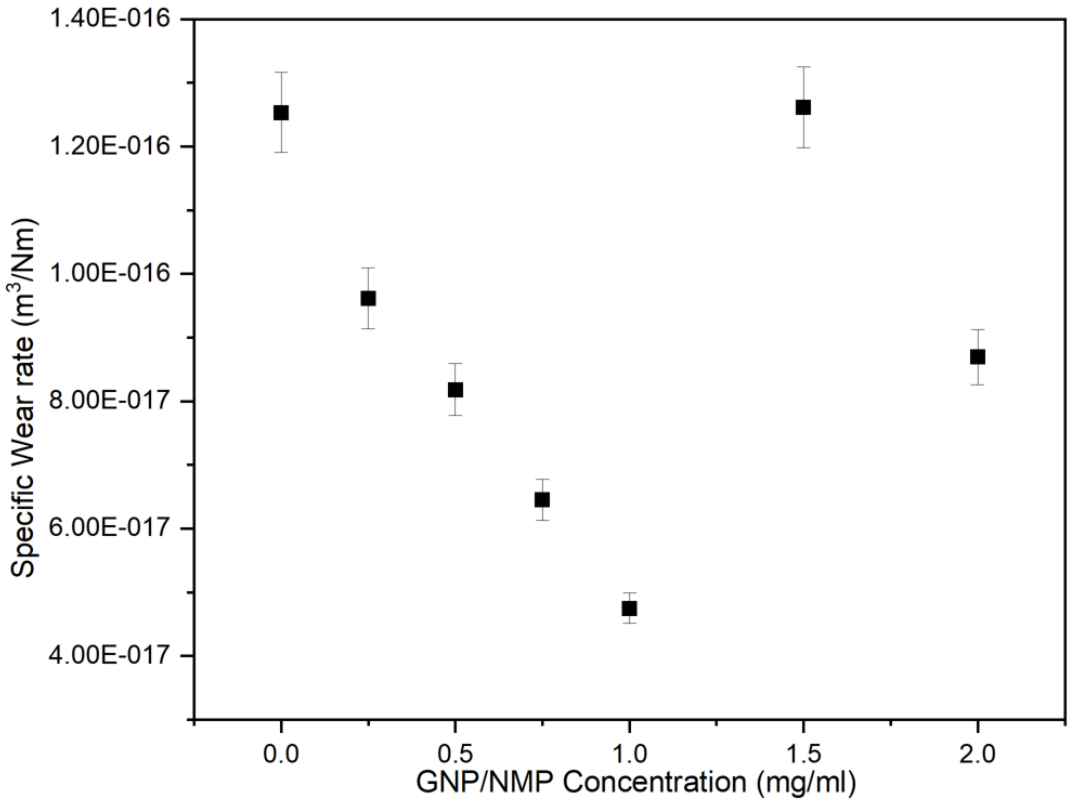

Figure 4.31 *CI wear rate after 6 hours of wear.*

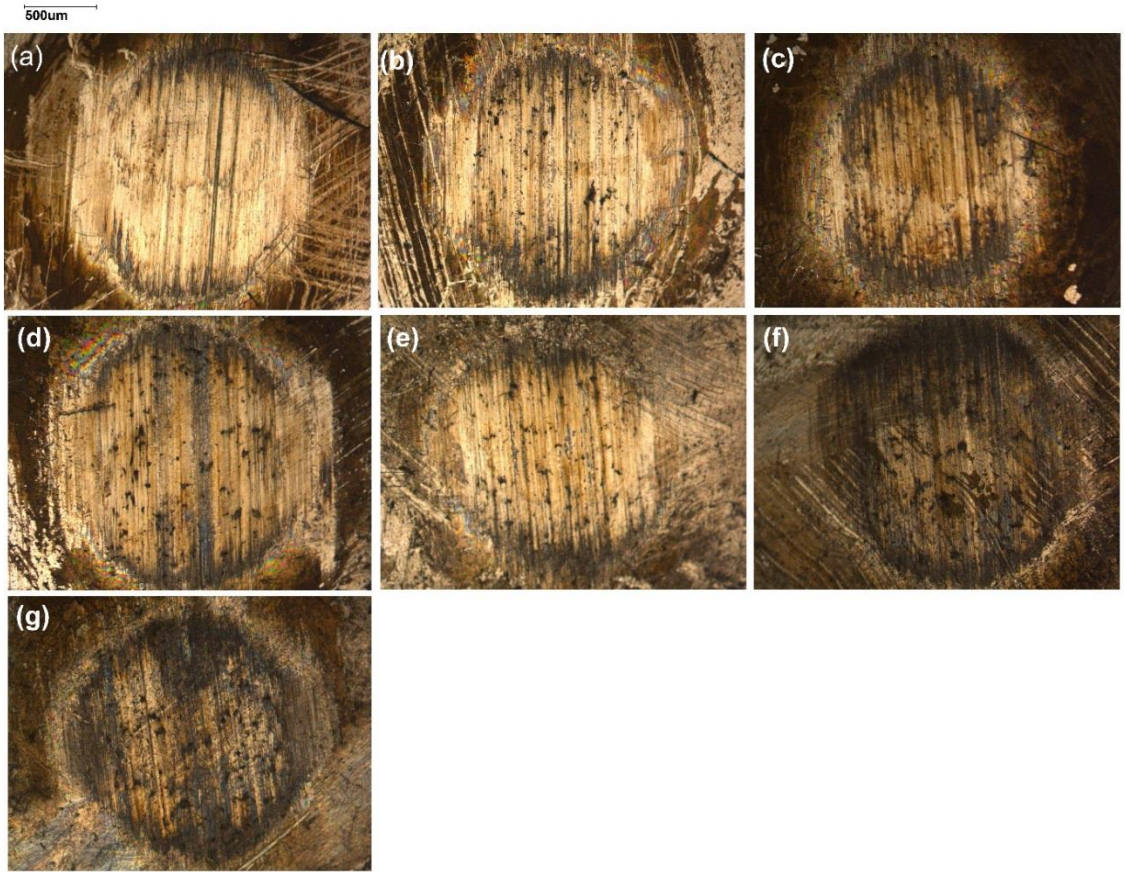

Figure 4.32 *CI Wear scar after wear tests against (a) pure DLC, (b) DLC-GNP0.25, (c) DLC-GNP0.5, (d) DLC-GNP0.75, (e) DLC-GNP1, (f) DLC-GNP1.5 and (g) DLC-GNP2 nanocomposite films* [199].

4.2.6.3. Transfer Film Formation

4.2.6.3.1. DLC-GNP Films

After conducting tribological testing on the DLC films, Raman spectra were obtained. The I_D/I_G ratio was calculated, along with D and G peak positions (**Table 4.9** and **Table 4.10**) and compared to as-deposited DLC-GNP films. All results were completed per the methodology.

The DLC-GNP nanocomposites are split into DLC areas and the GNP islands to determine any differences post-wear of the discrete areas.

Table 4.9 *I_D/I_G ratio for DLC-GNP nanocomposites post wear.*

	I_D/I_G	
Sample	**DLC Area**	**GNP Island**
Pure DLC	0.92 ± 0.04	-
DLC-GNP0.25	0.91 ± 0.04	1.02 ± 0.06
DLC-GNP0.5	0.89 ±0.01	0.94 ± 0.13
DLC-GNP0.75	0.87 ± 0.05	0.81 ± 0.10
DLC-GNP1	0.89 ± 0.12	0.71 ± 0.12
DLC-GNP1.5	0.88 ± 0.02	1.00 ± 0.34
DLC-GNP2	0.70 ± 0.20	0.94 ± 0.03

Figure 4.33 illustrates the I_D/I_G ratio difference between the as-deposited and worn samples. For DLC areas of the DLC-GNP worn surfaces, the I_D/I_G ratio remains stable within the range of 0.87 to 0.92, except for DLC-GNP2, which exhibits a lower value of 0.7 ± 0.2 along with a higher deviation. This significant deviation could be attributed to the shearing of GNP particles, which become detached during the wear process, forming a thin, highly graphitic film with fewer active A1g breathing modes (D peak contributions).

The decrease in I_D/I_G ratio for the GNP islands is explained by removal of the DLC above the islands during friction tests. This DLC removal brings GNP closer to the surface, becoming active in the Raman spectra due to the limited penetration depth. This breaks down above 1 mg/ml when the wear rate is higher, and the exposed GNP are subjected to more mechanical damage through wear, increasing the active A_{1g} mode, relative to the G intensity [200].

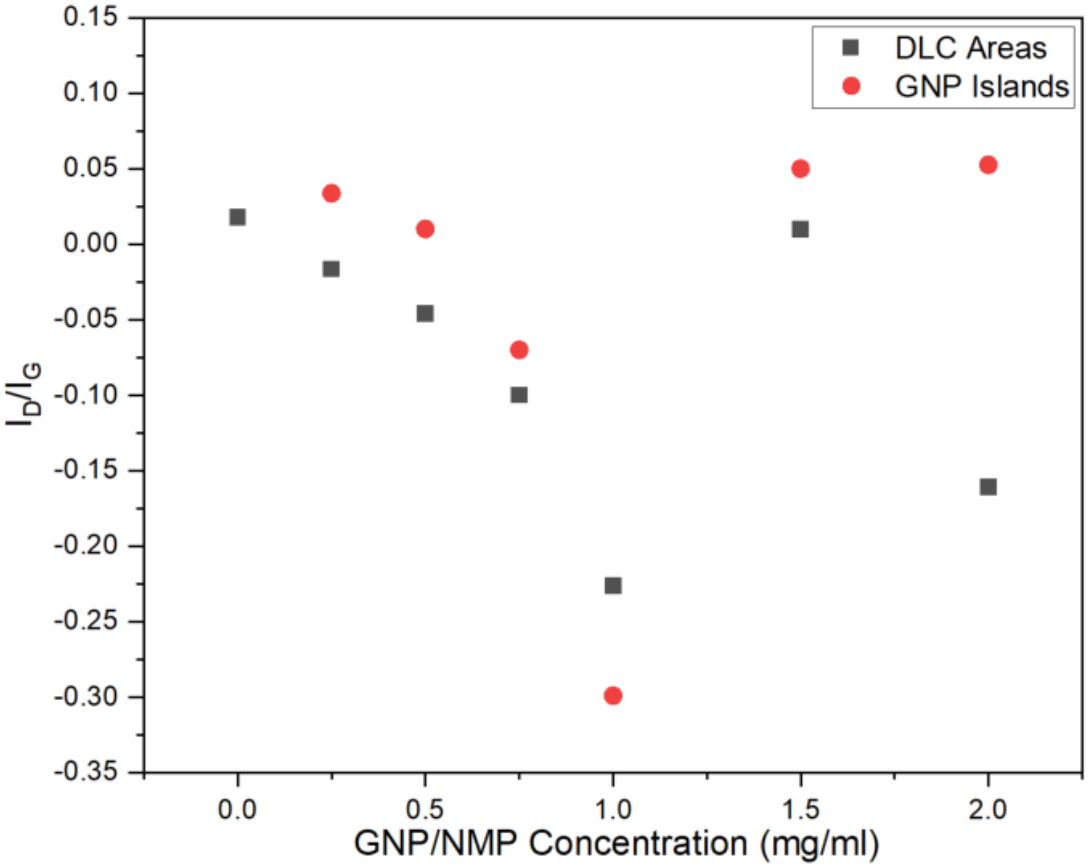

Figure 4.33 *Difference in I_D/I_G post wear for DLC-GNP nanocomposites.*[199]

The peak positions of the DLC-GNP nanocomposites (**Table 4.10**) vary greatly depending on the spectra taken from the DLC areas or the GNP islands, with the G peak position being consistent at ~1555cm^{-1} (DLC area) and moving to a higher frequency of ~1600cm^{-1} (GNP island) which is indicative of a more graphitic structure [26]. These differences between worn GNP islands / DLC are more pronounced than as-deposited spectra scan due to the removal of DLC above the GNP during the wear process. The D peak wavenumber position is lower for all post-wear GNP islands compared to their respective DLC areas and lower than the as-deposited DLC-GNP nanocomposites, which is also linked to more graphitic sp^2 clusters/chains [201].

Table 4.10 *D and G Peak position for worn DLC-GNP nanocomposites.*

	DLC Area		**GNP Island**	
	Peak Position (cm^{-1})		Peak Position (cm^{-1})	
	D Peak	**G Peak**	**D Peak**	**G Peak**
Pure DLC	1372 ± 5	1554 ± 2	-	-
DLC-GNP0.25	1377 ± 6	1555 ± 2	1365 ± 2	1600 ± 1
DLC-GNP0.5	1378 ± 2	1555 ± 1	1380 ± 23	1596 ± 6
DLC-GNP0.75	1376 ± 3	1555 ± 1	1370 ± 2	1599 ± 1
DLC-GNP1	1385 ± 9	1560 ± 9	1367 ± 4	1588 ± 2
DLC-GNP1.5	1381 ± 2	1556 ± 1	1372 ± 16	1579 ± 30
DLC-GNP2	1371 ± 11	1553 ± 4	1388	1560

4.2.6.3.2. Counter-body Transfer Film Analysis

After 6 hours of tribological testing, the counter-bodies were subjected to Raman Spectroscopy analysis (**Figure 4.34** and **Figure 4.35**) to investigate the presence of a graphitic transfer film. The I_D/I_G ratio and G peak intensity were examined to assess the level of graphitisation and the thickness of the transfer film, respectively. Before conducting the Raman measurements, the pins were rinsed in heptane to preserve the carbon transfer film while removing any oil residue.

Cross-sections of worn CI were analysed by TEM cross-sections, and no large graphitic structures were observed. Thus, the I_D/I_G ratio is an appropriate technique to determine the relative I_D/I_G extent of graphitisation within the transfer film. A higher I_D/I_G ratio suggests a higher degree of graphitisation, while a lower ratio indicates a lower degree. The G peak intensity, on the other hand, provides information about the thickness of the transfer film.

By analysing these parameters, it is possible to gain insights into the nature and characteristics of the carbon transfer film formed during tribological testing.

The presence of a graphitic transfer layer was detected by Raman on all CI counter-bodies, with the average I_D/I_G from each ranging from 0.65 – 1.45. A graphitic transfer layer is often observed on the counter-body in low friction DLC/Steel tribo-pair systems, creating a low shear strength interlayer, reducing friction and wear. However, it can be restrained under oil-lubricated conditions where a thin film can form between the surfaces, reducing direct contact between the two bodies [202].

The I_D/I_G increased as the GNP/NMP concentration increased, which indicates that the transfer film is more graphitic. The peak intensity also decreased as the concentration increased up to 1 mg/ml; after this, it presented an increase. This change in G peak intensity provides evidence that the transfer film's thickness decreased as the GNP/NMP concentration increased but only up to 1 mg/ml.

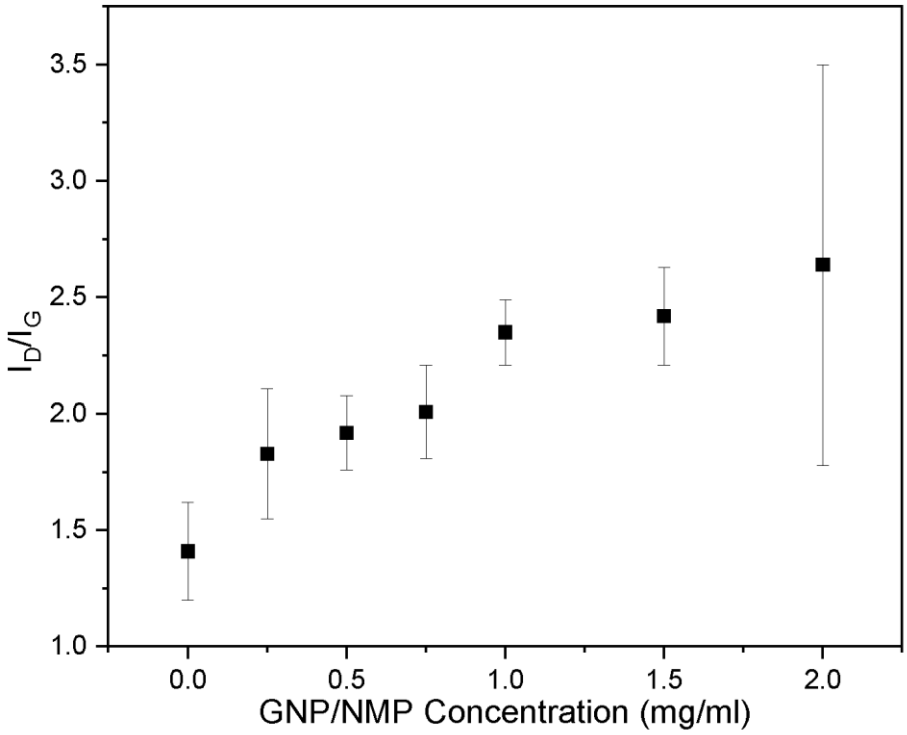

Figure 4.34 *I_D/I_G ratio for DLC-GNP CI counter-body post wear.* [199]

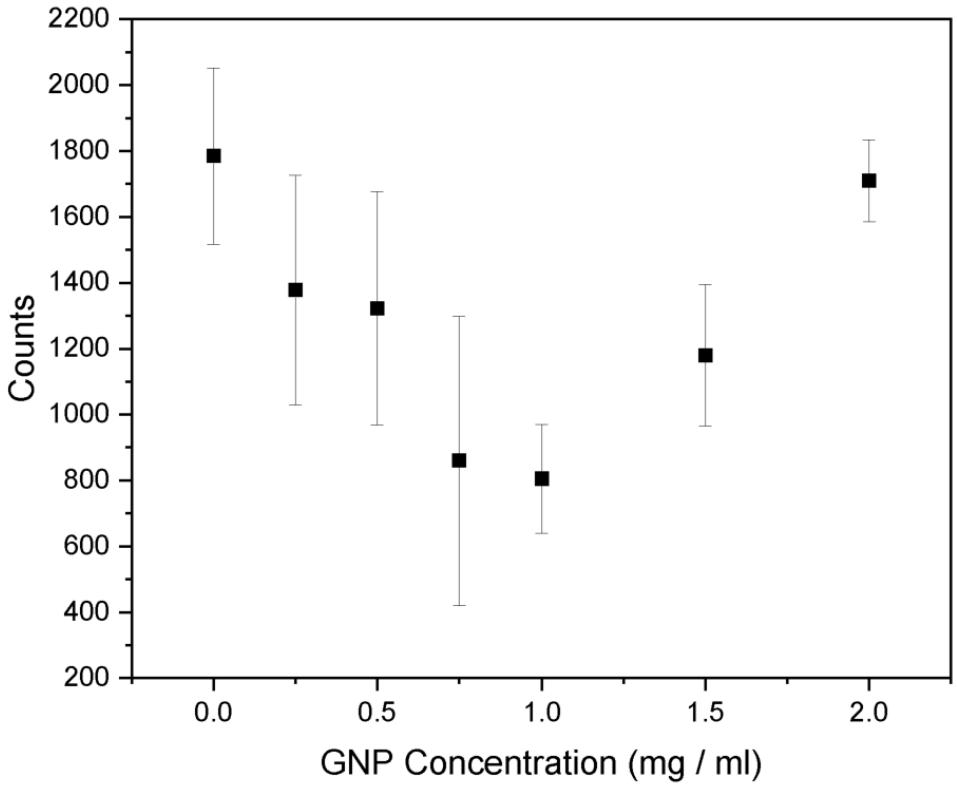

Figure 4.35 *G peak intensity for transfer film on CI counter-body.*

4.3. Summary of GNP Coverage on the Tribological Properties of DLC-GNP Nanocomposites

The incorporation of GNP into a DLC matrix has demonstrated significant improvements in friction and wear performance. Key findings from the study are as follows:

- The heat treatment process applied to the GNP did not introduce any additional defects, regardless of whether the GNP was covered.
- Friction and wear decreased as the GNP coverage increased, with the optimum coverage observed at 1 mg/ml (~4.5% coverage) for the tested samples.
- Higher GNP coverages resulted in agglomeration, leading to more significant peak heights and easier removal than lower coverages.
- Scratch tests revealed lower cohesive (L_{C1}) values but improved first adhesive failure (L_{C2}) load values with increasing GNP coverage. The final adhesive failure (L_{C3}) load also exhibited a slight improvement.
- Wear particles from pure DLC, and DLC-GNP1 exhibited differences, with pure DLC showing larger particles containing iron crystallites. DLC-GNP1 wear particles displayed unique "Salomon Perfecto" shaped particles absent in the pure DLC wear particles.

These findings highlight the beneficial effects of GNP incorporation in DLC coatings, reducing friction and wear rates, improving adhesion properties, and forming distinctive wear particles and transfer films.

Chapter 5 - The Effect of DLC Thickness on the Tribological Properties of DLC-GNP Nanocomposites

5.1. Introduction

The chapter aims to enhance our understanding of DLC-GNP films' mechanical and tribological properties by exploring the influence of DLC thickness in conjunction with heat treatment. The main focus is, therefore, to investigate how changes in DLC thickness deposited above the spin-coated GNP deposition affect the mechanical and tribological properties of the coatings.

Gaining a comprehensive understanding of the influence of DLC thickness on the tribological and mechanical properties is crucial for unravelling the underlying mechanisms behind low friction and wear in DLC-GNP films. As DLC is deposited atop the GNP islands, its thickness plays a pivotal role. In DLC films, variations in thickness can significantly impact the load-carrying capacity, hardness, elastic modulus, I_D/I_G ratio, and adhesion (often attributed to heightened internal stresses) [57,117,203,204]. Examining these interconnected factors can elucidate the fundamental mechanisms for achieving superior tribological performance.

In this chapter, four DLC-GNP nanocomposites were created by depositing DLC at 22.5 minutes, 45 minutes, 90 minutes, and 180 minutes. The resulting thickness is measured in ranges of 0.3 µm – 3.63 µm. All the tribological testing (n = 3 for repeatability) was completed as per the conditions of **Chapter 4.**

Figure 5.1 displays a map of the study conducted and presented in this chapter, outlining the characterisation techniques utilised.

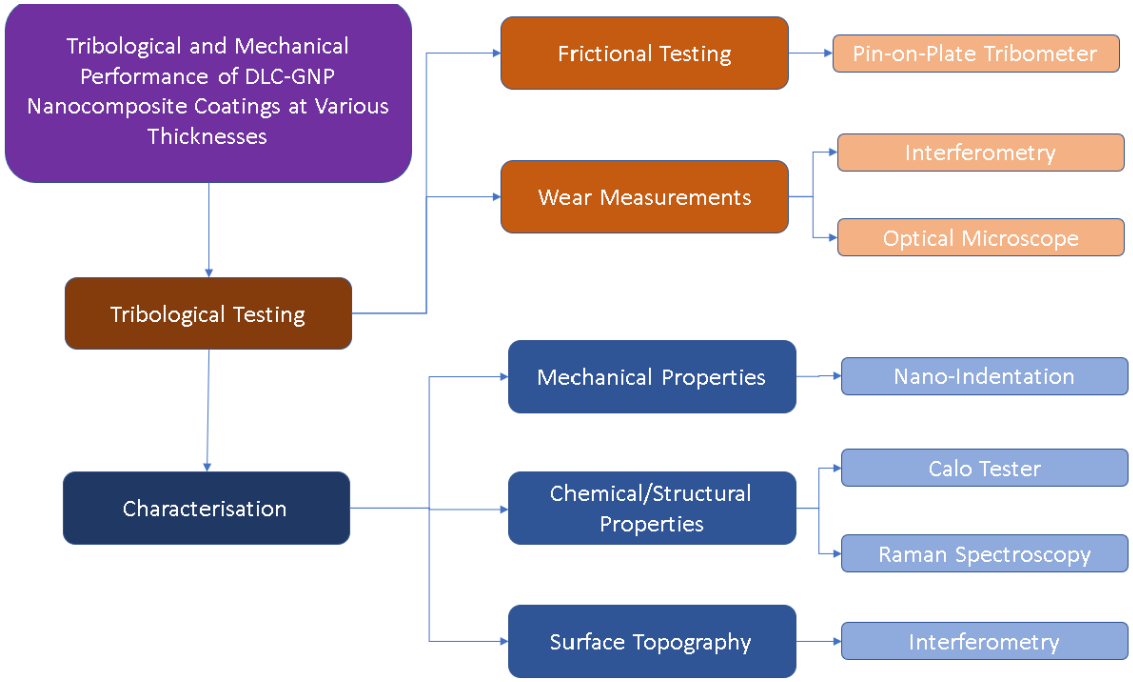

Figure 5.1 *Map of study in this chapter.*

5.2. Thickness Measurements and Topography

The thickness of the DLC layers was determined using a combination of Calo tests and FIB cross-sections. **Table 5.1** presents the thickness values corresponding to different deposition times. As anticipated, the results demonstrated an increase in thickness as deposition time increased. It is worth noting that the slowest deposition rate was observed during the 90-minute deposition period. However, it is essential to consider that the differences in thickness at this scale were relatively small and could fall within the margin of error when calculating the deposition rate.

Table 5.1 *DLC thickness and calculated deposition rates.*

Deposition Time (minutes)	DLC layer Thickness (µm)	Deposition Rate (µm/min)
22.5	0.45 ± 0.04	0.020 ± 0.004
45	0.73 ± 0.03	0.016 ± 0.002
90	1.27 ± 0.03	0.014 ± 0.002
180	3.63 ± 0.05	0.020 ± 0.002

The surface roughness (Ra) values are presented in **Table 5.2**, revealing that the average surface roughness tends to rise as the deposition time increases. This observation aligns with the findings of Huang *et al.* [205]. When the film thickness is low, the valleys and peaks may undergo distinct growth processes [206]. It is worth noting that DLC films can exhibit a trend of becoming smoother with increasing thickness, primarily due to reduced conformality to the original surface as the film grows [206]. However, due to internal stresses within the film, and changes to nucleation and growth, they can also increase in roughness [207]. Additionally, it is important to acknowledge that the uncertainty in the measurements increases with longer deposition times, indicating a decrease in homogeneity.

Table 5.2 *Surface roughness (R_a) of DLC-GNP nanocomposites at various DLC deposition times.*

Deposition Time (minutes)	**Mean Surface Roughness (R_a) (µm)**
22.5	0.042 ± 0.012
45	0.043 ± 0.011
90	0.077 ± 0.014
180	0.089 ± 0.026

Figure 5.2 illustrates the structure of the DLC-GNP composites obtained with the shortest and longest DLC deposition times. As anticipated, the thickness of the DLC layer above the GNP islands increases with longer deposition times. Consequently, the DLC layer with the smallest thickness (**Figure 5.3)** exhibits GNPs located closer to the surface. This configuration necessitates less wear before the GNPs come into contact with the counter-body. In contrast, the DLC layer with the greatest thickness (**Figure 5.4)** requires

substantial wear before the counter-body makes contact with the GNP during the tribological testing phase.

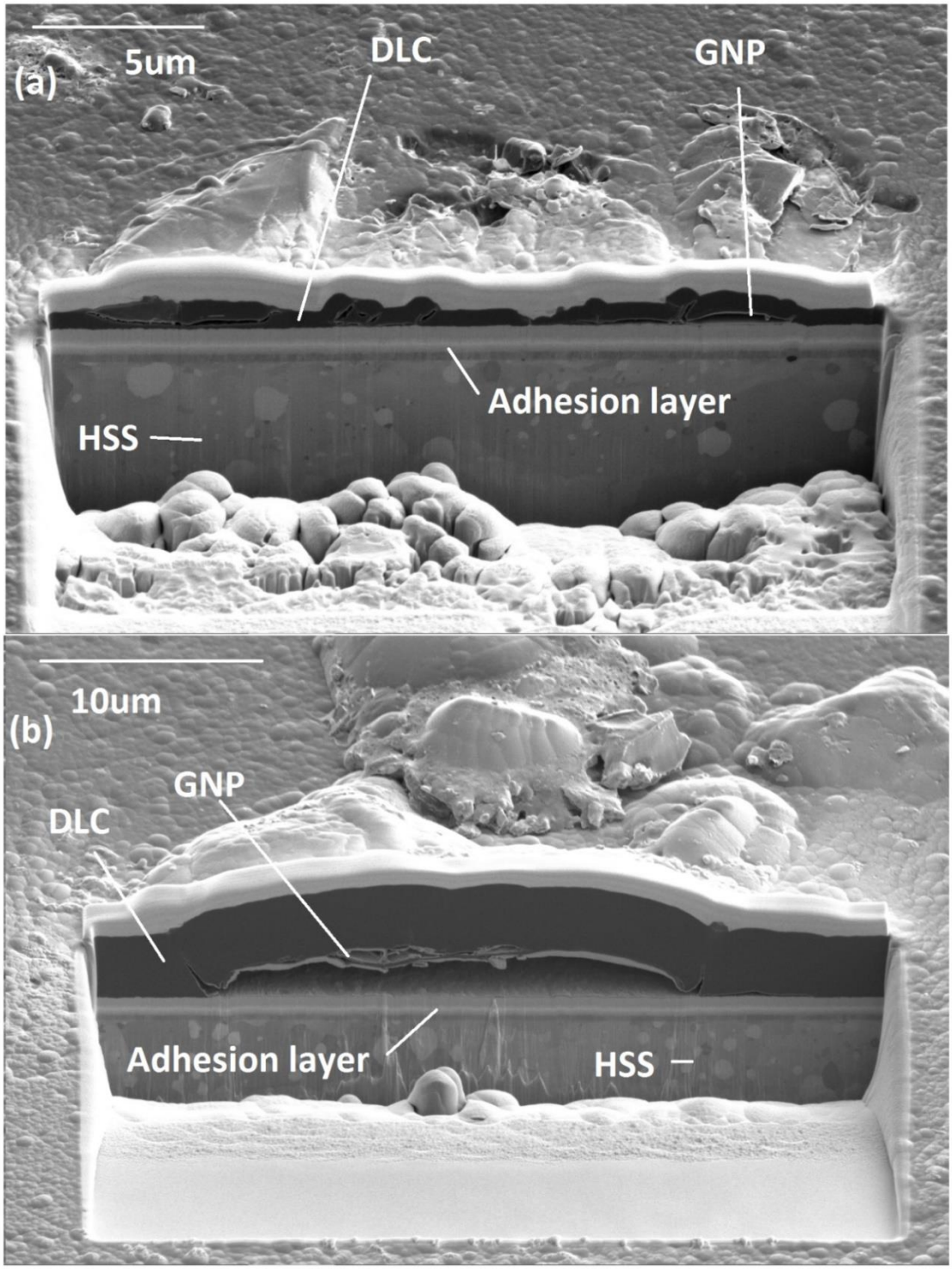

Figure 5.2 *Structure of (a) 22.5 minutes deposition time and (b) 180 hours deposition time using PECVD. The white layer above the DLC is a protective platinum layer used to protect the DLC during the FIB processing.*

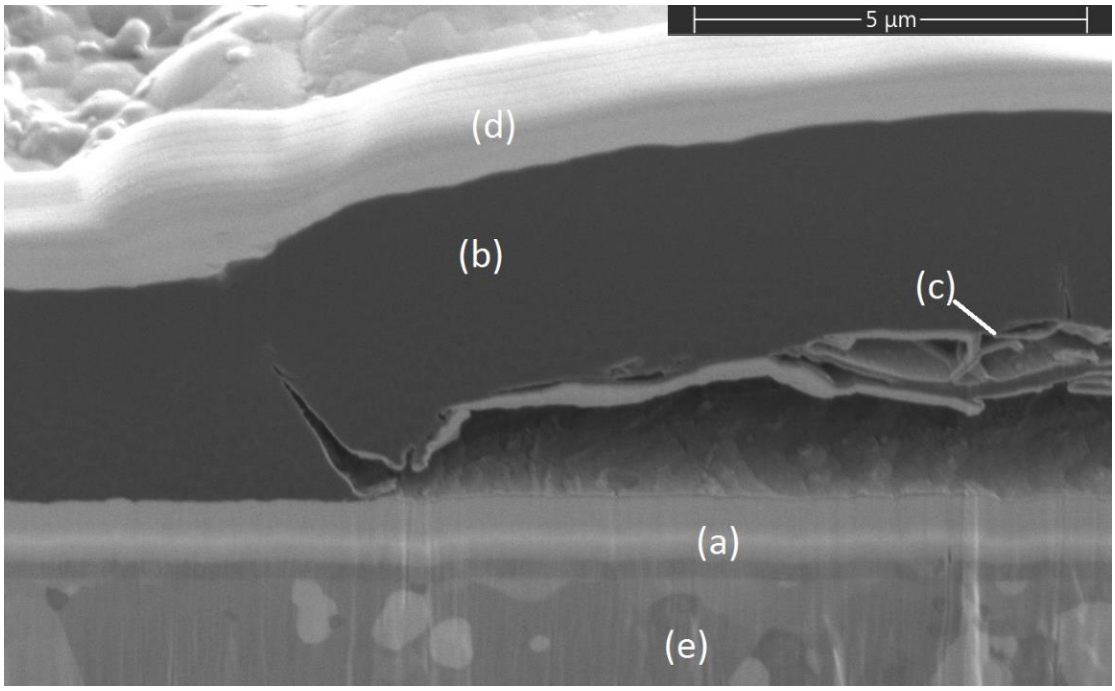

Figure 5.3 *Cross-section of DLC-GNP180 nanocomposite with the structure of (a) adhesion layer, (b) DLC, (c) GNP, (d) Platinum, and (e) HSS substrate*

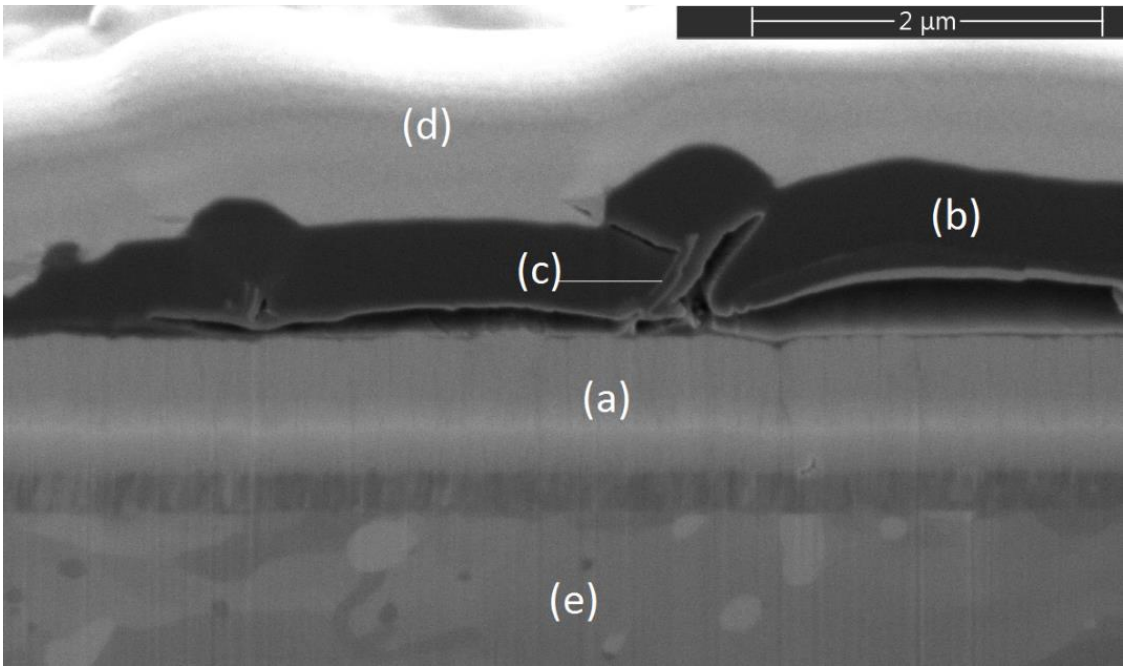

Figure 5.4 *Cross-section of DLC-GNP22.5 nanocomposite with the structure of (a) adhesion layer, (b) DLC, (c) GNP, (d) Platinum, and (e) HSS substrate*

SEM images were taken of the surface topography (**Figure 5.5 - Figure 5.8**). The thinnest coating shows that the DLC deposition above some of the GNP is insufficient to cover all the GNP.

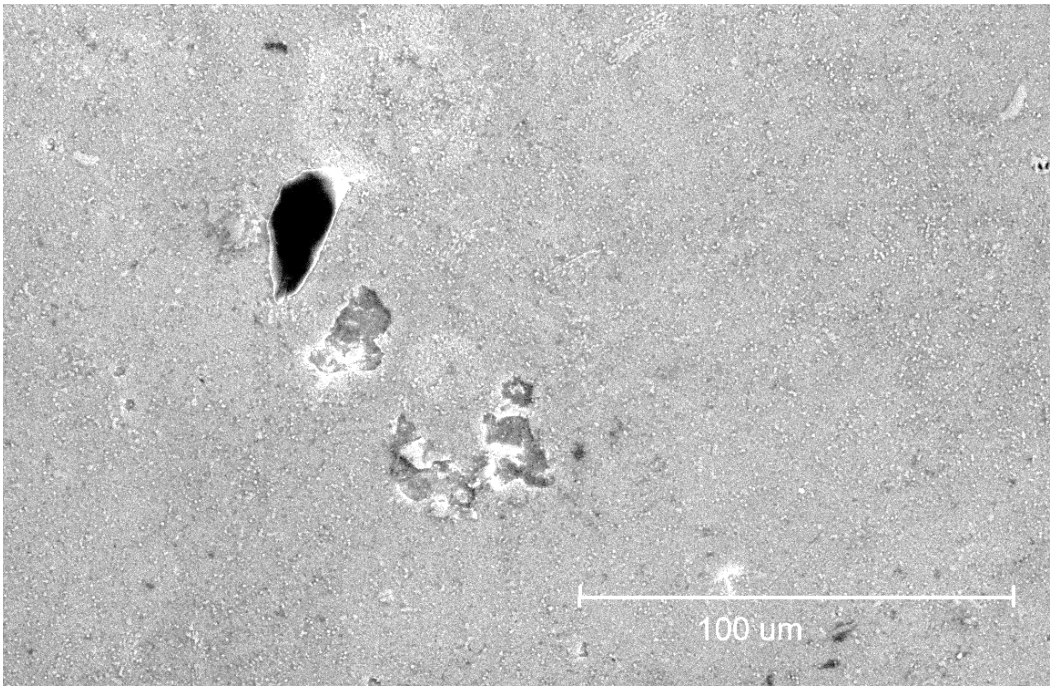

Figure 5.5 *SEM micrograph of as-deposited DLC-GNP22.5*

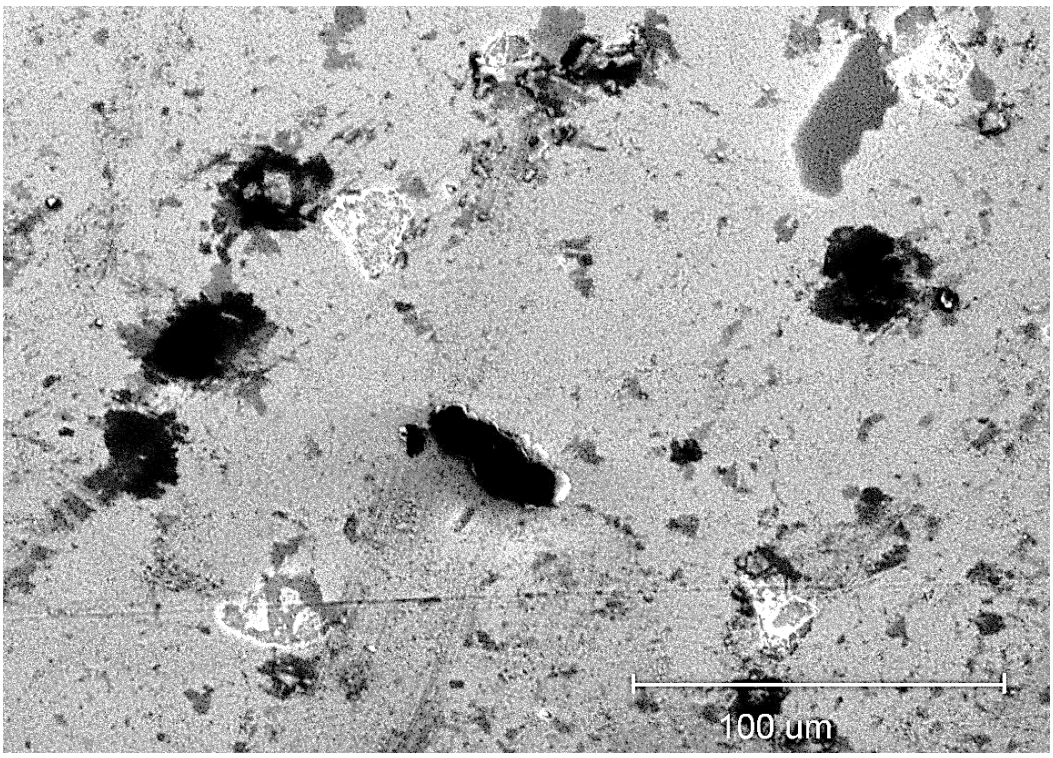

Figure 5.6 *SEM micrograph of as-deposited DLC-GNP45*

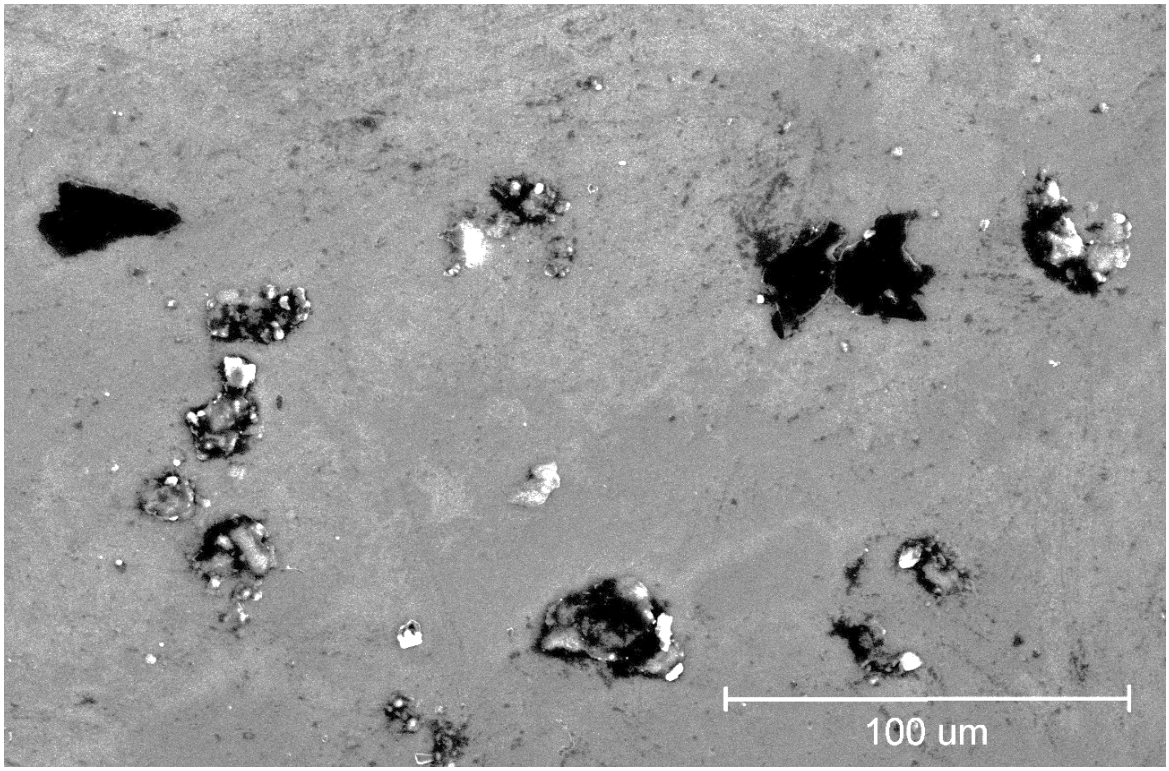

Figure 5.7 *SEM micrograph DLC-GNP90.*

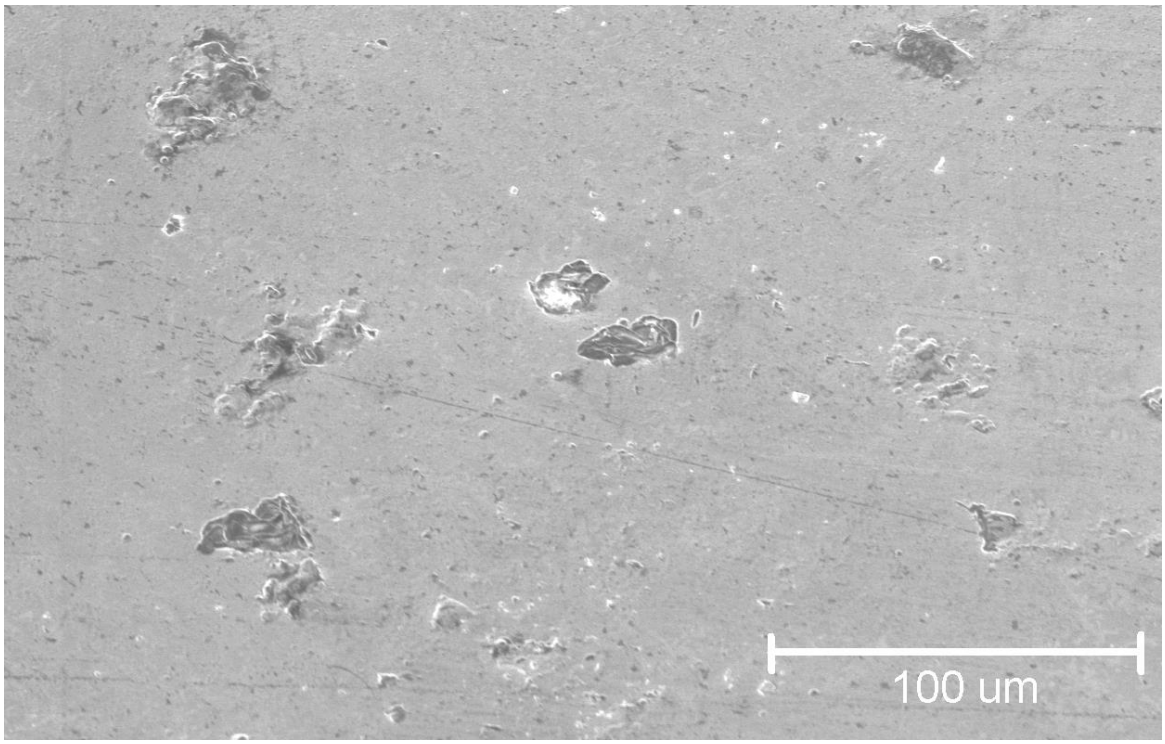

Figure 5.8 *SEM micrograph of as-deposited DLC-GNP180.*

Figure 5.9 provides a close-up view of the GNP islands for each deposition time. In the case of the longest deposition time, a thick DLC layer is observed above the GNP islands. Conversely, in the case of the thinnest DLC layer, the edges of the GNP islands are visible, indicating that the DLC only sometimes fully covers the GNP islands.

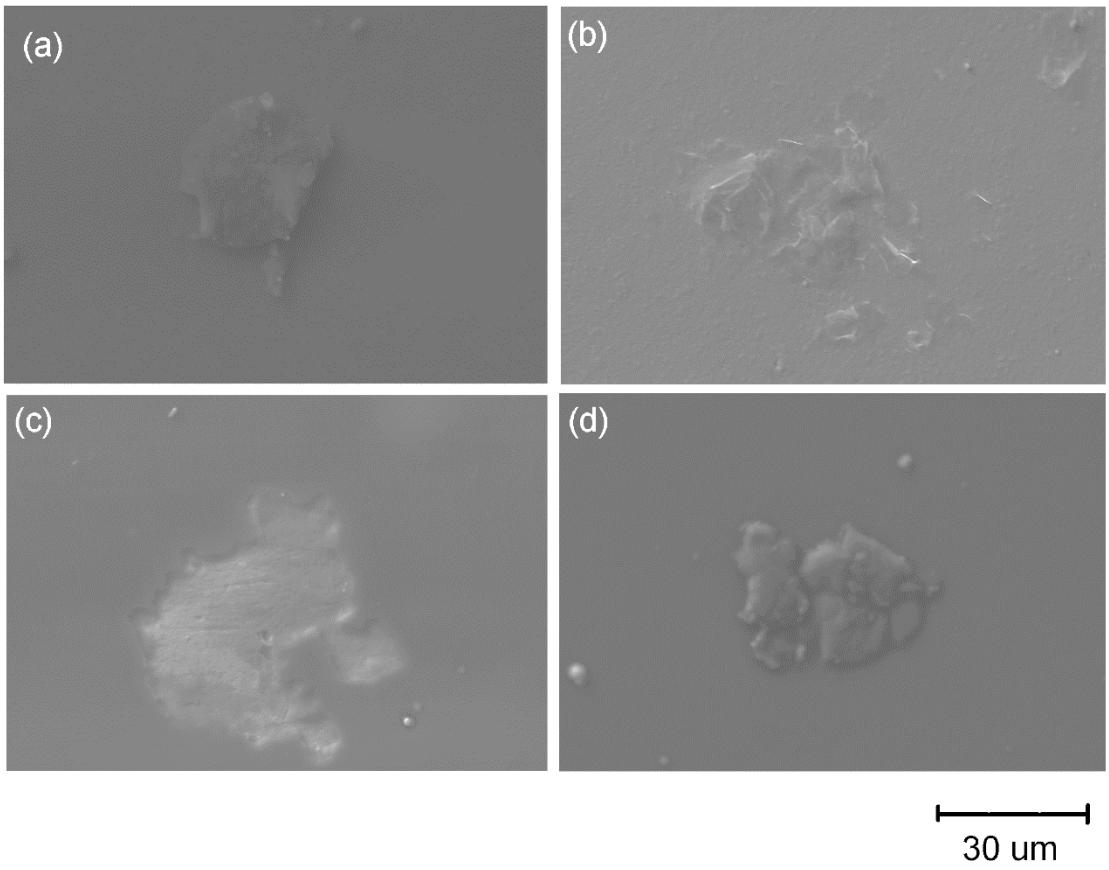

Figure 5.9 *SEM micrographs of (a) DLC-GNP22.5, (b) DLC-GNP45, (c) DLC-GNP90, and (d) DLC-GNP180.*

5.3. Mechanical Properties

5.3.1. Adhesion Testing

The adhesion of the DLC-GNP coatings to the substrate was evaluated using a scratch tester, and the critical failure loads (L_{C1}, L_{C2}, and L_{C3}) are presented in **Table 5.3** and visually depicted in **Figure 5.10**. The L_{C1} values observed in all the tested coatings correspond to the point at which tensile cracking first appeared. This critical load

remained relatively consistent throughout the testing, indicating a cohesive failure within the DLC film.

The second critical load (L_{C2}) is associated with the adhesive failure between the DLC coating and the interlayer, characterised by partial spallation in all coatings. It was observed that the L_{C2} value decreased as the thickness of the DLC coating increased. Specifically, with a deposition time of 180 minutes, the critical load reached only ~16.4 N.

The final critical load (L_{C3}) observed in all coatings represents adhesive failure, which entails complete DLC delamination or severe spallation. In the case of the 22.5-minute deposition time, no indications of severe spallation or delamination were observed in any of the repeated tests, indicating the coating can deform more elastically prior to L_{C2} failure [208]. However, nearly identical results were obtained for the 45-minute and 90-minute deposition times, suggesting similar resistance to severe spallation or delamination. The 180-minute deposition time presented the lowest L_{C3} value (by ~38%). The decrease in adhesion observed with longer deposition times could be attributed to the elevated internal stresses that arise as the thickness of the coating increases. Another factor contributing to this phenomenon is the interaction between the scratch tip and the film surface [209]. Previous work has shown similar results [210]; however, Chen *et al.* [211] showed with increasing DLC deposition time, the critical load capacity of the films increased. The difference between the two conflicting reports is the internal stresses within the DLC structure, which can increase with thickness [212].

Table 5.3 *Critical loads for DLC-GNP composites for various DLC deposition times.*

	Critical Load (N)		
Deposition Time (Minutes)	**L_{C1}**	**L_{C2}**	**L_{C3}**
22.5	12.7	45.0	-
45	13.2	41.6	48.0
90	9.5	37.8	-
180	13.6	16.4	28.9

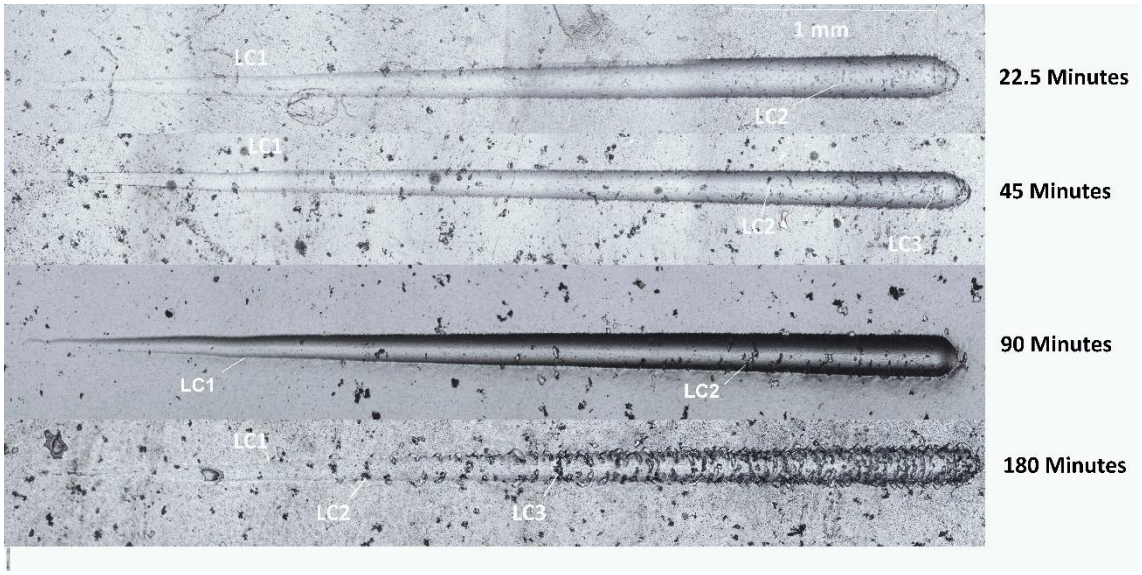

Figure 5.10 *Progressive load (0 – 50N) scratch testing for the DLC-GNP nanocomposites at various DLC deposition times.*

5.3.2. Nano-Mechanical Properties

The films' bulk mechanical properties (Elastic Modulus and Hardness) were assessed using nano-indentation. This technique was employed at 10% of the DLC thickness, employing the methodology described in Section 3.3.7. This depth (10%) is widely used as it predominantly represents the film's contribution rather than the substrate's when applying the Oliver-Pharr method [158]. The results were obtained using a 10 x 10 matrix with a spacing of 25 µm between each indent. This spacing was implemented to prevent

pileup effects. The obtained results are presented in **Table 5.4**. The hardness was found to be highest for the thickest DLC layer located above the deposited GNP. However, it is noteworthy that the standard deviation for all the coatings is significantly higher than what is typically observed in nano-indentation studies. This increased standard deviation can be attributed to two factors:

- The GNP being much softer than the (a-C:H) DLC matrix [213,214]
- The presence of voids at the GNP islands which would yield at a much lower load.

As the DLC layer thickness increases, the standard deviation decreases. This trend can be explained by the fact that the measurements were taken at a depth corresponding to only 10% of the DLC thickness, thus minimizing the contributions from voids or the softer GNP to the overall response.

Table 5.4 *Elastic Modulus and Hardness as a function of DLC thickness.*

DLC layer Thickness (µm)	Elastic Modulus (GPa)	Hardness (GPa)
0.45	164 ± 20	18 ± 3
0.73	182 ± 21	20 ± 5
1.27	195 ± 13	22 ± 6
3.63	226 ± 13	23 ± 1

5.4. Friction Results

Figure 5.11 provides representative frictional traces for DLC-GNP nanocomposites using the 4 DLC deposition times. The DLC-GNP180 took the longest time to observe a reduction in friction, with the DLC-GNP22.5 showing a reduction the quickest. The lowest friction was achieved by the DLC-GNP90, with the DLC-GNP45 also obtaining a

similar low COF of ~0.03 at the end of the 6-hour test. The DLC-GNP22.5 reduced instantly, maintaining a low, steady COF until ~15,000 seconds.

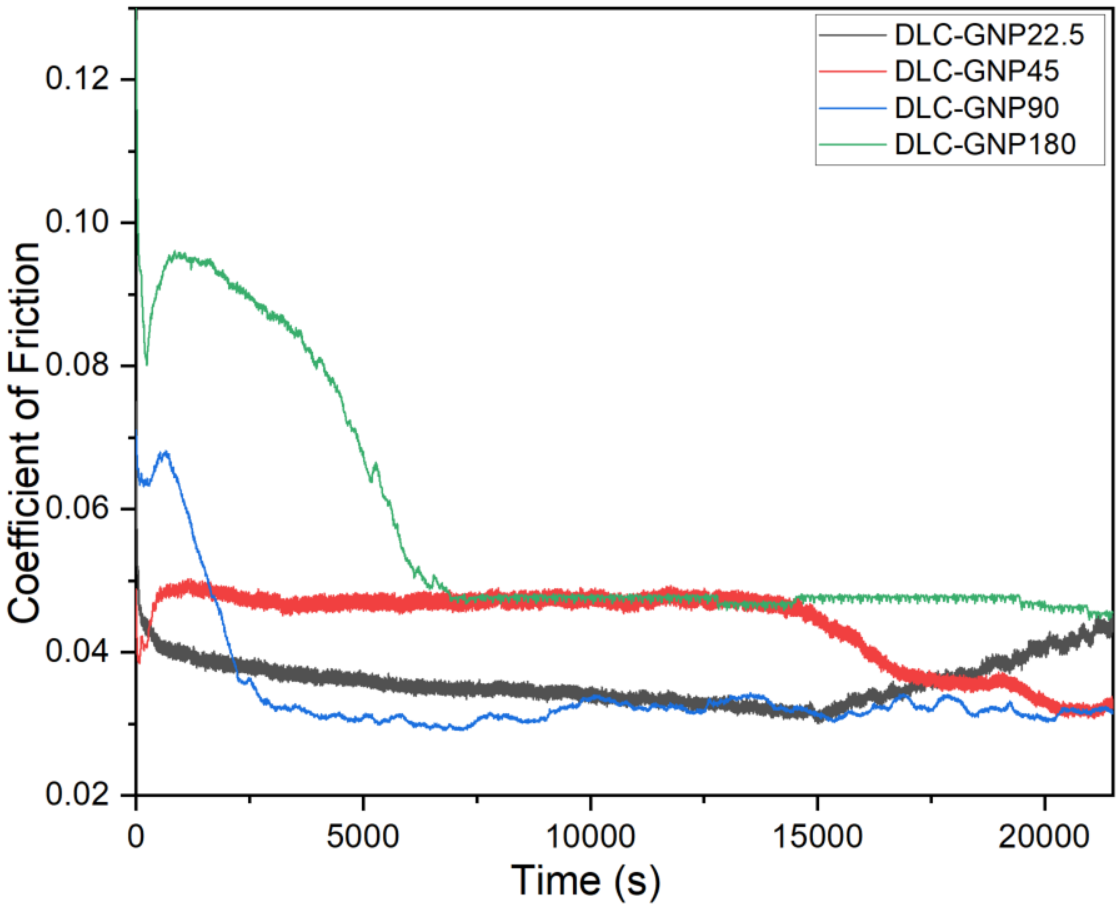

Figure 5.11 *Friction traces for DLC-GNP nanocomposites as a function of time for various DLC deposition times.*

Optical images (**Figure 5.12**) revealed a distinct difference in the behaviour of DLC-GNP coatings with various deposition times. Specifically, for DLC-GNP22.5, noticeable removal of GNP islands occurred during the wear process, while the GNP remained intact for longer deposition times. Based on these observations, it can be inferred that the removal of GNP during tribological testing has a detrimental effect on the frictional properties of the coatings. Removal of GNP within biomedical applications from within a composite can be detrimental to the tribological properties [215].

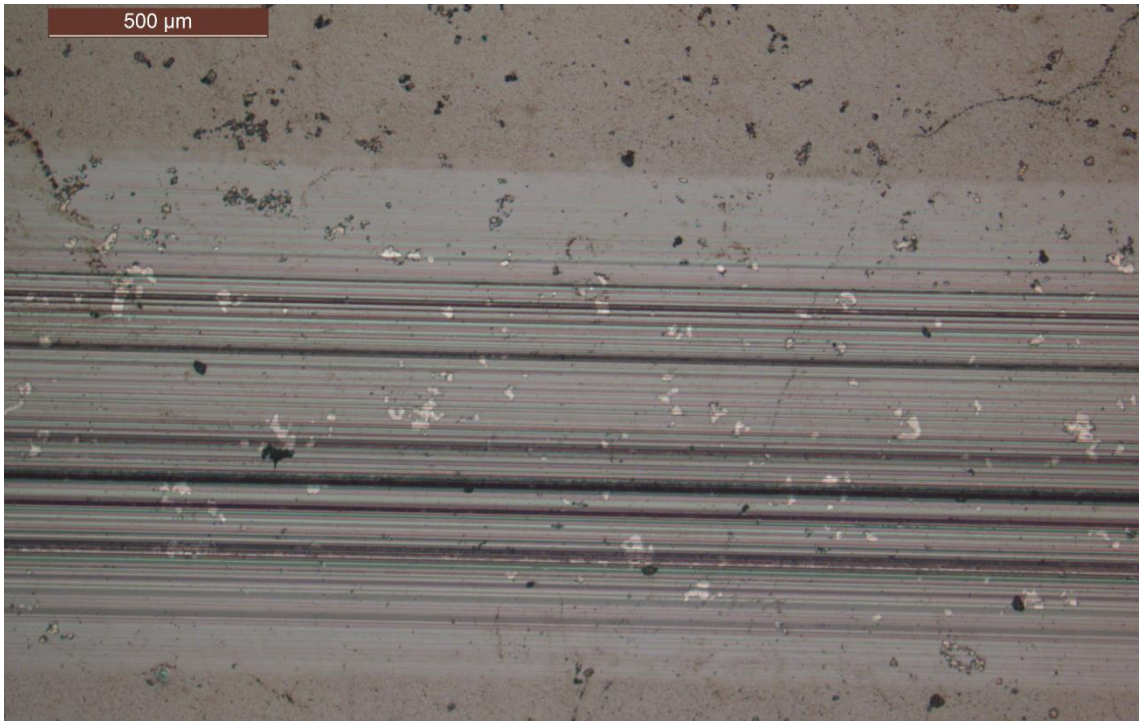

Figure 5.12 *Optical image of DLC-GNP22.5 post tribological testing.*

Table 5.5 presents the average friction results (n = 3) obtained from the experiments. The DLC-GNP22.5 coating, characterised by the thinnest DLC layer, achieved the lowest coefficient of friction (COF) among the tested samples. Conversely, the DLC-GNP180 coating, featuring the thickest DLC layer, exhibited the highest COF.

Table 5.5 *Mean COF for DLC-GNP with various DLC thicknesses (6 hours).*

DLC layer Thickness (µm)	Mean Average COF
0.43	0.035 ± 0.003
0.73	0.044 ± 0.07
1.24	0.038 ± 0.008
3.63	0.050 ± 0.009

5.4.1. Wear Measurements

5.4.1.1 DLC-GNP Film

Wear measurements were obtained by WLI, with the wear rates calculated and the corresponding average COF shown in **Figure 5.13**.

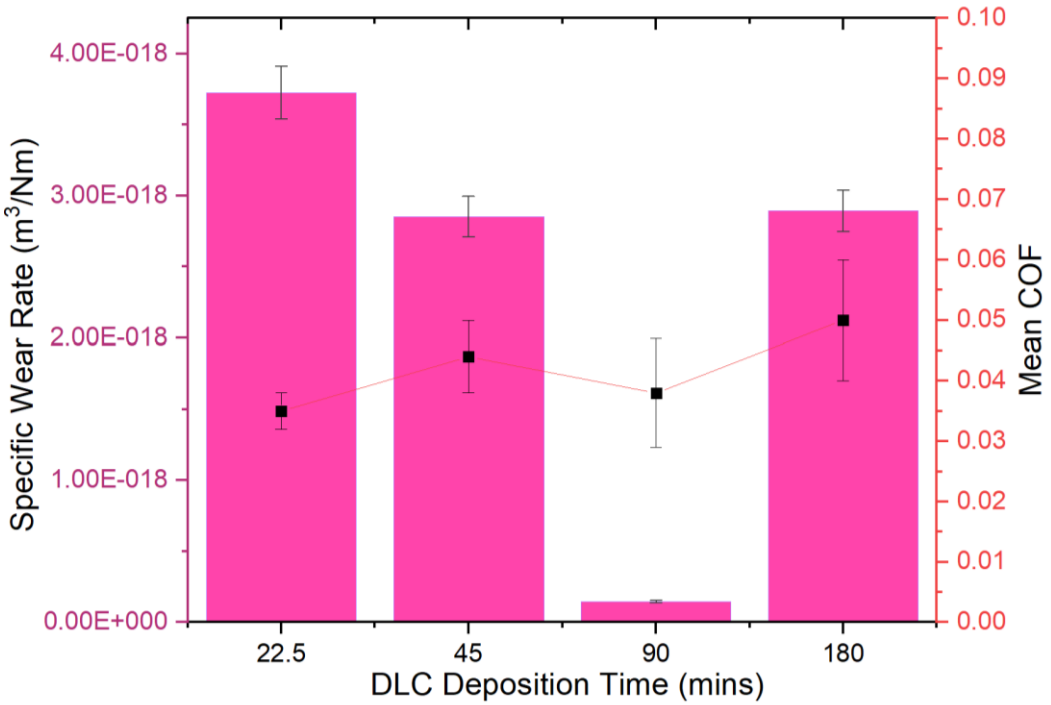

Figure 5.13 *Specific wear rate and mean COF over 6 hours for DLC-GNP nanocomposites with various deposition times.*

The film with the shortest deposition time exhibited the highest wear, while the DLC-GNP90 demonstrated the lowest wear among the samples. The DLC-GNP45 and DLC-GNP180 samples displayed similar wear rates. Interestingly, the mean COF values did not align with the wear rates, as the thinnest DLC film achieved the lowest COF, while the highest COF was observed in the thickest film.

A comparison of the line profiles of wear tracks is depicted in **Figure 5.14**. The DLC-GNP with the shortest deposition time exhibited the deepest wear track, which can be attributed to its higher wear rate. The deposition times of 45 minutes and 90 minutes

resulted in similar depths, but the wear scar width for the 45-minute DLC deposition time was wider.

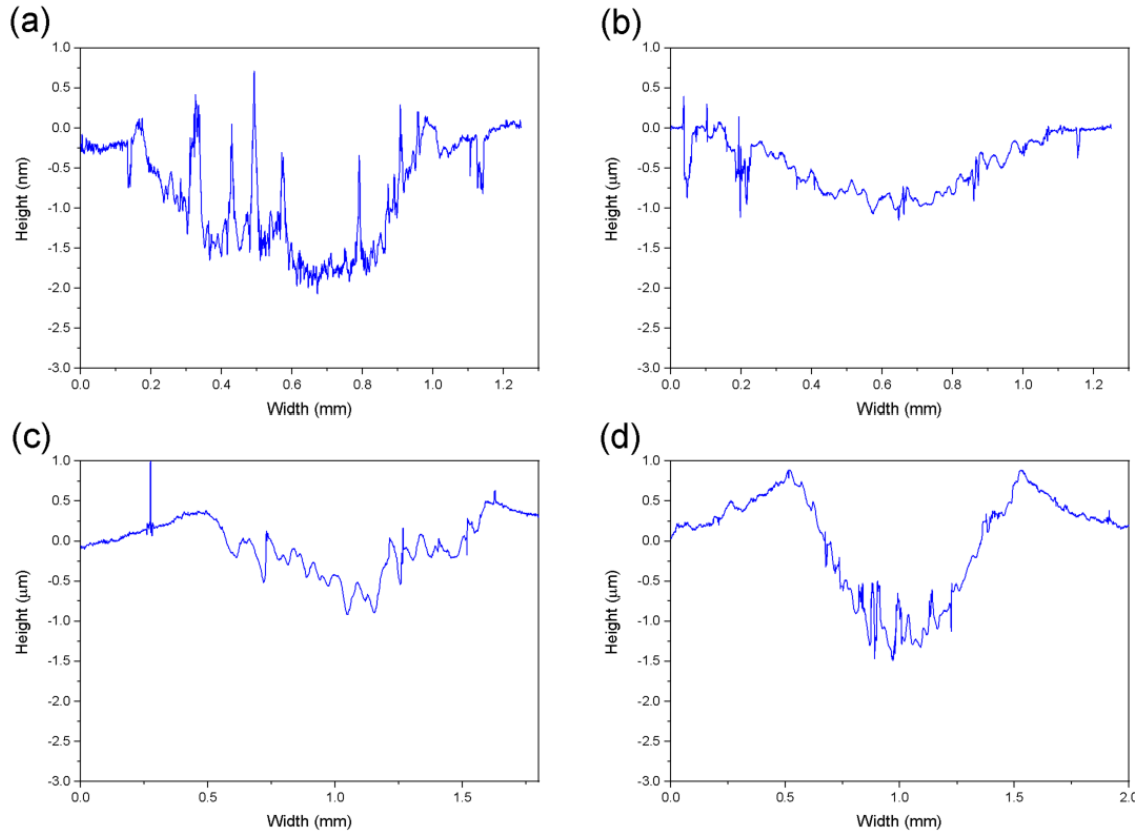

Figure 5.14 *Wear Profiles for DLC-GNP with various DLC deposition times, after 6 hours of wear testing. (a) 22.5 minutes, (b) 45 minutes, (c) 90 minutes, and (d) 180 minutes.*

5.4.1.2 CI Counter-body

The wear scar of the CI counter was measured using an optical microscope (**Figure 5.16**), and the wear volume and wear rate were calculated according to the established methodology. The wear rate for each pin was calculated and is presented in **Figure 5.15**. The CI wear rate decreased as the DLC deposition time increased but began to increase after 90 minutes of DLC deposition. The appearance of a dark transfer film is present on all counter-bodies but shows a noticeable darker colour for the 22.5 minutes and 45 minutes of DLC deposition.

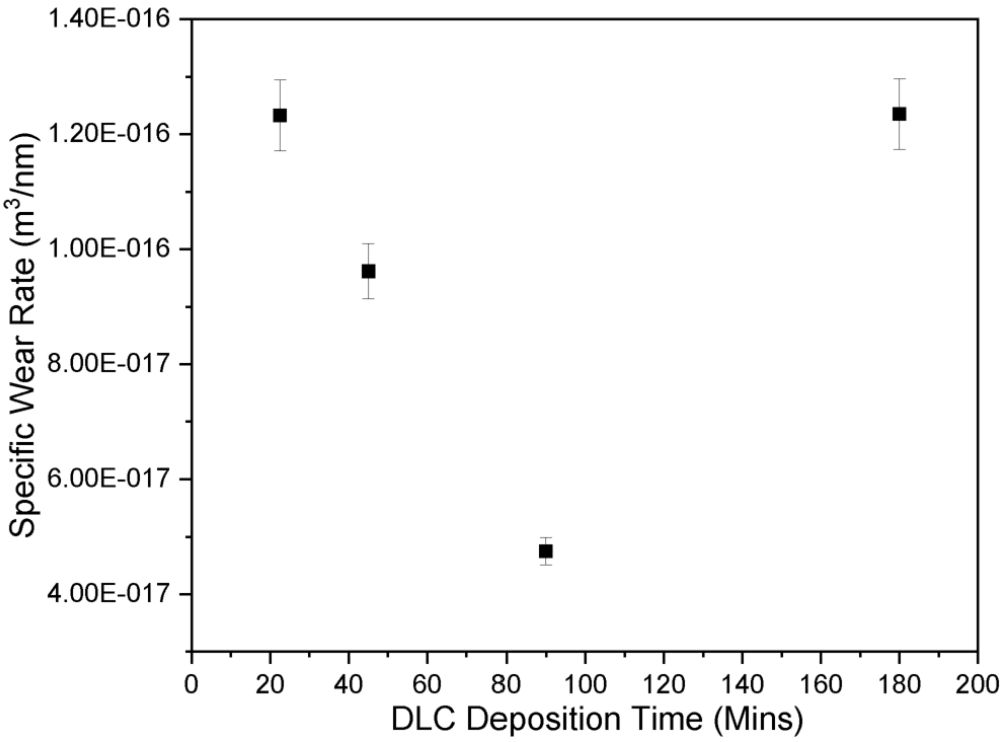

Figure 5.15 *Wear rate for CI pins against DLC-GNP nanocomposite for various DLC thicknesses.*

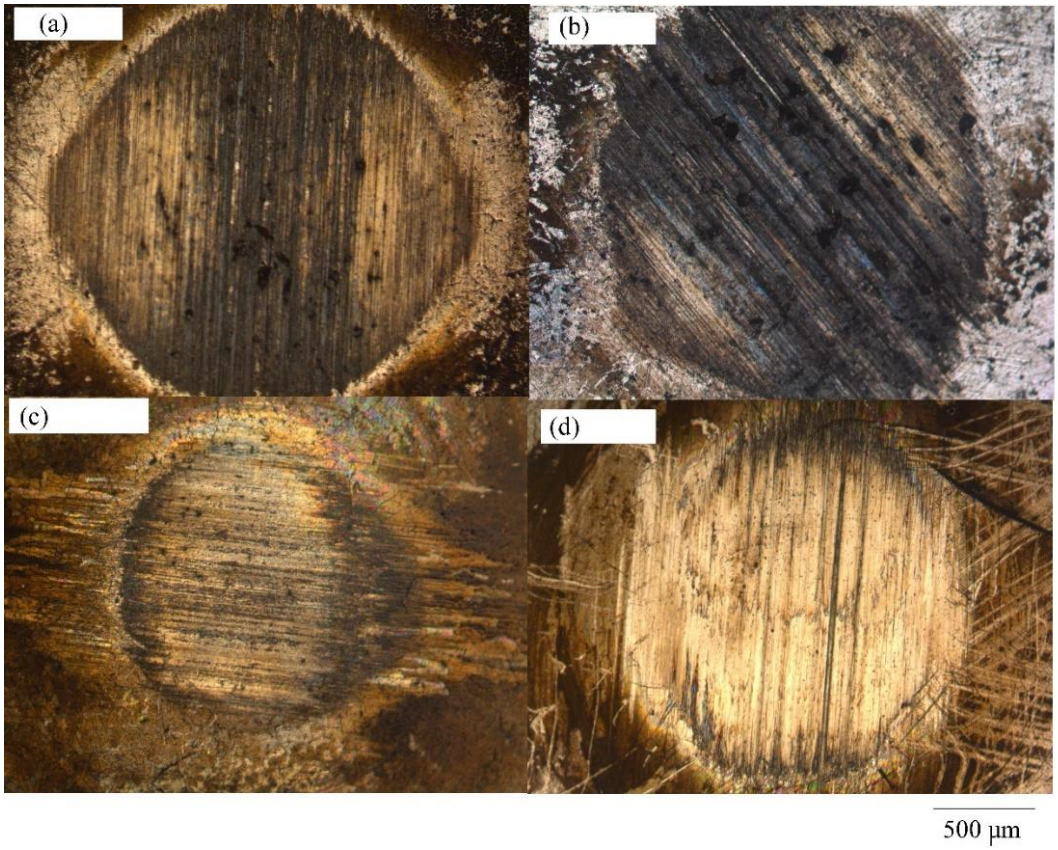

Figure 5.16 *Wear Scar of CI counter-body against DLC deposition times of (a)22.5 mins, (b) 45 mins, (c) 90 mins, and (d) 180 mins.*

5.5. Raman Analysis

The Raman spectra were obtained in the 1000 cm^{-1} to 2000cm^{-1} range for the DLC-GNP samples at different depositions times before and after wear, along with the worn CI counter-body, with the results analysed and described in the methodology section.

5.5.1. As-deposited

The Raman spectra were collected from the DLC-GNP samples at the DLC area and GNP island features. The as-deposited DLC-GNP22.5 film resulted in two distinct Raman spectra (**Figure 5.17)**. These two distinct spectra can be compared to those typically observed from GNP and DLC alone [152,216]. The GNP are either not being covered adequately during the DLC deposition, or the thickness of the DLC is thin enough not to extinguish the Raman signal from the underlying GNP [138].

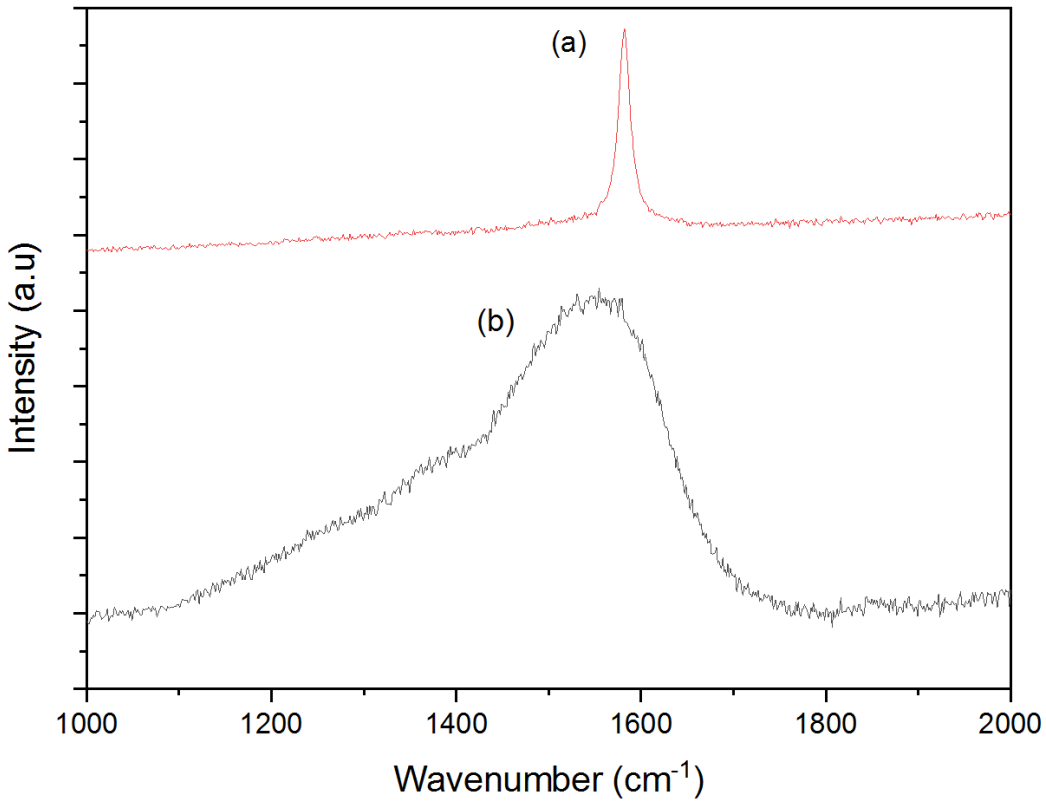

Figure 5.17 *Raman Spectra collected from DLC-GNP22.5 at the GNP islands, with (a) displaying a typical GNP spectrum, and (b) displaying a typical DLC spectra.*

Figure 5.18 provides the Raman spectra taken from the GNP islands after DLC deposition. The D peak for the DLC-GNP22.5 and DLC-GNP45 are around ~1360 cm^{-1}, which is not present in the DLC-GNP90 and DLC-GNP180. The G peak for the DLC-GNP22.5 is a Lorentzian shape, compared to the other samples, similar to that of a purely graphitic sample [216].

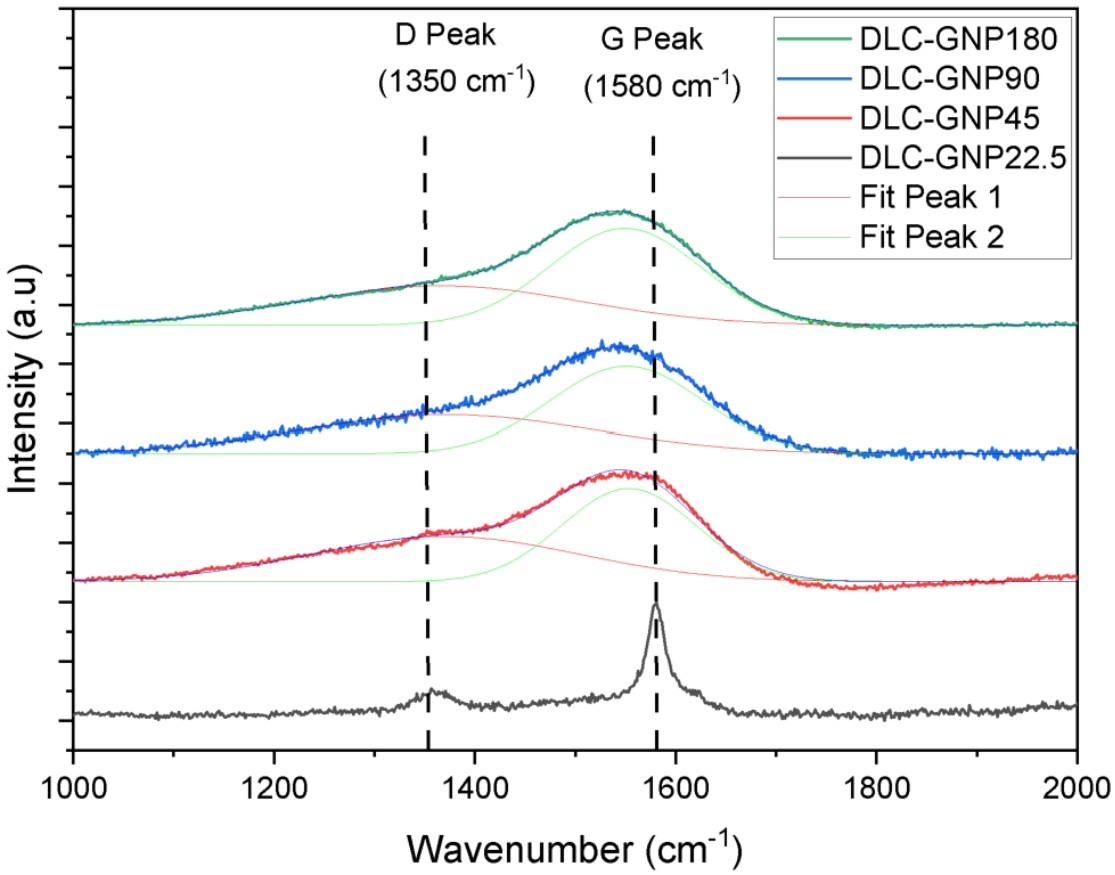

Figure 5.18 *Raman spectra taken from GNP islands after DLC deposition.*

Figure 5.19 provides the Raman spectra for the DLC area as the DLC deposition time increases. The differences between the deposition times do not show the exact peak observations observed in the GNP areas.

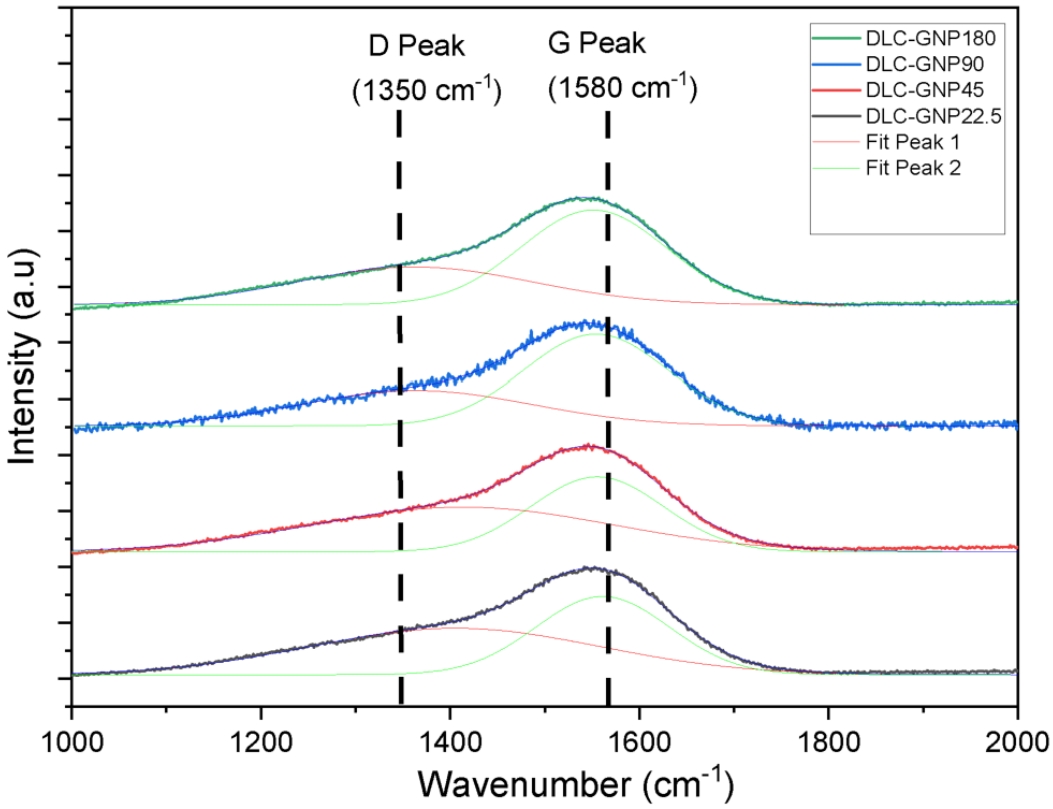

Figure 5.19 *Raman spectra taken from DLC areas after DLC deposition.*

Figure 5.20 to **Figure 5.22** presents the D peak position, G peak position and I_D/I_G ratio as a function of DLC deposition times for both the GNP islands and DLC areas of the DLC-GNP nanocomposite samples. The results demonstrate a decreasing trend in the D peak position as the deposition time increases. The G peak remains relatively constant at these thicknesses.

The observed shift of the D and G peaks towards higher frequencies typically indicates a higher sp^2 content or clustering [152]. However, it is crucial to remember that Raman spectroscopy primarily indicates the degree of amorphization. Several other factors, including clustering, chains of sp^2 sites, bond disorder, and the sp^2/sp^3 ratio, can influence the spectra [26,42,87]. These additional factors contribute to the complexity of interpreting Raman spectroscopy data in DLC-GNP nanocomposites where graphitic GNP islands coexist with amorphous DLC structures. The interpretation of the I_D/I_G ratio can mean different things in terms of the defects in graphite/graphene or sp^2 clusters in

DLC, such that the relative D peak intensity to the G peak could mean that the GNP are simply closer to the surface [217,218]

The D peak position exhibits a notable deviation for the DLC area and GNP islands in the case of the 22.5-minute DLC deposition time. This deviation can be attributed to the extremely thin DLC (~430nm) where the adhesion layer could contribute to the Raman spectra [154]. The Raman spectra at the GNP islands exhibited a noticeable change after 45 minutes of DLC deposition time. This change can be attributed to the improved coverage above GNP islands by DLC or the achievement of a sufficient thickness that eliminates contributions from the GNP. Consequently, the spectra observed at this stage differed from those obtained in previous deposition times (**Figure 5.17(a)**).

The G peak position demonstrates a decreasing trend as the DLC layer thickness increases. This behaviour is attributed to the changing Raman spectra from the GNP islands as the DLC thickness increases. This depth-dependent phenomenon has been previously observed by Scharf *et al.* [154], where the spectra contribution from a Si substrate significantly reduced with increasing DLC thickness. Furthermore, the reduction in the G peak position for the DLC area as the depth increases indicates a lower graphitic content within the region. This suggests that the DLC area has a different structural composition than the GNP islands, with less contributions from graphitic carbons within the G peak.

The high standard deviation for the 22.5- and 45-minute deposition times relates to the coverage above the GNP, which may not have been sufficiently covered by DLC, resulting in large deviations in the collected spectra.

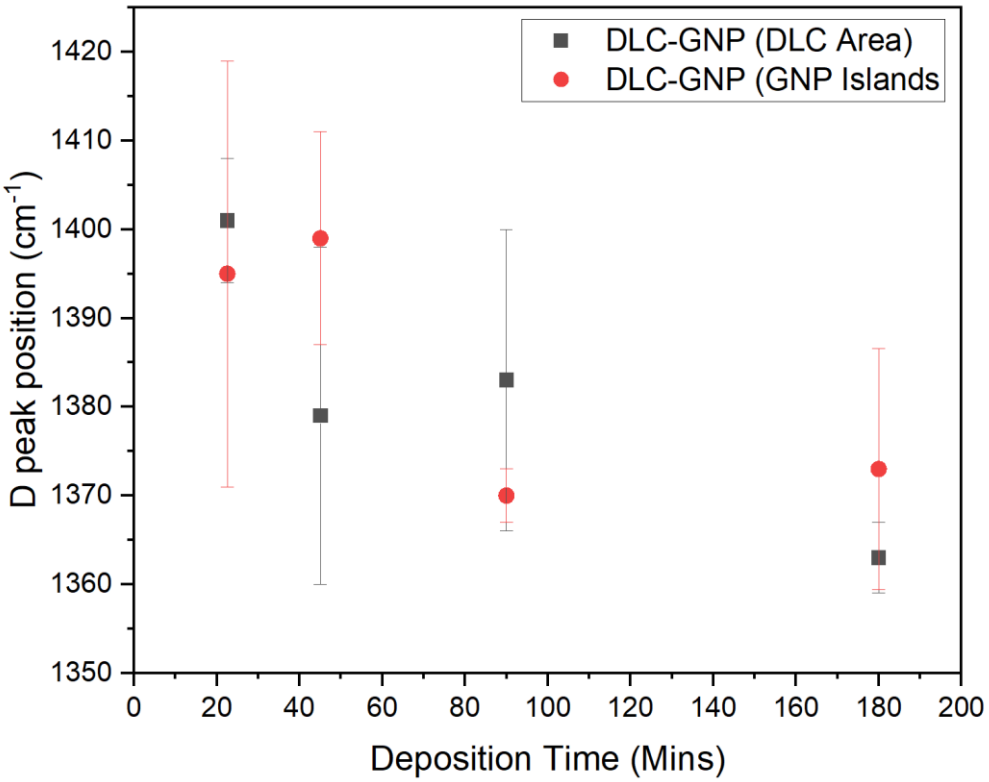

Figure 5.20 *D peak position as a function of deposition time.*

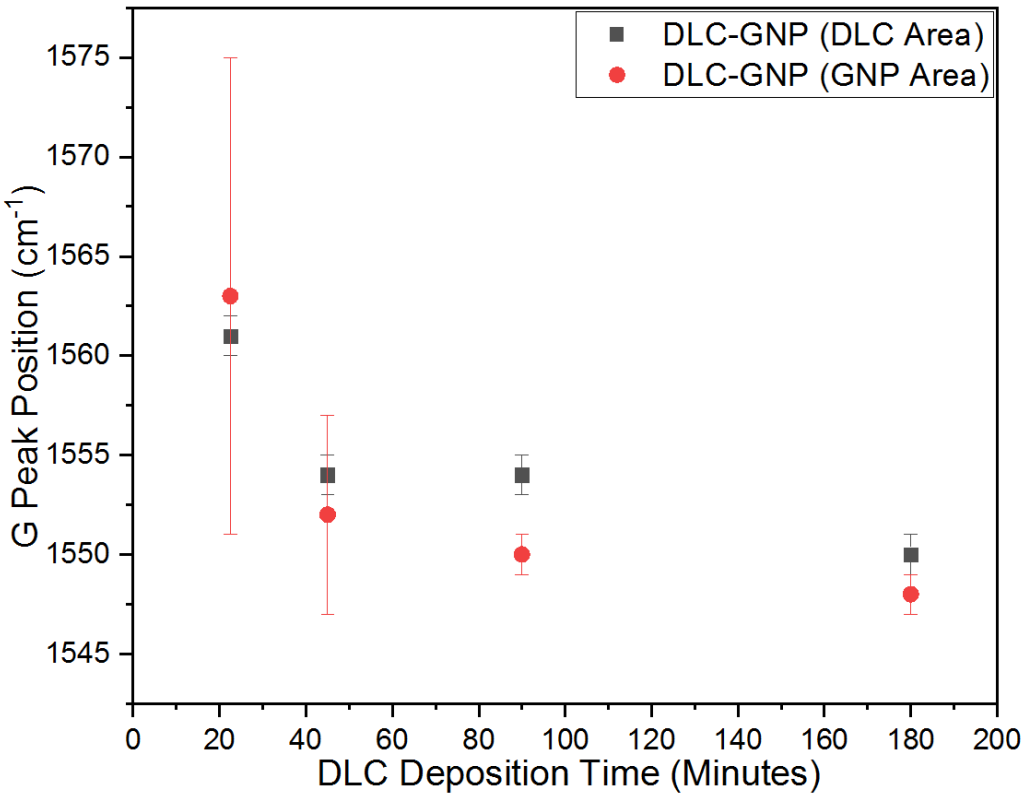

Figure 5.21 *G peak position as a function of deposition time.*

The I_D/I_G ratio, shown in (**Figure 5.22**) as a function of DLC deposition time, exhibits different patterns. For the shortest deposition time (22.5 minutes), the I_D/I_G ratio shows the least precision and the broadest range for the GNP islands. This observation suggests that the DLC may only adequately cover some GNP islands. The smallest I_D/I_G ratio was observed for the 180-minute deposition time. This indicates a higher degree of structural order within the DLC film for this extended deposition period.

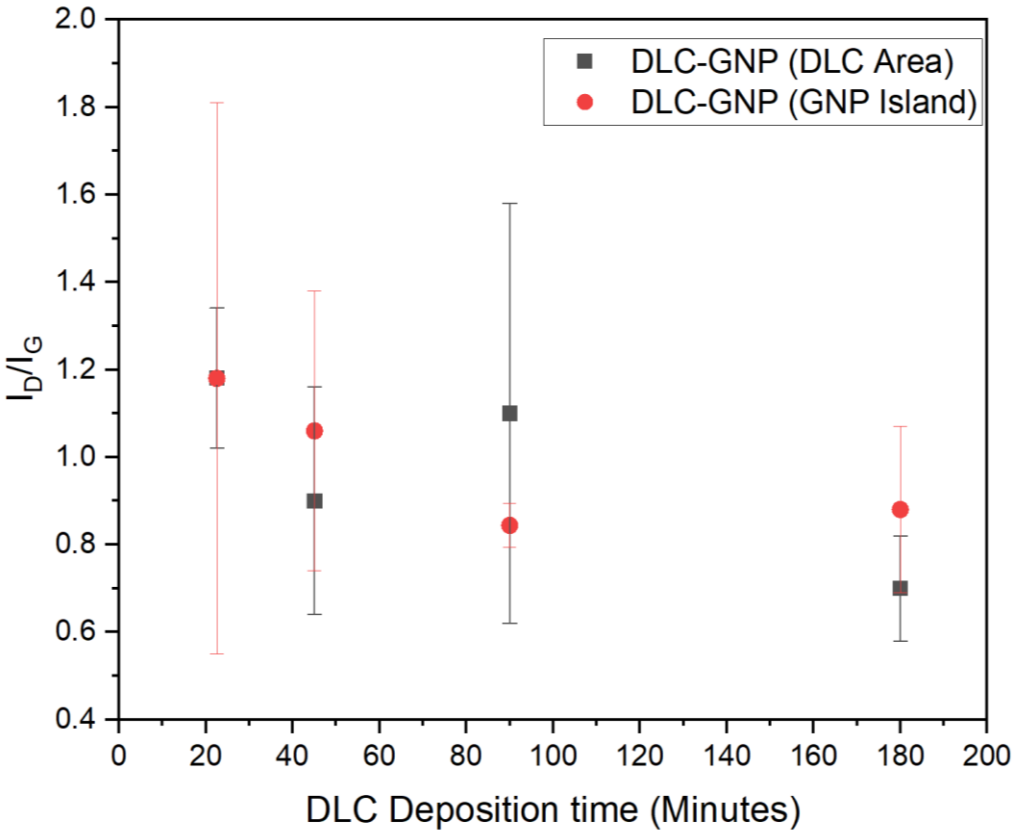

Figure 5.22 *I_D/I_G ratio as a function of DLC Deposition time.*

5.5.2. Post wear

5.5.2.1. DLC-GNP Films

The DLC-GNP films were analysed after 6 hours of tribological wear (as described in the methodology section of this report). The D and G peak positions were deconvoluted with the I_D/I_G ratio calculated. **Figure 5.23** gives the D peak position of the worn DLC-GNP samples as a function of DLC deposition time. The precision of the GNP islands increases

with longer deposition times; this results from DLC above the islands being worn, reducing the contribution of the DLC to the resultant spectra.

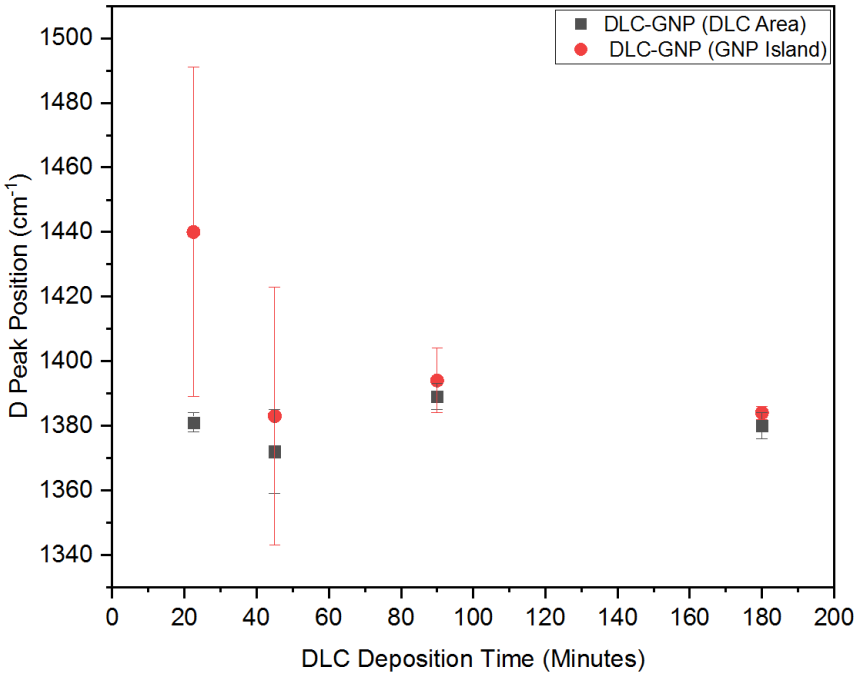

Figure 5.23 *Post wear D peak position of worn DLC-GNP nanocomposites as a function of DLC-deposition time.*

The deposition time of 22.5 minutes for the GNP islands is interesting as a significant number of the GNP were removed during the wear process, allowing only the remaining ones in the wear track analysed, which could influence the results. By only analysing the remaining GNP in the wear track, a similar problem to Walds [219] could be repeated (albeit with GNP and not bullet holes being analysed). When considering the remaining GNP islands for the DLC-GNP22.5 in the wear track, they may have survived due to:

- Better DLC coverage above them
- Orientation to the substrate

As only the remaining GNP are measured, it does not provide information about the ones released. This makes it difficult to determine how the GNP behaved before removal.

The DLC deposition time of 45 minutes they have exhibited low precision for the GNP islands, indicating similar issues with the shorter deposition time. In contrast, the peak positions for the two longest deposition times (90 and 180 minutes) yielded comparable results for the DLC and GNP areas. This similarity could be attributed to a significant thickness of DLC above the GNP islands, which would dominate the spectra.

In **Figure 5.24,** the G peak exhibits a different pattern from the D peak. The precision of the GNP islands was reduced dramatically for the 45-minute deposition. This is due to the increased thickness of the DLC layer above the islands, where some GNP are exposed after the DLC layer wears away.

The 90-minute deposition time produced the highest precision for the DLC and GNP islands. The GNP islands have the highest wavenumber, indicating they are more graphitic. This results in DLC above the GNP being worn away entirely or thin, thus contributing little to the collected G peak position.

The thickest DLC layer showed very little difference between the DLC and GNP islands, possibly due to the wear not being sufficient to reach the GNP islands, with the Raman spectra only being able to penetrate the DLC layer.

The change in I_D/I_G ratio between the as-deposited and worn samples is shown in **Figure 5.25.** The most significant change is observed for DLC-GNP22.5, with a reducing trend in I_D/I_G ratio until it reaches the DLC-GNP90, after which it starts to increase again.

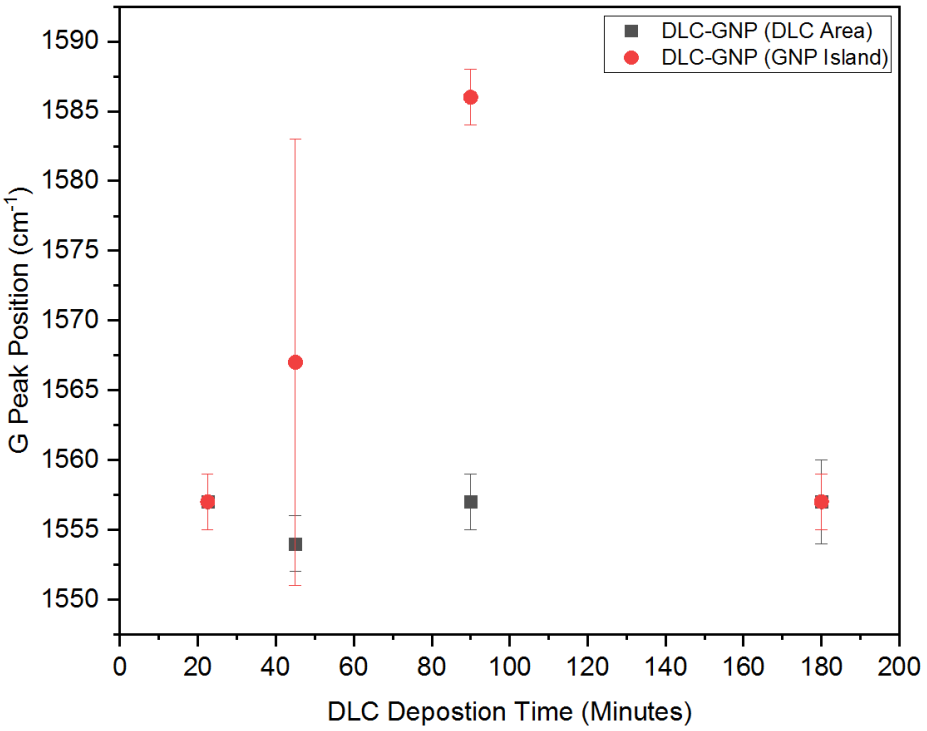

Figure 5.24 *Post wear G peak position of worn DLC-GNP nanocomposites as a function of DLC-deposition time.*

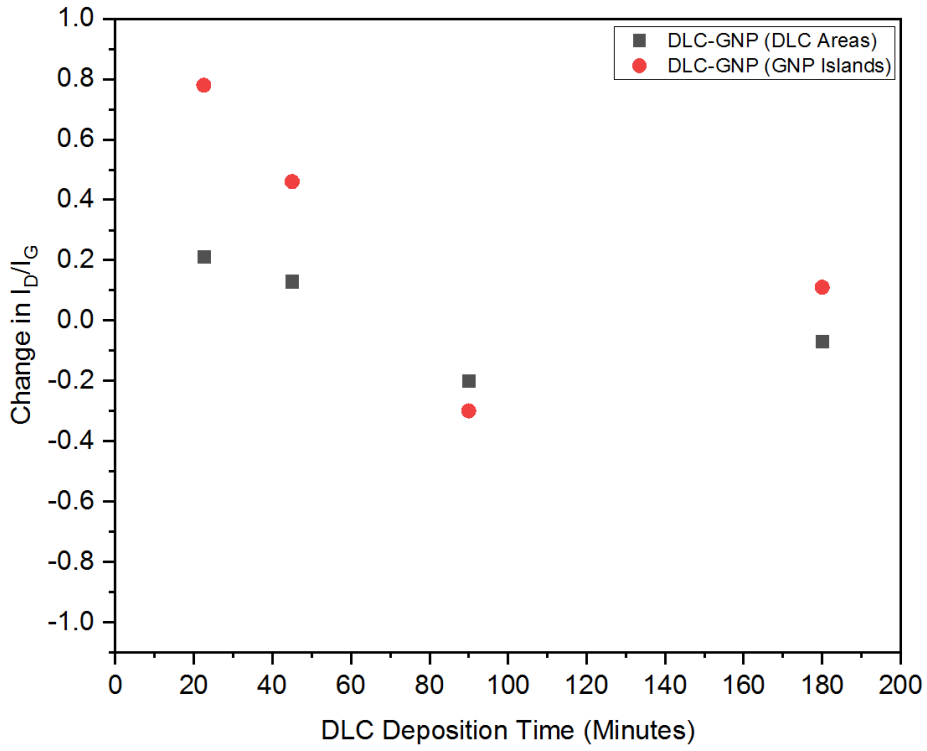

Figure 5.25 *Change I_D/I_G ratio post wear for DLC-GNP nanocomposites as a function of DLC deposition time.*

5.5.2.2. CI Counter-body

The G and D peak position, G peak intensity, and I_D/I_G ratio were obtained from the Raman spectra of worn CI pins (**Figure 5.26** to **Figure 5.28,** respectively).

The D peak position does not change dramatically as the DLC thickness increases. The G peak position decreases slightly with deposition time, with the DLC-GNP180 having the lowest value.

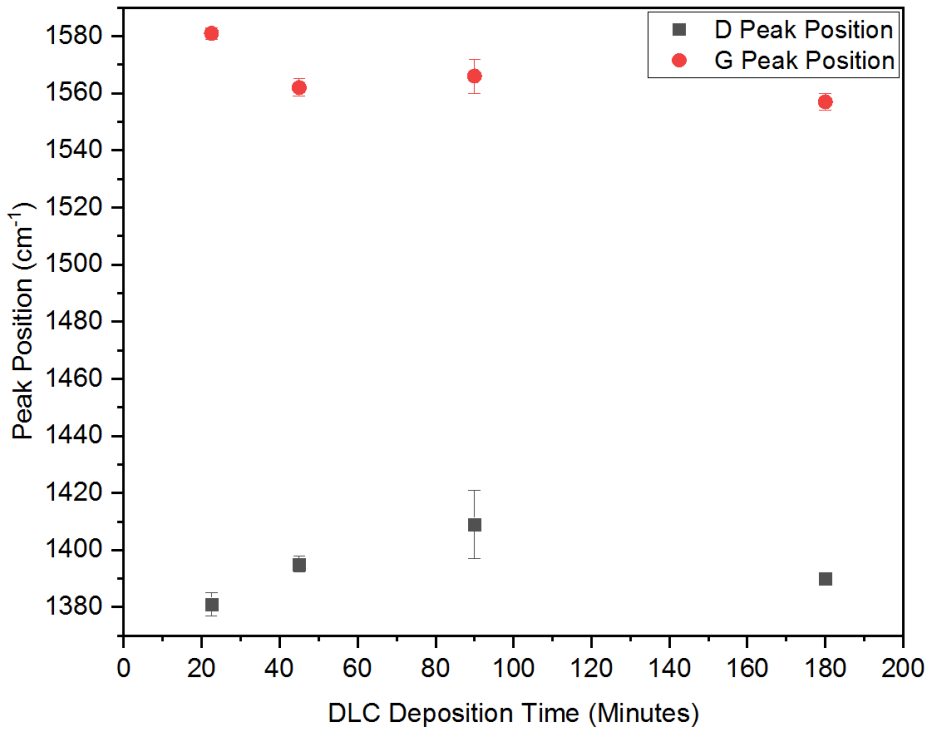

Figure 5.26 *D and G peak position for worn CI pins.*

The results from the I_D/I_G ratio (**Figure 5.28)** provide wide variations. However, the 180-minute deposition time provides a more minor deviation than the other tested samples.

The G peak intensity (**Figure 5.27**) provides a higher reading for the 22.5 minutes DLC deposition, which decreases as the deposition time increases. This relationship does not continue above 90 minutes and then begins to increase. The G peak intensity has been previously [220] linked to wear rate and transfer film thickness, which is also present when comparing the wear rate provided by **Figure 5.13**.

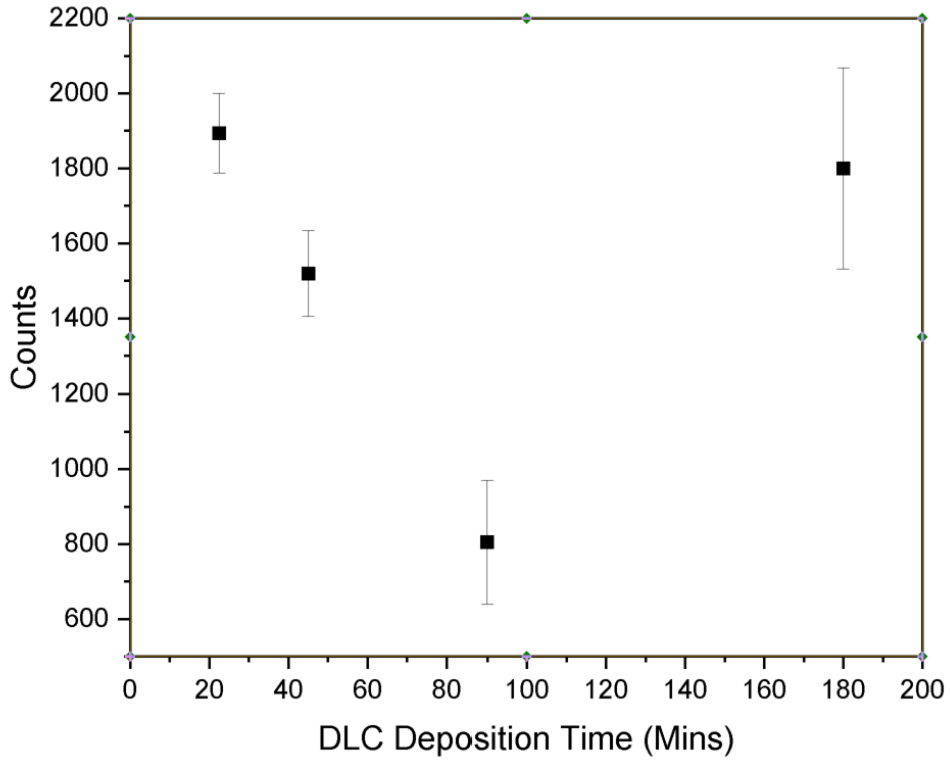

Figure 5.27 *G Peak Intensity CI Counter-body.*

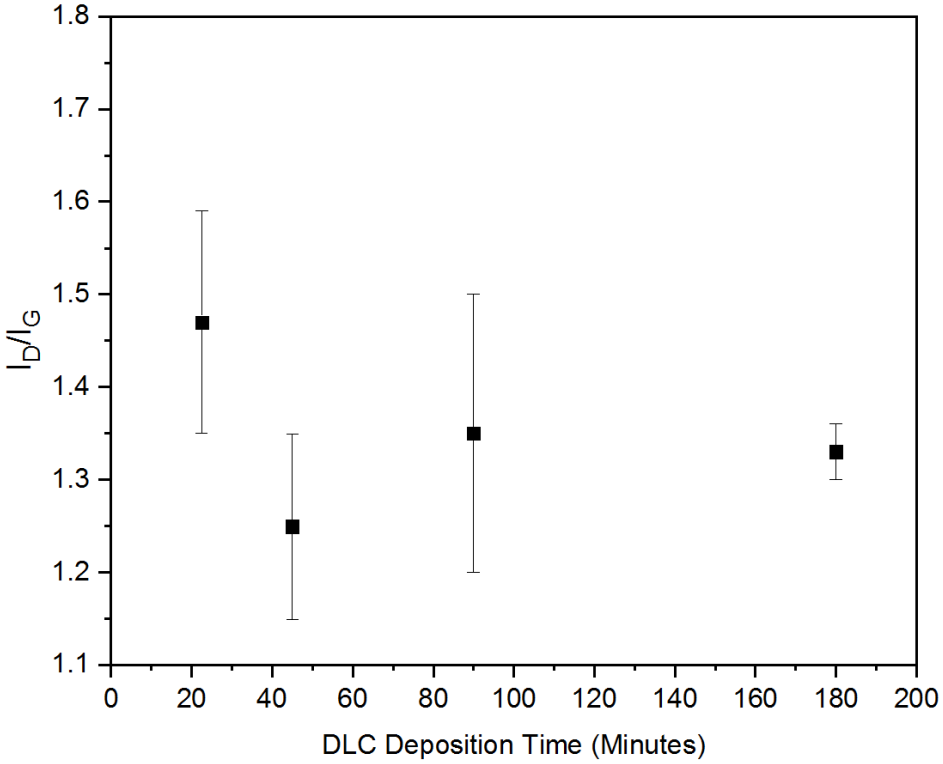

Figure 5.28 I_D/I_G ratio for worn CI Pins

5.6. Summary of the Effect of DLC Thickness on the Tribological Properties of DLC-GNP Nanocomposites

This study phase investigated DLC-GNP nanocomposites' friction and wear characteristics with different thicknesses under base-oil lubrication. The main findings can be summarized as follows:

- The DLC layer thickness above the deposited GNP significantly impacts the tribological properties of DLC-GNP films. If the layer is too thin, GNP is removed, and if the layer is too thick, it will require more wear to provide a benefit.
- The mechanical properties of the DLC-GNP nanocomposites displayed an increase in elastic modulus as the DLC thickness increased.
- The CI pins all showed the presence of a carbon film. A trend between the G peak intensity and wear rate can be eluded.

Chapter 6 - The Effect of Sliding Distance on the Tribological Properties of Single Layer DLC-GNP nanocomposites

6.1. Introduction

Following the initial series of experiments, it was observed that an optimal GNP surface coverage and DLC thickness exist to achieve the lowest friction and wear response. While the frictional response decreased with increasing sliding distance, as commonly observed in DLC coatings, the wear response over time for DLC-GNP nanocomposites has not been previously investigated.

This chapter examines the tribological response of a DLC-GNP coating over time. A comparative analysis will include the pure DLC coating and an FFO (tested against DLC-GNP1). The study aims to explore the mechanisms that govern the tribological properties of the DLC-GNP coating and how these mechanisms evolve with increasing sliding distance.

The FFO was used to investigate if the additives were a dominant friction mechanism for the surface tribochemistry and compare wear results over a 30 hour testing period.

In this chapter, the best performing DLC-GNP coating (1 mg/ml, 90 minutes deposition time) identified in previous chapters will undergo tribological testing for the maximum sliding time (30 hours) achievable with the Biceri tribometer. This study aims to investigate and analyse changes occurring on both the counter-body and DLC-GNP surface at different time intervals. These changes will be compared to those observed in a pure DLC sample with equivalent thickness.

6.2. Methodology

The wear testing in this chapter will be conducted under the same configuration and temperature conditions described in the methodology section. The sliding time for this series of experiments will span from 0.5 hours to 30 hours, resulting in a final sliding distance of 2160 m. This allows for gradual wear progression, enabling a thorough evaluation of the underlying mechanisms. It should be noted that this sliding distance is limited by the maximum duration provided by the equipment. It is important to avoid accelerated tribometer tests (such as faster sliding distances or increased loads) as they may alter the contact mechanics [66,221]. By remaining with the conditions (Section 3.4.2), comparisons with existing literature [17,222] and chapters can be made.

The GNP/NMP concentration used was 1 mg/ml, with a 90-minute deposition time using the same method as DLC-GNP1 in **Chapter 4.**

The wear of the counter-body is as previously explained in the methodology (**Section 3.3.3**). The changes to the graphitic layer on the sample surface and counter-body are explored using Raman microscopy, with TEM and EELS used to explore the chemical composition.

An FFO was used to provide a comparative friction and wear result for the pure DLC and DLC-GNP coating over extended tribological testing (30 hours). The test provides evidence to determine if the tribochemistry for the FFO is the dominating factor for friction compared to the GNP with the nanocomposite.

6.3. Friction Results

Figure 6.1 presents representative friction traces of DLC-GNP1 (in base-oil and FFO) and pure DLC (in base-oil) as a function of time. When tested against base-oil, both samples exhibited an initial increase in friction, a typical behaviour observed in DLC

coatings, before reaching a steady-state friction level [170,223]. DLC-GNP1 in base-oil maintained a consistent low and steady COF throughout the entire 30-hour. Over time, the pure DLC coating displayed a decreasing trend in friction, but it also exhibited more significant fluctuations compared to DLC-GNP1. The pure DLC coating also demonstrated a higher average COF than DLC-GNP1 (**Figure 6.*2***).

When DLC-GNP1 was tested with FFO oil, a steady frictional response was observed. This response was higher than pure DLC or DLC-GNP1 in the base-oil, providing a benchmark for tests conducted under similar conditions [17,170].

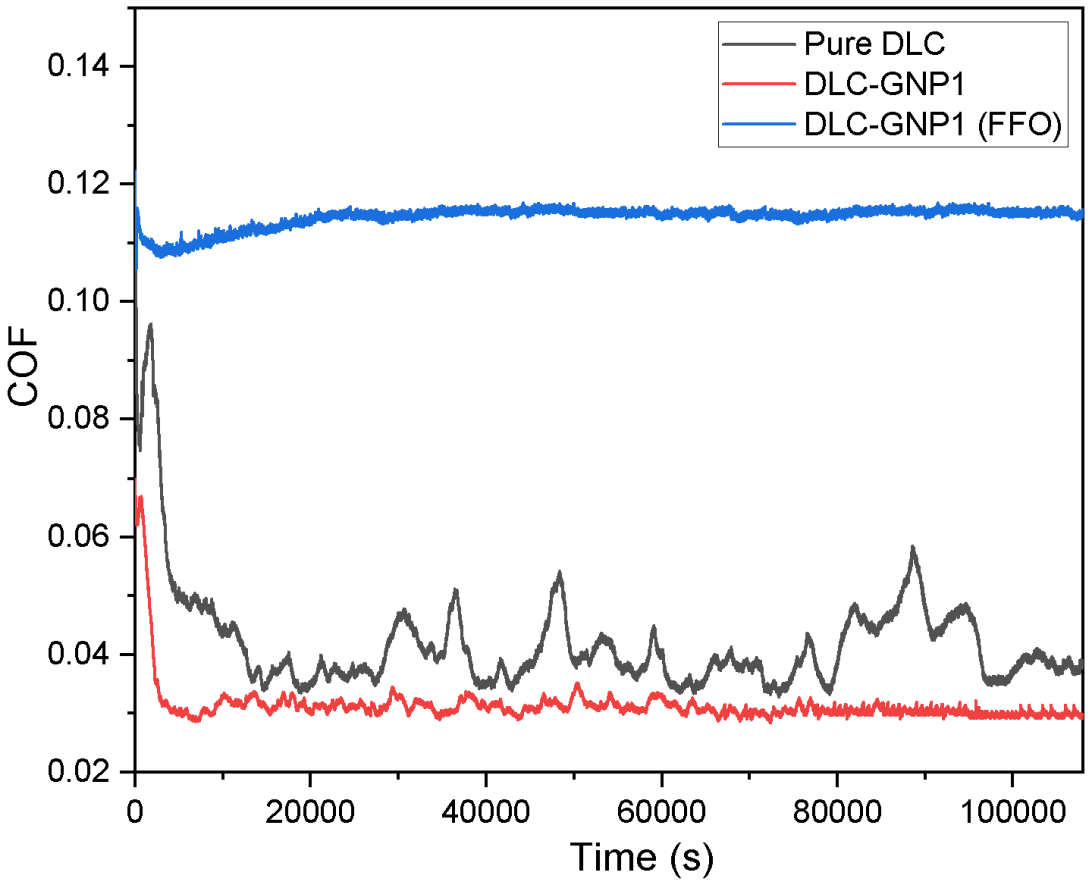

Figure 6.1 *Friction as a function of time for pure DLC and DLC-GNP1 for 30 hours of wear against a CI counter-body.*

Figure 6.2 presents the average friction values for the entire 30-hour testing period and separate segments for the first three hours and the final 27 hours. During the initial three

hours, the wear-in process initiates, and beyond this timeframe, the DLC-GNP1 coating demonstrates a low and stable steady-state friction response.

The DLC-GNP1 coating exhibited a lower mean coefficient of friction (COF) by approximately 30% throughout the entire 30-hour testing period, indicating that the steady-state friction was achieved more rapidly than the pure DLC. This difference between the samples is consistent during the initial three hours, reflecting a similar trend observed in the overall 30-hour mean. The final 27 hours of testing show a reduction in friction compared to the first 3 hours as low steady-state friction is achieved. The steady-state friction is expected in DLC coatings as sliding distance increases [124].

During the initial three hours, the DLC-GNP1 coating demonstrated a mean average coefficient of friction (COF) of approximately 0.05, while the pure DLC achieved a COF of around 0.07. This suggests a notable reduction in energy loss for the DLC-GNP1 during this timeframe. In the last 27 hours of testing for both samples, a smaller standard deviation was observed, indicating the attainment of steady-state friction. The DLC-GNP1 exhibited a COF of approximately 0.03, whereas the pure DLC had a COF of around 0.04. These results provide further evidence of the energy savings achieved by the DLC-GNP1 coating during the final 27-hour testing period.

The FFO provided a much higher COF for the entire 30 hours of testing and remained at that level for the first 3 hours and the final 27 hours. The higher friction would result in a

more significant energy loss in the system than DLC-GNP1 or pure DLC in base-oil. The COF (~0.11) of the FFO is in line with published results [224].

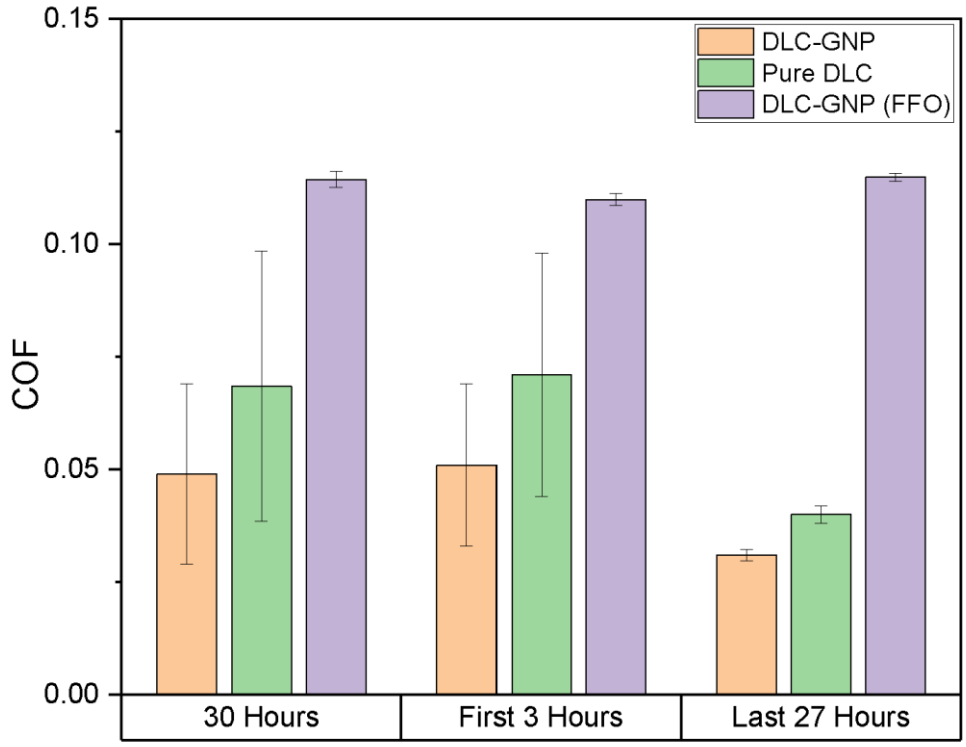

Figure 6.2 *Mean average COF for pure DLC and DLC-GNP1 (n=3)*

The wear scar images (**Figure 6.3**) revealed increased GNP coverage as the sliding distance increased. As the sliding time extended, the GNP seemed to smear from their original islands, leading to an enhanced coverage of GNP on the surface. The increase in coverage has been previously observed for graphene quantum dots (GQD) on a steel surface in glycerol and is considered a mechanism for friction reduction to create a low shear tribo-film [225].

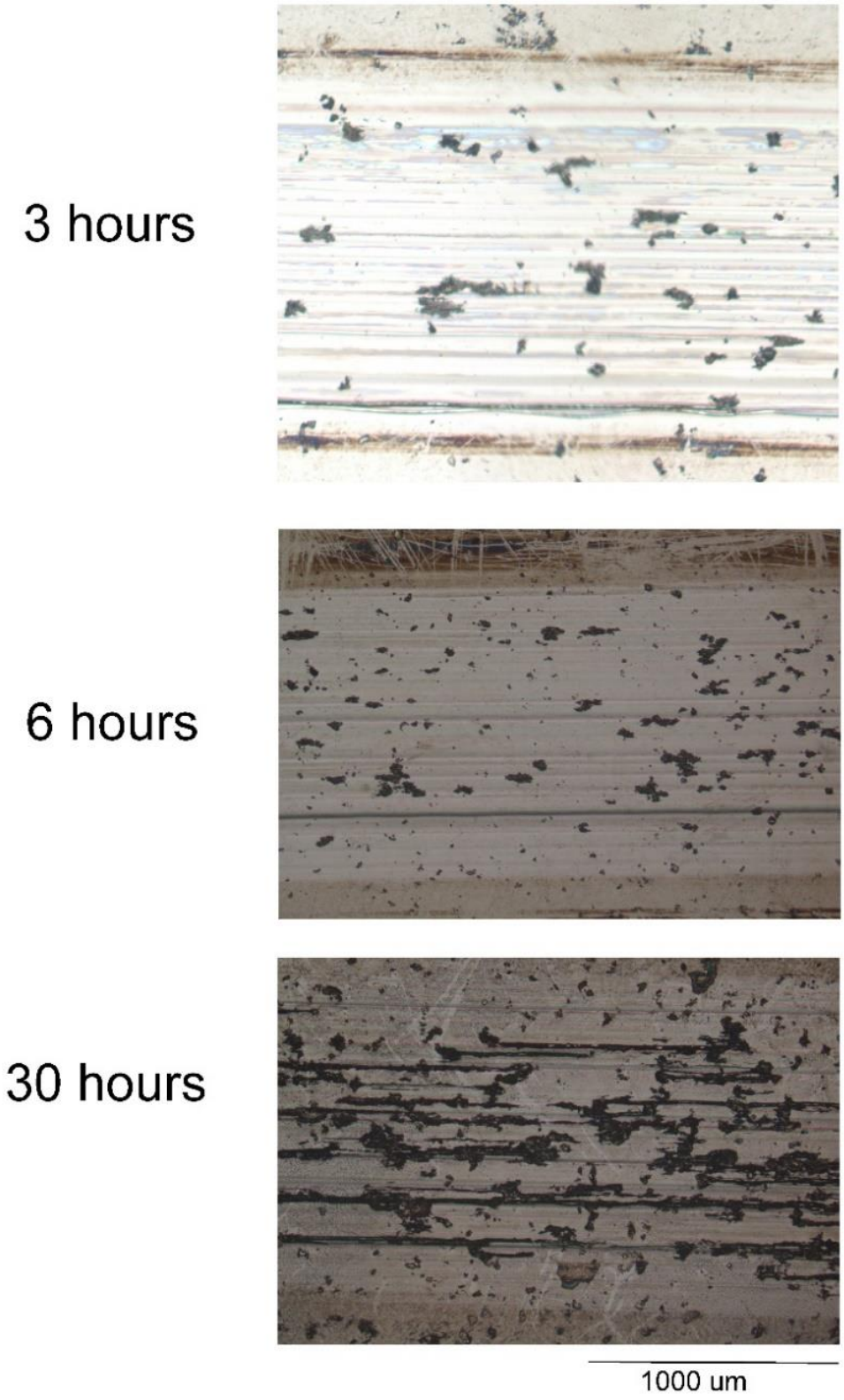

Figure 6.3 *Optical image of DLC-GNP (base-oil) at 3 hours, 6 hours, and 30 hours sliding time.*

6.4. Wear Results

This study collected wear measurements for pure DLC and DLC-GNP1 coatings (and CI) in a base-oil at selected time intervals ranging from 0.5 to 30 hours. The wear measurements were obtained using WLI to analyse the samples and an optical microscope to examine the CI. These techniques allowed for precise measurement and visualisation of wear characteristics at different time points throughout the testing duration.

6.4.1. DLC-GNP Film

The wear rate for the DLC-GNP1 and pure DLC is provided in **Figure 6.4**. Previous studies by Liu *et al.* [66] showed that the wear rate would decrease with increased sliding distance due to the formation of a protective transfer film. In this study, both the DLC and DLC-GN1 coating were produced simultaneously, so the only difference in the composition is the presence of the GNP.

The DLC-GNP1 nanocomposite exhibited a high initial wear rate, decreasing faster than the pure DLC. This initial high wear observed in the DLC-GNP1 can be attributed to the increased surface roughness of the sample, particularly in contact with the softer counter-body, as observed in previous studies [226]. It was reported [226] that the wear rate increased rapidly above a R_a value of 0.93 µm due to chips and flaking from the asperities rather than the adhesive wear typically observed in DLC films. The DLC-GNP films have high asperities compared to pure DLC, as shown in the Ra values in **Figure 4.6**.

The wear rate after 6 hours for the DLC-GNP1 composite remains at a low steady state, whereas the pure DLC exhibits a slight increase as sliding time continues.

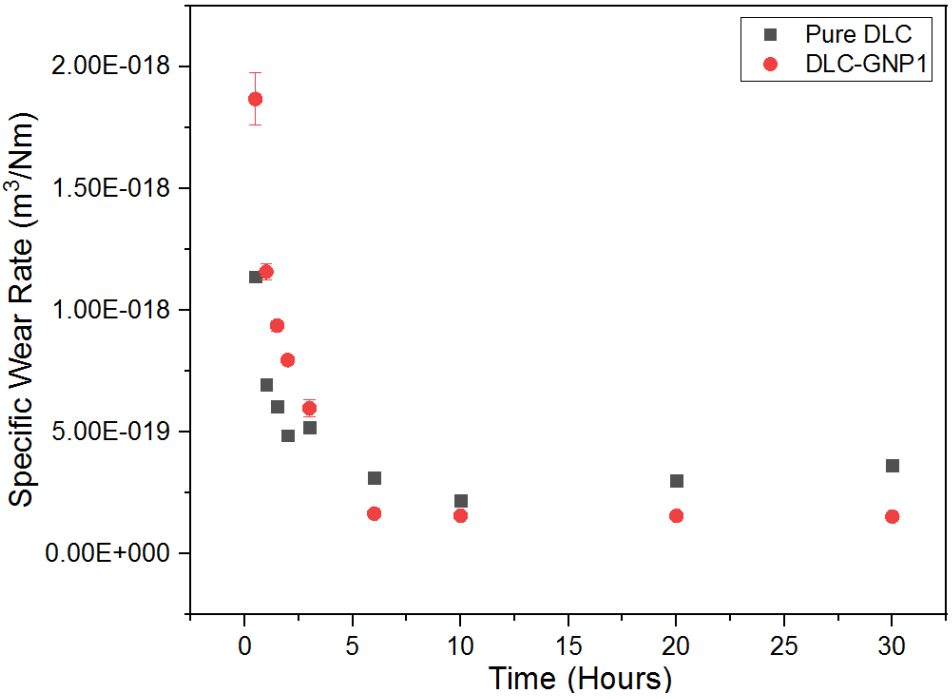

Figure 6.4 Wear rate of pure DLC and DLC-GNP1 (base-oil) as a function of time.

Figure 6.5. presents a comparison of the wear rates after 30 hours for DLC-GNP1 (in base-oil and FFO) and pure DLC. The wear of the DLC-GNP1 coating in FFO is significantly higher than that of the other samples tested in a base-oil. This observation aligns with previous works [17]. It was shown that in hydrogenated DLC tested in FFO, an acceleration of wear occurs.

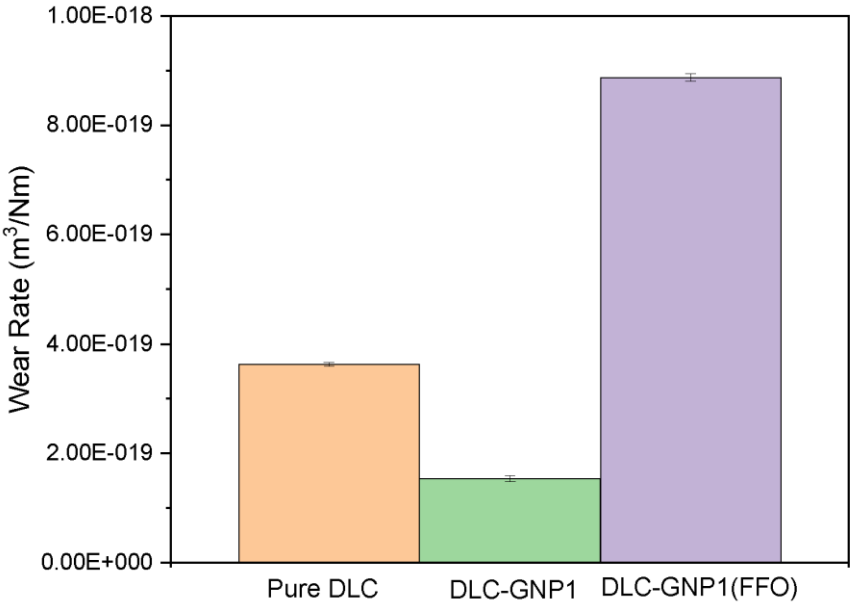

Figure 6.5 *Wear Rate of DLC-GNP films after 30 hours.*

6.4.2. CI Counter-body

Figure 6.6 provides the specific wear rate of the CI against pure DLC (base-oil) and DLC-GNP1 (base-oil only). The initial wear (0.5 – 3 hours) for the CI against the DLC-GNP1 is higher than shown for pure DLC. As the time progresses (≥6 hours), the wear rate reverses, with the CI exhibiting a greater wear rate against the pure DLC than DLC-GNP1. The wear rates provided in literature for similar conditions for cast iron pins are in the 10^{-17} m^3/ Nm [17].

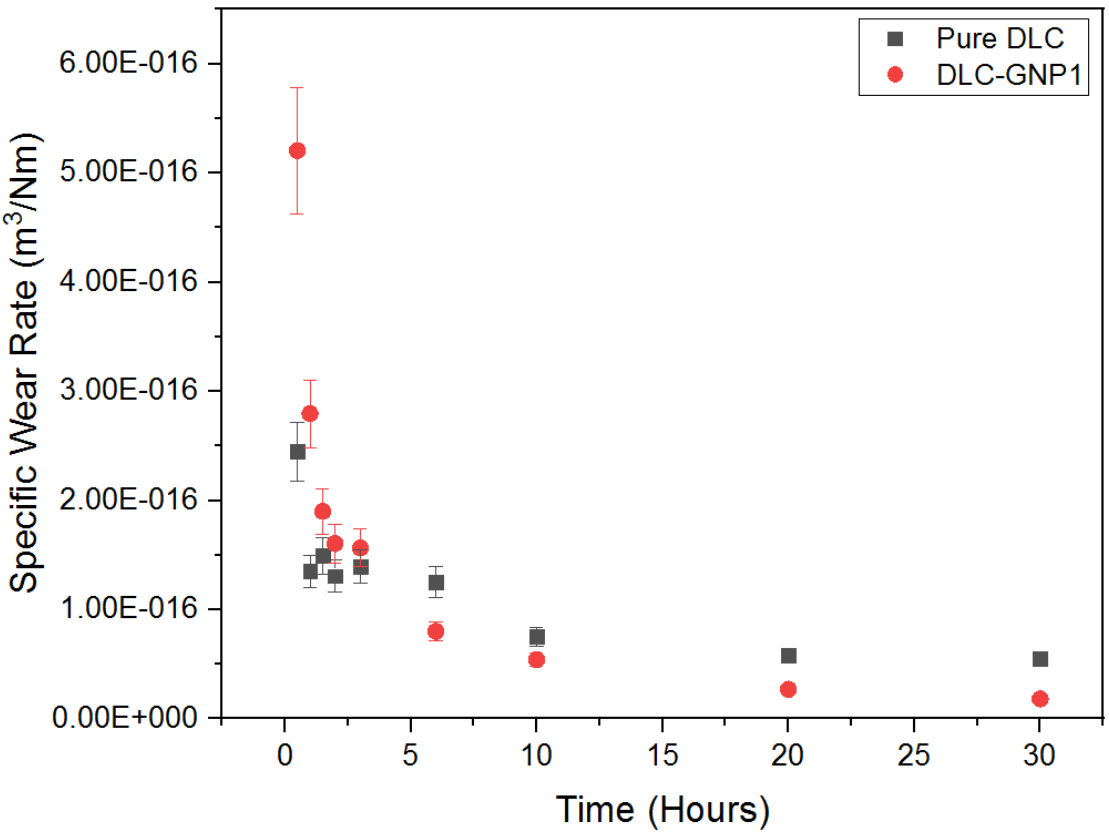

Figure 6.6 *Specific wear rate of CI pins as a function of time (0.5 hr – 30 hr)*

6.5.Raman Analysis

The Raman spectra for both DLC-GNP1 and pure DLC films and their corresponding CI pins (in base-oil) were acquired before and after wear, following the methodology (**Section 3.3.6**). The I_D/I_G ratio and G peak positions were calculated for all samples to

assess the relative graphitisation as a function of time. The Raman analysis was only completed for the samples in base-oil as the mechanism for low friction between the sample and counter is only of interest in this study.

6.5.1. DLC-GNP Film

The G peak position is commonly used to determine the graphitisation of carbon structures [227,228]. **Figure 6.7** provides the G peak position for the DLC-GNP and pure DLC as a function of time (0.5 hours to 30 hours). For the DLC-GNP1, the features of GNP islands and DLC are scanned separately.

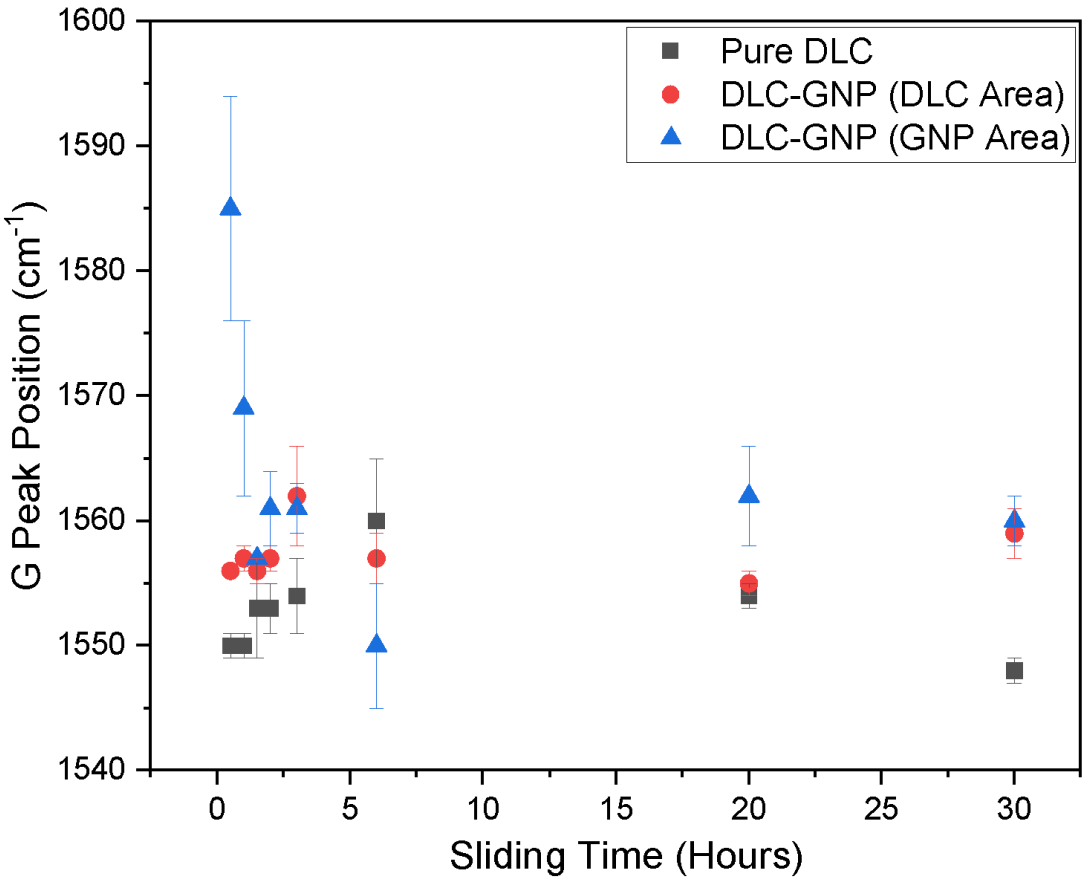

Figure 6.7 *G Peak position as a function of sliding time (0.5 hour – 30 hours)*

For the DLC-GNP film, the DLC area displays an initial decrease in wavenumber as the sliding time increases before stabilising at ~1560 cm^{-1} for the remainder of the test. A decrease in peak position would indicate that the DLC is moving to a lower graphitic content [228]. The GNP areas display an increase in G peak position, which decreases

and stabilises after 3 hours. The DLC is being removed from above GNP islands, and an increase in peak position would be expected. This would indicate that the sp^2 content for the GNP islands remains relatively steady throughout the testing.

The pure DLC sample shows a small initial increases in wavenumber where it then becomes steady at ~1550-1555 cm^{-1}. The rapid decrease in friction, shown in **Figure 6.1**, coincides with a change in G peak position, which decreases rapidly up to 6 hours, remaining relatively steady for the remainder of the test.

Figure 6.8 shows the I_D/I_G ratio of the DLC-GNP and pure DLC samples as a function of time. In DLC-GNP1, the I_D/I_G ratio for the GNP islands provides a significant deviation with a high ratio, decreasing rapidly as time increases. A large D peak would be generated from the vibrational mode, likely originating from the DLC above the GNP islands in comparison to the contributions from the G peak, which remain relatively constant. As DLC is removed (as sliding distance increases), a reduction in the D peak component is evident as the GNP, are then closer to the surface. The GNP due to the nature of the bonding, will not have active aromatic rings and thus will present as a lower I_D/I_G ratio.

Pure DLC has an I_D/I_G ratio that increases slightly as the sliding distance increases, which could result from little graphitisation or any graphitisation being removed as a wear particle [73].

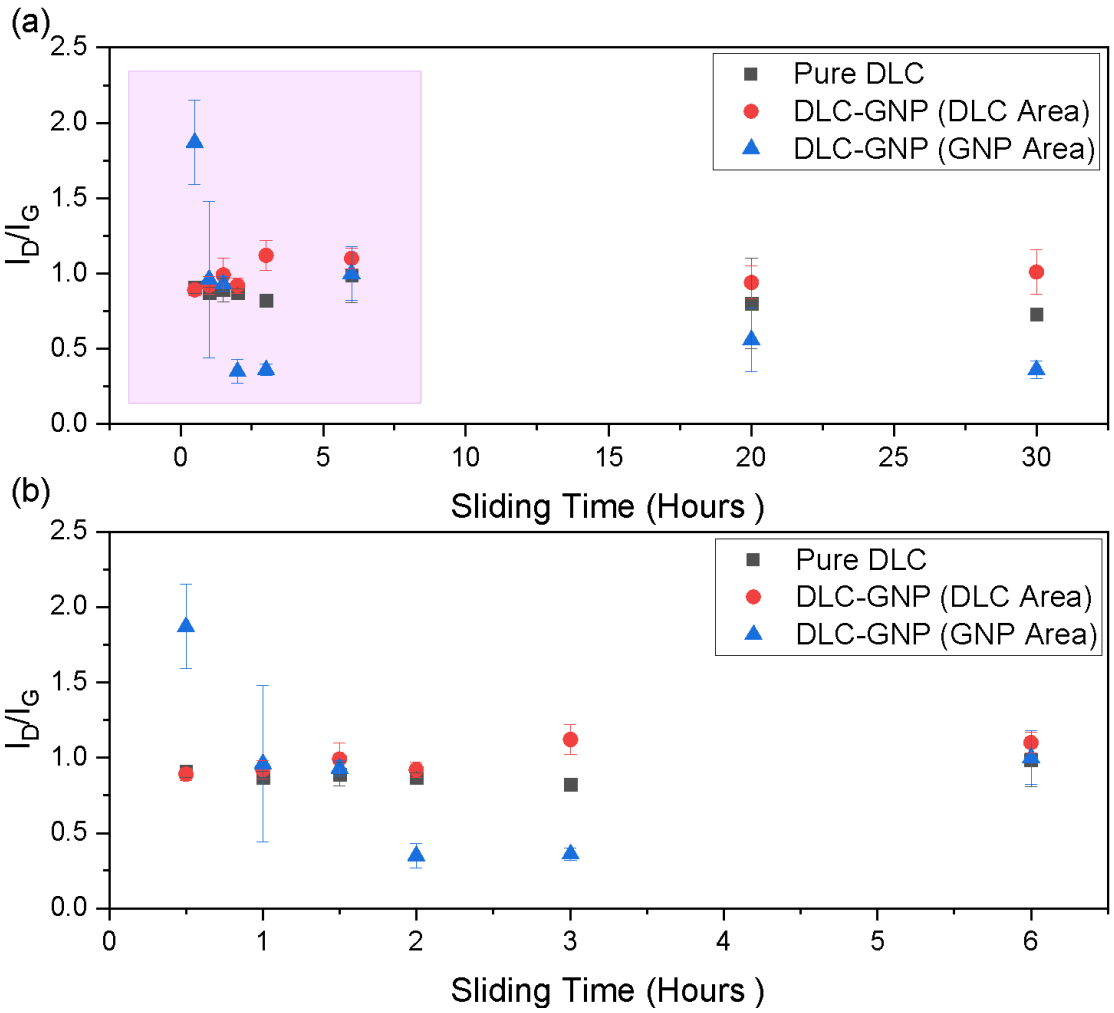

Figure 6.8 *Post wear I_D/I_G ratio for pure DLC and DLC-GNP nanocomposite. (a) provides the time period 0.5 – 30 hours, and (b) provides the 0.5 – 6.5 hours highlighted in the pink box.*

6.5.2. CI Counter-body

Raman spectra of the CI (base-oil) were taken at selected periods which were then analysed (as per **Section 3.3.6**) to determine D and G peak position, G peak intensity and I_D/I_G ratio. **Figure 6.9** displays the optical images capturing the wear scar on the CI pin.

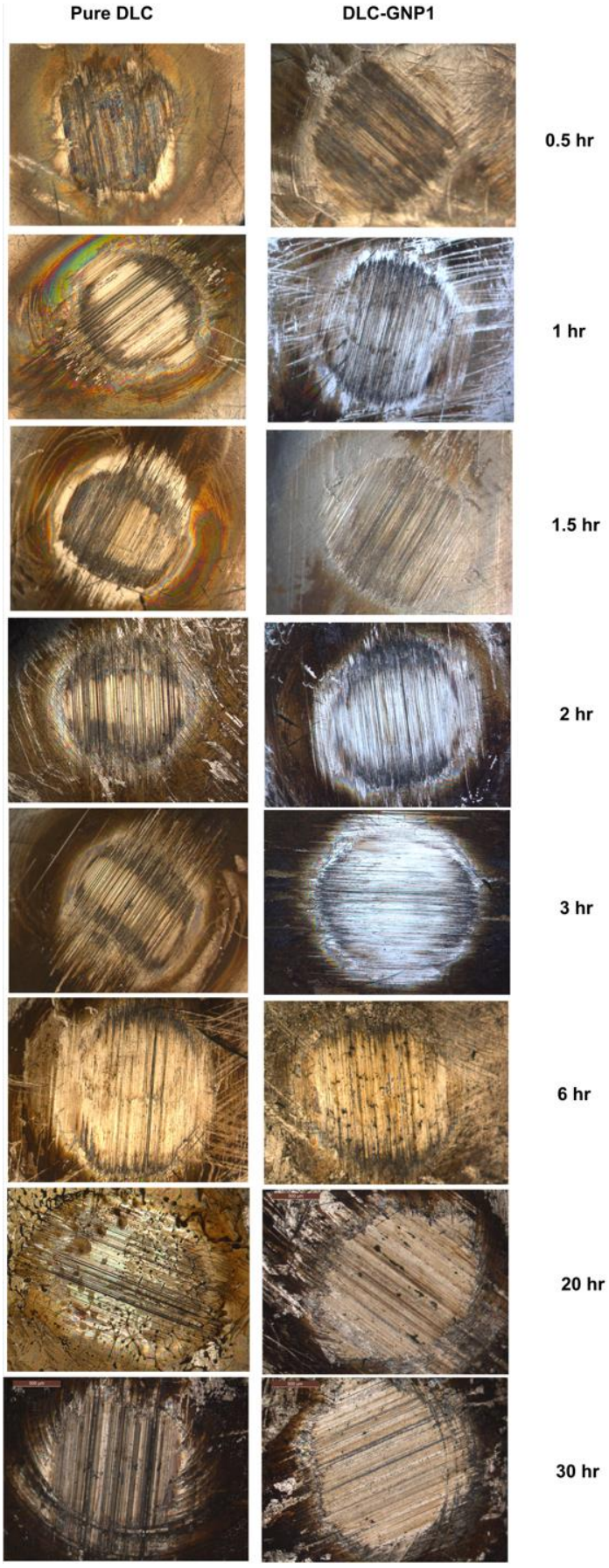

Figure 6.9 *Optical images of worn CI pins as a function of sliding time(base-oil).*

It can be observed that a formation of a darker transfer film occurs. This occurs from the generation of worn particles from the surface of the coatings. The striations in pure DLC CI pins appear rougher than the DLC-GNP, providing some evidence of the origins of deep groves seen in the SEM images (**Figure 4.29**) and line scans (**Figure 4.30**).

Figure 6.10 provides the D peak position for the CI pins as a function of sliding time. The D peak position for DLC-GNP displays an increase of up to 6 hours before it begins to steady with a high standard deviation. The pure DLC provides no describable pattern.

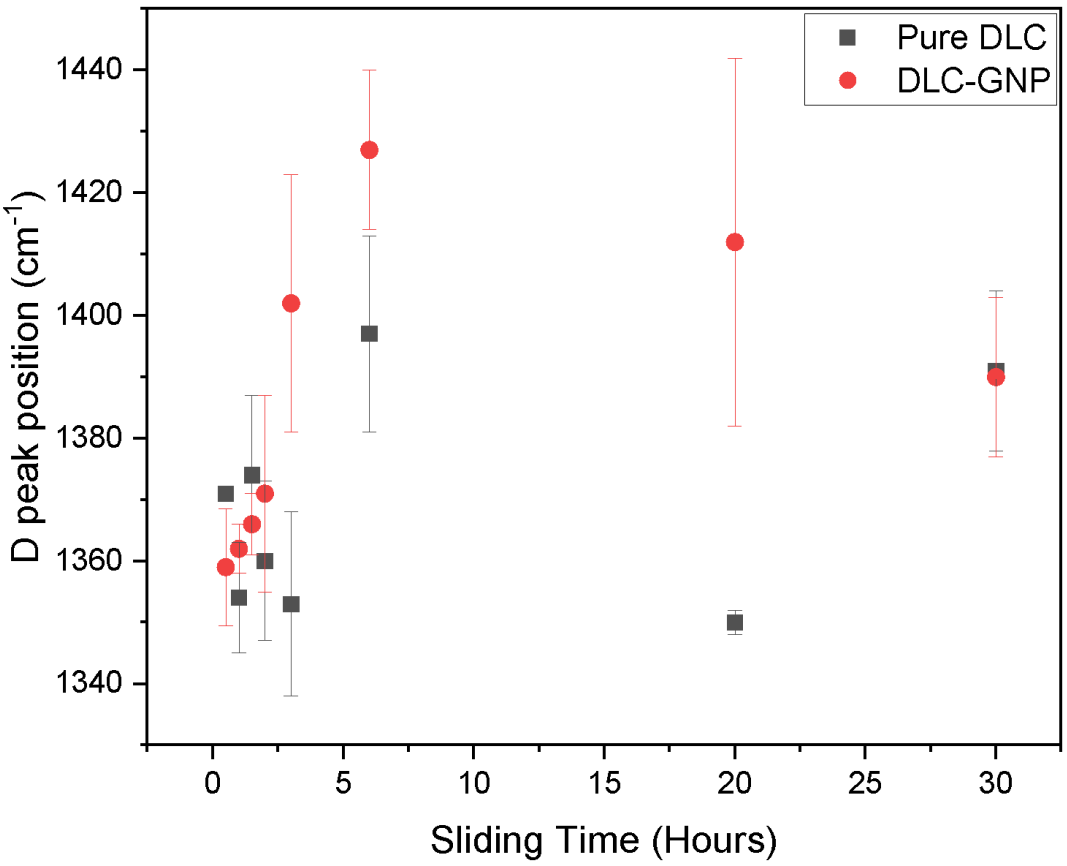

Figure 6.10 *D peak position for CI counter-body against pure DLC and DLC-GNP nanocomposite.*

Figure 6.11 provides the G peak position as a function of time. The change in G peak position is often used to determine if there is a transformation from sp^3 to sp^2 bonding during the wear process [229,230]. For the first 6 hours of sliding, both samples provide

opposing trends. The pure DLC G peak decreases in wavenumber, and the DLC-GNP increases.

At 6 hours of tribo-test, many of the points are overlapping. Comparisons to the raw friction curves (**Figure 6.1**) could explain the reduction in friction for the pure DLC as sliding time increases, with the formation of a steady graphitic transfer film. The formation of the graphitic film is beneficial to creating a low shear surface but increases the wear through graphitisation; as the graphitisation decreases, the wear rate would, in theory, decrease [73].

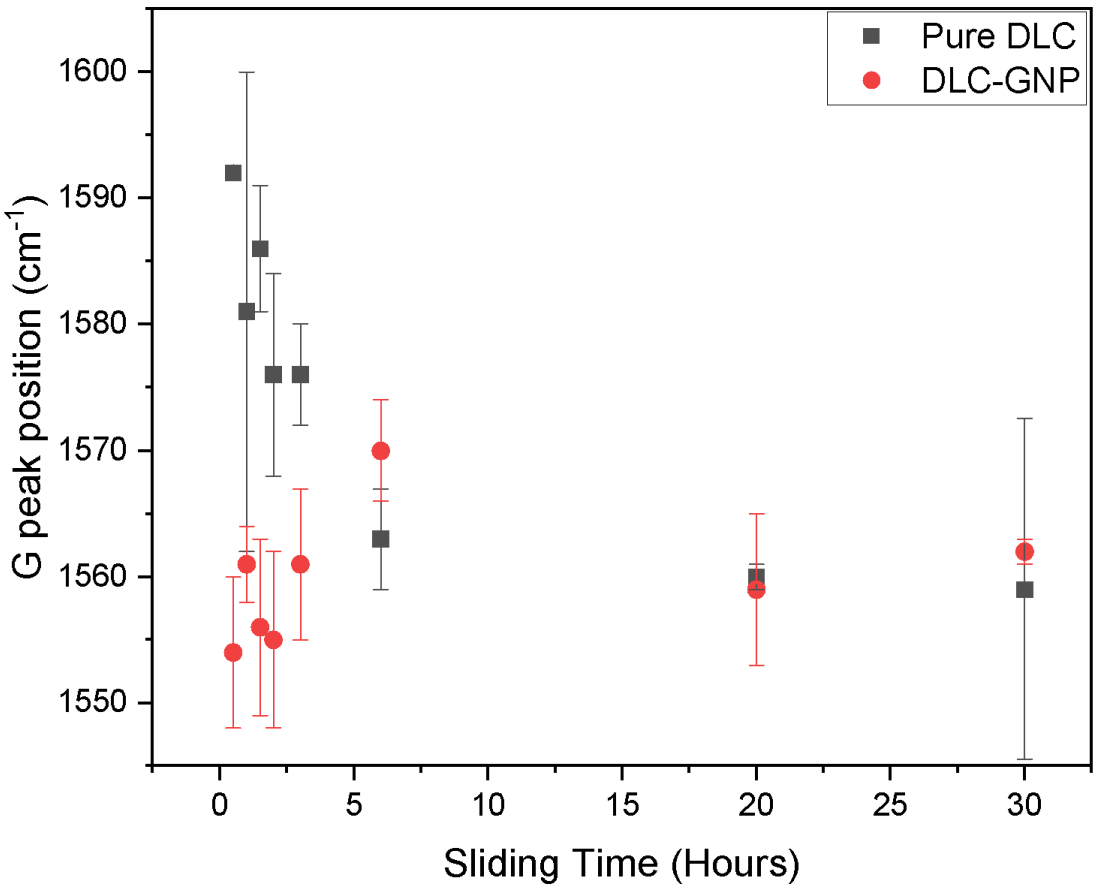

Figure 6.11 *G peak position as a function of sliding time for CI counter-body.*

Figure 6.12 presents the I_D/I_G ratio for the CI pins against pure DLC and DLC-GNP1. The spectra were obtained (0.5 to 30 hours) at the centre of the wear scar and calculated

by deconvolution of the Raman spectra in two Gaussian peaks (**Section 3.3.6**). The I_D/I_G ratio is commonly used to measure the relative graphitisation of DLC films [186,231].

The pure DLC I_D/I_G ratio remains relatively steady. The DLC-GNP I_D/I_G ratio increases up to 6 hours of wear and then begins to steady with a high standard deviation. Both samples present very similar results after 20 hours.

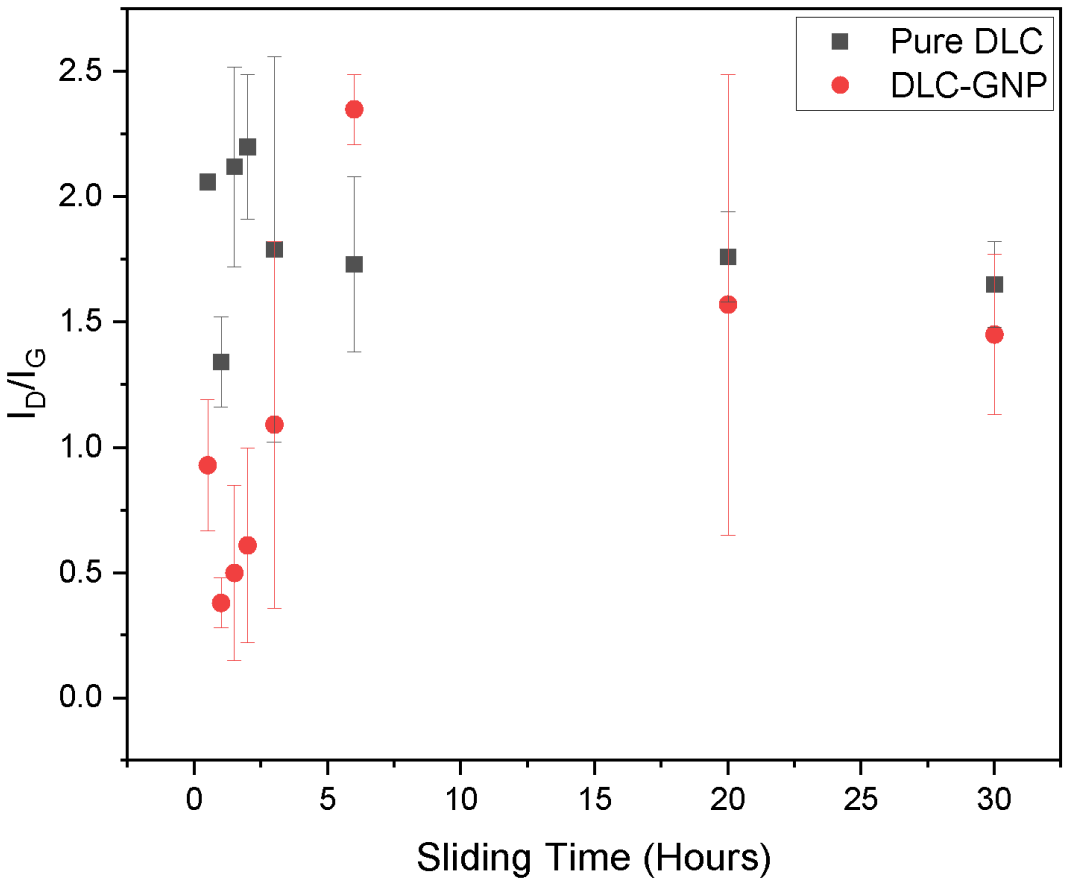

Figure 6.12 *I_D/I_G ratio for CI counter-body against Pure DLC and DLC-GNP nanocomposite.*

The G peak intensity is provided in **Figure 6.13**. The G peak intensity indicates the thickness of the transfer film forming on the CI. The intensity increases as the sliding time increases. The rate of increase slows after ~3 hours.

The pure DLC provides the highest G peak intensity after 3 hours and remains highest throughout. The DLC-GNP increases but stabilises at 6 hours.

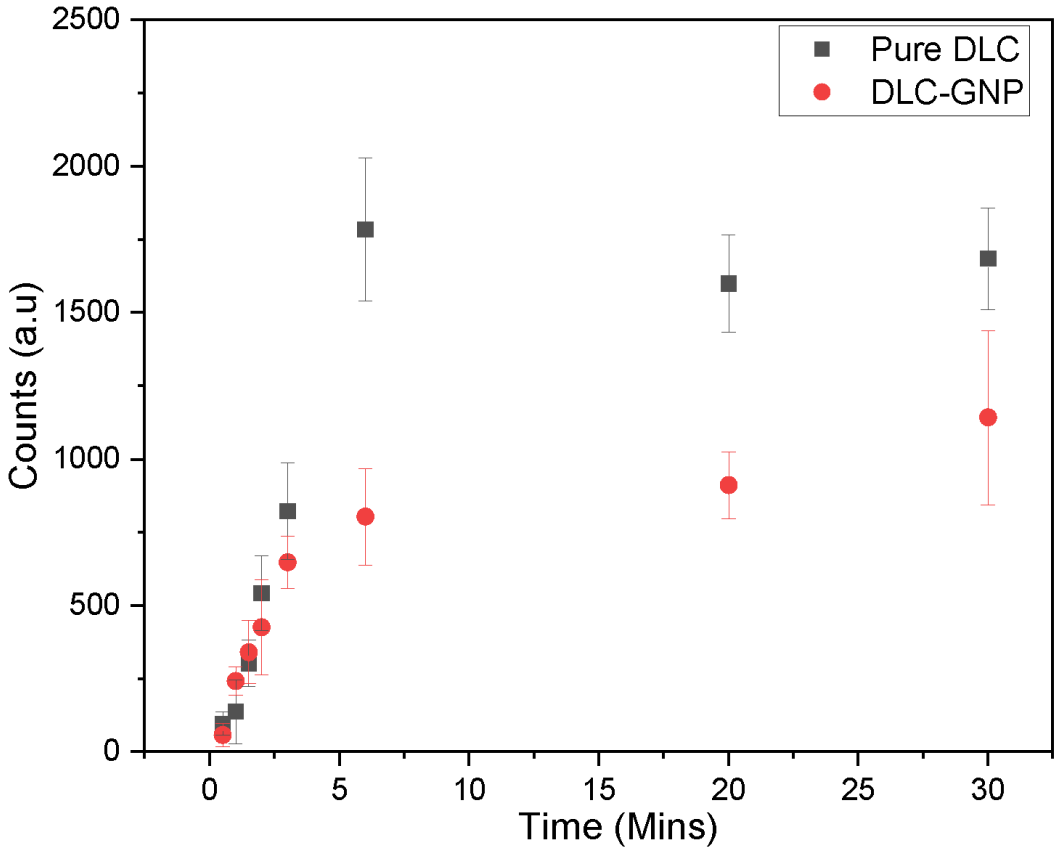

Figure 6.13 *G peak intensity as a function of sliding time for CI counter-body.*

6.6. Transfer Film Analysis

Transfer films have previously been reported to form in lubricated contacts and can form on the sample surface and counter-body [62,63]. The formation of a transfer film can be removed easily into the lubricant [17,74]. The transfer film using the VAM model can contain constituents of the coating and counter-body [71].

Hematite and Maghemite are likely to be wear products from the CI and have been previously reported [232,233]. To confirm the presence of Iron related products within the CI cross-sections (FIB perpendicular to the direction of the wear scar) were taken after 1, 6, and 30 hours of tribo-testing (pure DLC and DLC-GNP) and imaged using TEM (**Figure 6.14**) EDS was used to identify the chemical species, and EELS to quantify the sp^2 content (**Figure 6.15** and **Figure 6.16**).

Before cross-section, samples were rinsed with heptane to remove the presence of oil and were cross-sectioned perpendicular to the direction of the wear scar. A thin carbon transfer film was observed on all counter-bodies except for the 1hr DLC-GNP sample. The carbon transfer films presented as a thin layer; the thickness is provided in **Table 6.1**.

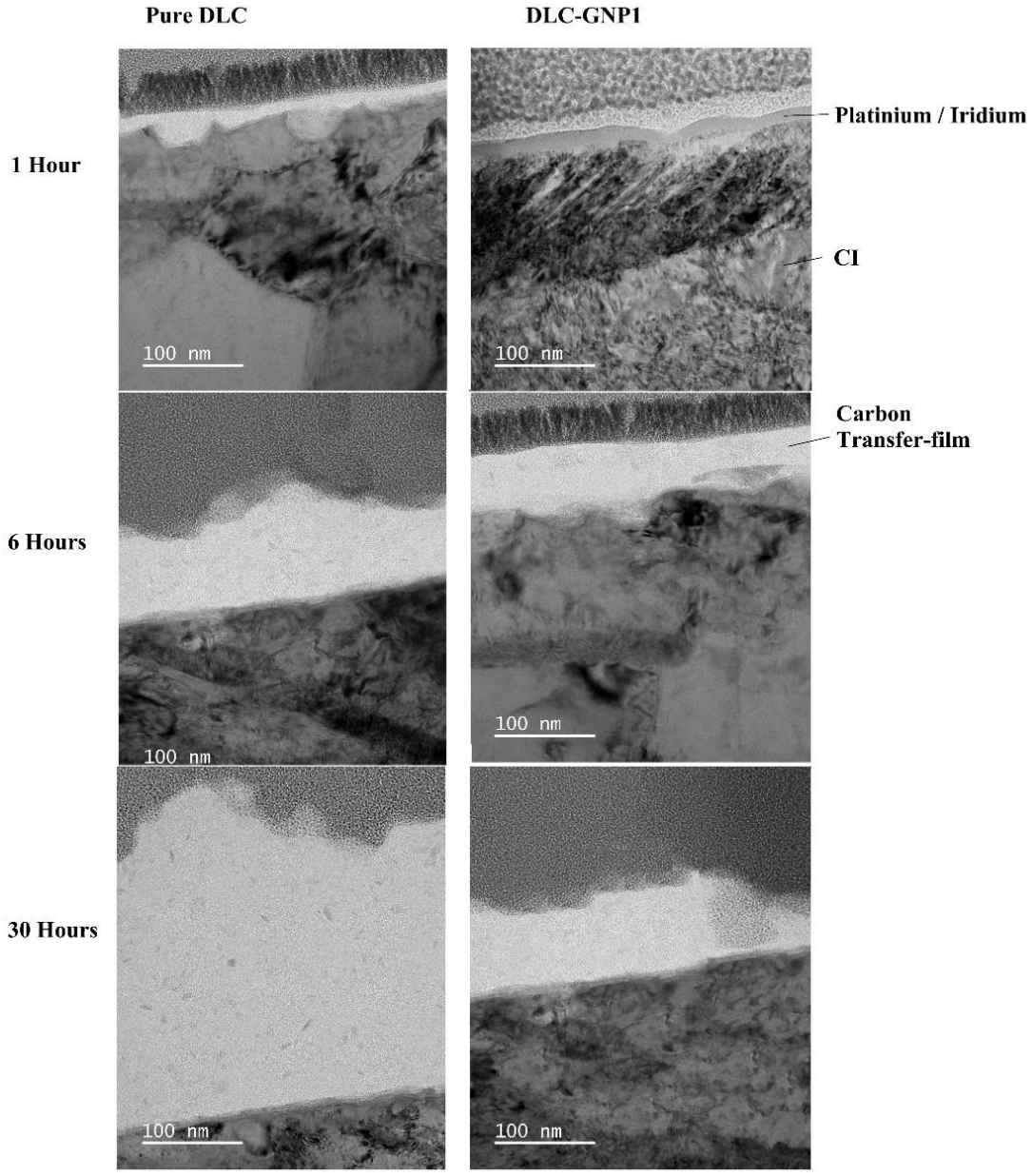

Figure 6.14 *TEM micrographs of CI counter-body at 1 hr, 6hr and 30hr of wear.*

For this report, the tribo-tests conducted using FFO were not cross-sectioned, as the primary focus of the study was to investigate the role of GNP in friction reduction rather than examining the impact of additives present in the oil. However, it should be noted

that the incorporation of additives within FFO can introduce additional mechanisms for friction reduction [17], resulting in frictional traces (**Figure 6.1**) that align more closely with previous research [170,234]

Table 6.1 *Transfer film thickness on counter-body.*

Sliding time	**Thickness (nm)**	
	Pure DLC	**DLC-GNP**
1 Hr	35	-
6 Hr	100	53
30 hr	315	95

The micrographs (> 6 hours) revealed the presence of crystallite particles embedded within the carbon film. The iron particles exhibited a crystal structure with a spacing of 0.253 nm, closely resembling Hematite's (110) plane. Conversely, no precise or consistent spacing was observed for the iron particles in the DLC-GNP1 transfer film. Although the FIB cross-section of DLC-GNP1 caused some redistribution of Iridium within the carbon transfer layer, this does not impact the validity of the findings.

The presence of iron within the transfer films of both pure DLC and DLC-GNP1 was confirmed by EDS analysis (**Figure 6.15** and **Figure 6.16**). While it is challenging to determine if these small iron crystallites originate from the CI pin, the absence of chromium or tungsten in the adhesion layer suggests that they have not penetrated deep enough to originate from the substrate or adhesion layer. Moreover, the presence of oxygen on the surface of the CI pin and within the carbon transfer film provides additional evidence supporting the hypothesis that the iron present is indeed derived from the CI pin.

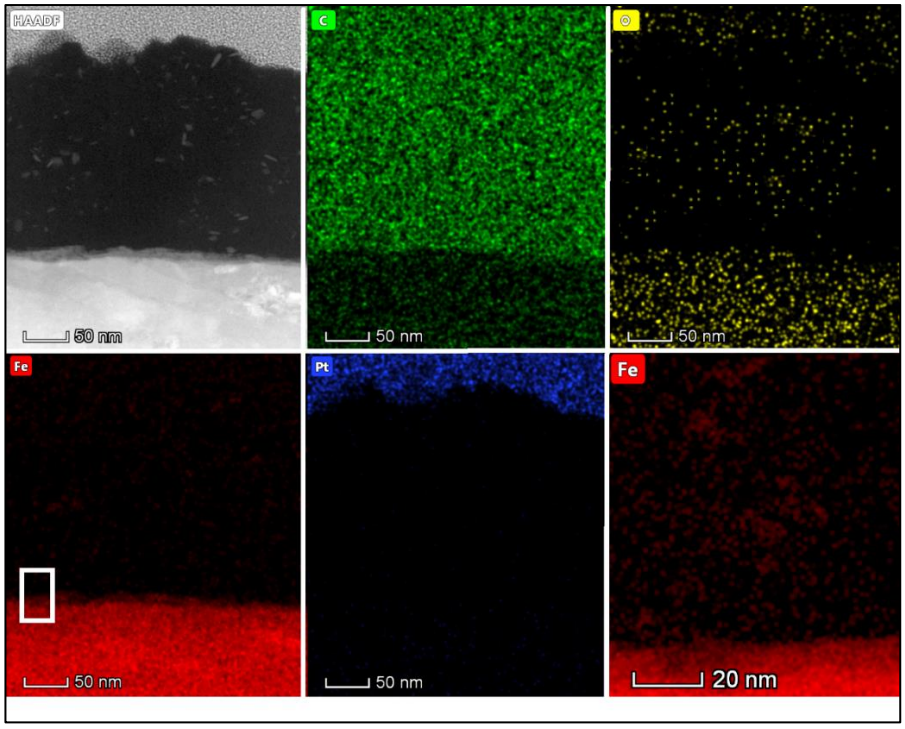

Figure 6.15 *EDS image of carbon transfer film for CI pin against pure DLC. The white box shows the area at which a more magnified iron scan.*

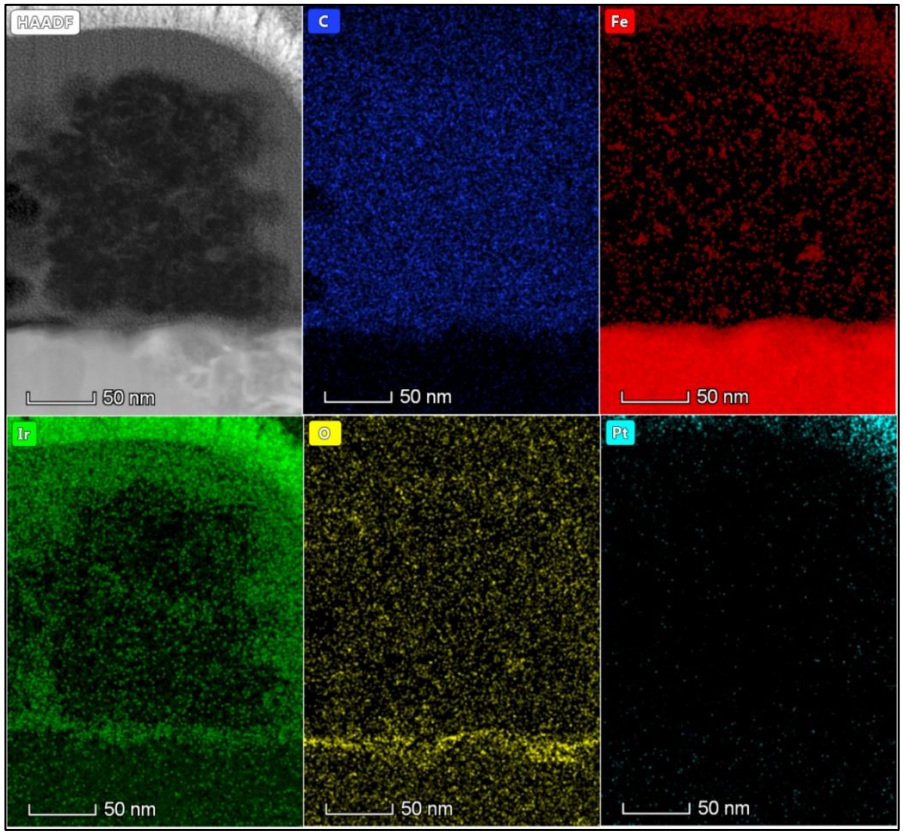

Figure 6.16 *EDS image of carbon transfer film for CI pin against DLC-GNP.*

The presence of Iron Oxides within the transfer film of the CI counter-body suggests the formation of a velocity accumulation mode (WAM) of the transfer film. In this mode, loose debris from the DLC/DLC-GNP coating and the CI counter-body undergo shearing and extrusion between the contacting surfaces. Subsequently, these particles adhere to the counter-body, forming a protective layer restricting direct contact between the articulating surfaces [71]. Iron oxides were also observed within the wear particles in **(Section 4.2.5.2)** and add evidence to the VAM model for the formation of the transfer film.

EELS spectra (**Table 6.2**) were obtained from the central region of the transfer films at 6 hours and 30 hours. It was observed that the DLC-GNP1 transfer film exhibits a higher graphitic nature compared to the pure DLC counter. As the sliding time increases, there is a slight rise in the sp^2 content of the DLC-GNP1 transfer film.

Table 6.2 *EELS results for pure DLC and DLC-GNP1 transfer films.*

	Sample	**sp^2/sp^3%**
	HOPG (Reference)	100
6 Hours	**Pure DLC**	54.8
	DLC-GNP	63.6
30 Hours	**Pure DLC**	56.8
	DLC-GNP	65.1

6.7. Summary of the Effect of Sliding Distance on the Tribological Properties of DLC-GNP Nanocomposites

- The wear rates of pure DLC and DLC-GNP decreased with increasing sliding distance. DLC-GNP initially had a higher wear rate than pure DLC, but at around 3 hours, their wear rates started to converge. After 6 hours of wear, DLC-GNP consistently exhibited low wear rates.
- The thickness of the transfer layer increased as the sliding distance increased; this was observed for both samples.
- The DLC-GNP transfer film is more graphitic after 30 hours of wear than the pure DLC CI counter-body, confirmed by EELS and Raman measurements.

Chapter 7 - Discussion

This thesis builds upon previous research [25], which focused on developing a heat treatment method to mitigate GNP removal and DLC delamination. However, no specific mechanism for friction reduction was elucidated in that study. The current research aims to address these gaps and provide insights into the friction reduction mechanism, as discussed in **Section 2.5.3**.

The primary aim of this thesis is to examine the underlying mechanism behind the reduced friction and wear observed when GNP are incorporated into a DLC matrix. This study encompasses three investigations (**Figure 7.1**), with the results of each feeding into the underlying low friction mechanism.

The best-performing coating from the first (optimum GNP coverage) and second study (optimum DLC thickness) were used for extended wear testing (30 hours).

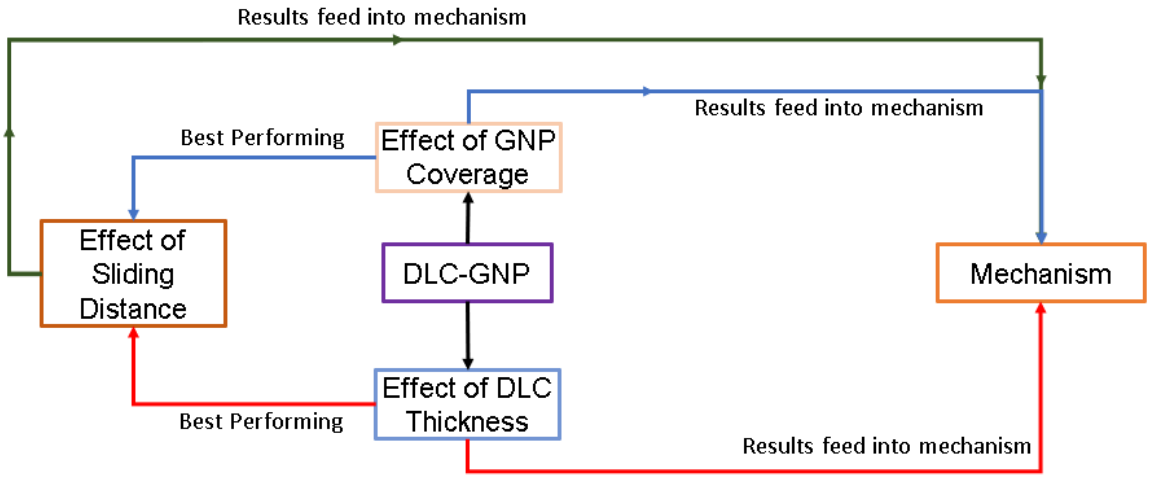

Figure 7.1 *Outline flow diagram linking the results chapters to the proposed mechanism for friction reduction.*

The results of these studies are tied together to produce a body of evidence to support a mechanism for low friction and wear in DLC-GNP nanocomposites in lubricated environments.

The most salient areas from the three studies are provided in this results section, which will converge to provide a mechanism for friction reduction:

1. GNP Distribution and Tribological Properties
2. Mechanical Properties
3. Contact Mechanics
4. Transfer-film formation

7.1. GNP Distribution and Tribological Properties

The first study **(Chapter 4)** provided various coverages by increasing the GNP/NMP suspension concentration during the spin coating process.

The GNP in this work has been shown to align parallel, but two types are present (**Figure 7.2**).

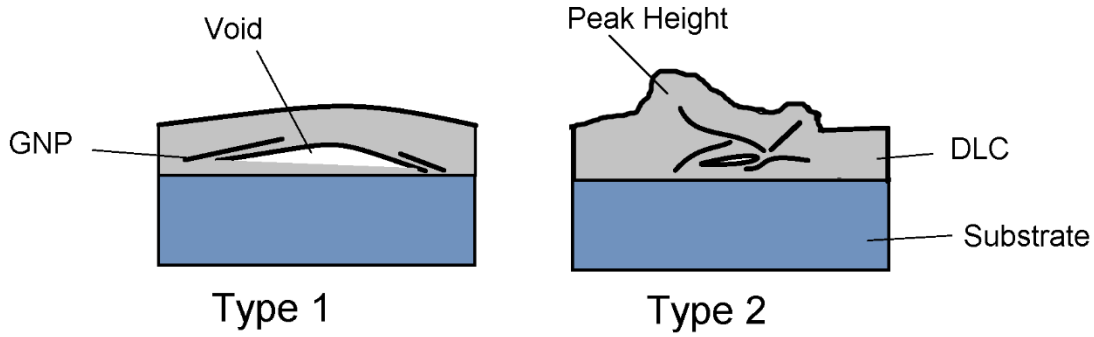

Figure 7.2 *The two different GNP structures observed.*

The increase in coverage provided an increase in Surface Roughness (R_a) and Peak Height due to agglomeration of the GNP. GNP agglomeration is common in graphitic materials due to the large volume to surface ratio [20][110]. Large peak heights increase the aspertity contact and can act as a leverage point on the coatings, which is removed under reciprocating wear. This asperity removal was observed for GNP/NMP concentrations of 1.5 mg/ml and 2 ml/ml leading to increased wear and negating the friction reduction effect of the GNP.

Figure 7.3 provides the mean COF versus the running-in period (first 3 hours) and the steady state period (final 3 hours) of tribo-testing. Notably, a clear overlap is observed between GNP coverage and mean average values, suggesting a correlation between GNP coverage and friction. Specifically, at a GNP coverage of 1.16-1.29%, friction is substantially reduced by approximately 45% compared to the reference pure DLC during the final 3 hours. Furthermore, as the GNP coverage increases up to 4.5%, there is a notable 65% reduction in friction compared to pure DLC during the final 3 hours of testing. It is important to note that the friction consistently decreases with increasing GNP coverage. However, at higher coverages achieved with concentrations of 1.5 mg/ml and 2 mg/ml, the wear process resulted in the removal of GNP.

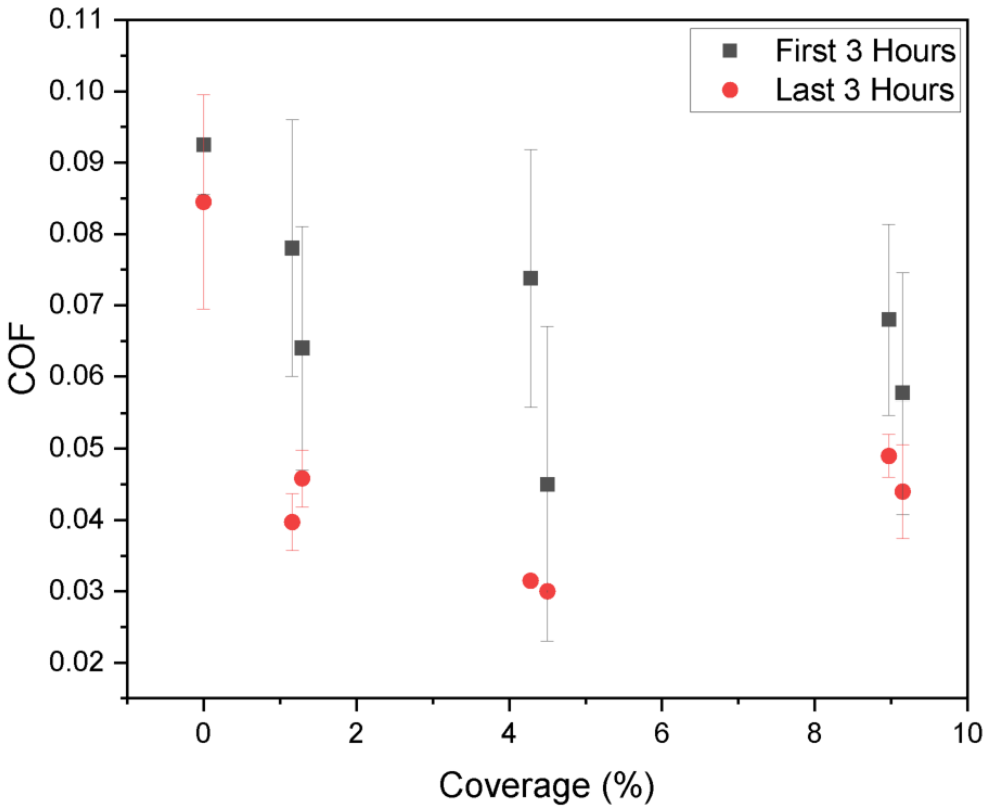

Figure 7.3 *Mean average COF for first and last 3 hours of wear tests.*

The wear particles in DLC-GNP nanocomposite coatings are smaller than pure DLC. Larger wear particles indicate that more material is being removed from the surface of the carbon film and would be a higher wear rate. The DLC-GNP1 provided smaller wear particles in more cylindrical shapes.

If a law of mixtures approach is undertaken for the DLC-GNP nanocomposites, using the average COF for the final 3 hours along with the calculations based on the upper and linear bands as seen in **Figure 7.4** overestimates the COF for coverages ≥4.5%. The equations used for the rules of mixtures are:

$$Lower\ band\ estimates: \mu_{(total)} = \frac{1}{\frac{C_{GNP}}{\mu_{GNP}} + \frac{1-C_{GNP}}{\mu_{DLC}}} \qquad \textit{Equation 7.2}$$

$$Upper\ linear\ band\ estimates: \mu_{(total)} = (C_{GNP} \times \mu_{GNP}) + (1 - C_{GNP}) \times \mu_{DLC} \qquad \textit{Equation 7.3}$$

With C_{GNP} being the coverage of GNP. The μ_{DLC} is taken as the mean value from the final 3 hours of friction for the pure DLC, and μ_{GNP} is taken to be 0.006 based on the lowest reported literature [235,236]. The results show a similar friction reduction trend as predicted mathematically, but the lower-band estimate at the lowest experimental point is almost double. These estimates provide insight into the fact that friction reduction is not solely from the low shear areas; another mechanism must be responsible for maintaining the low friction. The experimental results show an increase in frictional values above 4.5%. This could be from the agglomerated GNP islands becoming exposed during sliding wear due to the high peak height. The exposed step edges of the GNP islands will cause high adhesion to the CI pin and result in the GNPs being 'plucked out' [237].

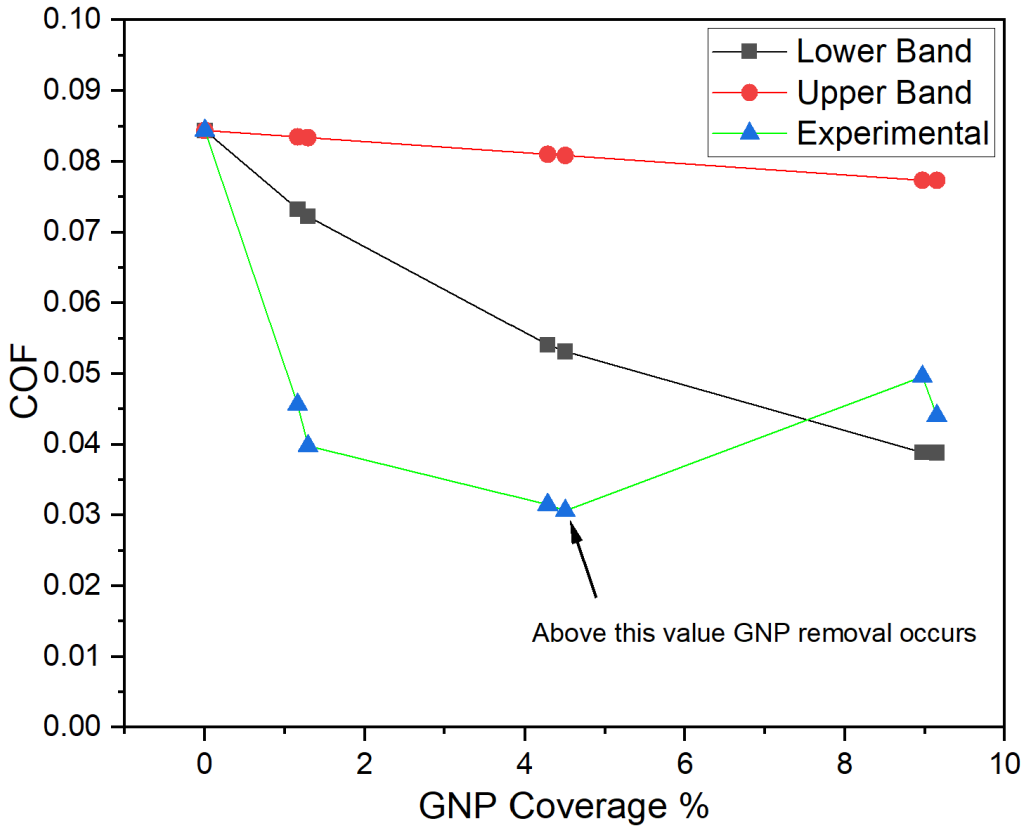

Figure 7.4 *The mean experimental COF for the final 3 hours of the wear test, with the calculated lower and linear band estimates using the rules of mixtures approach.*

When the DLC thickness is changed above GNP, but the GNP coverage remains constant, there are changes to the tribological response. The thinnest coating (DLC-GNP22.5) achieves the lowest friction, displaying an almost instant friction reduction, with the thickest coating (DLC-GNP180) taking the longest to reduce in friction.

The (DLC-GNP22.5) resulted in GNP removal from inside the wear track. When the DLC-GNP22.5 cross-section (**Figure 5.4**) is observed, a significant amount of GNP is close to surface, with the Raman spectra (**Figure 5.*17***) and SEM topography micrographs (**Figure 5.9**) confirming that not all of the GNP are cover by DLC.

DLC-GNP180 cross-sections, the GNP is entirely covered by 180 minutes of DLC deposition (**Figure 5.3**).

Assuming that the coatings all wear initially at a relatively steady rate, the time taken to wear down before GNP is reached is significantly shorter for the DLC-GNP22.5 than for the DLC-GNP180. This change in time before reaching the GNP is the reason for the low initial friction for the DLC-GNP22.5 and explains the time taken for friction to reduce in thicker coatings. The GNP islands are shown to be a source of graphitic lubricant [238], and if minor wear is needed to reach these GNP, it is concluded that this is the reason for the shorter time to reach a lower COF.

The GNP coverage and thickness of the DLC are shown to both be important factors that contribute to a friction reduction mechanism. The distribution of the GNP allows a sufficient source of lubricant to contact the counter-body, but these can become isolated by the thick DLC coating and will not reduce friction. Subsequently, if the DLC is too thin, the GNP are removed from the coating, increasing the wear.

7.2 Mechanical Properties

Research combining CNT and DLC [114,239,240] showed that hardness and elastic modulus depended on the CNT orientation. The presence of voids within the DLC-GNP structure introduced challenges in evaluating the properties.

When the bulk elastic modulus (**Table 7.*1***) was measured as the GNP coverage increased, a decrease was observed. The aimed single indentations (**Table 4.3**) show that regardless of the concentration, GNP islands' hardness and elastic modulus remains reasonably consistent (except for one erroneous sample).

Table 7.1 provides the calculated H/E ratio and Crack Propagation Resistance (CPR) for all DLC-GNP coatings using various GNP/NMP concentrations. A higher H/E ratio is often associated with lower friction and improved wear [178,179,181]. Lower values have been linked to improved impact resistance and increased toughness [241]. Comparing the specific wear rate, lower values correlate with improved wear rate, although this pattern

is not consistently observed. This suggests that the mechanisms leading to low friction are not solely reliant on hardness and elastic modulus. It is essential to consider the distinctions between the GNP islands and the surrounding matrix and the presence of high errors in the measurements. The presence of voids within the GNP islands may explain their lower elastic modulus, as compression from the applied load exerted by the nano-indentation tip would be more pronounced. Consequently, this compression could reduce the measured hardness and elastic modulus values across the 10 x 10 grid. Unfortunately, this limitation is inherent in the obtained results.

Table 7.1 *H/E ratio and wear rates for DLC-GNP nanocomposites.*

Sample	Elastic Modulus (GPa)	H/E	Wear Rate x 10^{-19} (m^3/Nm)	CPR (N^2) $L_{c1}(L_{c2}-L_{c1})$	Average Steady State COF
Pure DLC	204 ± 8	0.116	3.71 ± 0.19	254.2	0.084
DLC-GNP0.25	201 ± 23	0.114	2.03 ± 0.10	223.5	0.040
DLC-GNP0.5	195 ± 28	0.116	1.79 ± 0.08	226.6	0.046
DLC-GNP0.75	192 ± 29	0.115	1.55 ± 0.07	272.6	0.031
DLC-GNP1	195 ± 13	0.113	1.47 ± 0.07	268.9	0.031
DLC-GNP1.5	181 ± 37	0.120	2.86 ± 0.14	225.0	0.051
DLC-GNP2	176 ± 36	0.120	3.24 ± 0.16	260.0	0.044

The adhesion of DLC-GNP film was determined by scratch testing, with the first failures (cohesive) in all coatings appearing as a chevron cracking, where the L_{C1} value decreased by ~5N when GNP was introduced into the DLC matrix. The decrease is due to the bonding of the DLC/GNP being less than the C-C bonds within DLC itself. The second adhesion failure improved for all coatings by adding more GNP into the matrix, with the

1 mg/ml coating showing the highest load, provides the L_{C2} , mean steady-state friction and Crack Propagation Resistance (CPR) [161]. The best two performing coatings have the highest CPR values.

The Pearson Correlation Coefficient (described in **Section 3.5**) is employed to calculate the correlation between CRP and mean COF, as illustrated in (**Figure 7.5**). When considering all the values, the calculated R-value is -0.1857, indicating a weak correlation. However, when the pure DLC result is excluded from the analysis, the R-value becomes -0.7696, representing a strong negative correlation. This provides a relationship: as the CPR value increases, the COF decreases. This finding aligns with previous studies on DLC coatings, where accelerated wear is observed due to thickness cracks and significant material removal, often attributed to graphitisation [163].

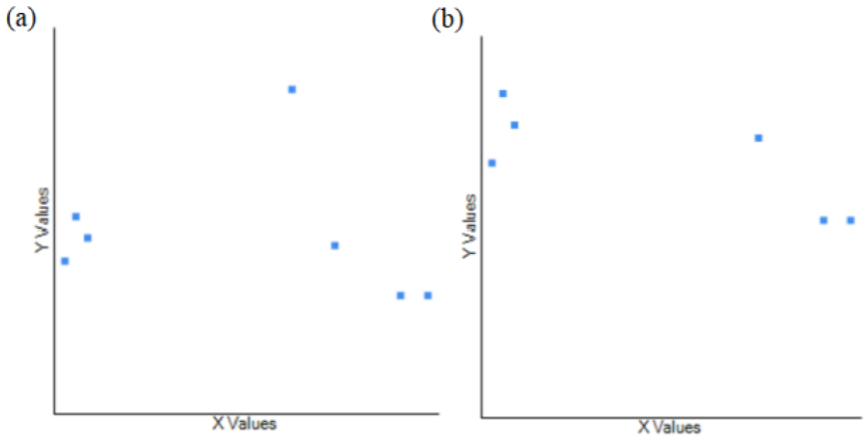

Figure 7.5 *R-values for (a) all samples and pure DLC, and (b) only DLC-GNP samples.*

When the thickness of the DLC above the GNP increased, the hardness and elastic modulus showed an increase. The Elastic Modulus, H/E ratio and CRP are shown in **Table 7.2**, along with the specific wear rate and the mean average COF over 6 hours of tribo-testing. The increase in DLC thickness for a pure DLC film has been shown in some studies to increase the elastic modulus and hardness due to less influence from the softer substrate, even when less than 10% of the coating thickness is measured [210,242]. Other

coatings, such as GLC, have shown slight hardness decreases as DLC thickness increases. [243].

The reason for the increases in elastic modulus and hardness as the DLC thickness increases is the result of the DLC above the GNP islands. For the thin layers, the substrate effects are observed yielding at lower forces [244] and would yield at lower forces. For thicker films, there would be more mechanical support from the DLC above the GNP, and 10% of the coating thickness would not yield as easily. The H/E ratio (**Table 7.2**) links to the lowest wear rate for the coatings. Due to the sample size being 4, it is impossible to calculate a statistically relevant Pearson correlation coefficient.

Table 7.2 *Mechanical properties of DLC-GNP films with various DLC thicknesses.*

DLC layer Thickness (µm)	**Elastic Modulus (GPa)**	**Hardness (GPa)**	**H/E (GPa)**	**Wear Rate x10^{-18} (m^3/Nm)**	**Mean COF**	**CPR N^2**
0.45	164 ± 20	18 ± 3	0.08	3.73 ± 0.18	0.035 ± 0.00	409.6
0.73	182 ± 21	20 ± 5	0.11	2.85 ± 0.14	0.044 ± 0.01	374.9
1.27	195 ± 13	22 ± 6	0.11	0.147± 0.007	0.038 ± 0.01	268.9
3.63	226 ± 13	23 ± 1	0.10	2.89 ± 0.14	0.050 ± 0.01	38.1

The adhesion testing results from **Section 5.3.1** show a general trend supporting that best-performing coatings did not fracture. It is therefore shown that both variables from Chapter 4 and Chapter 5 provide different aspects to the mechanical properties' response, by increasing the thickness the DLC provides more support above the GNP, and due to the presence of voids and lower hardness / elastic modulus the GNP islands provide discrete areas of lower mechanical properties in comparison to the surrounding matrix.

7.3. Contact Mechanics of DLC-GNP and Counter-body

Modifying mechanical properties significantly influences the interaction between the coating and the counter-body. Localised areas with low hardness and elastic modulus create distinct regions that experience different contact pressures during sliding. When increasing GNP coverage, the overall elastic modulus decreases, causing a reduction in Hertzian contact pressures. Consequently, these variations can decrease the effective contact area during sliding, increasing the localised contact pressure experienced. This elevated pressure often increases graphitisation, resulting in a lower friction coefficient [221].

Figure 7.6 provides the variations in maximum contact pressures based on the contact radius. The graph highlights the initial contact radius, representing the contact pressure for pure DLC. It is evident that as the contact radius decreases, the contact pressure increases exponentially. This substantial change in contact pressure has significant implications for the Tribochemistry within a DLC film.

The increased contact pressure can induce a phase transformation of carbon bonds from $sp^3 \rightarrow sp^2$ within the DLC film. Typically, this type of phase transformation would require much higher temperatures, typically ranging from 350 to 600°C. However, the pronounced contact pressures experienced during sliding can drive this phase transformation even at lower temperatures, altering carbon bonding within the DLC film. [63,207].

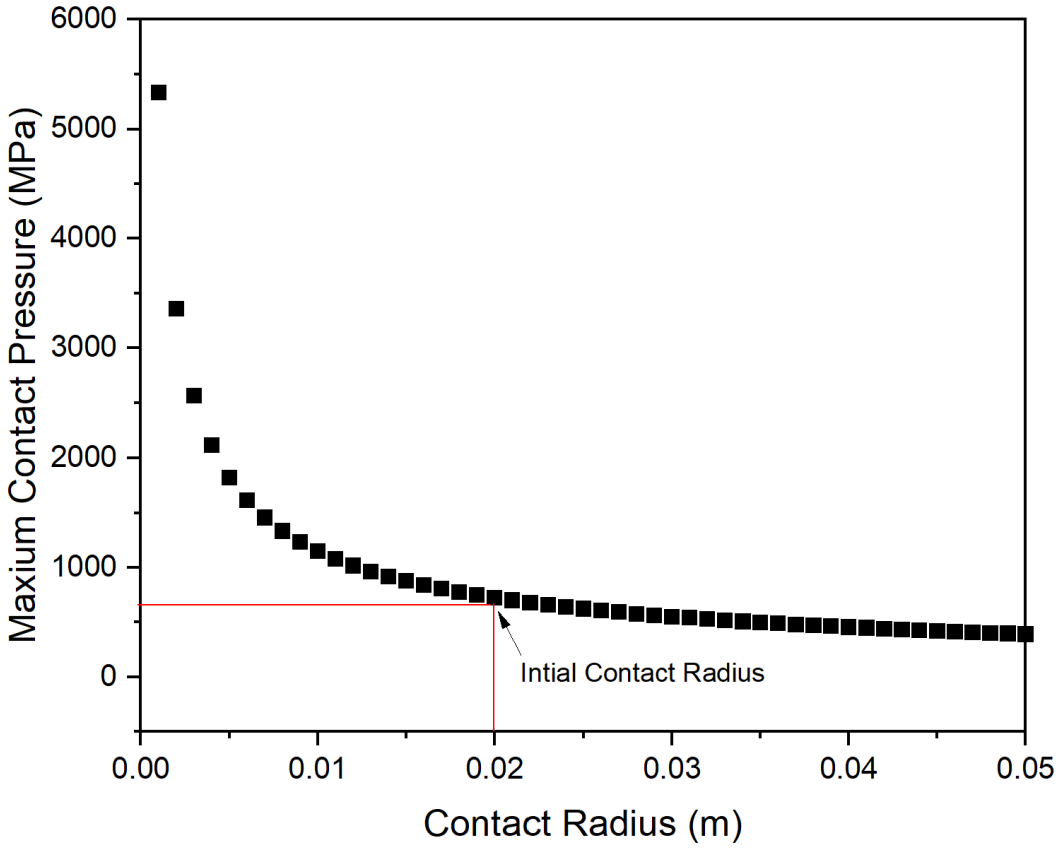

Figure 7.6 *Maximum Hertzian contact pressure as a function of contact radius.*

Huu *et al.* [64] proposed an equation expression of the critical phase transformation temperature (T_c) of a DLC film as a function of contact pressure:

$$T = T_c exp\left(\frac{-|\Delta v|}{L}\right)\Delta p \qquad \textit{Equation 7.1}$$

Where:

L = Phase transformation energy of diamond (15.6 x 10^4 Jkg^{-1}).

Δv = volumetric difference between the specific volume of hydrogenated and hydrogen free coating (m^3/kg).

Δp = pressure difference between atmospheric and Hertzian contact pressure.

Solis *et al.* [128] calculated the graphitisation temperature for specific hydrogenated coating volume as a function of contact pressure (**Figure 7.7**). Changing the contact pressure would lead to graphitisation occurring at much lower temperatures, which

decreased as the hydrogen content increased. For the DLC-GNP nanocomposites, when using the bulk elastic modulus (**Table 4.2**), the Hertzian contact pressure was highest for the pure DLC (714 MPa) and lowest for the DLC-GNP2 (677 MPa).

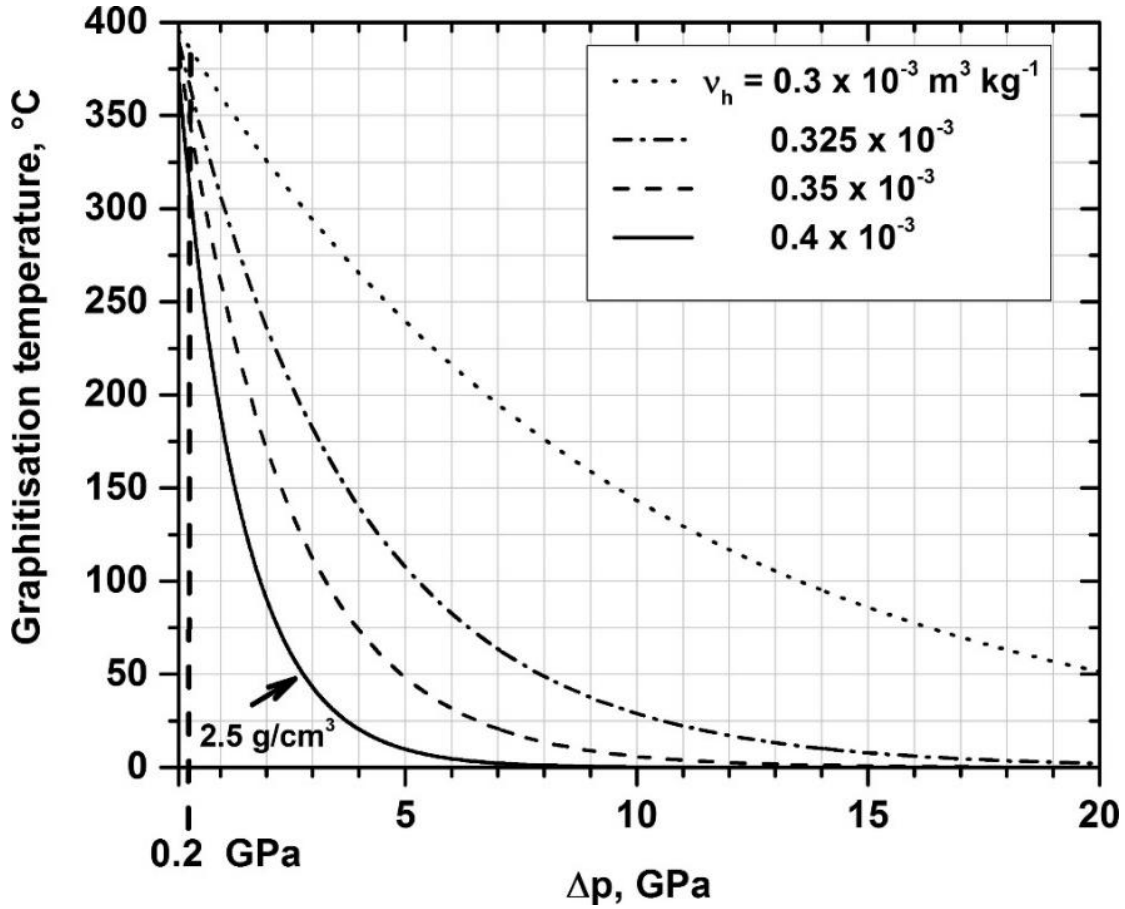

Figure 7.7 *Graphitisation Temperature for hydrogenated DLC at specific hydrogenated coating volume* [128]

The nano-indentations targeted at GNP islands, using the Poisson's ratio determined by Chiarello *et al.* [245], give a Hertzian contact pressure range between 52-85 MPa, significantly less than pure DLC. Depending on where (**Figure 7.8**) the nano-indentation results are obtained, the load could be above a GNP, on DLC, or a combination of the two. If an assumption is made that only the DLC supports the load (due to the low yield at these islands), the real area of contact is reduced by the GNP coverage (between 1.16% - 9.15%).

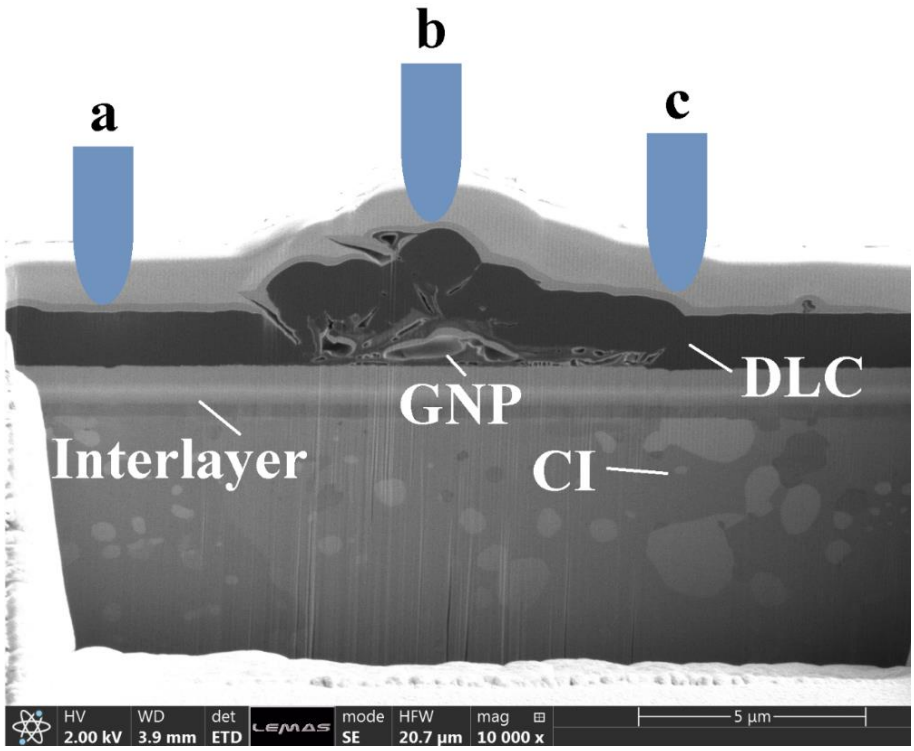

Figure 7.8 *Cross-section representation of (a) only DLC, (b) GNP island, and (c) 50% DLC / 50% GNP.*

The following contact pressures can be calculated in **Table 7.3** based on the assumption that the DLC is the only surface supporting the load and that between 1.16% - 9.15% is being reduced.

Table 7.3 *Contact pressure for reduced area of contact.*

Sample	Contact Pressure (MPa)
Pure DLC	714 MPa
DLC-GNP0.25 (1.16%)	738.1 MPa
DLC-GNP0.5 (1.29%)	740.3 MPa
DLC-GNP0.75 (4.29%)	787.4 MPa
DLC-GNP1 (4.5%)	790.9 MPa
DLC-GNP1.5 (8.97%)	870.5 MPa
DLC-GNP2 (9.15%)	873.9 MPa

The observed increases in contact pressure significantly drive the graphitic transformation of sp^3-bonded carbons during wear when considering **Figure 7.7**. This transformation is substantiated by the analysed Raman spectra, where the CI pin (**Figure 4.34**) exhibits a higher I_D/I_G ratio with increasing GNP coverage (ranging from 1.16% to 4.5%). Additionally, the EELS spectra (**Table 6.2**) indicate that the transfer film of DLC-GNP exhibits a higher sp^2 content than pure DLC. The increase in contact pressure might not be the sole factor influencing these results. The impact of GNP on the formation of the transfer film needs to be explicitly addressed in this section. Therefore, it is crucial to consider the combined effects of contact pressure and GNP presence when discussing the observed outcomes related to transfer film formation.

7.4. Low Friction Transfer Film Formation

The incorporation of GNP into an oil lubricant between two steel surfaces has consistently demonstrated a reduction in friction and wear. This beneficial outcome is attributed to forming a graphitic transfer layer between the contacting surfaces. This transfer layer acts as a protective barrier, lowering the shear strength between the surfaces and reducing the underlying material's wear [20,246].

In the reported results from this thesis, the I_D/I_G ratio on the counter-body is higher than that of the DLC-GNP films it is worn against (**Figure 4.17** & **Table 6.2**). This indicates the material transfer and graphitisation of the underlying DLC material onto the counter-body. The elevated I_D/I_G ratio provides evidence of the formation of a carbon graphitic transfer film during the wear process.

Supporting the presence of a carbon graphitic transfer film are the observations of the G peak intensity (**Figure 6.13**) and TEM cross-sections (**Figure 6.14**). Both these findings further corroborate the formation of the transfer film.

Additionally, **Figure 7.9** illustrates a weak relationship between the G peak intensity and the thickness of the transfer film. A higher G peak intensity corresponds to a comparatively thicker transfer film [112].

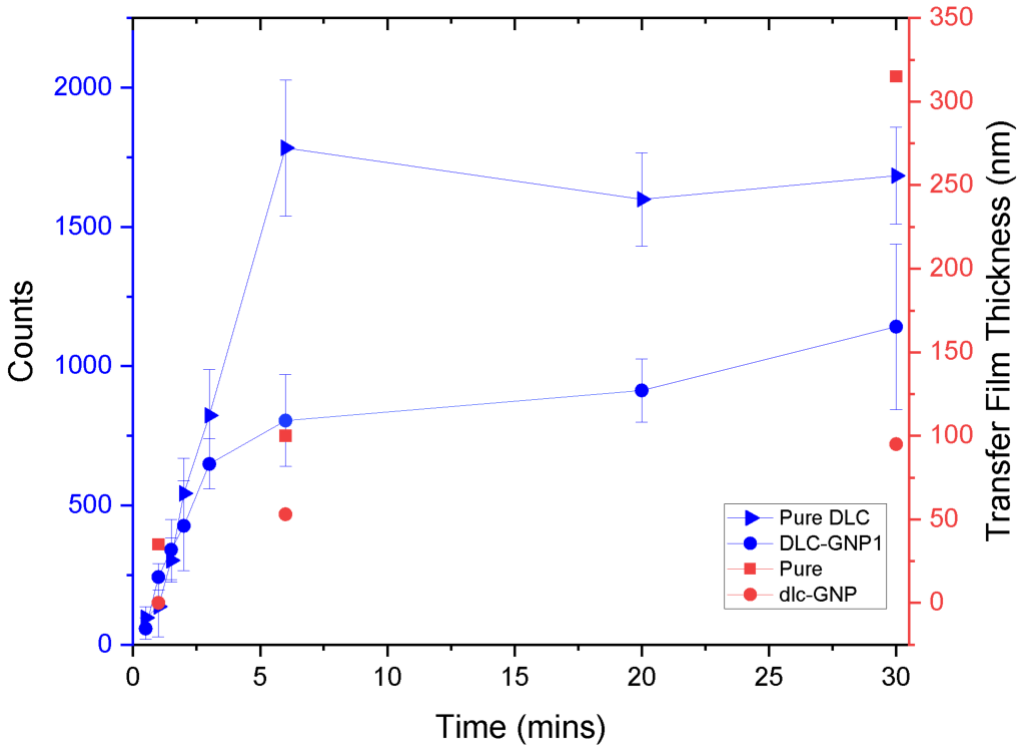

Figure 7.9 *Transfer film Thickness and G peak intensity as a function of time.*

Despite the conventional understanding that graphitisation is typically initiated by temperatures exceeding 400°C, it has been observed to occur at lower temperatures, which cannot be fully explained by the simplified model proposed by Rabinowicz *et al.* [247]. Liu *et al.* [248] calculated that a high Hertzian contact pressure induces a temperature rise of typically 100 - 300°C. However, these temperature increases alone do not entirely account for the occurrence of graphitisation at lower temperatures.

As the concentration of GNP increased, a notable observation was the formation of a graphitic transfer film on the CI counter-body. This phenomenon was supported by the increased G peak intensity observed in **Figure 4.35** and the changes in the I_D/I_G ratio depicted in **Figure 4.34**. The I_D/I_G ratio rise indicates a higher graphitic content within the film.

Interestingly, the formation of this transfer film is likely attributed to the high contact pressures experienced at the asperities rather than the generation of heat from friction alone. This suggests that shear-induced graphitisation occurs due to the intense contact pressures present, as supported by previous studies [63,64]. The findings highlight the complex interplay between pressure, shear forces, and graphitic transformation in the formation of the transfer film.

The formation of a transfer film on the DLC-GNP composite is indicated by the increased GNP coverage observed after wear (**Figure 4.23**). The shearing of the GNP layers generates this transfer film during the tribological wear process. Interestingly, the I_D/I_G ratio increased as the GNP coverage increased. Beyond a GNP coverage of 4.5%, there was a noticeable increase in the I_D/I_G ratio. This can be attributed to the high roughness of the surface from the removal of GNP particles during the tribological tests.

Figure 7.10 presents the I_D/I_G ratio variation as a function of the wear rate for both the GNP islands and DLC areas in the samples discussed in **Chapter 4**. A consistent pattern emerges, indicating an increase in the I_D/I_G ratio with an increase in wear, except for a specific region marked in blue. This anomaly is observed in the DLC region of the DLC-GNP2 sample after wear and can be attributed to the displacement and shearing of GNP particles into the wear track. The low I_D/I_G ratio observed in this region is likely to contribute to reduced friction and wear by promoting the formation of a highly graphitic transfer film. This transfer film acts as a low shear, low adhesion layer, minimizing the overlapping of σ-bonds and safeguarding the underlying DLC from undergoing the $sp^3 \rightarrow sp^2$ transformation. It is important to note that high wear is associated with increased graphitisation and subsequent removal into the wear track [73].

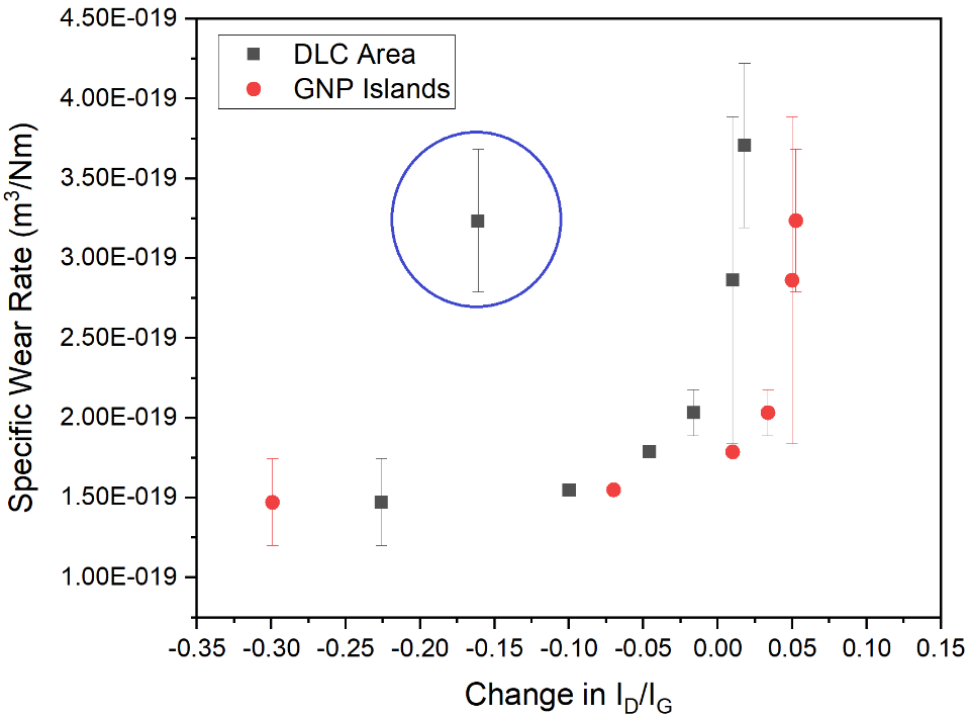

Figure 7.10 *Change in I_D/I_G as a function of specific wear rate.*

The presence of a graphitic transfer film on the CI counter-body was observed to increase as the sliding distance progressed. This observation was supported by Raman spectroscopy analysis of the wear scars on the pin, where the G peak intensity (**Figure 6.13**) exhibited higher values. Additionally, SEM/TEM cross-sections were obtained from DLC-GNP1 and pure DLC samples at different time intervals (**Figure 6.14**), further confirmed the formation of the transfer film. The structural changes, indicated by the sp^2/sp^3% ratios obtained from EELS spectra results (**Table 6.2**), demonstrated an increase in sliding time. The underlying mechanism for this phenomenon can be attributed to the contact mechanics at the interface between DLC-GNP and the counter-body.

The higher coverage of GNP results in a more significant load being carried by the DLC film, as the GNP has a lower hardness. Consequently, the real contact area decreases, increasing contact pressure on the DLC regions. This elevated pressure contributes to the conversion of sp^3 bonds to sp^2, promoting graphitisation due to the pressure-induced effects [63,64].

The formation of the transfer film can be explained by the Velocity Accommodation Mode (VAM) model, which suggests that the growth of the carbon transfer film is facilitated by the interaction of wear particles from the CI and DLC surfaces, as well as interfacial sliding. This phenomenon is illustrated in **Figure 7.11**. It is important to note that the VAM model is commonly observed in DLC films in dry and lubricated environments [71,249]. The presence of iron wear particles within the carbon transfer film, as confirmed by TEM and EDS analysis (**Section 6.6**), supports the validity of the VAM model for both pure DLC and DLC-GNP counter-bodies. However, it is worth mentioning that the iron wear particles also exhibited the presence of oxygen.

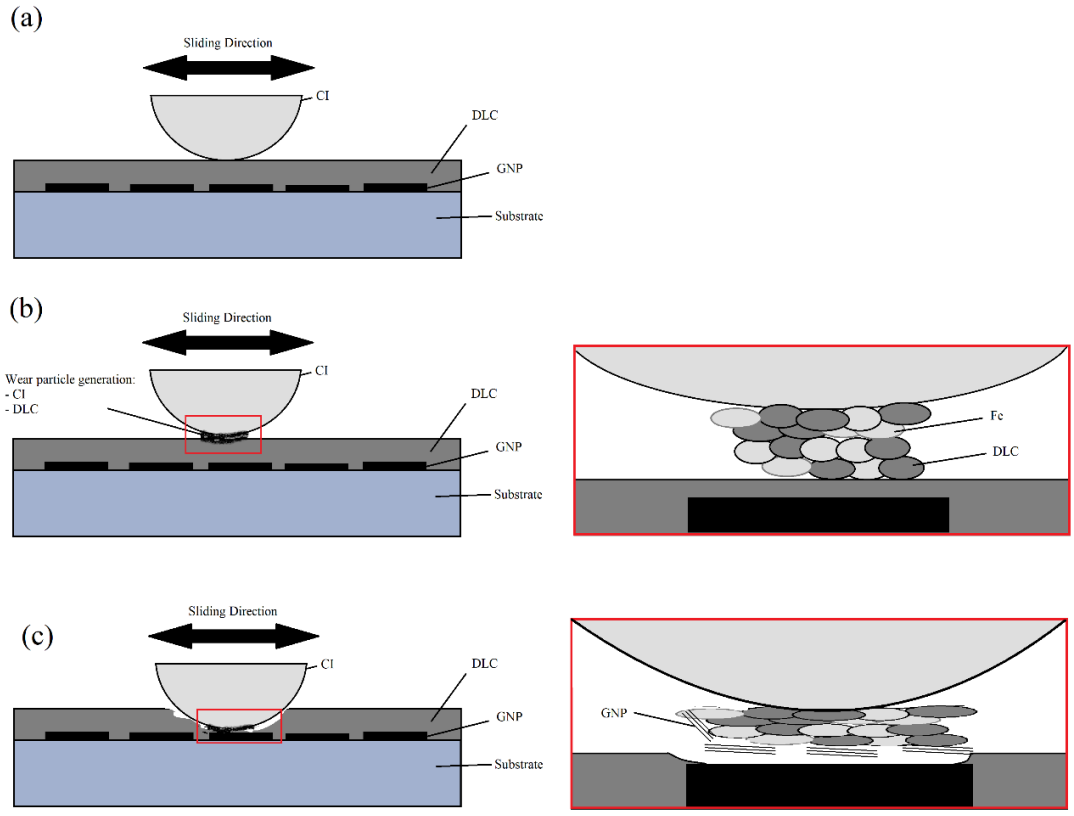

Figure 7.11 *Proposed transfer film formation for DLC-GNP nanocomposites, at (a) initial contact, (b) moments after wear, with wear particles (Fe and DLC) being generated and positioned between the CI counter-body and DLC, and (c) after wear reaches GNP islands, shearing of the GNP is observed, and the interfacial sliding DLC/Fe wear particles induces phase changes due to pressure.*

The research conducted by Al-Aziz [220] established a connection between the thickness of the transfer film and an elevated wear rate for the film. This can be attributed to the consumption of the film in the process of creating the transfer film, as depicted in **Figure 7.11**. The findings obtained in this study further validate this hypothesis, as higher G peak intensities are observed to correspond with increased wear.

EDS scans conducted on the CI transfer films have confirmed the presence of oxygen throughout the film. To investigate this further, a small study was conducted involving the placement of Teflon tape over GNP on a Si substrate, with another sample left uncovered. Both samples were subjected to an oven temperature of 200°C for 3 hours and subsequently analysed using Raman spectroscopy to detect any significant changes in the GNP structure and the presence of oxygen. It is worth noting that while the study did not detect significant changes in the GNP structure, it is possible that the more energetic edge sites of GNP could bind to oxygen, which may not have been detected [250]. Additionally, the oxygen could originate from the storage of the DLC-GNP in an atmospheric environment or from the surface layer of the CI pin itself [112].

7.5. Proposed Mechanism for Friction Reduction in DLC-GNP Nanocomposites

The proposed mechanism for low friction and wear in this thesis is predicated on the previous discussion in this chapter collating the information. When considering the discussion of the results of **Chapters 7.1 – 7.4**, the formation of a proposed low friction mechanism (**Figure 7.12**) observed in DLC-GNP nanocomposites is presented. The study's findings and relevant published literature support the mechanism presented in this section.

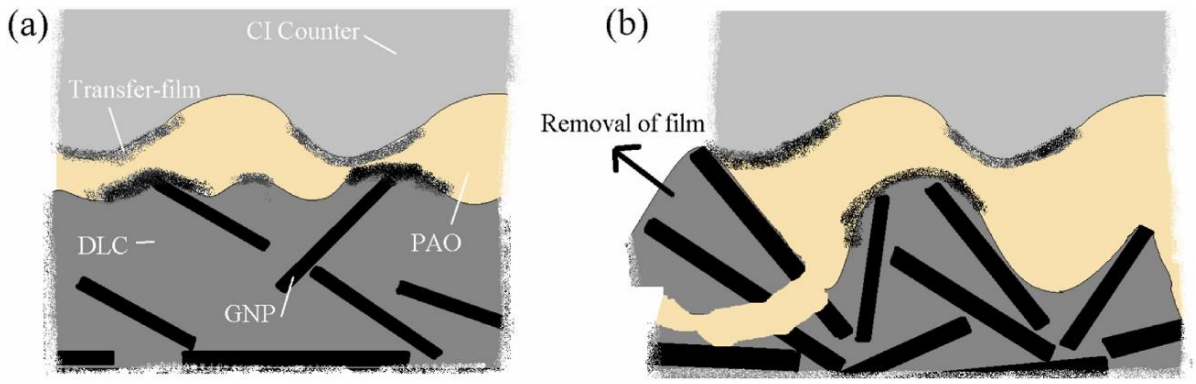

Figure 7.12 *Mechanism for friction and wear reduction in a DLC-GNP composite with (a) low concentration of GNP, and (b) high concentration of clustered GNPs within the DLC matrix, with removal of high asperity GNP islands* [199].

The mechanism for friction reduction is presented below with the evidence throughout the thesis presented to provide a reliable depth of defence:

I. Wear is initially high due to the size of the asperities between the two articulating surfaces.

Section 7.1 presents evidence that an increase in either GNP concentration or DLC thickness leads to a rise in the mean surface roughness and peak height. This observation aligns with the conclusions drawn from relevant published literature [226], which suggest that heightened surface roughness results in an augmented contact area through asperities, subsequently leading to increased wear. It is important to note that the wear rate demonstrates a decreasing trend as time progresses (**Figure 6.4**), and the occurrence of polishing wear can be observed in **Figure 4.29** for DLC-GNP.

II. The DLC becomes worn away as wear continues, exposing the bulk of GNP underneath. There will be some GNP close to the surface, but a thin layer of DLC covers most.

The thickness of the DLC is essential to the friction reduction. The thicker the layer, the longer it is before the GNP is exposed to the CI during wear. But thinner coatings allow

the removal of GNP during wear **Figure 5.11**. The SEM cross-section (**Figure 4.11** and **Figure 4.12**) proves that the GNP disperse throughout the coating.

III. *The GNP shears and forms a protective layer on the surface of the composite film. These form areas or pockets of lubrication.*

The increase in GNP coverage can be observed in **Figure 4.23** and **Figure 6.3**, providing compelling evidence for the shearing of GNP on the composite surface. These findings align with existing literature [238], which suggests the presence of pockets of lubrication within the composite, creating localized areas of enhanced lubrication.

IV. *The GNP, DLC, and CI wear and form a graphitic transfer film.*

A notable change in the I_D/I_G ratio and peak positions is observed over time, indicating the formation of a graphitic film (**Figure 6.7** & **Figure 6.8**). This is further supported by the increase in graphitic content within the transfer film, which is influenced by both time and GNP coverage (**Table 6.2** & **Figure 4.34**). Additionally, the thickness of the transfer layer on the CI counter-body exhibits a noticeable increase with time (**Table 6.1**). These findings collectively demonstrate the progressive development and growth of the transfer film over the sliding duration.

V. *The transfer film is higher-quality graphitic content (i.e. fewer dangling bonds), reducing the adhesive forces during sliding.*

The graphitic contact of the transfer film increases with both time and GNP coverage (**Table 6.2** & **Figure 4.34**). It is well-known that intermolecular bonds can contribute to increased friction in carbon-based materials; therefore, when these bonds are saturated or reduced, it decreases adhesion-based friction [99,251]. SEM images (***Figure 4.29)*** illustrate the wear mechanism's transition from adhesive to polishing wear. The composition of the transfer layer on the CI counter-body consists of carbon and iron,

which aligns with the Velocity Accommodation Mode (VAM) model (**Figure 6.15** & **Figure 6.16**).

VI. *The GNP shear and form small, cylindrical wear particles that roll between the articulating surfaces, reducing friction and wear.*

The shearing of GNP particles contributes to the formation of a protective layer on the surface of the composite film (**Figure 4.23**). TEM micrographs (**Figure 4.26**) and previous studies have demonstrated that the rolling effect of similar particles can effectively reduce friction and wear by minimizing the actual contact area [113].

VII. *The inclusion of GNP creates discrete areas of low pressure (GNP islands) but increases the pressure on the bulk DLC matrix. This reduces the real area of contact and leads to lower friction.*

In **Section 7.3**, contact mechanics are proposed based on the presence of discrete areas with low hardness and elastic modulus. These localised pressure differences can reduce the effective contact area and decrease friction. Similar behaviour has been observed in textured films and GLC composites [60,112].

VIII. *If the DLC is too thick, the GNP will not reach the contact to the CI counter-body to contribute to the friction reduction.*

It is observed that when the coating thickness is increased significantly (**Section 7.1)**, the time required to reach a steady-state coefficient of friction (COF) also increases. This indicates that a thicker coating isolates the GNP, providing a prolonged period before a steady state frictional response is observed. This finding highlights the importance of coating thickness in achieving long-lasting friction reduction effects.

Chapter 8 - Conclusion and Further Work

Section 2.6 conducted a comprehensive gap analysis to identify research gaps in the current state of art in DLC and graphene-based tribology. In **Sections 8.1.1** to **8.1.3,** specific reference will be made to the research gaps identified in **Section 2**, which pertains to the proposed mechanism in **Section 7.7**.

8.1. Overall Conclusion

This study aims to develop a friction and wear reduction method without environmentally hazardous additives, aligning with net zero requirements. The findings reveal a graphitic carbon film formation on the CI counter-body due to sliding wear against DLC-GNP films, leading to reduced adhesive forces. These insights advance our understanding and pave the way for future friction and wear reduction developments.

8.1.1. Effect of GNP Coverage on the Tribological Properties of DLC-GNP Nanocomposites (Research Gap 1, 4 and 5)

- The mechanical properties of DLC-GNP nanocomposites are modified by adding GNP into the DLC matrix. The discrete GNP islands have a lower mechanical property than the surrounding DLC matrix.
- The addition of GNP improves adhesion (L_{C2} and L_{C3}) but only up to 4.5% coverage; above this, the adhesion starts to decrease.
- The tribological performance of DLC-GNP nanocomposites improves up to 4.5% coverage and decreases above this value.
- The Raman spectra, specifically the I_D/I_G values, confirm the presence of a transfer film on the CI counter-body, increasing the GNP coverage.
- The wear particles generated from the DLC-GNP1 were smaller than that of pure DLC, with cigarillo-shaped particles, which could act as rollers during wear,

reducing the real contact area and changing the sliding mechanism into a rolling type.

8.1.2. Effect of DLC Deposition Time on the Tribological and Mechanical Properties of DLC-GNP Nanocomposites (Research Gap 3)

- A thickness of ~1.2 um was experimentally measured to ensure GNP are not removed during sliding wear.
- The elastic modulus and hardness increase as the DLC deposition time increases. This is likely due to the GNP having a thicker layer of DLC above them.
- The duration for frictional traces to reach a steady state increased with thicker DLC films. Notably, the DLC film deposited for 22.5 minutes demonstrated an almost instantaneous reduction in COF, while the thickest film required longer stabilisation.

8.1.3. Effect of Sliding Distance on the Tribological Properties of DLC-GNP Nanocomposites (Research Gap 2 & 4)

- The specific wear rate of the DLC-GNP decreases as a function of sliding distance. The frictional response of the DLC-GNP1 decreases at a faster velocity than that of pure DLC and manages to maintain low friction for the entire 30 hours of wear.
- The graphitic transfer film on the CI is thinner for DLC-GNP than pure DLC as a function of time. The transfer film is also more graphitic, reducing the dangling bonds' adhesive interactions.

8.2. Suggested Further Work

Incorporating GNP into a DLC matrix has demonstrated beneficial effects on tribological properties. While this thesis focused on specific environments and testing configurations, the potential applications of these coatings in alternative environments still need to be explored. Further research can build upon the findings presented in this study and investigate additional avenues to enhance and expand the understanding of the friction reduction mechanism in DLC-GNP nanocomposites. The suggested future work outlined below aims to bridge the existing research (Research Gap 6) with potential directions for further development and strengthening of this mechanism.

8.2.1. Testing Conditions

The testing conditions employed in this study were specifically tailored to a cam follower environment, simulating pressures ranging from 600 MPa to 700 MPa. Building upon the proposed mechanism presented in **Section 7.7**, which integrates transfer film formation and contact mechanics discussed in **Sections 7.3** and **7.5**, there are opportunities to further strengthen this mechanism by exploring two key variables: contact pressure and temperature. A deeper understanding of the friction reduction mechanism in DLC-GNP nanocomposites can be achieved by varying these factors.

8.2.1.1. Contact Pressure

Section 7.5 provides evidence that graphitisation can occur at temperatures below the phase transformation range of 350-600°C [59,221], suggesting the influence of contact pressure on the formation of the transfer film. To enhance the understanding of this mechanism and its relation to transfer film formation, it is crucial to investigate contact pressures that are significantly lower than those calculated using the equation presented by Solis *et al.* [128]**.** A more comprehensive understanding of the frictional and wear

response can be attained by studying the formation of the transfer film in response to varying pressures.

8.2.1.2. Temperature

To further investigate the effects of temperature on friction and wear behaviour, it is recommended to conduct experiments at a range of temperatures between 0°C and 200°C. This broader temperature range would allow for an exploration of the thermodynamics governing the $sp^3 \rightarrow sp^2$ phase transformation and its relation to the formation of the transfer film. Previous research [252] has indicated that higher temperatures can increase graphitisation and wear in DLC coatings, although the coefficient of friction (COF) tends to decrease. In the case of DLC-GNP coatings, it has been observed that they produce a thinner transfer film on the counter-body. Therefore, studying the behaviour of DLC-GNP coatings at elevated temperatures can provide valuable insights and potentially improve the proposed mechanism. On the other hand, the influence of lower temperatures is also crucial to consider, as the phase transformation of DLC typically occurs around 350-600°C [59,221]. Operating at lower temperatures may limit the synergistic effects between the GNP and DLC, potentially impacting the transfer film formation according to the Velocity Accommodation Mode (VAM) model.

8.2.1.3. Graphene Nanoplatelet Size

The size of graphene sheets can impact the frictional response, as demonstrated by previous studies [253–256]. Multi-layer graphene, for instance, has shown friction-reducing properties by transferring carbon material between sliding layers. By manipulating the particle size, it is possible to decrease the forces per unit length, which may facilitate the creation of a transfer layer on both the counter-body and the film. Thus, conducting further research to investigate the influence of GNP thickness and particle size on tribological properties would be valuable. These findings can then be compared

and analysed alongside the existing results, allowing for a comprehensive exploration of the observed differences.

8.2.1.4. Changing the DLC Structure

The work conducted in this thesis utilised an a-C:H coating, where hydrogen was employed to lower the transformation temperature through structural collapse, as described by the model developed by Solis *et al.* [128]. To compare the effects of hydrogen on friction and wear, it would be valuable to explore a coating without hydrogen, such as Ta-C. Ta-C films are known to exhibit less graphitisation compared to a-C:H films [257]. Consequently, incorporating GNP into the film structure may enhance the transfer of a graphitised layer, potentially reducing wear by introducing a low-shear graphitised layer. These findings would contribute to the existing proposed mechanism. Moreover, Ta-C coatings find application in various fields, offering an additional avenue for their utilisation.

8.2.1.5. Alternative Counter-body Materials

In this thesis, the utilisation of CI as the counter-body facilitated the diffusion of carbon into it, resulting in bond formation and the development of a transfer layer [73]. In contrast, materials like germanium exhibit low carbon solubility and have demonstrated reduced wear when sliding against a-C:H coatings [258].

By exploring different counter-body materials, a more thorough understanding of tribological performance can be achieved.

References

[1] Gilfillan D, Marland G. CDIAC-FF: global and national CO 2 emissions from fossil fuel combustion and cement manufacture: 1751–2017. Earth Syst Sci Data 2021;13:1667–80.

[2] Soeder DJ. Fossil Fuels and Climate Change. Fracking Environ., Springer; 2021, p. 155–85.

[3] H M Government. Net Zero Strategy: Build Back Greener 2021.

[4] Blasing TJ, Boden T, Broniak C, Gregg J, Losey L, Treanton K. An Introduction to CO2 Emissions from Fossil Fuels 2023.

[5] Holmberg K, Andersson P, Erdemir A. Global energy consumption due to friction in passenger cars. Tribol Int 2012;47:221–34.

[6] Holmberg K, Erdemir A. Influence of tribology on global energy consumption, costs and emissions. Friction 2017;5:263–84.

[7] Hannappel R. The impact of global warming on the automotive industry. AIP Conf. Proc., vol. 1871, AIP Publishing LLC; 2017, p. 60001.

[8] Tóth ÁD, Szabó ÁI, Leskó MZ, Rohde-Brandenburger J, Kuti R. Tribological properties of the nanoscale spherical Y2O3 particles as lubricant additives in automotive application. Lubricants 2022;10:28.

[9] Cha SC, Moon K Il, Yoon HW. Current Development of Automotive Powertrain Components for Low Friction and Wear Reduction through Coating and Heat Treatment Technology. Lubr Manag Frict Reduct n.d.

[10] Thornley A, Wang Y, Wang C, Chen J, Huang H, Liu H, et al. Optimizing the Mo concentration in low viscosity fully formulated oils. Tribol Int 2022;168:107437.

[11] Bruce RW. CRC Handbook of Lubrication: Theory and Practice of Tribology, Volume II: Theory and Design. CRC Press; 2010.

[12] Ogbeide SO. An investigation to the recycling of spent engine oil. J Eng Sci Technol Rev 2010;3:32–5.

[13] Osman DI, Attia SK, Taman AR. Recycling of used engine oil by different solvent. Egypt J Pet 2018;27:221–5.

[14] Alimova Z, Makhamajanov M-I, Magdiev K. The effect of changes in the viscosity parameters of engine oils on the operation of engine parts. Eurasian J Acad Res 2022;2:151–4.

[15] Bouchet M de B, Martin JM, Matta C, Joly-Pottuz L. The future of boundary lubrication by carbon coatings and environmentally friendly additives. Adv. Tribol. Proc. Cist. ITS-IFToMM2008, Springer; 2010, p. 598–9.

[16] Kano M. Overview of DLC-coated engine components. Coat Technol Veh Appl 2015:37–62.

[17] Kosarieh S, Morina A, Flemming J, Lainé E, Neville A. Wear Mechanisms of

Hydrogenated DLC in Oils Containing MoDTC. Tribol Lett 2016;64:4.

[18] Donnet C, Erdemir A. New horizon in the tribology of diamondlike carbon films. Surf Eng 2008;24:399–401.

[19] Vejpravová J. Mixed sp2–sp3 Nanocarbon Materials: A Status Quo Review. Nanomaterials 2021;11.

[20] Berman D, Erdemir A, Sumant A V. Graphene: a new emerging lubricant. Mater Today 2014;17:31–42.

[21] Meng Q, Kuan H-C, Araby S, Kawashima N, Saber N, Wang CH, et al. Effect of interface modification on PMMA/graphene nanocomposites. J Mater Sci 2014;49:5838–49.

[22] Puértolas JA, Castro M, Morris JA, Ríos R, Ansón-Casaos A. Tribological and mechanical properties of graphene nanoplatelet/PEEK composites. Carbon N Y 2019;141:107–22.

[23] Lin J, Wang L, Chen G. Modification of graphene platelets and their tribological properties as a lubricant additive. Tribol Lett 2011;41:209–15.

[24] Kogovšek J, Kalin M. Lubrication performance of graphene-containing oil on steel and DLC-coated surfaces. Tribol Int 2019;138:59–67.

[25] Roselina. Nik Roselina binti Nik Roseley - Fabrication and Characterization of DLC-graphene Nanocomposite Coatings for Tribological Application - Leeds University PhD thesis. 2018.

[26] Robertson J. Diamond-like amorphous carbon. Mater Sci Eng R Reports 2002;37:129–281.

[27] Pierson HO. Handbook of Carbon, Graphite, Diamonds and Fullerenes: Processing, Properties and Applications. Elsevier Science; 2012.

[28] Chung DDL. Review graphite. J Mater Sci 2002;37:1475–89.

[29] RozpAlocha F, Patyka J, Stankowskib J. Graphenes bonding forces in graphite 2007.

[30] Geim AK, Novoselov KS. The rise of graphene. Nat Mater 2007;6:183–91.

[31] Scendo M, Staszewska-Samson K. Effect of Temperature on Anti-Corrosive Properties of Diamond-Like Carbon Coating on S355 Steel. Materials (Basel) 2019;12:1659.

[32] Rajak DK, Kumar A, Behera A, Menezes PL. Diamond-like carbon (DLC) coatings: Classification, properties, and applications. Appl Sci 2021;11:4445.

[33] Grill A. Diamond-like carbon: state of the art. Diam Relat Mater 1999;8:428–34.

[34] Lemoine P, Quinn JP, Maguire PD, McLaughlin JA. Mechanical characterisation and properties of DLC films. Tribol Diamond-Like Carbon Film 2008:83–101.

[35] Erdemir A, Donnet C. Tribology of diamond-like carbon films: recent progress and future prospects. J Phys D Appl Phys 2006;39:R311.

[36] Major GH, Fairley N, Sherwood PMA, Linford MR, Terry J, Fernandez V, et al.

Practical guide for curve fitting in x-ray photoelectron spectroscopy. J Vac Sci Technol A Vacuum, Surfaces, Film 2020;38:61203.

[37] Paik N. Raman and XPS studies of DLC films prepared by a magnetron sputter-type negative ion source. Surf Coatings Technol 2005;200:2170–4.

[38] Mérel P, Tabbal M, Chaker M, Moisa S, Margot J. Direct evaluation of the sp3 content in diamond-like-carbon films by XPS. Appl Surf Sci 1998;136:105–10.

[39] Galvan D, Pei YT, De Hosson JTM, Cavaleiro A. Determination of the sp3 C content of aC films through EELS analysis in the TEM. Surf Coatings Technol 2005;200:739–43.

[40] Shard AG. Practical guides for x-ray photoelectron spectroscopy: Quantitative XPS. J Vac Sci Technol A Vacuum, Surfaces, Film 2020;38:41201.

[41] Mabuchi Y, Higuchi T, Weihnacht V. Effect of sp2/sp3 bonding ratio and nitrogen content on friction properties of hydrogen-free DLC coatings. Tribol Int 2013;62:130–40.

[42] Ferrari AC, Robertson J. Interpretation of Raman spectra of disordered and amorphous carbon. Phys Rev B 2000;61:14095.

[43] Ferrari AC. Raman spectroscopy of graphene and graphite: Disorder, electron–phonon coupling, doping and nonadiabatic effects. Solid State Commun 2007;143:47–57.

[44] Donnet C, Erdemir A. Tribology of Diamond-like Carbon Films: Fundamentals and Applications. Springer US; 2007.

[45] Sha B, Lukianov A, Klyui M, Dusheiko M, Kasatkin V, Lozinskii V, et al. Optical properties of carbon films obtained by plasma-enhanced chemical vapor deposition. 2019 IEEE 39th Int. Conf. Electron. Nanotechnol., IEEE; 2019, p. 365–8.

[46] Choy KL. Chemical vapour deposition of coatings. Prog Mater Sci 2003;48:57–170.

[47] Meyer DE, Dillon RO, Woollam JA. Radio-frequency plasma chemical vapor deposition growth of diamond. J Vac Sci Technol A Vacuum, Surfaces, Film 1989;7:2325–7.

[48] Fedosenko G, Schwabedissen A, Engemann J, Braca E, Valentini L, Kenny JM. Pulsed PECVD deposition of diamond-like carbon films. Diam Relat Mater 2002;11:1047–52.

[49] Hainsworth S V, Uhure NJ. Diamond like carbon coatings for tribology: production techniques, characterisation methods and applications. Int Mater Rev 2007;52:153–74.

[50] Robertson J. Classification of diamond-like carbons. Tribol. Diamond-Like Carbon Film., Springer; 2008, p. 13–24.

[51] Neyts E, Bogaerts A, van de Sanden MCM. Modeling PECVD growth of nanostructured carbon materials. High Temp Mater Process An Int Q High-Technology Plasma Process 2009;13.

[52] Wolf S. Silicon processing for the VLSI era. LATTICE, 1995, p. 559–81.

[53] Kim YT, Cho SM, Choi WS, Hong B, Yoon DH. Dependence of the bonding structure of DLC thin films on the deposition conditions of PECVD method. Surf Coatings Technol 2003;169–170:291–4.

[54] Win Khun N, Neville A, Kolev I, Zhao H. Effects of Substrate Bias on Tribological Properties of Diamondlike Carbon Thin Films Deposited Via Microwave-Excited Plasma-Enhanced Chemical Vapor Deposition. J Tribol 2016;138:31301.

[55] Lin Z, Lv S-B, Yu Z-J, Li M, Lin T-Y, Ba D-C, et al. Effect of bias voltage on Diamond-like carbon film deposited on PMMA substrate. Surf Coatings Technol 2008;202:5386–9.

[56] Wang Y, Pu J, Wang J, Li J, Chen J, Xue Q. Interlayer design for the graphite-like carbon film with high load-bearing capacity under sliding-friction condition in water. Appl Surf Sci 2014;311:816–24.

[57] Wei C, Yen J-Y. Effect of film thickness and interlayer on the adhesion strength of diamond like carbon films on different substrates. Diam Relat Mater 2007;16:1325–30.

[58] Chen C-C, Hong FC-N. Interfacial studies for improving the adhesion of diamond-like carbon films on steel. Appl Surf Sci 2005;243:296–303.

[59] Liu J, Muíños HV, Nordlund K, Djurabekova F. Structural properties of protective diamond-like-carbon thin films grown on multilayer graphene. J Phys Condens Matter 2019;31:505703.

[60] He D, He C, Li W, Shang L, Wang L, Zhang G. Tribological behaviors of in-situ textured DLC films under dry and lubricated conditions. Appl Surf Sci 2020;525:146581.

[61] Tasdemir HA, Wakayama M, Tokoroyama T, Kousaka H, Umehara N, Mabuchi Y, et al. Ultra-low friction of tetrahedral amorphous diamond-like carbon (ta-C DLC) under boundary lubrication in poly alpha-olefin (PAO) with additives. Tribol Int 2013;65:286–94.

[62] Hauert R. An overview on the tribological behavior of diamond-like carbon in technical and medical applications. Tribol Int 2004;37:991–1003.

[63] Voevodin AA, Phelps AW, Zabinski JS, Donley MS. Friction induced phase transformation of pulsed laser deposited diamond-like carbon. Diam Relat Mater 1996;5:1264–9.

[64] Le Huu T, Zaidi H, Paulmier D, Voumard P. Transformation of sp3 to sp2 sites of diamond like carbon coatings during friction in vacuum and under water vapour environment. Thin Solid Films 1996;290:126–30.

[65] Zeng Q, Eryilmaz O, Erdemir A. Superlubricity of the DLC films-related friction system at elevated temperature. Rsc Adv 2015;5:93147–54.

[66] Liu Y, Erdemir A, Meletis EI. An investigation of the relationship between graphitization and frictional behavior of DLC coatings. Surf Coatings Technol 1996;86–87:564–8.

[67] Jaoul C, Jarry O, Tristant P, Merle-Méjean T, Colas M, Dublanche-Tixier C, et al. Raman analysis of DLC coated engine components with complex shape: Understanding wear mechanisms. Thin Solid Films 2009;518:1475–9.

[68] Okubo H, Tadokoro C, Hirata Y, Sasaki S. In Situ Raman observation of the graphitization process of tetrahedral amorphous carbon diamond-like carbon under boundary lubrication in poly-alpha-olefin with an organic friction modifier. Tribol Online 2017;12:229–37.

[69] Cui L, Lu Z, Wang L. Probing the low-friction mechanism of diamond-like carbon by varying of sliding velocity and vacuum pressure. Carbon N Y 2014;66:259–66.

[70] Mistry KK, Morina A, Neville A. A tribochemical evaluation of a WC–DLC coating in EP lubrication conditions. Wear 2011;271:1739–44.

[71] Sutton DC, Limbert G, Stewart D, Wood RJK. The friction of diamond-like carbon coatings in a water environment. Friction 2013;1:210–21.

[72] Ronkainen H, Holmberg K. Environmental and thermal effects on the tribological performance of DLC coatings. Tribol. diamond-like carbon Film., Springer; 2008, p. 155–200.

[73] Aboua KAM, Umehara N, Kousaka H, Tokoroyama T, Murashima M, Mustafa MM Bin, et al. Effect of Mating Material and Graphitization on Wear of a-C:H Coating in Boundary Base Oil Lubrication. Tribol Lett 2020;68:24.

[74] Okubo H, Sasaki S. In situ Raman observation of structural transformation of diamond-like carbon films lubricated with MoDTC solution: Mechanism of wear acceleration of DLC films lubricated with MoDTC solution. Tribol Int 2017;113:399–410.

[75] Gao F, Erdemir A, Tysoe WT. The Tribological Properties of Low-friction Hydrogenated Diamond-like Carbon Measured in Ultrahigh Vacuum. Tribol Lett 2005;20:221–7.

[76] Donnet C, Grill A. Friction control of diamond-like carbon coatings. Surf Coatings Technol 1997;94:456–62.

[77] FONTAINE J, LE MOGNE T, LOUBET J-L, BELIN M. How to achieve superlow friction with DLC films? J Adv Sci 2005;17:55–63.

[78] Guo H, Qi Y. Environmental conditions to achieve low adhesion and low friction on diamond surfaces. Model Simul Mater Sci Eng 2010;18:34008.

[79] Li H, Xu T, Wang C, Chen J, Zhou H, Liu H. Effect of relative humidity on the tribological properties of hydrogenated diamond-like carbon films in a nitrogen environment. J Phys D Appl Phys 2004;38:62.

[80] Warner JH, Schaffel F, Rummeli M, Bachmatiuk A. Graphene: Fundamentals and emergent applications. Elsevier Science; 2012.

[81] Spear JC, Ewers BW, Batteas JD. 2D-nanomaterials for controlling friction and wear at interfaces. Nano Today 2015;10:301–14.

[82] Spreadborough J. The frictional behaviour of graphite. Wear 1962;5:18–30.

[83] Landau LD. On the theory of phase transitions. I. Zh Eksp Teor Fiz 1937;11:19.

[84] Kalyoncu RS, Taylor Jr HA. Natural graphite. Kirk-Othmer Encycl Chem Technol 2000.

[85] Wissler M. Graphite and carbon powders for electrochemical applications. J Power Sources 2006;156:142–50.

[86] Vasumathi N, Kumar TVV, Ratchambigai S, Rao SS, Raju GB. Flotation studies on low grade graphite ore from eastern India. Int J Min Sci Technol 2015;25:415–20.

[87] FC T, SL T. Correlation between ID/IG ratio from visible raman spectra and sp2/sp3 ratio from XPS spectra of annealed hydrogenated DLC film. Mater Trans 2006;47:1847–52.

[88] Franklin RE. Crystallite growth in graphitizing and non-graphitizing carbons. Proc. R. Soc. London A Math. Phys. Eng. Sci., vol. 209, The Royal Society; 1951, p. 196–218.

[89] Zuckerman JJ, Atwood JD. Inorganic Reactions and Methods, Formation of Ceramics. Wiley; 2009.

[90] Zhao Q, Nardelli MB, Bernholc J. Ultimate strength of carbon nanotubes : A theoretical study. Phys Rev Appl 2002;65:1–6.

[91] Lee C, Wei X, Kysar JW, Hone J. Measurement of the elastic properties and intrinsic strength of monolayer graphene. Science (80-) 2008;321:385–8.

[92] Kuan C-F, Chiang C-L, Lin S-H, Huang W-G, Hsieh W-Y, Shen M-Y. Characterization and properties of graphene nanoplatelets/XNBR nanocomposites. Polym Polym Compos 2018;26:59–68.

[93] Savage RH. Graphite lubrication. J Appl Phys 1948;19:1–10.

[94] Deacon RF, Goodman JF. Lubrication by Lamellar Solids. Proc R Soc Lond A Math Phys Sci 1958;243:464–82.

[95] Gould T, Simpkins K, Dobson JF. Theoretical and semiempirical correction to the long-range dispersion power law of stretched graphite. Phys Rev B 2008;77:165134.

[96] Wang W, Dai S, Li X, Yang J, Srolovitz DJ, Zheng Q. Accurate Measurement of the Cleavage Energy of Graphite. ArXiv Prepr ArXiv150600536 2015.

[97] Rowe GW. Some observations on the frictional behaviour of boron nitride and of graphite. Wear 1960;3:274–85.

[98] Yen BK, Schwickert BE, Toney MF. Origin of low-friction behavior in graphite investigated by surface x-ray diffraction. Appl Phys Lett 2004;84:4702–4.

[99] Xiao J, Zhang L, Zhou K, Li J, Xie X, Li Z. Anisotropic friction behaviour of highly oriented pyrolytic graphite. Carbon N Y 2013;65:53–62.

[100] Jones GA. On the tribological behaviour of mechanical seal face materials in dry line contact: Part I. Mechanical carbon. Wear 2004;256:415–32.

[101] Xue CY, Wang SR, Leng JF, Wang Y, Wang GQ. Tribological Performance Of

Modified Flocculent Graphite As Lubricant Additives. Surf Rev Lett 2020;27:1950108.

[102] Huang HD, Tu JP, Gan LP, Li CZ. An investigation on tribological properties of graphite nanosheets as oil additive. Wear 2006;261:140–4.

[103] Stoyanov P, Chromik RR. Scaling Effects on Materials Tribology: From Macro to Micro Scale. Materials (Basel) 2017;10.

[104] Kim K-S, Lee H-J, Lee C, Lee S-K, Jang H, Ahn J-H, et al. Chemical vapor deposition-grown graphene: the thinnest solid lubricant. ACS Nano 2011;5:5107–14.

[105] Li Q, Lee C, Carpick RW, Hone J. Substrate effect on thickness-dependent friction on graphene. Phys Status Solidi 2010;247:2909–14.

[106] Shi Z, Shum P, Wasy A, Zhou Z, Li LK-Y. Tribological performance of few layer graphene on textured M2 steel surfaces. Surf Coatings Technol 2016;296:164–70.

[107] Aissou T, Veilleux J, Braidy N. A New One-Step Deposition Approach for a Low Friction Graphene Nanoflakes Coating. ITSC2021, ASM International; 2021, p. 676–81.

[108] Senatore A, D'Agostino V, Petrone V, Ciambelli P, Sarno M. Graphene oxide nanosheets as effective friction modifier for oil lubricant: materials, methods, and tribological results. ISRN Tribol 2013;2013.

[109] Zheng D, Cai Z, Shen M, Li Z, Zhu M. Investigation of the tribology behaviour of the graphene nanosheets as oil additives on textured alloy cast iron surface. Appl Surf Sci 2016;387:66–75.

[110] Marlinda AR, Thien GSH, Shahid M, Ling TY, Hashem A, Chan K-Y, et al. Graphene as a Lubricant Additive for Reducing Friction and Wear in Its Liquid-Based Form. Lubricants 2023;11:29.

[111] Guo Y, Guo P, Sun L, Li X, Ke P, Li Q, et al. Tribological properties of Ti-doped diamond-like carbon coatings under dry friction and PAO oil lubrication. Surf Interface Anal 2019;51:361–70.

[112] Al-Azizi AA, Eryilmaz O, Erdemir A, Kim SH. Nano-texture for a wear-resistant and near-frictionless diamond-like carbon. Carbon N Y 2014;73:403–12.

[113] Berman D, Deshmukh SA, Sankaranarayanan SKRS, Erdemir A, Sumant A V. Macroscale superlubricity enabled by graphene nanoscroll formation. Science (80-) 2015;348:1118–22.

[114] Wei C, Yang J-F, Wang C-I. The effect of CNT content on the tribological properties of CNTs doped diamond-like carbon films. Key Eng Mater 2015;642.

[115] Wei C, Wang C-I, Tai F-C, Ting K, Chang R-C. The effect of CNT content on the surface and mechanical properties of CNTs doped diamond like carbon films. Diam Relat Mater 2010;19:562–6.

[116] Li X, Dai W, Wang Q, Liang Y, Wu Z. Diamond-like/graphite-like carbon composite films deposited by high-power impulse magnetron sputtering. Diam

Relat Mater 2020;106:107818.

[117] Shi X, Liskiewicz TW, Beake BD, Chen J, Wang C. Tribological performance of graphite-like carbon films with varied thickness. Tribol Int 2019:105586.

[118] McGrath SP, Micó C, Zhao FJ, Stroud JL, Zhang H, Fozard S. Predicting molybdenum toxicity to higher plants: estimation of toxicity threshold values. Environ Pollut 2010;158:3085–94.

[119] Kano M. Super low friction of DLC applied to engine cam follower lubricated with ester-containing oil. Tribol Int 2006;39:1682–5.

[120] Abdullah Tasdemir H, Wakayama M, Tokoroyama T, Kousaka H, Umehara N, Mabuchi Y, et al. The effect of oil temperature and additive concentration on the wear of non-hydrogenated DLC coating. Tribol Int 2014;77:65–71.

[121] Dörr N, Agocs A, Besser C, Ristić A, Frauscher M. Engine Oils in the Field: A Comprehensive Chemical Assessment of Engine Oil Degradation in a Passenger Car. Tribol Lett 2019;67:68.

[122] Wang P, Wang X, Xu T, Liu W, Zhang J. Comparing internal stress in diamond-like carbon films with different structure. Thin Solid Films 2007;515:6899–903.

[123] Liu K, Kang J, Zhang G, Lu Z, Yue W. Effect of temperature and mating pair on tribological properties of DLC and GLC coatings under high pressure lubricated by MoDTC and ZDDP. Friction 2021;9:1390–405.

[124] Li X, Deng X, Kousaka H, Umehara N. Comparative study on effects of load and sliding distance on amorphous hydrogenated carbon (a-C:H) coating and tetrahedral amorphous carbon (ta-C) coating under base-oil lubrication condition. Wear 2017;392–393:84–92.

[125] Yorkshire Steel, M2 Tool Steel n.d. https://www.westyorkssteel.com/steel-specifications/bs-steel/bs4659/bm2/.

[126] Miihkinen VTT, Pietikäinen J. Fracture toughness, strain hardening and life of AISI M2 high speed steel taps. Mater Sci Eng 1986;78:45–53.

[127] Takeno T, Sugawara T, Miki H, Takagi T. Deposition of DLC film with adhesive W-DLC layer on stainless steel and its tribological properties. Diam Relat Mater 2009;18:1023–7.

[128] Solis J, Zhao H, Wang C, Verduzco JA, Bueno AS, Neville A. Tribological performance of an H-DLC coating prepared by PECVD. Appl Surf Sci 2016;383:222–32.

[129] Shahsavari F, Ehteshamzadeh M, Amin MH, Barlow AJ. A comparative study of surface morphology, mechanical and tribological properties of DLC films deposited on Cr and Ni nanolayers. Ceram Int 2020;46:5077–85.

[130] Beake BD, Liskiewicz TW, Vishnyakov VM, Davies MI. Development of DLC coating architectures for demanding functional surface applications through nano- and micro-mechanical testing. Surf Coatings Technol 2015;284:334–43.

[131] SigmaAldrich. Graphene Nanoplatelets Sigma Aldrich n.d. https://www.sigmaaldrich.com/catalog/product/aldrich/900412?lang=en&region=

GB.

[132] Hong J, Park MK, Lee EJ, Lee D, Hwang DS, Ryu S. Origin of new broad Raman D and G peaks in annealed graphene. Sci Rep 2013;3:2700.

[133] Archard J. Contact and rubbing of flat surfaces. J Appl Phys 1953;24:981–8.

[134] Bruker. NPFLEX 3D Surface Metrology 2018. https://www.bruker.com/products/surface-and-dimensional-analysis/3d-optical-microscopes/npflex/learn-more.html.

[135] Bai M, Yang L, Li J, Luo L, Sun S, Inkson B. Mechanical and tribological properties of Si and W doped diamond like carbon (DLC) under dry reciprocating sliding conditions. Wear 2021;484–485:204046.

[136] Hevia SA, Bejide M, Duran B, Rosenkranz A, Ruiz HM, Favre M, et al. Nanometric thin films of non-doped diamond-like carbon grown on n-type (P-doped) silicon substrates as electrochemical electrodes. J Solid State Electrochem 2018;22:2845–53.

[137] Urbonaite S, Wachtmeister S, Mirguet C, Coronel E, Zou WY, Csillag S, et al. EELS studies of carbide derived carbons. Carbon N Y 2007;45:2047–53.

[138] Xu N, Wang C, Yang L, Barimah EK, Jose G, Neville A, et al. Nano-scale coating wear measurement by introducing Raman-sensing underlayer. J Mater Sci Technol 2022;96:285–94.

[139] Zhang Z, Brydson R, Aslam Z, Reddy S, Brown A, Westwood A, et al. Investigating the structure of non-graphitising carbons using electron energy loss spectroscopy in the transmission electron microscope. Carbon N Y 2011;49:5049–63.

[140] Mironov BE, Freeman HM, Brown AP, Hage FS, Scott AJ, Westwood AVK, et al. Electron irradiation of nuclear graphite studied by transmission electron microscopy and electron energy loss spectroscopy. Carbon N Y 2015;83:106–17.

[141] Chhowalla M, Robertson J, Chen CW, Silva SRP, Davis CA, Amaratunga GAJ, et al. Influence of ion energy and substrate temperature on the optical and electronic properties of tetrahedral amorphous carbon (ta-C) films. J Appl Phys 1997;81:139–45.

[142] Jones BEM and AVKW and AJS and RB and AN. Structure of different grades of nuclear graphite. J Phys Conf Ser 2012;371:12017.

[143] Pang H, Wang X, Zhang G, Chen H, Lv G, Yang S. Characterization of diamond-like carbon films by SEM, XRD and Raman spectroscopy. Appl Surf Sci 2010;256:6403–7.

[144] Wang Y, Alsmeyer DC, McCreery RL. Raman spectroscopy of carbon materials: structural basis of observed spectra. Chem Mater 1990;2:557–63.

[145] Tadayyoni MA, Dando NR. Normal and surface-enhanced Raman investigations of carbon materials. Appl Spectrosc 1991;45:1613–6.

[146] Bokobza L, Bruneel J-L, Couzi M. Raman spectroscopy as a tool for the analysis of carbon-based materials (highly oriented pyrolitic graphite, multilayer graphene

and multiwall carbon nanotubes) and of some of their elastomeric composites. Vib Spectrosc 2014;74:57–63.

[147] He M, Yeo C. Evaluation of Thermal Degradation of DLC Film Using a Novel Raman Spectroscopy Technique. Coatings 2018;8.

[148] Adar F. Use of Raman Spectroscopy to Qualify Carbon Materials. Spectroscopy 2022;37:11–5.

[149] Haddock D, Parker T, Spindloe C, Tolley M. Characterisation of Diamond-Like Carbon (DLC) laser targets by Raman spectroscopy. J. Phys. Conf. Ser., vol. 713, IOP Publishing; 2016, p. 12007.

[150] Ying REN, Hai-Kuo W, DEUERLER F. Multi-peak fitting analysis of visible raman spectra on DLC coatings deposited by vacuum arc. DEStech Trans Mater Sci Eng 2016.

[151] Martins Ferreira EH, Moutinho MVO, Stavale F, Lucchese MM, Capaz RB, Achete CA, et al. Evolution of the Raman spectra from single-, few-, and many-layer graphene with increasing disorder. Phys Rev B 2010;82:125429.

[152] Cui WG, Lai QB, Zhang L, Wang FM. Quantitative measurements of sp3 content in DLC films with Raman spectroscopy. Surf Coatings Technol 2010;205:1995–9.

[153] Endo M, Kim YA, Takeda T, Hong SH, Matusita T, Hayashi T, et al. Structural characterization of carbon nanofibers obtained by hydrocarbon pyrolysis. Carbon N Y 2001;39:2003–10.

[154] Scharf TW, Singer IL. Thickness of diamond-like carbon coatings quantified with Raman spectroscopy. Thin Solid Films 2003;440:138–44.

[155] Pimenta MA, Dresselhaus G, Dresselhaus MS, Cancado LG, Jorio A, Saito R. Studying disorder in graphite-based systems by Raman spectroscopy. Phys Chem Chem Phys 2007;9:1276–90.

[156] Ferrari AC, Robertson J. Resonant Raman spectroscopy of disordered, amorphous, and diamondlike carbon. Phys Rev B 2001;64:75414.

[157] ISO EN. 14577-1: 2015-11; Metallic Materials—Instrumented Indentation Test for Hardness and Materials Parameters—Part 1: Test Method (ISO 14577-1: 2015); German Version EN ISO 14577-1: 2015 (DIN EN ISO 14577-1: 2015-11). Dtsch Inst Für Normung EV DIN Berlin, Ger 2015.

[158] Pharr GM, Oliver WC. Measurement of thin film mechanical properties using nanoindentation. Mrs Bull 1992;17:28–33.

[159] Bull SJ. Failure modes in scratch adhesion testing. Surf Coatings Technol 1991;50:25–32.

[160] Zaidi H, Djamai A, Chin KJ, Mathia T. Characterisation of DLC coating adherence by scratch testing. Tribol Int 2006;39:124–8.

[161] Zhang S, Sun D, Fu Y, Du H. Effect of sputtering target power on microstructure and mechanical properties of nanocomposite nc-TiN/a-SiNx thin films. Thin Solid Films 2004;447:462–7.

[162] Sui X, Liu J, Zhang S, Yang J, Hao J. Microstructure, mechanical and tribological characterization of CrN/DLC/Cr-DLC multilayer coating with improved adhesive wear resistance. Appl Surf Sci 2018;439:24–32.

[163] Mustafa MM Bin, Umehara N, Tokoroyama T, Murashima M, Shibata A, Utsumi Y, et al. Effect of mesh structure of tetrahedral amorphous carbon (ta-C) coating on friction and wear properties under base-oil lubrication condition. Tribol Int 2020;147:105557.

[164] Nayak N, Lakshminarayanan PA, Babu MKG, Dani AD. Predictions of cam follower wear in diesel engines. Wear 2006;260:181–92.

[165] Priest M, Taylor CM. Automobile engine tribology — approaching the surface. Wear 2000;241:193–203.

[166] Ahmad A, Khurram M, Mufti RA, Umar M. Simulating cam and follower wear in valve train. Tribol - Mater Surfaces Interfaces 2020;14:59–65.

[167] Erdemir A. Review of engineered tribological interfaces for improved boundary lubrication. Tribol Int 2005;38:249–56.

[168] Hamrock BJ, Dowson D. Minimum film thickness in elliptical contacts for different regimes of fluid-film lubrication 1978.

[169] Williamson BP, Bell JC. The effects of engine oil rheology on the oil film thickness and wear between a cam and rocker follower. SAE Trans 1996:1767–82.

[170] Kosarieh S, Morina A, Lainé E, Flemming J, Neville A. Tribological performance and tribochemical processes in a DLC/steel system when lubricated in a fully formulated oil and base oil. Surf Coatings Technol 2013;217:1–12.

[171] Towery D, Fury MA. Chapter 6 - Chemical Mechanical Polishing of Organic Polymeric Materials for IC Applications A2 - Nalwa, Hari Singh BT - Handbook of Low and High Dielectric Constant Materials and Their Applications, Burlington: Academic Press; 1999, p. 241–73.

[172] Mobil Super™ 3000 0W-16 low viscosity fully synthetic engine oil n.d. https://www.mobil.com/en/lubricants/for-personal-vehicles/our-products/motor-oils/mobil-0w-16-low-viscosity-oils#t=https%3A%2F%2Fwww.mobil.com%2Fen%2Flubricants%2Ffor-personal-vehicles%2Four-products%2Fmotor-oils%2Fmobil-0w-16-low-viscosity-oils (accessed June 20, 2023).

[173] Akoglu H. User's guide to correlation coefficients. Turkish J Emerg Med 2018;18:91–3.

[174] Govindaraj P, Sokolova A, Salim N, Juodkazis S, Fuss FK, Fox B, et al. Distribution states of graphene in polymer nanocomposites: A review. Compos Part B Eng 2021;226:109353.

[175] Mypati S, Sellathurai A, Kontopoulou M, Docoslis A, Barz DPJ. High concentration graphene nanoplatelet dispersions in water stabilized by graphene oxide. Carbon N Y 2021;174:581–93.

[176] Gegner J. Tribology: Fundamentals and Advancements. IntechOpen; 2013.

[177] Jiang X, Reichelt K, Stritzker B. The hardness and Young's modulus of amorphous hydrogenated carbon and silicon films measured with an ultralow load indenter. J Appl Phys 1989;66:5805–8.

[178] Chen X, Du Y, Chung Y-W. Commentary on using H/E and H3/E2 as proxies for fracture toughness of hard coatings. Thin Solid Films 2019;688:137265.

[179] Leyland A, Matthews A. On the significance of the H/E ratio in wear control: a nanocomposite coating approach to optimised tribological behaviour. Wear 2000;246:1–11.

[180] Leyland A, Matthews A. Design criteria for wear-resistant nanostructured and glassy-metal coatings. Surf Coatings Technol 2004;177:317–24.

[181] Ni W, Cheng Y-T, Lukitsch MJ, Weiner AM, Lev LC, Grummon DS. Effects of the ratio of hardness to Young's modulus on the friction and wear behavior of bilayer coatings. Appl Phys Lett 2004;85:4028–30.

[182] Manier C-A, Theiler G, Spaltmann D, Woydt M, Ziegele H. Benchmark of thin film coatings for lubricated slip-rolling contacts. Wear 2010;268:1442–54.

[183] Trtik P, Kaufmann J, Volz U. On the use of peak-force tapping atomic force microscopy for quantification of the local elastic modulus in hardened cement paste. Cem Concr Res 2012;42:215–21.

[184] European Standard, prEN 1071-3:2002 E: Determination of Adhesion by a Scratch Test, CEN Central Secretariat, Stassartstraat 36, 1000 Brussels, Belgium. n.d.

[185] Owens AG, Brühl S, Simison S, Forsich C, Heim D. Comparison of Tribological Properties of Stainless Steel with Hard and Soft DLC Coatings. Procedia Mater Sci 2015;9:246–53.

[186] Kasiorowski T, Lin J, Soares P, Lepienski CM, Neitzke CA, de Souza GB, et al. Microstructural and tribological characterization of DLC coatings deposited by plasma enhanced techniques on steel substrates. Surf Coatings Technol 2020;389:125615.

[187] Rafiee MA, Rafiee J, Wang Z, Song H, Yu Z-Z, Koratkar N. Enhanced Mechanical Properties of Nanocomposites at Low Graphene Content. ACS Nano 2009;3:3884–90.

[188] Li H, Sun P, Cheng D. Structure and properties of DLC films deposited on Mg alloy at different C2H2 flows of magnetron sputtering process. Coatings 2021;11:815.

[189] Li ZQ, Lu CJ, Xia ZP, Zhou Y, Luo Z. X-ray diffraction patterns of graphite and turbostratic carbon. Carbon N Y 2007;45:1686–95.

[190] Yatsuzuka M, Oka Y, Nishijima M, Hiraga K. Microstructure of interface for high-adhesion DLC film on metal substrates by plasma-based ion implantation. Vacuum 2008;83:190–7.

[191] Brydson R, Daniels H, Brown A, Scott A, Nichells A, Rand B. Electron Energy Loss Spectroscopy (EELS) At the Magic Angle. Microsc Microanal 2001;7:1178–9.

[192] Liu ACY, Arenal R, Miller DJ, Chen X, Johnson JA, Eryilmaz OL, et al. Structural order in near-frictionless hydrogenated diamondlike carbon films probed at three length scales via transmission electron microscopy. Phys Rev B 2007;75:205402.

[193] Tuinstra F, Koenig J Lo. Raman spectrum of graphite. J Chem Phys 1970;53:1126–30.

[194] Singha A, Ghosh A, Roy A, Ray NR. Quantitative analysis of hydrogenated diamondlike carbon films by visible Raman spectroscopy. J Appl Phys 2006;100:44910.

[195] Laukkanen A, Holmberg K, Ronkainen H, Stachowiak G, Podsiadlo P, Wolski M, et al. Topographical orientation effects on surface stresses influencing on wear in sliding DLC contacts, Part 2: Modelling and simulations. Wear 2017;388:18–28.

[196] Egerton RF. Physical Principles of Electron Microscopy: An Introduction to TEM, SEM, and AEM. Springer International Publishing; 2016.

[197] Noval VE, Carriazo JG. Fe 3 O 4-TiO 2 and Fe 3 O 4-SiO 2 core-shell powders synthesized from industrially processed magnetite (Fe 3 O 4) microparticles. Mater Res 2019;22:e20180660.

[198] Guimarey MJG, Viesca JL, Abdelkader AM, Thomas B, Hernández Battez A, Hadfield M. Electrochemically exfoliated graphene and molybdenum disulfide nanoplatelets as lubricant additives. J Mol Liq 2021:116959.

[199] Brittain R, Liskiewicz T, Morina A, Neville A, Yang L. Diamond-like carbon graphene nanoplatelet nanocomposites for lubricated environments. Carbon N Y 2023;205:485–98.

[200] Won M-S, Penkov O V, Kim D-E. Durability and degradation mechanism of graphene coatings deposited on Cu substrates under dry contact sliding. Carbon N Y 2013;54:472–81.

[201] Swain BP. The analysis of carbon bonding environment in HWCVD deposited a-SiC: H films by XPS and Raman spectroscopy. Surf Coatings Technol 2006;201:1589–93.

[202] Zhiqiang F, Jian S, Chengbiao W, Wei Z, Wen Y, Zhijian P, et al. Tribological performance of DLC coatings deposited by ion beam deposition under dry friction and oil lubricated conditions. Vacuum 2013;94:14–8.

[203] Manoharan MP, Lee H, Rajagopalan R, Foley HC, Haque MA. Elastic properties of 4–6 nm-thick glassy carbon thin films. Nanoscale Res Lett 2010;5:14–9.

[204] Qi J, Chan CY, Bello I, Lee CS, Lee ST, Luo JB, et al. Film thickness effects on mechanical and tribological properties of nitrogenated diamond-like carbon films. Surf Coatings Technol 2001;145:38–43.

[205] Huang Y, Wang Q, Wang M, Fei Z, Li M. Characterization and analysis of DLC films with different thickness deposited by RF magnetron PECVD. Rare Met 2012;31:198–203.

[206] Salvadori MC, Martins DR, Cattani M. DLC coating roughness as a function of

film thickness. Surf Coatings Technol 2006;200:5119–22.

[207] Erdemir A, Martin JM. Superior wear resistance of diamond and DLC coatings. Curr Opin Solid State Mater Sci 2018;22:243–54.

[208] Wang YX, Zhang S. Toward hard yet tough ceramic coatings. Surf Coatings Technol 2014;258:1–16.

[209] Lara LOC, De Mello JDB. Influence of layer thickness on hardness and scratch resistance of Si-DLC/CrN coatings. Tribol Surfaces Interfaces 2012;6:168–73.

[210] Dorner A, Schürer C, Reisel G, Irmer G, Seidel O, Müller E. Diamond-like carbon-coated Ti6Al4V: influence of the coating thickness on the structure and the abrasive wear resistance. Wear 2001;249:489–97.

[211] Chen K-W, Lin J-F. The study of adhesion and nanomechanical properties of DLC films deposited on tool steels. Thin Solid Films 2009;517:4916–20.

[212] Takeuchi S, Tanji A, Miyazawa H, Murakawa M. Synthesis of thick DLC film for micromachine components. Thin Solid Films 2004;447:208–11.

[213] Patterson JR, Kudryavtsev A, Vohra YK. X-ray diffraction and nanoindentation studies of nanocrystalline graphite at high pressures. Appl Phys Lett 2002;81:2073–5.

[214] McMaster SJ. Nanomechanical Characterisation of Diamond-Like Carbon Coatings for Tribological Performance 2020.

[215] Mohseni Taromsari S, Salari M, Bagheri R, Faghihi Sani MA. Optimizing tribological, tensile & in-vitro biofunctional properties of UHMWPE based nanocomposites with simultaneous incorporation of graphene nanoplatelets (GNP) & hydroxyapatite (HAp) via a facile approach for biomedical applications. Compos Part B Eng 2019;175:107181.

[216] Casimir D, Alghamdi H, Ahmed IY, Garcia-Sanchez R, Misra P. Raman spectroscopy of graphene, graphite and graphene nanoplatelets. IntechOpen London, UK; 2019.

[217] Ferrari AC, Basko DM. Raman spectroscopy as a versatile tool for studying the properties of graphene. Nat Nano 2013;8:235–46.

[218] Ferrari AC, Robertson J. Raman spectroscopy of amorphous, nanostructured, diamond–like carbon, and nanodiamond. Philos Trans R Soc London Ser A Math Phys Eng Sci 2004;362:2477–512.

[219] Mangel M, Samaniego FJ. Abraham Wald's work on aircraft survivability. J Am Stat Assoc 1984;79:259–67.

[220] Ala'A A-A, Eryilmaz O, Erdemir A, Kim SH. Nano-texture for a wear-resistant and near-frictionless diamond-like carbon. Carbon N Y 2014;73:403–12.

[221] Kim D-W, Kim K-W. Effects of sliding velocity and normal load on friction and wear characteristics of multi-layered diamond-like carbon (DLC) coating prepared by reactive sputtering. Wear 2013;297:722–30.

[222] Austin L, Liskiewicz T, Kolev I, Zhao H, Neville A. The influence of anti-wear additive ZDDP on doped and undoped diamond-like carbon coatings. Surf

Interface Anal 2015;47:755–63.

[223] Podgornik B, Sedlaček M, Vižintin J. Compatibility of DLC coatings with formulated oils. Tribol Int 2008;41:564–70.

[224] Kolawole FO, Kolawole SK, Varela LB, Owa AF, Ramirez MA, Tschiptschin AP. Diamond-like carbon (DLC) coatings for automobile applications. Eng Appl Diam 2020.

[225] Nadeem I, Malok M, Kovač J, Bin Yaqub T, Cavaleiro A, Kalin M. Superior macro-scale tribological performance of steel contacts based on graphene quantum dots in aqueous glycerol. Tribol Int 2023;181:108328.

[226] Jiang J, Arnell RD. The effect of substrate surface roughness on the wear of DLC coatings. Wear 2000;239:1–9.

[227] Ogwu AA, Lamberton RW, Morley S, Maguire P, McLaughlin J. Characterisation of thermally annealed diamond like carbon (DLC) and silicon modified DLC films by Raman spectroscopy. Phys B Condens Matter 1999;269:335–44.

[228] Kaneko S, Aono M, Pruna A, Can M, Mele P, Ertugrul M, et al. Carbon Related Materials: Commemoration for Nobel Laureate Professor Suzuki Special Symposium at IUMRS-ICAM2017. Springer Nature Singapore; 2020.

[229] Polaki SR, Kumar N, Madapu K, Ganesan K, Krishna NG, Srivastava SK, et al. Interpretation of friction and wear in DLC film: role of surface chemistry and test environment. J Phys D Appl Phys 2016;49:445302.

[230] Sanchez-Lopez JC, Erdemir A, Donnet C, Rojas TC. Friction-induced structural transformations of diamondlike carbon coatings under various atmospheres. Surf Coatings Technol 2003;163:444–50.

[231] Suzuki M, Saito T, Tanaka A. Tribological properties of DLC films against different steels. Wear 2013;304:83–7.

[232] de Faria DLA, Venâncio Silva S, de Oliveira MT. Raman microspectroscopy of some iron oxides and oxyhydroxides. J Raman Spectrosc 1997;28:873–8.

[233] Oh SJ, Cook DC, Townsend HE. Characterization of iron oxides commonly formed as corrosion products on steel. Hyperfine Interact 1998;112:59–66.

[234] Haque T, Morina A, Neville A, Kapadia R, Arrowsmith S. Effect of oil additives on the durability of hydrogenated DLC coating under boundary lubrication conditions. Wear 2009;266:147–57.

[235] Chen X, Li J. Superlubricity of carbon nanostructures. Carbon N Y 2020;158:1–23.

[236] Huang Y, Yao Q, Qi Y, Cheng Y, Wang H, Li Q, et al. Wear evolution of monolayer graphene at the macroscale. Carbon N Y 2017;115:600–7.

[237] Chen Z, Vazirisereshk MR, Khajeh A, Martini A, Kim SH. Effect of atomic corrugation on adhesion and friction: A model study with graphene step edges. J Phys Chem Lett 2019;10:6455–61.

[238] Dai W, Li X, Wu L, Wang Q. Influences of target power and pulse width on the

growth of diamond-like/graphite-like carbon coatings deposited by high power impulse magnetron sputtering. Diam Relat Mater 2021;111:108232.

[239] Kinoshita H, Ippei I, Sakai H, Ohmae N. Synthesis and mechanical properties of carbon nanotube/diamond-like carbon composite films. Diam Relat Mater 2007;16:1940–4.

[240] Wei C, Yang J-F. A finite element study on the hardness of carbon nanotubes-doped diamond-like carbon film. J Mater Res 2012;27:330–8.

[241] McMaster SJ, Liskiewicz TW, Neville A, Beake BD. Probing fatigue resistance in multi-layer DLC coatings by micro- and nano-impact: Correlation to erosion tests. Surf Coatings Technol 2020;402:126319.

[242] Kodali P, Walter KC, Nastasi M. Investigation of mechanical and tribological properties of amorphous diamond-like carbon coatings. Tribol Int 1997;30:591–8.

[243] Shi X, Liskiewicz TW, Beake BD, Chen J, Wang C. Tribological performance of graphite-like carbon films with varied thickness. Tribol Int 2020;149:105586.

[244] Chung J-W, Lee C-S, Ko D-H, Han JH, Eun KY, Lee K-R. Biaxial elastic modulus of very thin diamond-like carbon (DLC) films. Diam Relat Mater 2001;10:2069–74.

[245] Politano A, Chiarello G. Probing the Young's modulus and Poisson's ratio in graphene/metal interfaces and graphite: a comparative study. Nano Res 2015;8:1847–56.

[246] Berman D, Erdemir A, Sumant A V. Approaches for Achieving Superlubricity in Two-Dimensional Materials. ACS Nano 2018;12:2122–37.

[247] Rabinowicz E, Tanner RI. Friction and wear of materials. J Appl Mech 1966;33:479.

[248] Liu Y, Erdemir A, Meletis EI. A study of the wear mechanism of diamond-like carbon films. Surf Coatings Technol 1996;82:48–56.

[249] Scharf TW, Singer IL. Third Bodies and Tribochemistry of DLC Coatings BT - Tribology of Diamond-Like Carbon Films: Fundamentals and Applications. In: Donnet C, Erdemir A, editors., Boston, MA: Springer US; 2008, p. 201–36.

[250] Deng D, Yu L, Pan X, Wang S, Chen X, Hu P, et al. Size effect of graphene on electrocatalytic activation of oxygen. Chem Commun 2011;47:10016–8.

[251] Grill A. Tribology of diamondlike carbon and related materials: an updated review. Surf Coatings Technol 1997;94:507–13.

[252] Kim D-W, Kim K-W. Effects of sliding velocity and ambient temperature on the friction and wear of a boundary-lubricated, multi-layered DLC coating. Wear 2014;315:95–102.

[253] Cao Z, Zhao W, Liu Q, Liang A, Zhang J. Super-Elasticity and Ultralow Friction of Hydrogenated Fullerene-Like Carbon Films: Associated with the Size of Graphene Sheets. Adv Mater Interfaces 2018;5:1701303.

[254] Ye Z, Balkanci A, Martini A, Baykara MZ. Effect of roughness on the layer-

dependent friction of few-layer graphene. Phys Rev B 2017;96:115401.

[255] Penkov O, Kim H-J, Kim H-J, Kim D-E. Tribology of graphene: a review. Int J Precis Eng Manuf 2014;15:577–85.

[256] Li S, Li Q, Carpick RW, Gumbsch P, Liu XZ, Ding X, et al. The evolving quality of frictional contact with graphene. Nature 2016;539:541–5.

[257] Ronkainen H, Varjus S, Koskinen J, Holmberg K. Differentiating the tribological performance of hydrogenated and hydrogen-free DLC coatings. Wear 2001;249:260–6.

[258] Aboua KAM, Umehara N, Kousaka H, Deng X, Tasdemir HA, Mabuchi Y, et al. Effect of carbon diffusion on friction and wear properties of diamond-like carbon in boundary base oil lubrication. Tribol Int 2017;113:389–98.

[259] Bartocha D, Janerka K, Suchoń J. Charge materials and technology of melt and structure of gray cast iron. J Mater Process Technol 2005;162:465–70.

[260] Papadopulos F, Spinelli M, Valente S, Foroni L, Orrico C, Alviano F, et al. Common Tasks in Microscopic and Ultrastructural Image Analysis Using ImageJ. Ultrastruct Pathol 2007;31:401–7.

[261] Menezes PL, Nosonovsky M, Ingole SP, Kailas S V, Lovell MR. Tribology for Scientists and Engineers: From Basics to Advanced Concepts. Springer New York; 2013.

[262] Sudarshan TS. Surface Modification Technologies: Proceedings of the 20th International Conference on Surface Modification Technologies. ASM International; 2007.

Appendix A – Initial Testing: Uncoated Substrate

Initial testing was completed on an uncoated polished HSS sample to determine a baseline of a CI counter-body for both friction and transfer film formation. This test (**Figure A.1**) was undertaken for 6 hours, with a hanging load of 11.5 Kg, in a 100°C base-oil at a speed of 20 mm/s.

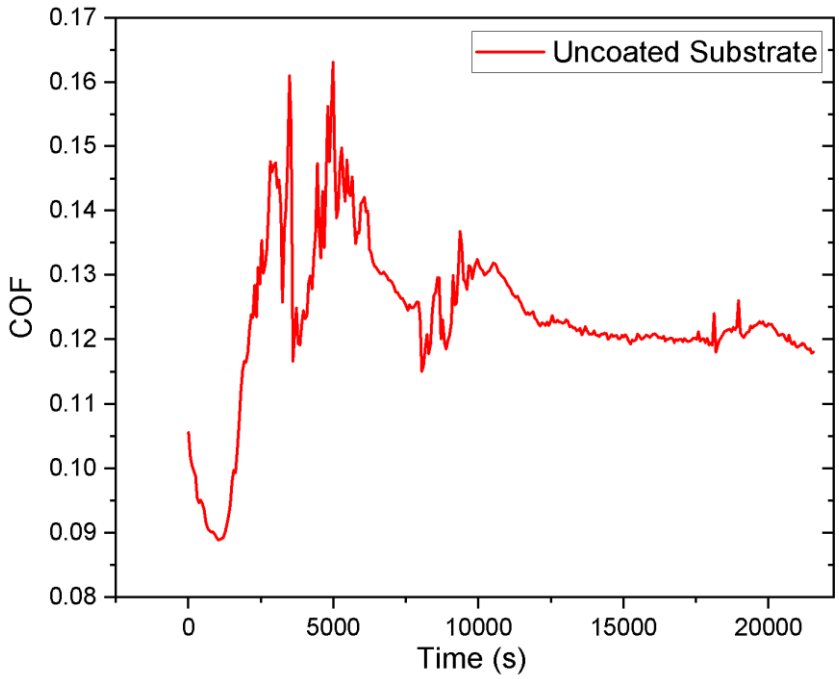

Figure A.1 *Frictional trace for a CI counter-body on an uncoated HSS substrate.*

The initial testing show that the frictional trace is initially unstable, lowering to a COF of ~0.09 to a maximum of ~0.16, before remaining around 0.12 to'0.13. Raman Spectra were collected before and after the testing on both the counter-body and substrate to determine if there was any graphitisation of the CI counter-body during tribological testing. Grey cast iron contains some graphite crystals [259], and there were some initial concerns that this may interfere with the results from a composite consisting of DLC and GNP. The Raman spectra from the unworn and worn counter-body, along with wear scar on a HSS substrate are shown in **Figure A.2** and **Figure A.3** respectively.

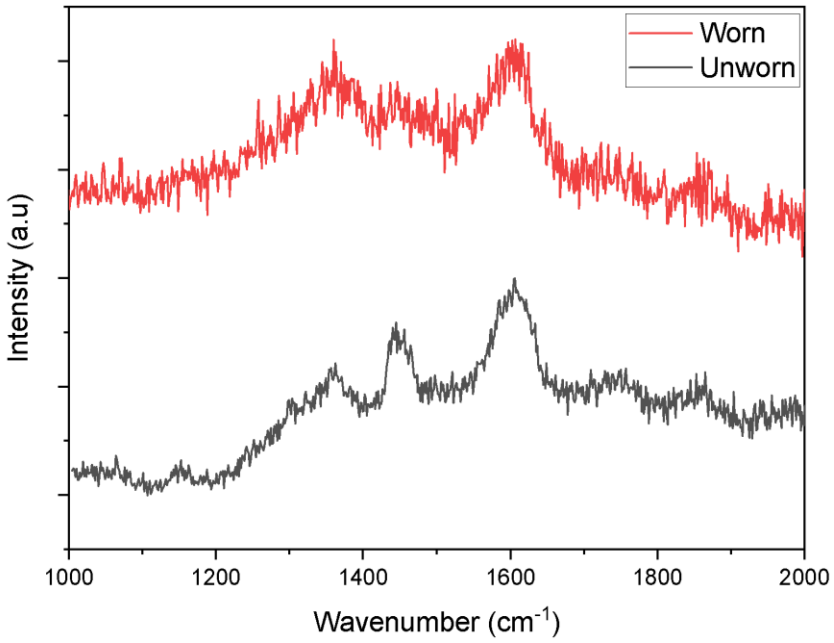

Figure A.2 *Raman spectra from the CI counter-body before and after 6 hours of wear.*

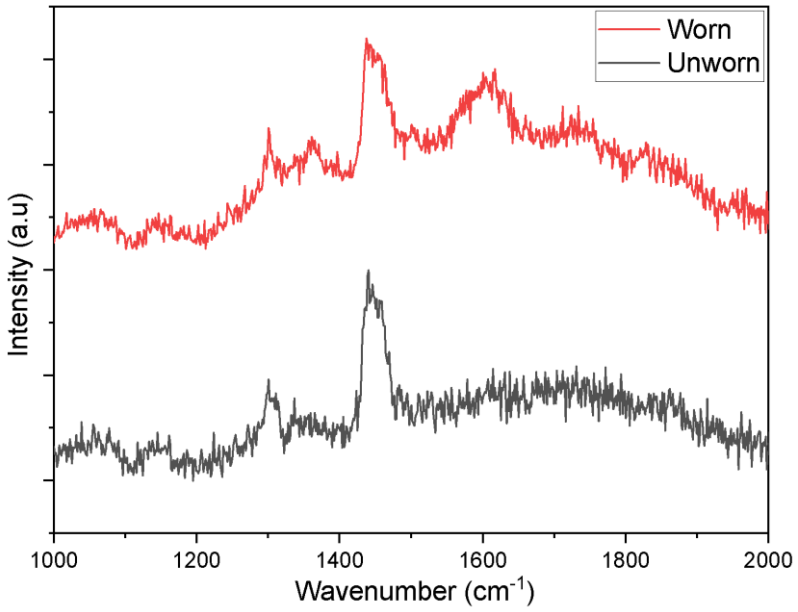

Figure A.3 *Raman spectra for wear scar on uncoated HSS substrate before and after 6 hours of wear.*

The presence of D (~1350 cm^{-1}) and G (1580cm^{-1}) peaks on the CI counter-body were detected and unchanged after wear, indicating that if graphitisation was occurring it is not at a scale large enough to affect the results. There were no clear results to indicate the presence of a carbon graphitic layer on the uncoated HSS substrate.

Appendix B – Initial Testing: GNP Layer Before DLC Deposition

Initial tribological testing was completed on the GNP layer after heat treatment but before DLC deposition. The test was completed using the same methodology as presented in Section 3.4.

The GNP/NMP concentration used was 1 mg / ml and the heat treatment was completed for 180 minutes at 200°C. The frictional trace is presented in **Figure B.1.** The frictional trance was lower than that of uncoated steel.

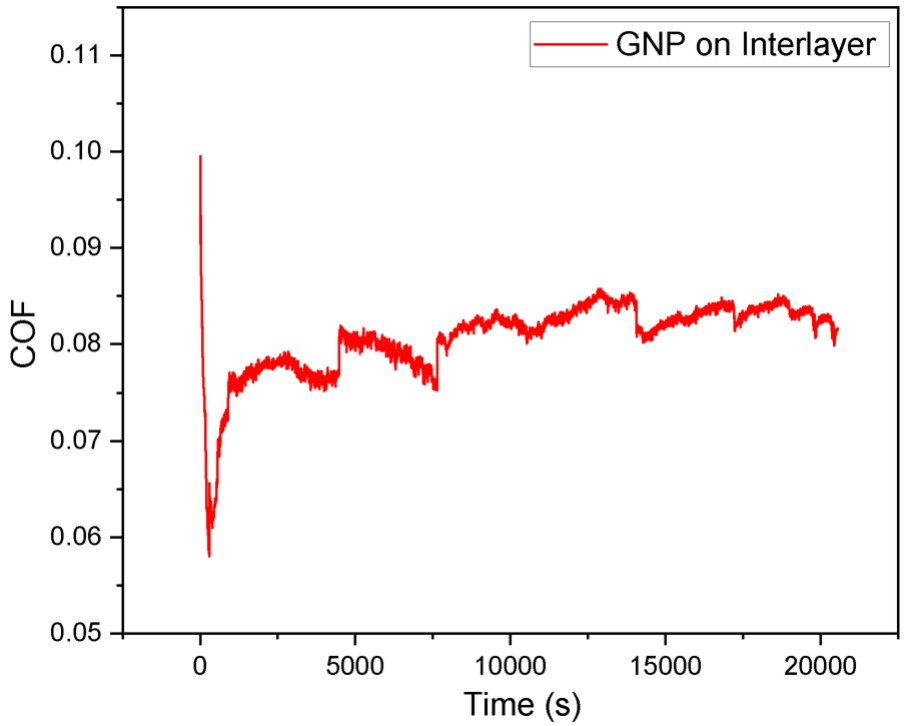

Figure B.1 *Frictional Trace GNP on Adhesion Layer.*

Appendix C – Initial Testing: Testing in Unlubricated Conditions

Tribological testing was conducted in dry (unlubricated) conditions to determine the effectiveness of the DLC-GNP films. The initial results using a 280N load resulted in delamination of the film almost instantly (**Figure C-1**), so the testing at this load was stopped.

Figure C.1 *Delamination of DLC-GNP film under 280N load unlubricated.*

Appendix D - GNP Coverage Measurements

The coverage of GNP is evaluated post-DLC deposition using an optical microscope equipped with a 5x objective lens, while the turret lens is set to 1x, providing a pixel size of 3.95 µm. The microscope was equipped with an in-build scale bar which auto calibrates to ensure accuracy. For each sample, a total of five images are captured at predetermined areas, as indicated in **Figure D.1.** The acquired images are analysed using the freeware ImageJ software package. The images are first converted to 8-bit black and white, and the colour threshold is adjusted to isolate only the GNP islands. This analytical approach aligns with the method employed by Papadopulos *et al.* [260]. The before and after images processed using the ImageJ software are presented in **Figure D.2**. The coverage percentage is determined by the 'analyse' function in the software, accompanied by the calculation of standard deviation. Additionally, the ImageJ software offers the capability to measure the sizes of individual GNP islands through the built-in size measurement feature.

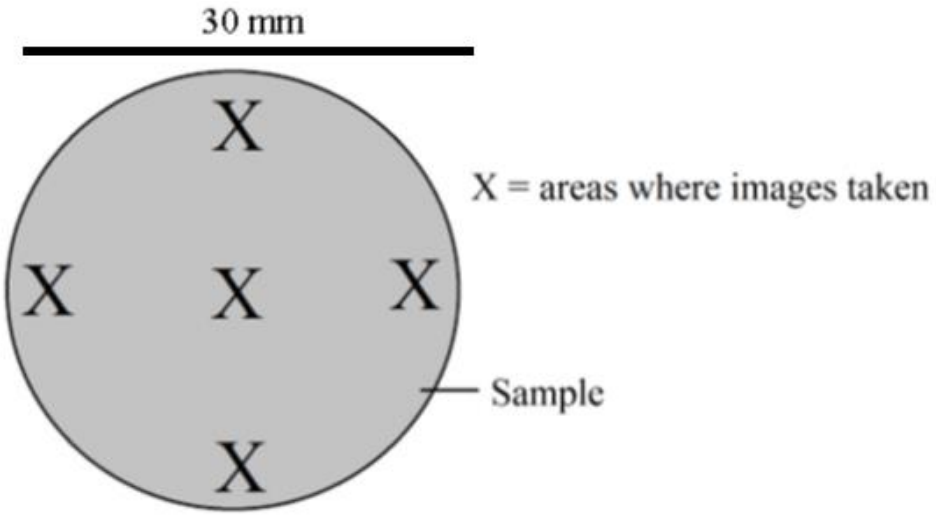

Figure D.1 *Areas on all samples where images are taken.*

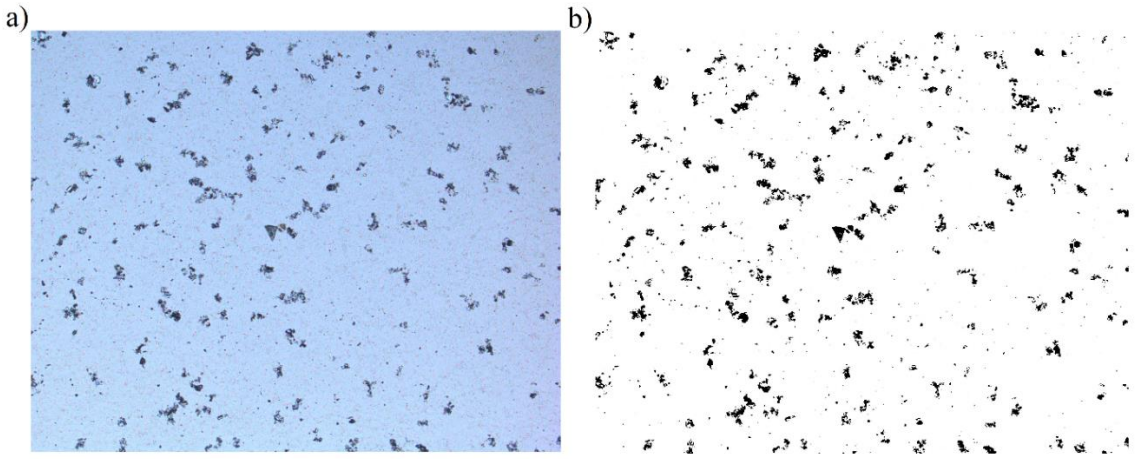

Figure D.2 *Optical images showing (a) raw image and (b) processed image of GNP islands on a sample after spin coating and DLC deposition.*

Appendix E – Calotest Thickness Procedures

The rotation speed is set to 300 rpm, which is set between 180 – 420 seconds, depending on the coating DLC deposition time. The general principle for the calotest ball crater method is shown in **Figure E.1**.

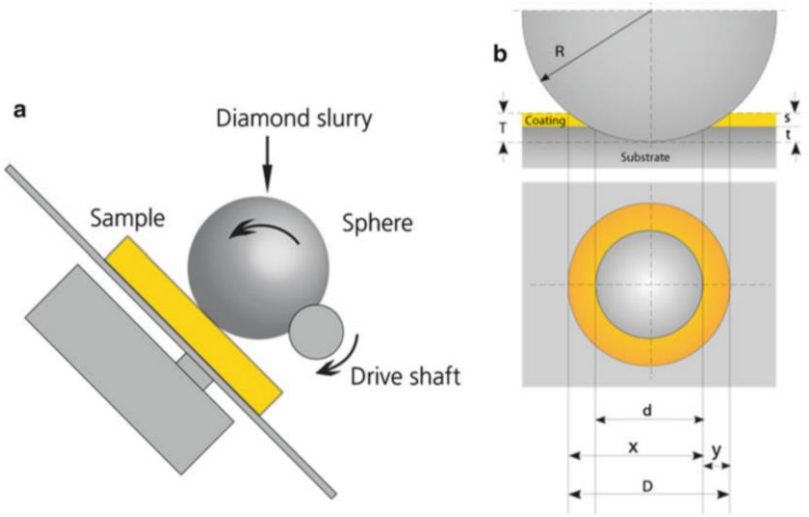

Figure E.1 (a) General principle for the creation of a ball crater, and (b) parameters used to calculate the coating thickness [261].

The surface is imaged after the ball crater has been created, with the x and y components (m) identified as shown in the example (**Figure E.2)**. S is the thickness (m) of the coating and calculated using the **Equation E.1**:

$$t = \frac{x \times y}{\phi\ ball} \qquad \textit{Equation E.1}$$

Where ϕ ball is the diameter of the ball used (m), x is the inner diameter (m) of the crater. And y being the out diameter (m).

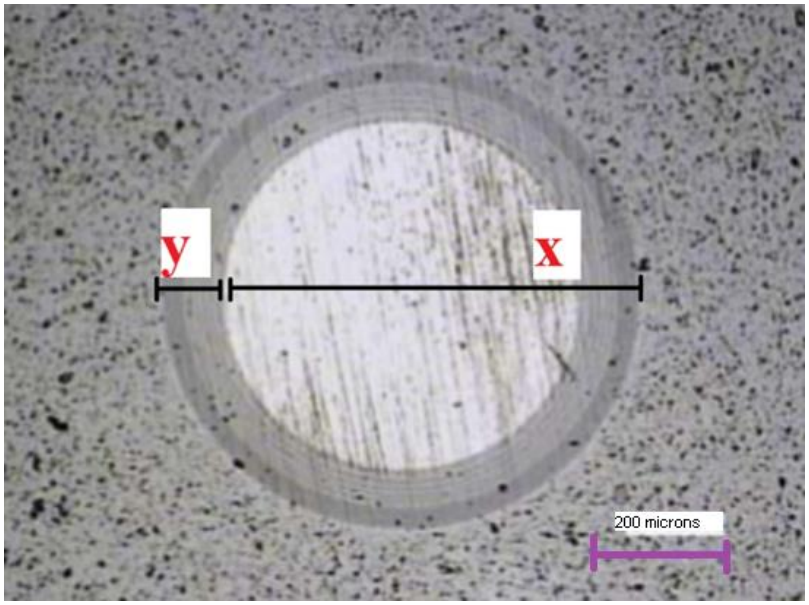

Figure E.2 - *Example of a calotest with the x and y components identified* [262]

To ensure accuracy, the thickness of the coatings is verified for specific samples by cross-sectioning using a Focused Ion Beam - Scanning Electron Microscopy (FIB-SEM) technique. The SEM section (**Section 3.3.4**) presents a detailed discussion of this process, providing comprehensive insights into its implementation and analysis.